Development and application of numerical modeling for evaluating and predicting hydrogeochemical processes temporally and spatially evolving in petroleum reservoirs

Case studies: Miller oilfield (UK North Sea) and Siri oilfield (Danish North Sea)

Doctoral Thesis
(Dissertation)

to be awarded the degree
Doctor rerum naturalium (Dr. rer. nat.)

submitted by

M. Sc. Yunjiao Fu
from Chengdu, P.R. China

approved by the Faculty of Energy and Management Science
Clausthal University of Technology

Date of oral examination
07 March 2014

Chairperson of the Board of Examiners

Professor Dr.-Ing. Daniel Goldmann (TU Clausthal)

Supervising tutor

Professor Dr. Wolfgang van Berk (TU Clausthal)

Reviewer

PD Dr. Hans-Martin Schulz (Helmholtz Centre Potsdam)

Acknowledgments

Several persons have made dedicated and kind contributions to this Ph.D. thesis and to me personally. I would sincerely like to express my gratitude to all these persons

I would like to gratefully acknowledge Prof. Dr. Wolfgang van Berk for his advice, guidance, support and beneficial academic discussions.

I express my gratitude to PD. Dr. Hans-Martin Schulz (Helmholtz Centre Potsdam) for his encouragement, ideas, organization of sampling and analyzing, as well as intense academic discussions.

Special thanks go to DONG Energy and the Geological Survey of Denmark and Greenland for supporting with respect to samples and data for this research. Dr. Niels H. Schovsbo (Geological Survey of Denmark and Greenland) and Dr. Johan B. Svendsen (Dong Energy) are particularly thanked for organizing und supporting sampling and for many useful discussions.

Many thanks to Prof. Dr. Kurt Mengel, Dr. Thomas Schirmer and Dr. Carl-Diedrich Sattler for their assistance in performing the XRD and XRF measurements (all afore mentioned from Clausthal University of Technology).

Nana Mu (Helmholtz Centre Potsdam) is thanked for her helpful academic discussions.

Further thanks go to Dr. Helga Kemnitz und Ilona Schäpan for support at the SEM. Dr. Richard Wirth is acknowledged for HRTEM measurements (all three afore mentioned from Helmholtz Centre Potsdam).

I am grateful to Prof. Dr. Philippe Vieillard (University of Poitiers) for helping to calculate the thermodynamic data of silicates.

Finally, I also would like to thank all employees of the Institute of Geology and Paleontology and of the Institute of Disposal Research.

Kurzfassung

Die Gesteinsmatrix der meisten Ölreservoire kann als chemisch reaktiv aufgefasst werden. Technische Maßnahmen oder geogene Prozesse in solchen Reservoiren ändern Temperatur- und Druckbedingungen sowie die hydrogeochemischen Verhältnisse der diagenetischen Milieus. Solche Änderungen lösen eine komplexe hydrogeochemische Reaktionskette aus, an der Mineralphasen, Formationswässer, ölbürtige, im Wasser gelöste Kohlenwasserstoffe und Gase beteiligt sind. Einerseits können solche Reaktionen eine Auflösung von Mineralphasen verursachen und folglich die Porosität und die Permeabilität der Gesteinsmatrix verbessern. Andererseits können sie zur Ausfällung von Mineralen führen und dadurch die Gesteinsporosität und -permeabilität stark verringern.

Um hydrogeochemische Prozesse und ihre Auswirkungen auf die Eigenschaften von Reservoiren zu beurteilen, ist es für ein effizientes Reservoir-Engineering notwendig, die im geologisch-technischen System ablaufenden Prozesse qualitativ zu identifizieren und quantitativ mit ihrer räumlich-zeitlichen Entwicklung abzubilden. Wegen der Schwierigkeiten bei der Probenahme und einer begrenzten Anzahl von repräsentativen Proben aus Reservoiren reichen chemisch-mineralogische und petrographische Untersuchungsverfahren allein nicht aus, um hydrogeochemische Prozesse zu identifizieren und zu quantifizieren. Im Gegensatz dazu kann eine kombinierte Anwendung hydrogeochemischer Modellierungen mit ausgewählten Untersuchungsverfahren diese Anforderungen erfüllen und zusätzlich die weitere Entwicklung der Prozesse prognostizieren.

Hydrogeochemische Prozesse werden als diagenetische Merkmale im Gestein gespeichert und zeigen sich in der Entwicklung der Porenwasserbeschaffenheit. In der vorliegenden Arbeit werden hydrogeochemische Modelle vorgestellt, die (1) die zeitliche Entwicklung der Formationswasserbeschaffenheit im Miller-Ölfeld (UK North Sea) abbilden und (2) die für die diagenetischen Merkmale der Reservoirgesteine des Siri-Ölfelds (Danish North Sea) relevanten Prozesse ermitteln können. Um ein vertieftes und quantitatives Prozessverständnis zu gewinnen, werden auf chemisch-thermodynamischen Gesetzen basierende hydrogeochemische Modelle stufenweise von einfachen Batch-Modellen zu 1D oder 3D Transportmodellen mit den Programmen PHREEQC, PHREEQCI und PHAST aufgebaut. Batch-Modellierungen ermöglichen lediglich einen ersten Einblick, welche Prozesse abgelaufen sein könnten. Hydrogeochemische 1D- und/oder 3D-Transportportmodelle erlauben es zusätzlich, zeitliche und räumliche Entwicklungen zu prognostizieren. Deshalb stellen hydrogeochemische Modellierungen hilfreiche Werkzeuge dar, um räumlich-zeitliche Entwicklungen hydrogeochemischer Prozesse besser zu verstehen. Darauf aufbauend können Prozesse und ihre Auswirkungen auf die Reservoireigenschaften mit ingenieurtechnischen Maßnahmen beeinflusst und optimiert werden.

Abstract

Most rock matrices of oil reservoirs can be considered to be chemically reactive. Technical measures or geological processes alter temperature, pressure and hydrogeochemical conditions in oil reservoirs. Such changes trigger a complex hydrogeochemical reaction chain among minerals, formation water, oil-derived aqueous hydrocarbons and gases. On the one hand, such reactions can result in mineral dissolution which could enhance reservoir porosity-permeability properties. On the other hand, hydrogeochemical processes can cause formation of minerals. These processes could dramatically reduce porosity and permeability, and may cause formation damage.

To evaluate such hydrogeochemical processes and their consequences on reservoir properties, it is necessary for successful reservoir engineering (1) to identify such hydrogeochemical processes in reservoirs and (2) to plausibly predict the spatial and temporal distribution of these processes. Difficulties in obtaining samples from deep subsurface oil reservoirs and a limited number of representative samples may limit a meaningful application of analytical methods to exactly investigate hydrogeochemical processes in oil reservoirs. Moreover, the exclusive application of analytical methods has limited potential for quantitative predictions of processes which are high on the agenda for successful petroleum reservoir engineering. In contrast, a combination of hydrogeochemical modeling with analytical results could satisfy such demands and additionally predict further process evolution.

Hydrogeochemical processes are reflected by diagenetic features in sediments and by the associated compositional development of pore water. Thus, a quantitative reproduction of one of the both features by hydrogeochemical modeling can enables us to conclude on hydrogeochemical processes. In this study, analytical and modeling results are applied to retrace the hydrogeochemical processes in two case studies: the Miller oilfield (UK North Sea) in terms of the compositional development of its produced water and the Siri oilfield (Danish North Sea) based on its diagenetic features in sediments. This study applies hydrogeochemical modeling based on thermodynamics of chemical equilibrium. For a better understanding of processes, hydrogeochemical models are gradually developed from simple batch models to 1D and/or 3D reactive transport models by using the program codes PHREEQC, PHREEQCI or PHAST. Batch modeling is one of a series of basic prerequisites for building up a transport model and provides a first insight which hydrogeochemical processes tend to occur. Moreover, 1D and/or 3D hydrogeochemical models integrate temporal and spatial aspects. Therefore, 1D and/or 3D modeling can exactly identify hydrogeochemical processes and quantitatively predict their spatial and temporal distribution. Hydrogeochemical modeling is therefore a reasonable tool to quantify hydrogeochemical processes in oilfields and deepens the reservoir understanding. Consequently, hydrogeochemical modeling provides an efficient tool for a better reservoir management.

Contents

1. Introduction

The term petroleum comprises oil and gas which are the main source of energy. Petroleum is generated by mass conversions and chemical reactions in source rocks, and its migration and accumulation in reservoir rocks result from a sequence of geological events under specified conditions (Seewald, 2003). After charging of a reservoir by oil and/or gas, chemical processes do not completely cease and several new chemical components form in the system. Displacement of aqueous fluids (pore water) by hydrocarbons results in the generation of an extensive oil-water interface (Seewald, 2003). The term oil-water contact (OWC) or oil-water transition zone (OWTZ), which stretches between the oil leg and the water leg of the reservoir rock column. In addition to these "macro" OWC or OWTZ, "micro" OWC develop at water-coated mineral surfaces (irreducible, immobile water) within the oil-filled parts of the water-wet reservoirs. Due to establishment of metastable equilibrium conditions at oil-water contacts (Helgeson et al., 1993), organic-inorganic interactions among hydrocarbons, aqueous solutions, mineral phases and coexisting gas phase inevitably proceed at these oil-water interfaces. Moreover, methanogenic oil degradation occurs as a primary mechanism at the reactive site OWC (Head et al., 2003; Later et al., 2006; van Berk et al., 2013). In consequence, the OWC or OWTZ is a hot spot of hydrogeochemical processes in the reservoir rocks. Besides such geological processes, technical measures applied in petroleum reservoirs (e.g., water injection into oil reservoirs) can also trigger a series of hydrogeochemical processes. Investigating such organic-inorganic interactions is high on the agenda for successful petroleum reservoir engineering, because they could strongly affect the petroleum reservoir's porosity-permeability properties, as well as the composition of oil and gas.

1.1 Hydrogeochemical processes evolving in petroleum reservoirs

Most rock matrices of oil reservoirs can be considered to be chemically reactive. A complex hydrogeochemical reaction chain among minerals, formation water (mobile, irreducible, or connate water), oil-derived aqueous hydrocarbons and gas (e.g., carbon dioxide) can be induced by a number of processes, such as technical measures (water injection for pressure maintenance) and geological processes (e.g., oil degradation, sedimentary deposition, inflow of external water by seismic pumping). Technical measures or geological processes alter temperature, pressure and hydrogeochemical conditions of diagenetic environments. In the wake of such changes, the equilibrium state previously prevailing in the environments is disturbed. This sequentially triggers a series of hydrogeochemical processes in order to approach a new state of chemical equilibrium with respect to organic-inorganic interactions. Helgeson et al. (1993) demonstrated by means of the Gibbs free energy minimization calculations that aqueous species (e.g., H^+, Ca^{2+}, CH_3COO^-, etc.) in oilfield formation water may achieve metastable equilibrium conditions with hydrocarbons and with minerals in reservoir rocks at

oil-water contacts. Dissolution and formation of minerals consequently occur, which strongly alter the reservoir mineral assemblage and affect the reservoir porosity-permeability properties. Besides porosity and permeability, wettability of reservoir rocks is a key factor characterizing valuable reservoir properties (Thomas et al., 1993). Wettability strongly affect the fluid flow (water and oil flow) and the wetting heterogeneity has a significant impact on oil recovery (Thomas et al., 1993; Abdallah et al., 2007). Additionally, wettability affects hydrogeochemical reactions at the rock-water interfaces and in the irreducible water within water-wet oil columns.

Water injection is commonly applied in oil reservoirs to maintain reservoir pressure, and further to increase oil production as well as to enhance oil recovery. However, the chemical incompatibility between original reservoir formation water and injected water (injection of seawater and of low salinity water into off-shore and on-shore reservoirs, respectively) triggers a web of complex hydrogeochemical water-rock-gas interactions, and consequently, causes significant scaling problems occurring in production wells as well as within the reservoir aquifer. A good example in this regard is the Miller oilfield located in the North Sea, UK. Seawater injection was applied in the siliciclastic Miller oilfield for ca. 10 years (Houston et al., 2007), but created the “arguably harshest oilfield scaling regime in the North Sea” (Wylde et al., 2006). The Miller oilfield’s scale mineral assemblage is dominated by barite ($BaSO_{4(s)}$) and may additionally contain celestite ($SrSO_{4(s)}$) and calcite ($CaCO_{3(s)}$; Wylde et al, 2006). In addition to seawater, low-salinity water injection is also often used in oil reservoirs, for instance the Ghawar oilfield which is a carbonate reservoir (Raju and Nasr-El-Din, 2004). Calcite is greatly favored over calcium- and strontium -earing sulfates in the Ghawar oilfield’s scale mineral assemblage (Raju and Nasr-El-Din, 2004). The type of scale minerals strongly varies with the type of injected water and of the reservoir rocks (siliciclastic or carbonate).

On the other hand, geological processes, which occur in petroleum reservoirs and are unaffected by technical measures, also lead to diagenetic features. However, such diagenetic features commonly differ strongly from the anthropogenic-induced processes. Such geological processes and their sequential impacts are of inevitability. Early diagenetic processes (e.g., sulfate reduction, methanogenesis), driven by re-mineralization of sedimentary organic matters, strongly alter the hydrogeochemical environment (modeled by Arning et al., 2011). In analogy, further burial causes temperature and pressure changes, which furthermore force a new round of hydrogeochemical processes. Dispersive advective mass transport of aqueous components (e.g., inflow of external water by seismic pumping) replaces the pore water which formerly filled the pore space of the reservoir rocks. This results in disequilibria among minerals, pore water and gas phase, and consequently, in a new development of hydrogeochemical processes in a dynamic system. Afterwards, parts of the hydrogeochemical processes could continue or new processes will be induced due to diffusive mass transport, although the systems gradually evolves to stagnant conditions, even more or less to closed conditions by the end. For instance, effective mass transport through the oil column can be achieved by diffusion of aqueous components dissolved in the irreducible water of a water-wet sediment

column filled by oil, although high petroleum saturation can be considered to effectively cease the advective mass transport of such aqueous components through the oil column (Worden and Morad, 2003). Even in closed systems spontaneous processes cannot be avoided. Oil degradation may evolve in closed systems (Head et al., 2003) instead of by organic carbon oxidation by oxygen or sulfate (Palmer, 1993). For instance, intensive oil degradation in the Gullfaks oilfield (North Sea, Norway) led to hydrogeochemical processes which are characterized (1) by nearly complete dissolution of plagioclase, (2) by massive formation of kaolinite, and (3) by formation of Ca-Mg-Fe carbonate to a lesser degree. Moreover, the oil degradation occurring in the Gullfaks oilfield caused a anomalously high CO_2 partial pressure (Ehrenberg and Jakobsen, 2001).

1.2 Aims

Formation of authigenic minerals possibly causing solid blockage, as well as formation of expandable clay minerals and their swelling, which are attributed to the significant mechanisms of formation damage, can result from hydrogeochemical processes. On the other hand, hydrogeochemical processes could cause mineral dissolution and therefore enhance the reservoir porosity-permeability properties. Vaughan (1987) performed experiments, in which a decrease in porosity by 8% due to $SiO_{2(s)}$ formation in intact granite results in an observed permeability reduction by 96%. Meier (2012) carried out flow through experiments in the samples of Rotliegende sandstones by using deionized water at elevated temperature and pressure conditions. Her experiment results show that the measured permeability increased by 9-16%, although no change in porosity was proven. To evaluate hydrogeochemical processes and their consequences on reservoir properties, it is thus necessary to consider that slightest decrease in porosity caused by mineral formation can induce strong reduction in permeability. For successful reservoir engineering in view of the development and fate of porosity-permeability properties in petroleum systems, a basic understanding about relevant hydrogeochemical processes has far-reaching implications. Applicable knowledge should be based on the understanding (1) whether any minerals can form in specified environments, and if so, which type and which amount of them can form, (2) which mechanisms induce their formation, (3) how their subsequent behavior develops under changed conditions, and (4) where and when their formation is distributed in petroleum systems. Such basic thinking is a prerequisite for predicting the (positive or negative) impacts of hydrogeochemical processes on reservoir properties in terms of temporal and spatial aspects. Integration of hydrogeochemical modeling results will thus support to assess the technical treatments.

Hydrogeochemical processes do not “leave everything spotless”. They can on the one hand mark diagenetic features in sediments, and on the other hand are reflected by the compositional development of pore water. Thus, a quantitative reproduction of one of both features (diagenetic features or the compositional development of pore water) by means of hydrogeochemical modeling

allows concluding on hydrogeochemical processes. In this study, the both features are used as key factors, respectively, to retrace the hydrogeochemical processes in two case studies: the Miller oilfield in terms of the compositional development of its produced water and the Siri oilfield based on its diagenetic features inherited in the reservoir sediment. The hydrogeochemical processes were induced by technical measures (the Miller oilfield) or purely geological processes (the Siri oilfield), respectively. A reproduction of the compositional trends observed in produced water or reservoir sediment by means of hydrogeochemical modeling leads (1) to the identification of hydrogeochemical processes, (2) of the prediction of their mass transfer, and (3) to the interpretation about the reasons for changes in the porosity-permeability properties of reservoir rocks.

2. Hydrogeochemical modeling approach

Hydrogeochemical processes trigger dissolution and precipitation of minerals. They could strongly affect the reservoir porosity-permeability properties. Such processes must be well investigated in order to avoid or minimize their negative consequences, before technical measures are performed in a specific reservoir system. In general, a complex web of interconnected hydrogeochemical processes temporally and spatially evolves in petroleum reservoirs. In consequence, investigating and forecasting such processes are not as straightforward as one might imagine. However, evaluation of such hydrogeochemical processes and their consequences on reservoir properties is of great necessity. This is due to the fact that slightest decrease in porosity caused by mineral formation can induce massive permeability reduction (Vaughan, 1987). Thus, it is substantial for successful reservoir engineering

(1) to specify whether any mineral can form in specific environments, and, if so, which type and which amount of them can form,

(2) to identify which mechanisms induce their formation, and

(3) to plausibly quantitatively predict the spatial and temporal distribution of their formation.

Modeling approaches are commonly applied for incorporating an accurate understanding of the hydrogeochemical processes in addition to analytical investigations of sediment and water samples. A reasonable and useful modeling technique should meet at least one of the three abovementioned requirements. Generally, calculation of saturation indices, zero-dimensional (batch) modeling, analytical modeling and reactive mass transport modeling are the most common approaches applied for investigating hydrogeochemical processes in petroleum reservoirs. Several approaches focus only on specific aspects, and as a result, their applicability could be limited. The applicability of such modeling approaches, as well as their advantages and disadvantages are discussed in the following sections.

2.1 Calculation of saturation indices

Various approaches aim to evaluate hydrogeochemical processes by calculating states of thermodynamic disequilibrium among selected minerals and pore water (in other words, by calculating saturation indices), such as the model software Downhole SAT^{TM} (French Creek Software, 2012), as well as the modeling approaches developed by Yuan and Todd (1991) and by Yuan et al. (1994). Such modeling approaches calculating saturation indices are commonly applied for evaluating scale formation in oilfields where seawater injection is performed. These approaches generally consider one injected seawater analysis and one formation water analysis that was taken from reservoirs before seawater breakthrough. These approaches mix the both water types for various mixing ratios.

Sequentially, such approaches calculate the saturation indices in the formation water-seawater mixtures under reservoir temperature-pressure conditions with respect to different minerals. For instance, the computer program DownHole SAT™ (French Creek Software, 2012) takes account of barite ($BaSO_{4(s)}$), celestite ($SrSO_{4(s)}$), calcite ($CaCO_{3(s)}$), anhydrite ($CaSO_{4(s)}$), aragonite ($CaCO_{3(s)}$), dolomite ($CaMg(CO_3)_{2(s)}$), magnesite ($MgCO_{3(s)}$), strontianite ($SrCO_{3(s)}$), witherite ($BaCO_{3(s)}$) etc. as potential scale minerals. The modeling results provided by such approaches propose that the minerals can form as scale minerals, provided that their calculated saturation indices have a positive value.

Fu et al. (2013a, 2013b) stated that the approaches based on calculations of saturation indices are incapable of achieving the demands of correctly predicting scaling processes, because water-rock gas interactions are involved in a complex reaction web. A positive calculated saturation index (SI > 0) with regard to a specific mineral does not mean that this mineral does actually form. To demonstrate this, Fu et al. (2014) considered one formation water analysis and one seawater analysis. They assumed that a formation water-seawater mixture is created from the both water types with a given mixing ratio. Additionally, it is assumed that the formation water-seawater mixture is supersaturated with regard to barite and anhydrite by calculating the initial saturation indices (SI > 0 for these two minerals). Barite precipitation will reduce the sulfate concentration of the formation water-seawater mixture. Consequently, this change in the sulfate concentration can result in an anhydrite undersaturation of this water mixture, although the initial SI calculation indicates an oversaturation with regard to anhydrite. Thus, calculations of saturation indices are incapable of correctly estimating which hydrogeochemical processes actually occur, and much less to quantify their intensity. However, modeling approaches based on calculations of saturation indices provide a first insight which hydrogeochemical processes tend to occur. This helps us to establish the basis for planning additional investigations of oil reservoirs or for developing further modeling approaches.

2.2 Zero-dimensional approach

Hydrogeochemical processes alter the chemical composition of aqueous solutions by dissolution and precipitation of minerals. In consequence, hydrogeochemical processes are on one hand reflected by diagenetic features in sediments, and on the other hand are characterized by the compositional development of water. In consequence, Houston et al. (2007) developed a new approach without temporal and spatial aspects to assess hydrogeochemical processes triggered by seawater injection into the Miller oilfield (North Sea, UK). The measured chemical composition of the produced water is the key signal to conclude on the hydrogeochemical processes in the Miller field. This approach is based on the comparison between (1) the measured chemical composition of the produced water in the Miller oilfield and (2) the chemical composition predicted from the non-reactive mixing of the injected seawater and the original formation water (Houston et al., 2007). Positive deviations of the calculated

non-reactive compositional development depending on the seawater fraction in the produced water from the measured data ($c_{calculted} > c_{measured}$) indicate dissolution of minerals containing specific elements. On the contrary, negative deviations of the calculated development from the measured data ($c_{calculted} < c_{measured}$) demonstrate precipitation of minerals comprising specific elements. The results calculated by the Houston et al. (2007)'s approach indicate that several hydrogeochemical reactions involving silica-, calcium-, barium-, sulfate-, strontium-bearing minerals were induced by seawater injection into the Miller oilfield. However, this approach is incapable of identifying which hydrogeochemical processes occurred, and still less to quantify their intensity.

Alternatively, several zero-dimensional (batch) modeling approaches were developed. They are based on equilibrium thermodynamics and aim to identify hydrogeochemical processes by calculating a new state of equilibrium among aqueous solutions, mineral phases and gas phase. In contrast to calculations of saturation indices, such approaches can calculate the changes in the chemical composition of an aqueous solution, which result from dissolution and precipitation of minerals. Thus, they are capable of considering the effects of such chemical changes on the saturation state with respect to other minerals. Moreover, establishment of equilibrium conditions can calculate the mass conversion of the minerals equilibrating with aqueous solutions. As a result, such batch modeling can quantify hydrogeochemical processes to a certain degree. However, several such batch modeling approaches generally isolate specifically selected hydrogeochemical processes from the entire system. For instance, approaches, provided by Yuan and Todd (1999), Yuan et al., (1994), Bethke (2008) and ScaleSoftPitzer™ (Rice University Brine Chemistry Consortium, 2009) for predicting scale formation, focus exclusively on the formation of pure sulfate minerals or specific scale minerals. In addition to formation of pure sulfate minerals, these approaches disregard formation of other minerals and dissolution of primary minerals. Formation and dissolution of minerals can strongly alter the chemical composition of aqueous solutions, and consequently, affect scale formation. As a result, these approaches are incapable of correctly assessing the intensity of scaling processes. Fu et al. (2013b) stated thus that any modeling approach should integrate all relevant hydrogeochemical processes potentially occurring in order to correctly evaluate them.

2.3 Analytical modeling

In contrast to modeling approaches based on chemical equilibrium of thermodynamics, several other modeling approaches were also developed and applied for estimating processes involved in petroleum reservoirs. Bedrikovetsky et al. (2009) presented an analytical model that investigates the effects of co-injection of seawater treated by sulfate reduction with barium containing produced water on injectivity. Sorbie and Mackay (2000) developed 1D and 2D frontal oil displacement models that appropriate displacement processes of oil triggered by waterflooding and incorporate dispersive

mixing of injected seawater, formation water and oil leg connate water. Such modeling approaches consist of a hydrogeochemical and a hydraulic model part. The hydraulic model part describes various hydraulic flow processes (advection, dispersion and/or diffusion, even multiphase flow), and consequently, consider temporal and spatial aspects which are excluded in calculations of saturation indices and batch modeling approaches. However, the hydrogeochemical model part of these modeling approaches is commonly oversimplified and focuses exclusively on specific reactions. As a result, these approaches are incapable of correctly estimating the interplay of hydrogeochemical processes and pore water flow. For instance, the analytical model from Bedrikovetsky et al. (2009) isolates the barium sulfate formation resulting from free barium and sulfate ions without consideration of any dissolution and precipitation of other minerals. The 1D and 2D frontal oil displacement models provided by Sorbie and Mackay (2000) bypass any calculations of equilibrium of species distribution that are based on chemical thermodynamics. Thus, the applicability of these modeling approaches is strongly restricted to estimate the effects of coupled hydraulic and hydrogeochemical processes on the reservoir properties, although these approaches can well describe the flow conditions of oil reservoirs.

2.4 Reactive transport modeling

So far, no temporal and spatial aspects are considered by the approaches above discussed. Knowledge of the temporal and spatial development of the type and the intensity of hydrogeochemical reactions is a prerequisite for any effective technical measures which are applied for petroleum reservoirs (e.g., removal of scale minerals by using scale dissolvers). Moreover, hydrogeochemical processes are coupled to the simultaneously occurring hydraulic processes (fluid flow including advection, dispersion and diffusion during mass transport). The chemical composition of aqueous solutions flowing through aquifers is continually altered by hydrogeochemical processes (dissolution and precipitation of minerals), as well as by a combination of diffusive, dispersive and advective mass transport processes. Batch modeling is thus a non-suitable approach to correctly resolve a reactive reservoir aquifer dynamically and continually developing.

In the light of the disadvantages of the aforementioned modeling approaches (sections 2.1 to 2.3), several reactive transport modeling approaches were developed for predicting hydrogeochemical processes in oilfields and evaluating their effects on the properties of the petroleum reservoirs. For instance, Mackay et al. (2012) used the STARS reactive transport finite difference reservoir simulator (CMG, 1999) to three-dimensionally assess scale risk in oilfields where seawater injection was applied. Their modeling approach well describes the temporal and spatial development of the distribution of injected seawater in the oilfields. However, they presented their modeling results by representing calculated saturation indices of barite and celestite versus (1) seawater fraction, (2) time and (3) water production rate, as well as by plotting calculated concentrations of barium, strontium

and sulfate versus seawater fraction. In view of the temporal and spatial development (1) of scale formation in the reservoir aquifer and within the production wells and (2) of the mineral alterations in the reservoir matrix, any quantitative presentation about modeling results is lacking in the contribution of Mackay et al. (2012). Moreover, it is not retraceable whether the reactive transport model provided by Mackay et al. (2012) also considers hydrogeochemical processes others than formation of barium-, strontium- and calcium-bearing sulfate minerals. Modeling approaches, which only consider hydrogeochemical processes purposefully selected, are incapable of correctly describing the temporal and spatial evolution of hydrogeochemical processes, and certainly cannot assessing their intensity, although such modeling approaches are of 3D-dimension (see section 2.2). Moreover, positive calculated saturation indices are incapable of concluding on which hydrogeochemical processes actually proceed.

In view of the pros and cons of the aforementioned models, a combination of different hydrogeochemical modeling approaches is developed in this study to identify and quantify hydrogeochemical processes. The applicability of the developed hydrogeochemical modeling approaches will be verified in two case studies: the Miller oilfield and the Siri oilfield. A multidisciplinary study is performed to identify hydrogeochemical processes in the both oilfields and to quantify their effects on the porosity-permeability properties of the reservoir rocks (only modeling for the Miller field; a combination of analytical methods (Petrographic microscope, XRF; XRD, SEM, HRTEM) and modeling for the Siri oilfield; for details, see sections 3 to 5). The both oilfields fulfill the requirements of a case study due to the following reasons. On one hand, various investigation results in the Miller oilfield and the Siri oilfield clearly show that the reservoir rocks of the both oilfields are characterized by diagenetic features which are connected with considerable changes in the reservoir properties (for details see section 3 and 4). A complex hydrogeochemical reaction chain among minerals, aqueous solutions and gas phase was triggered by technical measures and spontaneously geological processes in the Miller oilfield and in the Siri oilfield, respectively. On the other hand, the Miller oilfield was widely investigated and its investigation results of high quality were accessible. The Siri oilfield is investigated in this study by different analytical methods (Petrographic microscope, XRF; XRD, SEM, HRTEM; for details, see section 4).

Hydrogeochemical modeling approaches (batch modeling, as well as 1D and/or 3D hydrogeochemical transport modeling) are used (1) to construct a reproduction to a certain degree for the reservoir aquifer of the Miller oilfield and the Siri oilfield, respectively, (2) to identify hydrogeochemical processes resulting in the reservoir rock alterations observed in the both oilfields, and (3) to predict the consequences of such processes (for details, see sections 3 and 5).

3. Case study – Miller oilfield

The Miller oilfield is located in the South Viking Graben of the UK North Sea and its sandstones are currently deeply buried up to ca. 4000 m (Lu et al., 2011, and references therein). First oil was produced in 1992 in the Miller oilfield into which seawater injection began in 1995 (Houston, 2007; Houston et al., 2007). Many research studies widely investigated the Miller oilfield, such as the chemical composition of its produced water (Houston, 2007; Houston et al., 2007), and the mineralogical composition of its reservoir rocks (e.g., Marchand et al., 2002; Houston, 2007; Lu et al., 2011). Houston et al. (2007) clarified that seawater injection triggered a series of hydrogeochemical processes occurring in the Miller oilfield reservoir's aquifer. The Miller oilfield is chosen as test site to reproduce its hydrogeochemical processes by numerical modeling.

3.1 Introduction and aims

The Miller oilfield covers 45 km^2 (Houston, 2007) and its reservoir rocks have probably been exposed to high CO_2 content over a long period (Lu et al., 2009). The CO_2 content contributes 28 mol% to the gas released from the oil (Baines and Worden, 2004). The reservoir sandstones have an average porosity of ca. 14% and exhibit a slightly decreasing trend of the porosity from the oil-filled rocks to the reservoir sandstones filled by water (Marchand et al., 2002). The reservoir rocks are dominated by quartz and consist of K-feldspar, clay minerals, pyrite and calcite (Marchand et al., 2002; Houston, 2007; Lu et al., 2010). Wylde et al. (2006) stated (1) that seawater injection probably created the "arguably harshest oilfield scaling regime in the North Sea", and (2) that the scale mineral assemblage is dominated by barite and may additionally contain celestite and calcite. Roughly $1.9x10^{11}$ L of formation water-seawater mixtures were produced from all wells during ca. 10 years and almost daily measured (Houston et al., 2007). The temporal development of measured chloride concentrations in the produced water reveals that the injected seawater arrived at the production well after 611 days (Fig. 1 in Houston et al. (2007)).

Understanding the mechanisms of hydrogeochemical processes is essential for successful reservoir engineering, for instance, for prediction of the type and the amount of scale minerals, and also for a successful and efficient scaling removal. Hydrogeochemical processes are on one hand reflected by diagenetic features in sediments, and on the other hand characterized by the compositional development of water. Thus, the chemical composition of the measured produced water allows concluding on the hydrogeochemical processes in the Miller field. Houston et al. (2007) developed an approach in which the measured chemical composition of the produced water is compared with the results predicted from the non-reactive mixing of the injected seawater and the original formation water. The deviations from the measured data and the calculated results can only indicate that several hydrogeochemical reactions involving silica-, calcium-, barium-, sulfate-, strontium-bearing minerals

were induced by seawater injection into the Miller oilfield (Houston et al., 2007). However, this approach is incapable of determining the exact types of such processes. In this study, the chemical composition of the produced water measured in the Miller field is the key factor to allow concluding on the hydrogeochemical processes. Thereby, hydrogeochemical models (zero- and one-dimensional models) that rely on chemical equilibrium thermodynamics are developed in the following. The aim is to identify and to quantify the hydrogeochemical processes triggered by seawater injection into the Miller oilfield.

3.2 Zero-dimensional modeling

Zero-dimensional (batch) model considers a reactor that comprises an aqueous solution, a defined mineral assemblage and a gas phase. It excludes any temporal and spatial aspects. The batch model only considers the chemical interactions and calculates their mass transfer, as the original formation water is diluted by the injected seawater in a closed system. Developing the batch model aims to test whether the relevant reactions have quickly achieved a new equilibrium state in the Miller oilfield. If this can be demonstrated, the batch model enables two applications. On the one hand, hydrogeochemical modeling can resolve the identification which hydrogeochemical processes including scale formation participated in the complex web of the interconnected water-rock-gas reactions of the Miller oilfield. On the other hand, calculation of the corresponding mass conversion of minerals can be achieved. However, results of a batch modeling could merely give an indication (1) of processes probably occurring, (2) of interconnections among these processes, and (3) of parameters affecting the intensity of such processes.

The PHREEQC computer code (Parkhurst and Appelo, 1999) is the modeling tool. Its thermodynamic database Wateq4f.dat is used for the batch modeling. All solubility constants of minerals and equilibrium (association/dissociation) constants of aqueous species, as well as their temperature dependence are defined in the Wateq4f.dat database. Controls of the total pressure over solubility constants of minerals and over the equilibrium constants of dissolved species are ignored. All calculations are performed for a total pressure of 1.0 atm. The conceptual modeling setup, the modeling results, discussion of the modeling results and conclusions refer to Fu et al. (2012) unless otherwise indicated.

3.2.1 Conceptual modeling setup

Admixture of injected seawater to original formation water is performed in a closed reactor that is exposed to the reservoir temperature of 120 °C and a pre-assigned CO_2 partial pressure (pCO_2). The reactor has a total volume of 7.1 L and a pore volume of 1.0 L with consideration of a porosity of

14%. A pre-assigned mineral assemblage occupies the remaining 6.1 L of the total volume (Table 1). In total, 11 identical reactors, which show the same properties with respect to the mineral assemblage, the porosity etc., are filled with 1.0 L formation water-seawater mixture resulting from different seawater fractions (ranging from 0% to 100%). Primary quartz is excluded from the reactive primary mineral list, because it is considered as a non-reactive mineral phase. The formation water-seawater mixtures equilibrate with the primary mineral phases and with the gas phase with consideration of a pre-assigned mineral composition and $pCO_{2(g)}$ (Table 1). Assuming a bulk density of 2.65 kg L^{-1} and the mineralogical composition, the amount of the reactive primary minerals (e.g., K-feldspar, kaolinite and calcite) in each reactor can be calculated for starting conditions (Table 1). Although the mineral assemblage of the reservoir rocks contains trace amount of pyrite, pyrite is excluded from the model. The formation water used in the batch model is free in degradable organic matter. On the other hand, any oxidizing agent (e.g., dissolved oxygen, nitrate) is ignored. Consequently, sulfate species dissolved in the injected seawater and S(−I) bound to pyrite cannot be reduced and oxidized, respectively.

Table 1: Assemblage of reactive primary and secondary minerals as well as their pre-assigned amount in the modeling reactors at starting conditions (modified after Fu et al., 2012).

		Amount	
		(wt.%)	(mol)
Primary phase	Microquartz	0.01	0.03
	K-feldspar	3.0	2.04
	Kaolinite	1.5	1.1
	Calcite	2.1	3.97
Secondary phase	Dolomite	0.0	0.0
	Strontianite	0.0	0.0
	Witherite	0.0	0.0
	Barite	0.0	0.0
	Celestite	0.0	0.0
	Sr-bearing barite	0.0	0.0
	Gypsum	0.0	0.0
	Anhydrite	0.0	0.0
Gas phase	$CO_{2(g)}$	30 atm	

Scanning electron microscope studies performed by Houston (2007) show that several samples have quartz coatings on the surface of the primary quartz grains. Thus, a $SiO_{2(s)}$ mineral phase, which shows a higher solubility at a same temperature compared to quartz, is used to equilibrate with the formation water-seawater mixtures. It is assumed that this $SiO_{2(s)}$ phase used in the batch model is characterized by the solubility investigated by Azaroual et al. (1997). The solubility constant and its

temperature dependence of this $SiO_{2(s)}$ phase are re-calculated from the data provided by Azaroual et al. (1997) and are defined as microquartz in the model (Eqs. 1a and 1b).

$$SiO_{2(Microquartz)} + 2H_2O = H_4SiO_4 \quad \text{(Eq. 1a)}$$

$$\log K = -3.857 \text{ (for 298 K and 1.0 atm)}$$

and its temperature dependence (temperature T in K)

$$\log K = 96.13 + 0.0311T - 434.06T^{-1} - 41.02\log T - 559298.3T^{-2} \quad \text{(Eq. 1b)}$$

$$Ba_xSr_{(1-x)}SO_4 = xBa^{2+} + (1-x)Sr^{2+} + SO_4^{2-} \quad \text{(Eq. 2)}$$

A gas phase, which is characterized by a pre-assigned pCO_2 of 30 bar, equilibrates with the formation water-seawater mixtures, as the reservoir rocks have probably undergone high CO_2 contents for a long period (Lu et al., 2009). Alternative modeling scenarios consider different pCO_2 levels to test its effect on the calculated results. The chemical incompatibility between the injected seawater and the formation water leads to disequilibrium between aqueous solutions and minerals, provided that the formation water filling the pore space at starting conditions (prior to seawater injection) is diluted by the injected seawater. Thus, secondary minerals (dolomite, barite, celestite, etc.) are allowed to form (Table 1). Formation of barite is often accompanied by celestite precipitation, which results in formation of solid solutions consisting of strontium sulfate and barium sulfate (Eq. 2). Many studies reported that formation of strontium barium sulfate solid solutions is commonly observed as one of typical scaling processes in formation water or basinal brines (Gordon, et al., 1954; Todd and Yuan, 1992). The batch model calculates the ideal behavior of solid solutions comprising strontium, barium and sulfate. It is unknown which calcium sulfate phase (anhydrite or gypsum) forms. Two scenarios, which consider anhydrite and gypsum, respectively, are calculated to identify which hydrogeochemical process with respect to calcium sulfate phase actually occurred in the Miller oilfield.

Due to the lack of data about the chemical composition of the injected seawater, the present-day seawater composition according to Parkhurst and Appelo (1999) is considered as the generic seawater admixed to the Miller oilfield's formation water. Dissolved molecular O_2 and N(5)-, N(-3)-, and uranium species are ignored in the batch model (Table 2). To complete the seawater analysis (given by Parkhurst and Appelo (1999)), total concentrations of barium, strontium, aluminum and lithium are taken from Turekian (1968) and Bearman (1989). The formation water sample no. 5 provided by Lu et al. (2011) shows high sodium and chloride concentrations of 25,898 and 41,767 ppm, respectively, which are in good agreement with the chemical composition of the produced water measured by Houston (200) prior to the seawater breakthrough. In consequence, this formation water analysis (sample no. 5 from Lu et al. (2011)) is used in the model in combination with the additional data on the concentrations of strontium, aluminum, dissolved silica and lithium which are provided by

Houston (2007; Table 2). The batch modeling is based on two assumptions: (1) constant chemical composition of injected seawater and formation water, and (2) no participation of dissolved Cl^- in any heterogeneous reactions among aqueous solution, mineral phases and gas. The reservoir rocks in the Miller field show low clay content (Lu et al., 2011). It can thus be assumed that the effect of cation exchange on calculated species distribution and mass conversion is of a low level. No description of hydrous ferric oxides as one of major or even minor components within the reservoir aquifer rocks is available. As a result, cation exchange and surface complexation are excluded in the model.

Table 2: Chemical composition of injected seawater and formation water prior to seawater injection (modified according to Fu et al., 2012).

	Concentration	
	Seawater[a]	Formation water[b]
pH (unitsless)	8.22	7.5
pe (unitsless)	8.451	n.a.[c]
Temperature (°C)	4	120
units, species	ppm	ppm
Density	1.023	1.055
Calcium	412.3	307
Magnesium	1291.8	82
Sodium	10768	25898
Potassium	399.1	1399
Iron	0.002	1
Manganese	0.0002	n.a.
Silica (as SiO_2)	4.28	70[d]
Chloride	19353	41767
Alkalinity (as HCO_3^-)	41.682	2221
Sulfate (as SO_4^{2-})	2712	4
Barium	0.02[e]	643
Strontium	8[e]	39
Lithium	0.17[f]	28[g]
Aluminum	0.001[f]	1[g]
Zinc	n.a.	0.4[g]

[a] Given by Parkhurst and Appele (1999; Example 1) without consideration of nitrate, nitrite. uranium and dissolved oxygen;
[b] Provided by Lu et al. (2011; original data from Smalley and Warren, 1994);
[c] Not analyzed;
[d] Measured concentration at 0% seawater fraction according to Houston (2007);
[e] Mean concentration according to Turekian (1968) and Bearman (1989);
[f] from Turekian (1968);
[g] Mean concentration in the seawater fraction ranging from 0% to 1.58% provided by Houston (2007).

Equilibration among the primary mineral assemblage, the pure CO_2 gas phase and the formation water is established at starting conditions (prior to the admixture of seawater to the formation water). At this modeling step, no secondary mineral phases are presented in each reactor. At the second

modeling step, one liter of a formation water-seawater mixture resulting from different mixing ratios occupies the pore space of each reactor and equilibrates with the primary mineral assemblage and the pure CO_2 gas phase; secondary minerals form, provided that their saturation is achieved. As a result, changes in the chemical composition of the pore water resulting from the formation water dilution by admixed seawater are the driving force for establishing a new equilibrium state among aqueous solutions, minerals and gas phase. Mineral dissolution and precipitation are thus induced. An alternative modeling scenario (non-reactive mixing; abbreviated as NRM) suppresses any dissolution and precipitation of mineral phases and the equilibration between the aqueous solution and the gas phase; in other words, this scenario considers pure dilution of the formation water by the injected seawater. This scenario calculates the effects of formation water–seawater mixing on total concentrations of dissolved components resulting exclusively from non-reactive mixing. However, dissociation and association of species are included within scenario NRM. All scenarios exclude the artificial effects on the chemical composition of the produced water. Artificial effects could result from sampling or analysis and cause changes in several physical parameters (e.g., temperature and total pressure). Such changes furthermore drive hydrogeochemical processes, such as CO_2 outgassing, and consequently, strong alterations of the chemical composition of the produced water. On the one hand, the chemical composition of the produced water is used as the key factor in the model to reproduce the processes driven by seawater injection. On the other hand, artificial processes are impossible to avoid and difficult to quantify. It is thus assumed that the measured composition of the Miller oilfield's produced water was unaffected by such artificial effects.

Lacking data (e.g., pCO_2, the exact type of minerals equilibrating with the formation water-seawater mixtures) results in a large number of the modeling scenarios. Only one parameter is changed in the alternative scenarios compared to the standard scenario RM. These scenarios provide possibilities to test single parameters as well as their influence on the chemical composition of the produced water and on the mass conversion of minerals especially of scale minerals newly formed. The standard scenario RM calculates reactive mixing of formation water and seawater. It considers a pCO_2 level of 30 atm, and its primary mineral assemblage includes calcite, microquartz and kaolinite. Mixing of the both chemical incompatible water types can cause formation of dolomite, strontianite, witherite, barite, celestite, strontium barite sulfate solid solutions and anhydrite. In comparison, an alternative scenario, for instance, considers gypsum as the secondary calcium sulfate phase instead of anhydrite, replaces microquartz by quartz, uses another pCO_2 level or includes K-feldspar as an additional primary mineral.

3.2.2 Modeling results

This study presents and discusses exclusively the modeling results of scenarios NRM and RM in detail, while the calculated results of the alternative scenarios are briefly discussed (for details, see Fu et al. (2012)). Figures 1 to 4 illustrate the comparison of the measured data with the modeled chemical composition of the produced water at various seawater fractions. PHREEQC gives the calculated result in molal units (mol per kg water). Using factors, which consider the density of the aqueous solution, re-converts the calculated concentrations to mol L^{-1} (for details, see Fu et al. (2012)). Moreover, Figure 5 represents the type of minerals precipitated and dissolved as well as their mineral conversions per one liter of formation water-seawater mixtures calculated by scenario RM. Comparison of the modeled distribution of aqueous species at equilibrium (1) with the measured data (from Houston, 2007) and with (2) the concentrations separately calculated by scenario NRM allows evaluating the hydrogeochemical processes characterizing the measured development of the produced water.

Scenario NRM calculates the effects on the chemical composition of the produced water, when the formation water is merely diluted by the injected seawater without any heterogeneous reactions. Consequently, the calculated concentrations display a linear development with increasing seawater fraction (a trend named “Mod_NRM-line” of aqueous components). The linear decrease in calculated $c_{tot}Na^+$ (the total concentration of dissolved sodium) within scenario RM with the increasing seawater fraction is in good accordance with the measured development of $c_{tot}Na^+$ and with the $c_{tot}Na^+$ development calculated by scenario NRM (Fig. 1). This clarifies that no sodium-bearing mineral precipitation is involved in the complex web of the hydrogeochemical processes in the Miller oilfield; in other words, neither precipitation nor dissolution of sodium-bearing minerals occurred (e.g., precipitation of halite or dissolution of albite). As a result, sodium concentration can be used as an indicator for the admixed seawater fraction in the Miller oilfield’s produced water others than chloride concentration. A constant pCO_2 prevailing in the reactor resulting in an almost constant pH level of ca. 5.2 that is independent on the seawater fraction (Fig. 1; scenario RM). The pH calculated by scenario RM is much lower than it measured in the seawater; note that measured pH in the formation water is unavailable.

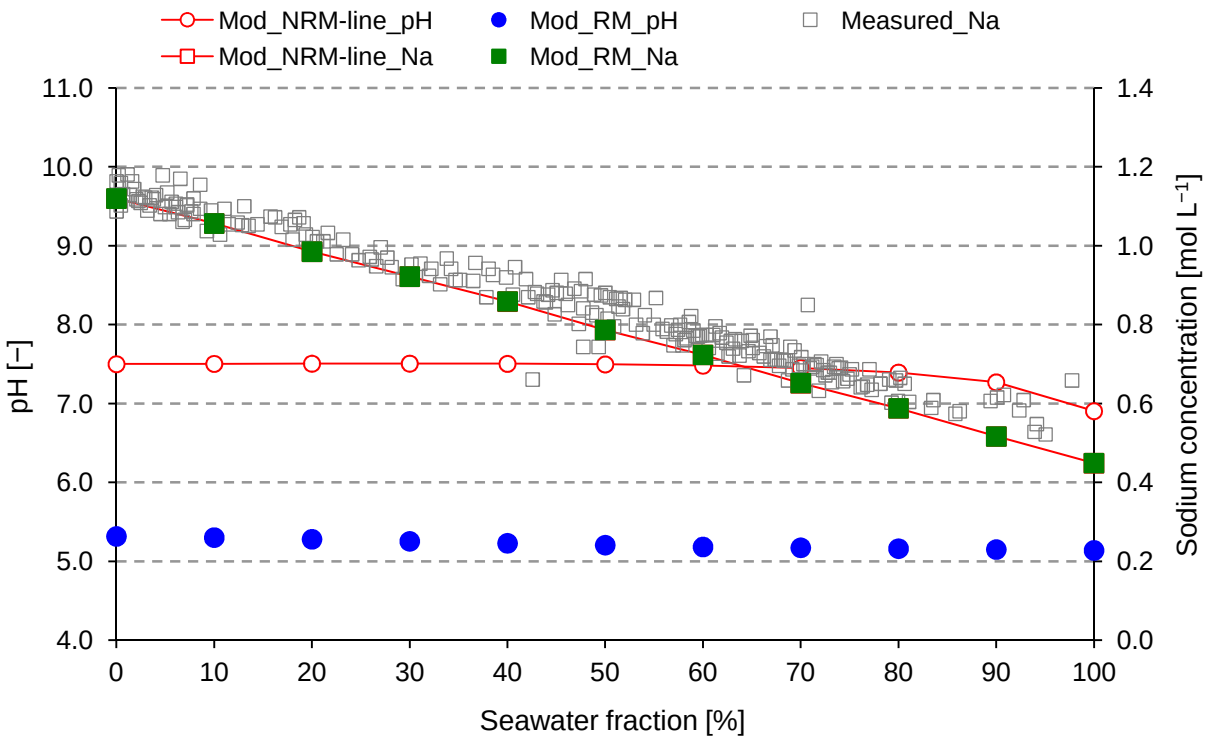

Fig. 1: Measured and modeled pH (no available measured data) and concentrations of sodium in the produced water versus seawater fraction from scenarios NRM and RM (modified after Fu et al., 2012). Measured data: Houston (2007); Mod_NRM-line: scenario NRM; Mod_RM: scenario RM.

Calculated barium concentrations ($c_{tot}Ba^{2+}$ from scenario RM) versus the seawater fraction strongly deviate from the barium NRM-line (Fig. 2). In comparison to the barium NRM-line, the marked decrease in $c_{tot}Ba^{2+}$ (ranging 4.6 to <0.01 mmol L^{-1}) caused by reactive admixture of seawater indicates that precipitation of barium-bearing minerals occurred in the Miller oilfield. The calculated mineral conversion shows that strontium barite solid solutions (Sr-bearing barite) form from the formation water-seawater mixtures. The chemical composition of this Sr-bearing barite precipitate varies from almost pure barite at low seawater fractions to $Ba_{0.88}Sr_{0.12}SO_4$ at high seawater fractions (Fig. 5). The good match between $c_{tot}Ba^{2+}$ from scenario RM and the measured data confirms this conclusion. In consequence of Sr-bearing barite formation, reactive mixing of the formation water and the seawater results in a marked decrease of $c_{tot}Sr^{2+}$ (from 0.4 to 0.1 mmol L^{-1}; Fig. 3). The modeled development of the modeled $c_{tot}Sr^{2+}$ versus the seawater fraction is similar to the measured $c_{tot}Sr^{2+}$.

Massive precipitation of Sr-barite causes the negative deviation of the c_{tot}Sulfate from the sulfate NRM-line up to the seawater fraction of ca. 60%. A concurrent formation of anhydrite is driven by seawater injection besides Sr-barite precipitation, provided that the seawater fraction is higher than 70% (Fig. 5). The modeled c_{tot}Sulfate quite well match the measured data up to the seawater fraction of 80%.

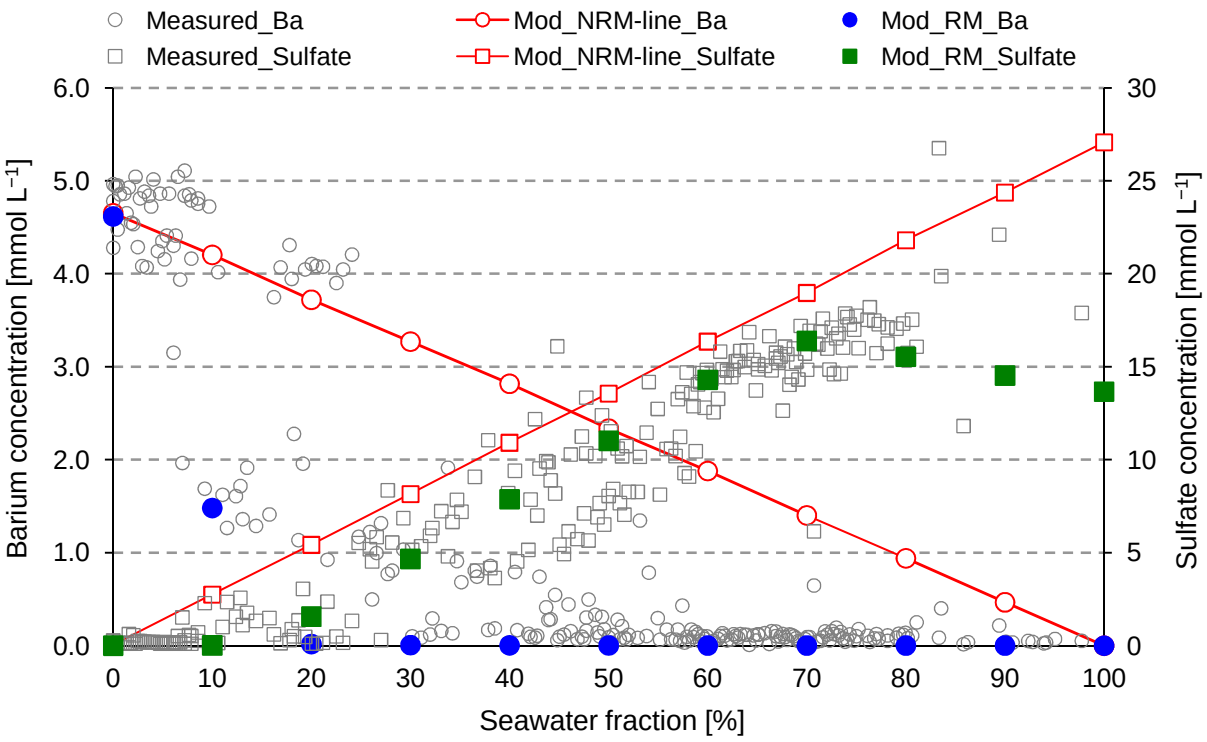

Fig. 2: Measured and modeled concentrations of barium and sulfate in the produced water versus seawater fraction for scenarios NRM and RM (modified according to Fu et al., 2012). Measured data: Houston (2007); Mod_NRM-line: scenario NRM; Mod_RM: scenario RM.

The elevated pCO_2 level prevailing in the reservoir sandstones drives calcite dissolution (Fig. 5), liberates calcium species to the pore water, and consequently, results in a positive deviation of the $c_{tot}Ca^{2+}$ calculated by scenario RM from the calcium NRM-line (Fig. 3). At the seawater fraction >70% and >80%, anhydrite and dolomite are precipitated from the pore water, respectively (Fig. 5). The modeled $c_{tot}Ca^{2+}$ match most measured calcium concentrations (Fig. 3).

The trend of dissolved total silica concentration ($c_{tot}SiO_2$) calculated by considering equilibration of silicate phases with the pore water significantly differs from the NRM scenario (Fig. 4). This indicates that silica-bearing phases dissolve and release silica species into the formation water-seawater mixture. On the other hand, the injected seawater is undersaturated with respect to the primary reservoir minerals containing silica. Figure 5 represents that dissolution of microquartz is responsible for the almost constant $c_{tot}SiO_2$ which are independent on the seawater fraction. In contrast, the mineral conversion of kaolinite is negligible (less than 10^{-7} mol L^{-1}). The modeled $c_{tot}SiO_2$ at equilibrium with microquartz show a same trend as the measured data. However, the absolute level of modeled $c_{tot}SiO_2$ with consideration of microquartz dissolution is slightly lower than the measured concentrations.

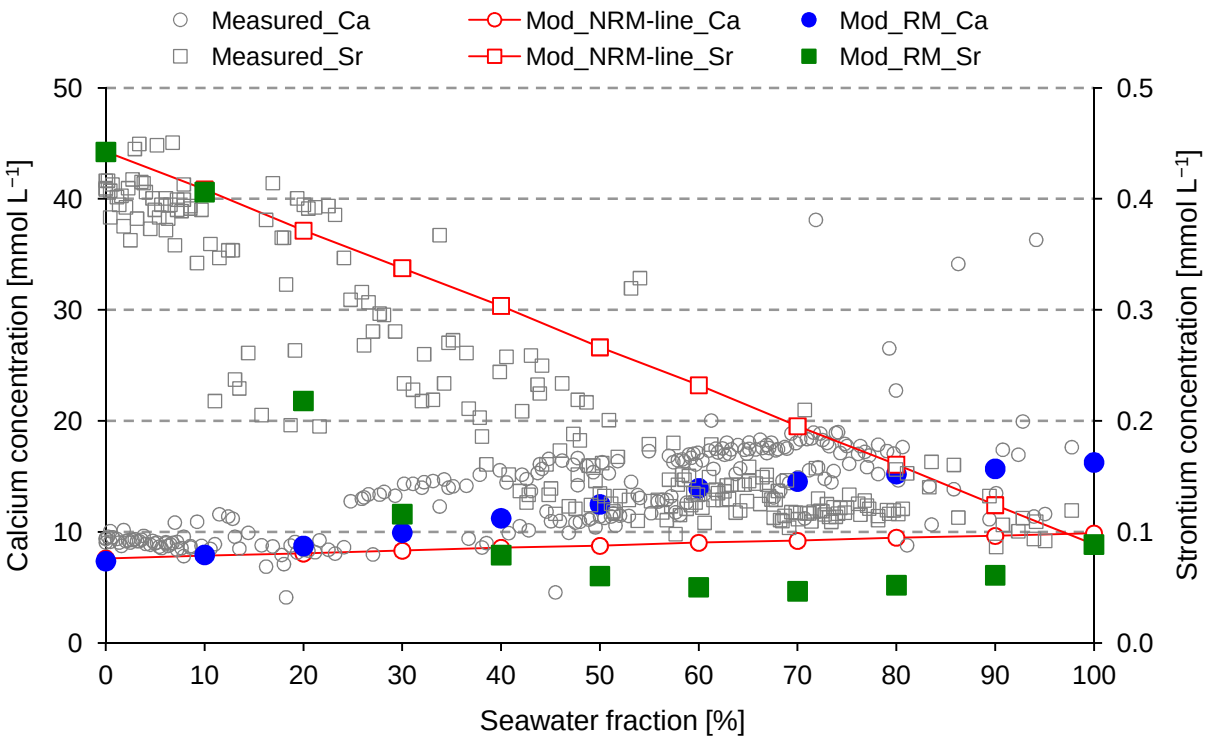

Fig. 3: Measured and modeled concentrations of calcium and strontium in the produced water versus seawater fraction from scenarios NRM and RM (modified after Fu et al., 2012). Measured data: Houston (2007); Mod_NRM-line: scenario NRM; Mod_RM: scenario RM.

In comparison to other parameters, the modeled $c_{tot}Mg^{2+}$ mismatch the measured concentrations (Fig. 4). The calculated magnesium NRM-line show a same trend as the development of the modeled $c_{tot}Mg^{2+}$ within scenario RM with increasing seawater fraction, provided that the seawater fraction is lower than 80%. This indicates that no magnesium bearing mineral forms at the seawater fractions <80%. The calculated $c_{tot}Mg^{2+}$ positively deviate from the measured data, although dolomite forms at the seawater fraction >80% (Fig. 5). Substitution of dolomite by "Dolomite$_{(d)}$" (disordered dolomite defined in the Wateq4f.dat) is incapable of improving this deviation, due to the fact that dolomite$_{(d)}$ show a higher solubility compared to dolomite.

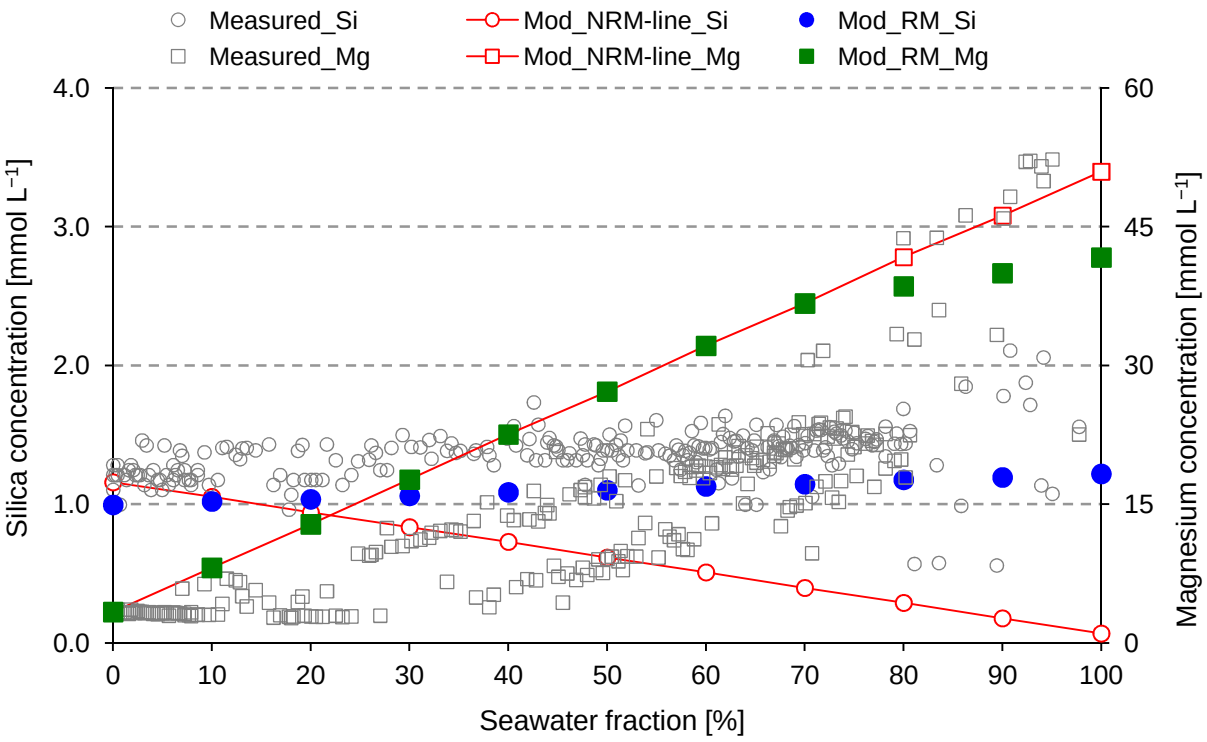

Fig. 4: Measured and modeled concentrations of silica and magnesium in the produced water versus seawater fraction from scenarios NRM and RM (modified according to Fu et al., 2012). Measured data: Houston (2007); Mod_NRM-line: scenario NRM; Mod_RM: scenario RM.

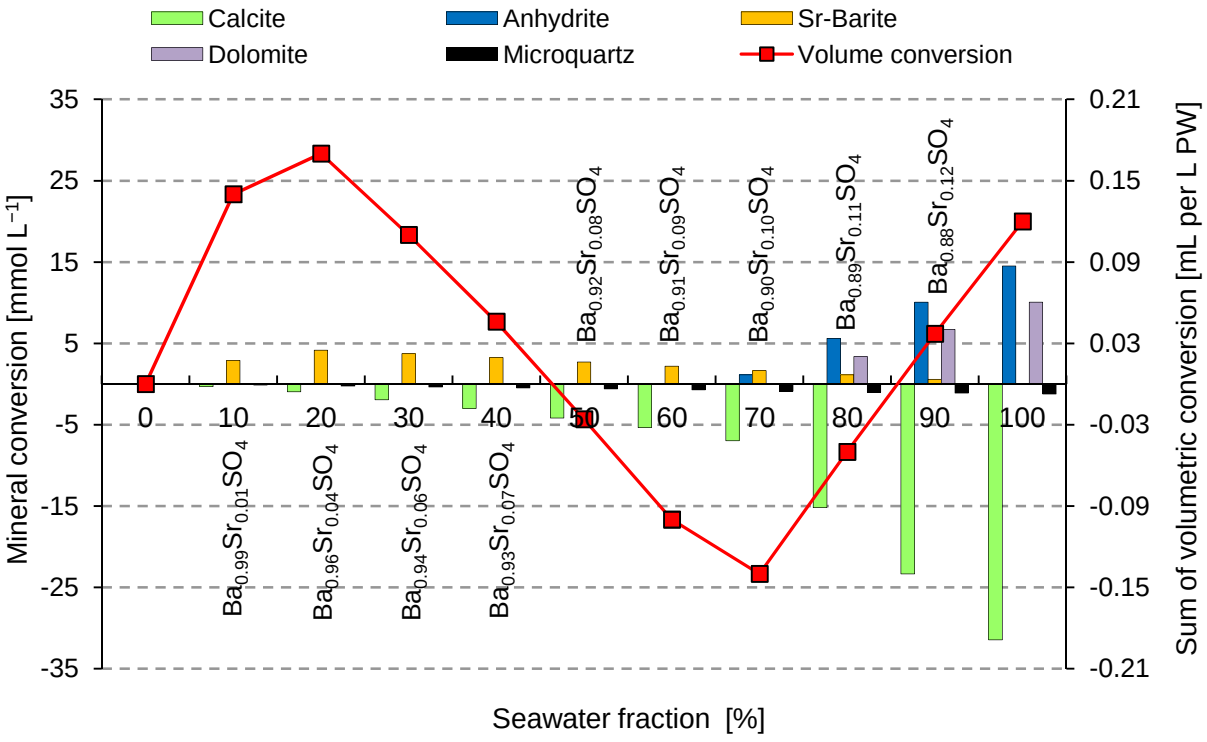

Fig. 5: Modeled mineral conversions, sum of their corresponding volumetric conversions per one liter of produced water and modeled chemical composition of strontium-bearing barite solid solutions versus seawater fraction from scenario RM (modified after Fu et al., 2012); PW: produced water.

In summary, the chemical composition of the mineral assemblage markedly depends on the seawater fraction. Increasing seawater fraction in the produced water drives an increasing intensity of calcite and microquartz dissolution, as the injected seawater is undersaturated with respect to the both minerals at elevated reservoir temperature and pCO_2 level. Newly formed Sr-barite dominates in the secondary mineral assemblage at seawater fractions ranging from 0% to 70%. Formation of anhydrite and dolomite is restricted to the seawater fractions >80%. However, they show dominance over other secondary minerals at the seawater fractions ranging from 80% up to 100%. In terms of the individual density of all minerals[1], an overall volumetric balance can be calculated with regard to one liter of the formation water-seawater mixtures for various mixing ratios (Fig. 5). The volume of newly Sr-bearing barite (no precipitation of dolomite and anhydrite) overcompensates for the loss of pore space caused by dissolution of calcite and microquartz at seawater fractions ranging 0% to 50%; in other words, the pore space could be blocked. A possible blockage could also occur at high seawater fractions from 90% up to 100%, but by formation of dolomite and anhydrite. In contrast, secondary porosity could be created, as dissolution of calcite and microquartz is of stronger intensity compared to formation of Sr-barite. The calculated overall volumetric balance refers to only one liter of the produced water. Thus, a large volume of seawater injection and water production can strongly affect the reservoir porosity-permeability properties.

3.2.3 Discussion of batch modeling results

Calculations of the most probable standard scenario RM create a reasonable accordance between the measured and modeled concentrations of chloride, sodium, lithium, barium, strontium, sulfate, calcium and silica (except for magnesium). It follows that the batch modeling can reproduce most hydrogeochemical processes which were triggered by seawater injection into the Miller oilfield. In addition to chloride, the concentration development of sodium and lithium also provides information about the seawater admixture to the formation water in the Miller oilfield. The complex web of the interconnected reactions involves dissolution of calcite, microquartz and $CO_{2(g)}$, as well as precipitation of Sr-barite and anhydrite (maybe). All modeling results of the alternative modeling scenarios are documented in Fu et al. (2012) in detail, whereas several modeling results are briefly discussed here.

An alternative modeling scenario (RM_Gyp) replaces anhydrite by gypsum as secondary calcium sulfate phase compared to the standard scenario RM. The modeled sulfate concentrations from scenario RM_Gyp are identical with the calculated NRM line of sulfate, provided that the seawater fraction is higher than 80% (Fig. 6). The formation water-seawater mixtures are always

[1] ρ(calcite) = 2.71 kg L^{-1}; ρ(anhydrite) = 2.96 kg L^{-1}; ρ(dolomite) = 2.872 kg L^{-1}; assuming ρ(microquartz) and ρ(Sr-bearing barite) equals to ρ(quartz) of 2.648 kg L^{-1} and to ρ(pure barite) of 4.5 kg L^{-1}, respectively; all ρ taken from Dean (1999); ρ: Mineral density.

undersaturated with regard to gypsum (no details here). However, the calculated c_{tot}Sulfate within scenario RM_Gyp (considering gypsum) differ from the c_{tot}Sulfate calculated by scenario RM considering anhydrite merely at high seawater fractions (>80%; Fig. 6). The measured sulfate concentrations show a broad rang at these high seawater fractions and a limited number of measured data. This does not allow concluding whether any calcium sulfate actually forms. The type of the secondary calcium sulfate mineral equilibrating with the formation water-seawater mixtures slightly affects the concentrations of the other components (partly presented in Fig. 7). Anhydrite forms at higher seawater fractions (>80%), whereas minor Sr-barite is precipitated. Consequently, the equilibration of calcium sulfate phases with the water mixtures has minor effects on the calculated strontium concentrations (Fig. 7). In analogy to strontium concentration, the calcium concentrations calculated by scenario RM_Gyp deviate from those modeled by scenario RM (including anhydrite) merely at higher seawater fractions due to anhydrite formation (Fig. 7).

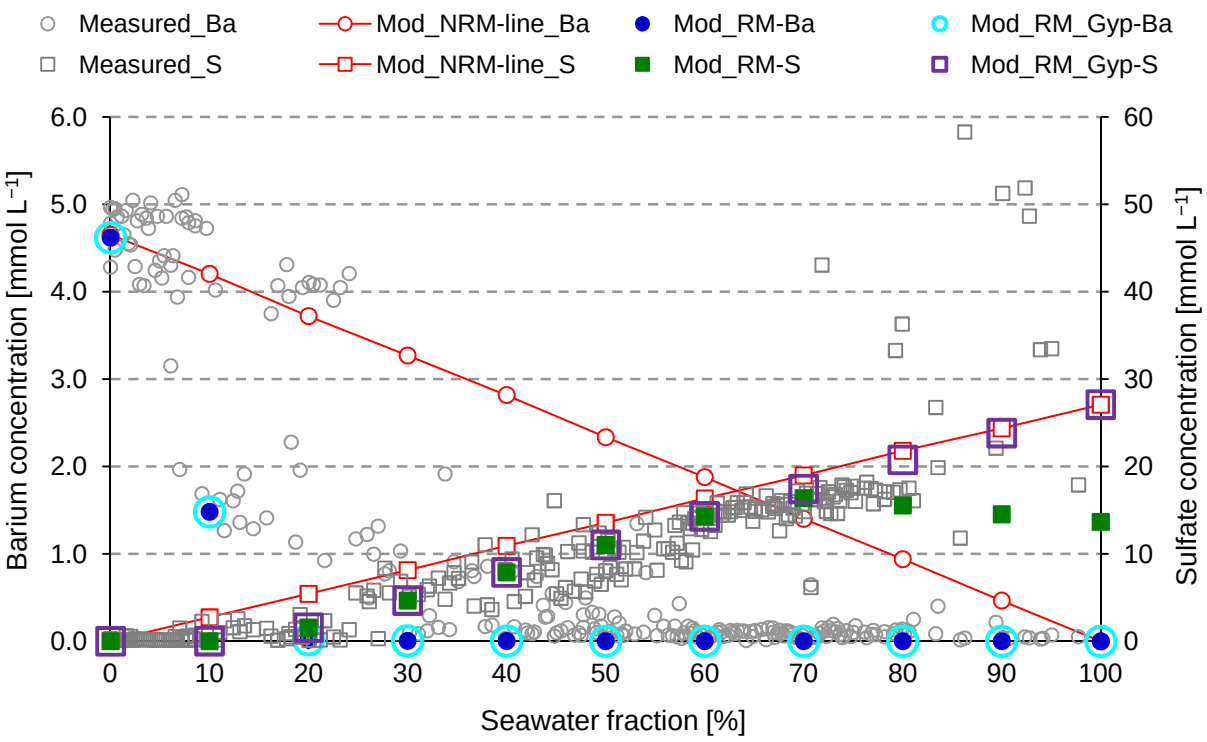

Fig. 6: Measured and modeled concentrations of barium and sulfate from scenarios NRM, RM, and RM_Gyp (modified according to Fu et al., 2012). Measured data: Houston (2007); Mod: calculated results; NRM-line: scenario NRM; Mod_RM: scenario RM (considering anhydrite); Mod_RM_Gyp: scenario RM_Gyp (substituting anhydrite by gypsum); Ba: total barium concentration; S: total sulfate concentration.

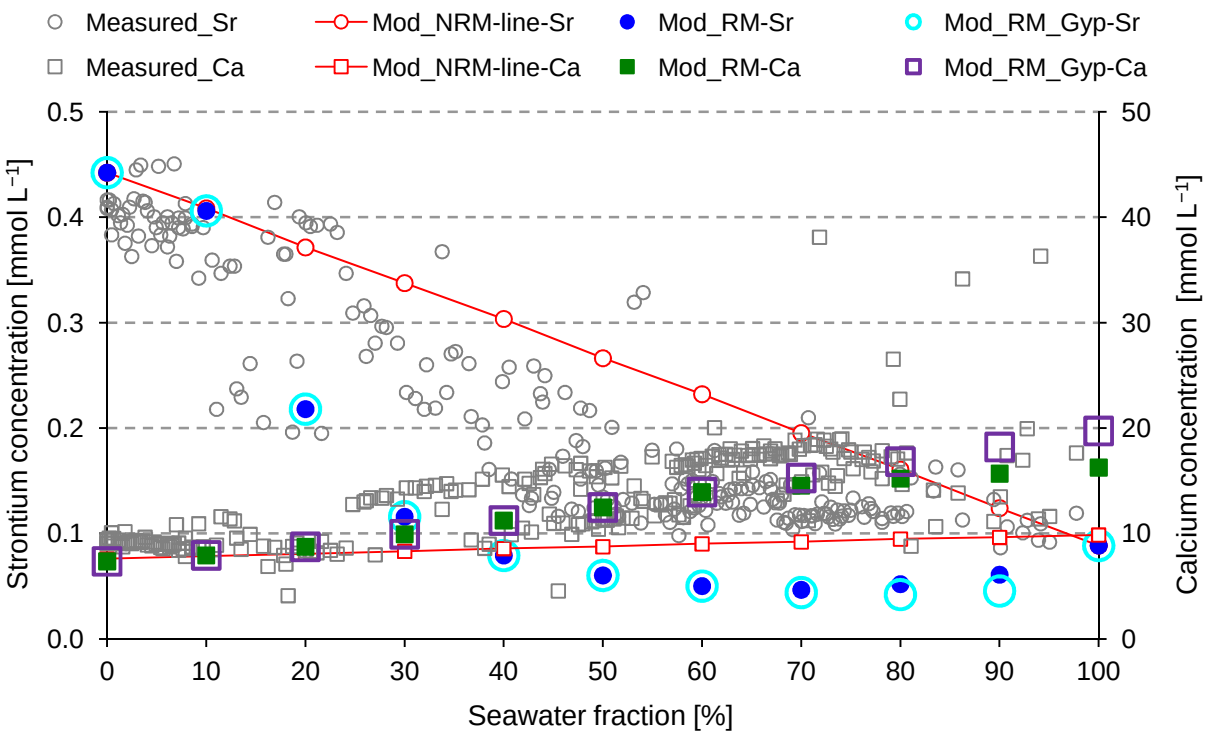

Fig. 7: Measured and modeled concentrations of strontium and calcium from scenarios NRM, RM, and RM_Gyp (modified according to Fu et al., 2012). Measured data: Houston (2007); Mod: calculated results; NRM-line: scenario NRM; RM: scenario RM (considering anhydrite); RM_Gyp: scenario RM_Gyp (substituting anhydrite by gypsum); Sr: total strontium concentration; Ca: total calcium concentration.

Several studies have highlighted the effects of changes in temperature and pCO_2 on scale formation and scaling rate by performing laboratory experiments (Moghadasi et al., 2003; Merdhah and Yassin, 2009). Data about pCO_2 prevailing in the Miller oilfield reservoir is lacking. Several studies presented different reservoir temperatures, such as 120 °C from Rooksby (1991) or 140 °C from Haszeldine et al. (2006). Determination of the *in situ* reservoir temperature and of the reservoir aquifer temperature of the mixing zone during or after seawater injection is a common reservoir engineering task. Alternative modeling scenarios vary the reservoir temperature and pCO_2 to test their effects on the chemical composition of the produced water and on the corresponding mass conversion. Comparing the measured data with the modeling results calculated at different reservoir temperature and pCO_2 conditions could achieve this challenge. Changes in temperature markedly affect the solubility constants and equilibrium constants of species dissociation and association. The pCO_2 level at a given temperature condition strongly influences the master variable –the pH of aqueous solutions, and thereby, specially has a strong effect on the calcium concentration. Thus, such hydrogeochemical modeling can help us to quantify the temperature and pCO_2 conditions which characterize the measured chemical composition of the produced water. Equilibration of calcite and $CO_{2(g)}$ specially strongly depends on temperature in the investigated Miller oilfield. Three modeling scenarios, RM-pCO2=3, RM and RM-pCO2= 100, consider a pCO_2 level of 3, 30, 100 atm, respectively (Figs. 8 to 9).

The modeling results of these three scenarios reveal (1) that a lower $pCO_{2(g)}$ results in a higher pH and (2) that a higher pH correspondingly causes lower calcium concentrations at an unchanged temperature. Additionally, a lower $pCO_{2(g)}$ level (e.g., 3 atm in the model) can result in high activities of aqueous carbonate ($CO_3^{2-}{}_{(aq)}$) which induce witherite with minor amounts at the seawater fraction of 0%. As a result, the modeled barium concentration in the original formation water (prior to seawater breakthrough) is lower than the measured data (Fig. 9). This clarifies that the actual pCO_2 level is higher than 3 atm. Additionally, the barium concentration in the produced water prior to seawater breakthrough suggest the pCO_2 level prevailing in the reservoir aquifer. Changes in the barium concentrations drive the different developments of the modeled sulfate concentrations at different pCO_2 levels versus seawater fraction (Fig. 8). Higher calcium concentrations result in lower sulfate concentrations due to formation of more anhydrite. Temperature strongly affects the equilibrium solubility of minerals and gases (e.g., calcite, $CO_{2(g)}$). The modeling results of three modeling results considering three different temperatures (100, 120 and 140 °C) at a pCO_2 level of 30 atm reveal that increasing temperature on the one hand reduces the concentrations of calcium, strontium and sulfate and on another hand results in higher concentrations of sulfate (partly presented in Fig. 10).

In summary, varying the temperature or pCO_2 modifies not only one parameter, but also several parameters. This indicates that all hydrogeochemical processes are interconnected in a complex reaction web. To correctly identify and subsequently quantify hydrogeochemical processes, all relevant chemical reactions must be thus integrated to the modeling approach. Therefore, the modeling results reveal that the temperature and pCO_2 conditions, which characterized the chemical composition of the produced water measured in Miller oilfield, are probably in the range of 120 °C and 140 °C with a slight increase pCO_2 ranging from 30 atm to 60 atm (no detail presented here; for details, see Fu et al. (2012)).

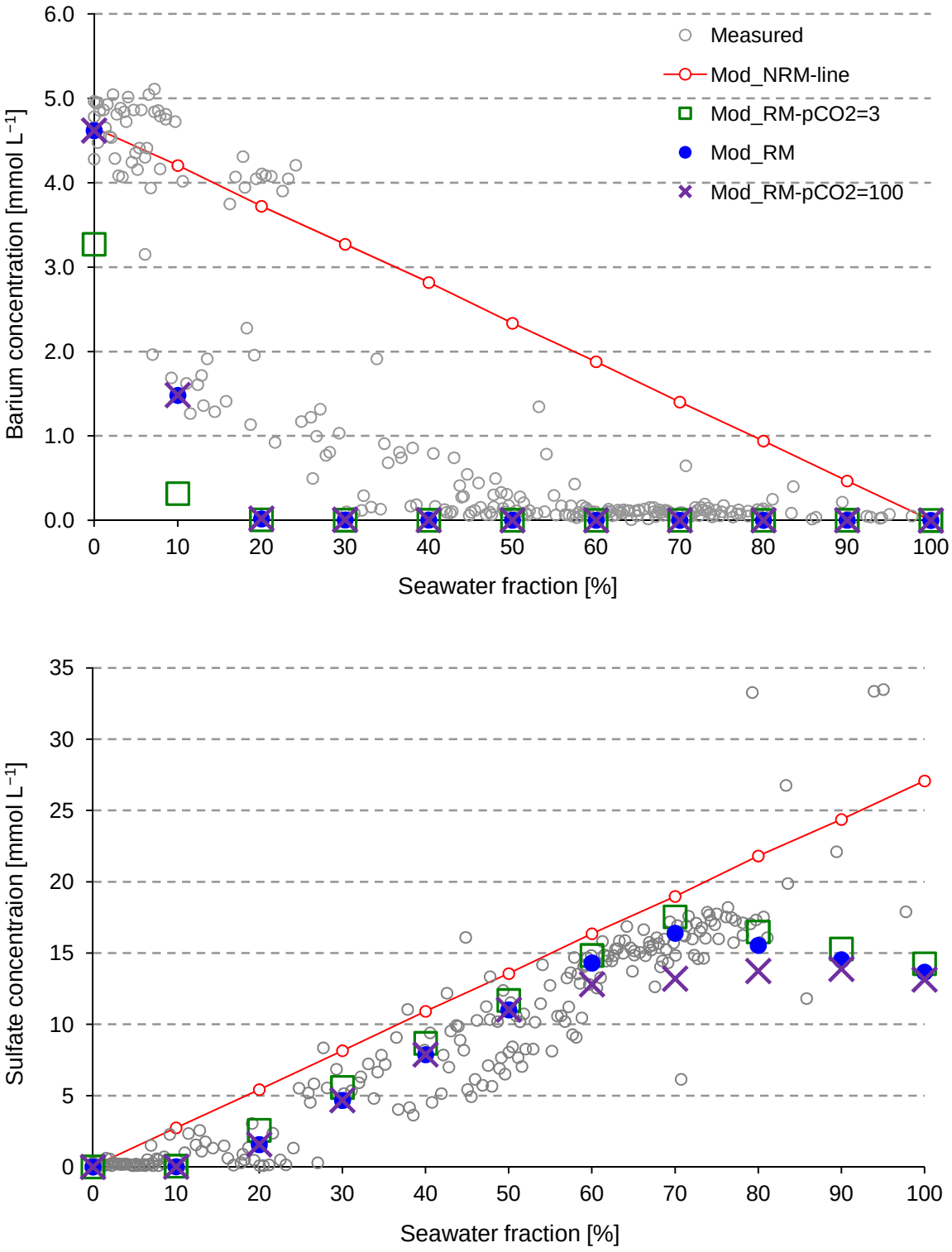

Fig. 8: Measured and modeled concentrations of barium (above) and sulfate (below) for different $CO_{2(g)}$ partial pressures from scenarios NRM, RM_pCO2=3, RM, and RM_pCO2=100 (modified after Fu et al., 2012). Measured data: Houston (2007); Mod: calculated resulted; NRM-line: scenario NRM; RM_pCO2=3: pCO_2 of 3 atm; RM: pCO_2 of 30 atm; RM_pCO2=100: pCO_2 of 100 atm.

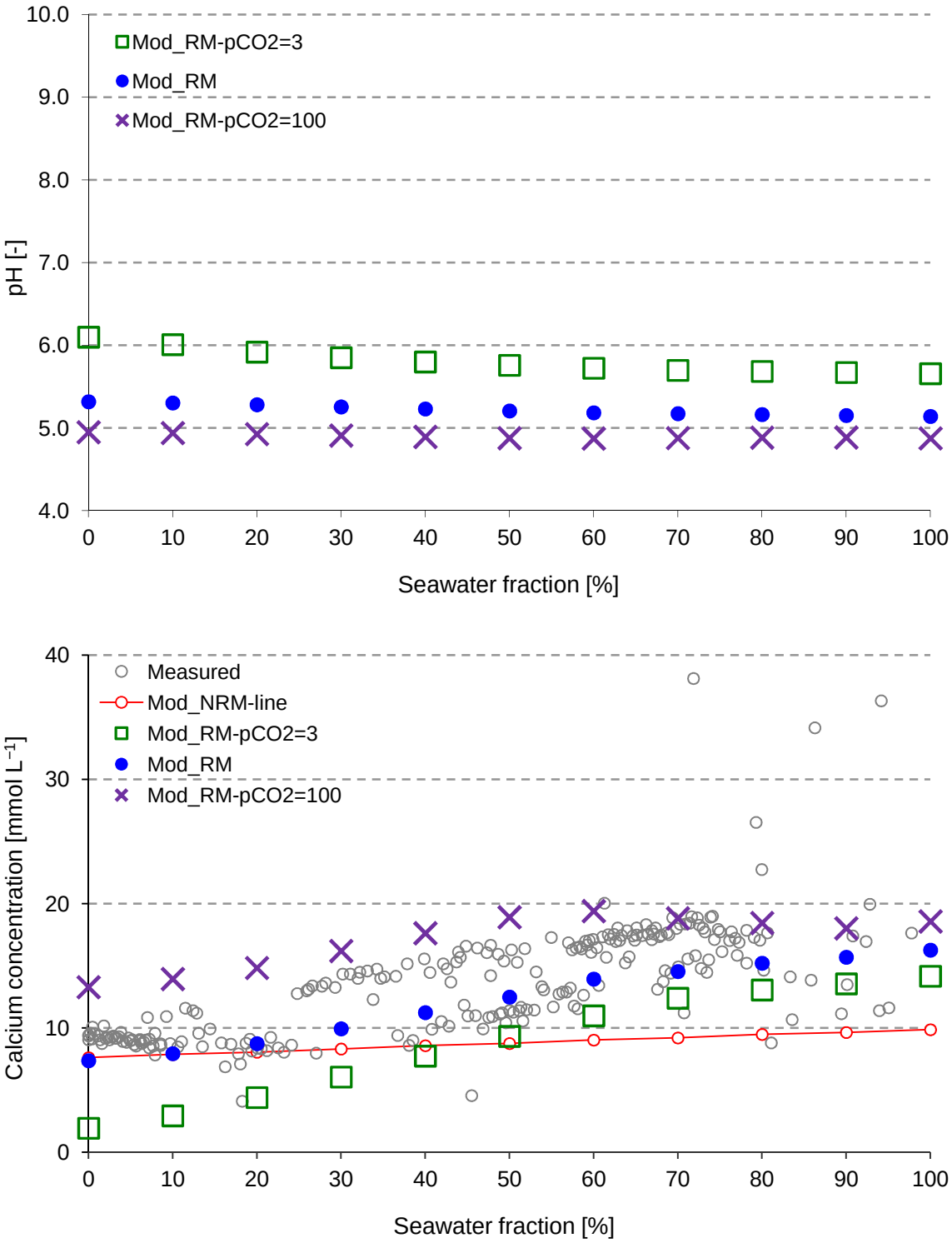

Fig. 9: Measured and modeled results of pH (above; no available measured data) and calcium concentrations (below) for different $CO_{2(g)}$ partial pressures from scenarios NRM, RM_pCO2=3, RM, and RM_pCO2=100 (modified after Fu et al., 2012). Measured data: Houston (2007); Mod: calculated results; NIRM-line: scenario NRM; RM_pCO2=3: pCO_2 of 3 atm; RM: pCO_2 of 30 atm; RM_pCO2=100: pCO_2 of 100 atm.

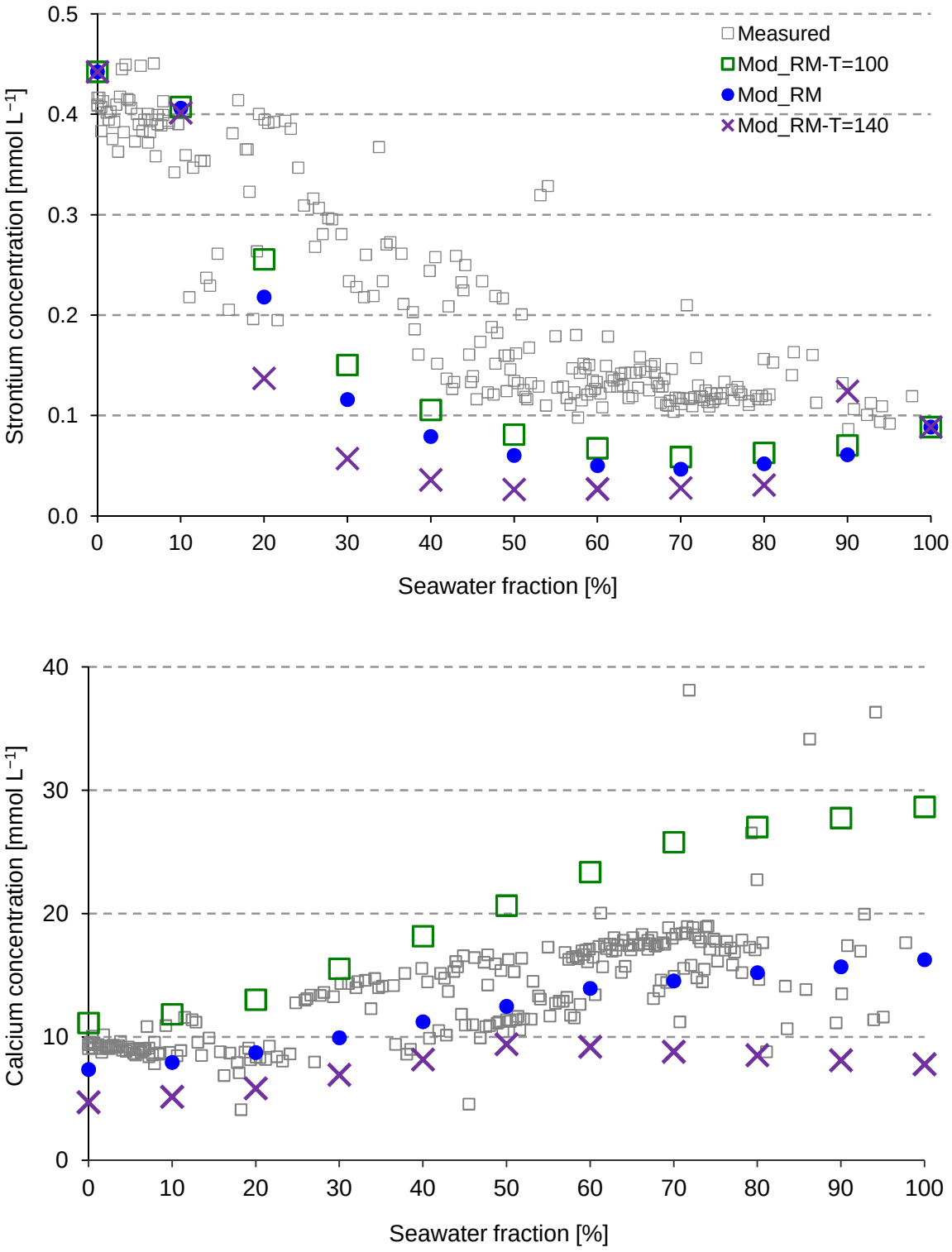

Fig. 10: Measured and modeled concentrations of strontium (above) and calcium (below) for different reservoir temperature conditions from scenarios RM-T=100, RM, and RM-T=140 (modified according to Fu et al., 2012). Measured data: Houston (2007); Mod: calculated results; RM-T=100: temperature of 100 °C; RM: temperature of 120 °C; RM-T=140: temperature of 140 °C.

Additionally, another scenario (RM-Kfs) considers K-feldspar as one of the primary minerals, because K-feldspar is the single proven feldspar phase in the Miller oilfield (Houston, 2007). Van Berk et al. (2009) stated that K-feldspar provides carbonic acid buffering capacity and can control pH at high pCO_2. Equilibration of K-feldspar with the formation water-seawater mixtures results in a high pH level of ca. 6.0 (no detailed results here). This relative high pH induces a low barium concentration in the formation water prior to seawater breakthrough due to witherite precipitation. Consequently, the modeling concentrations of barium and sulfate from scenario RM-Kfs are not in good agreement with the measured data and the modeling results from scenario RM (Fig. 11). Additionally, the modeled high pH lead to a strong deviation of the modeled $c_{tot}Ca^{2+}$ and $c_{tot}Mg^{2+}$ at equilibrium with K-feldspar from the measured data (Fig. 11). Such marked mismatches between the measured data and the modeled results of this scenario suggest that the chemical reactive K-feldspar, which was exposed to the formation water-seawater mixtures, was consumed prior to seawater injection due to the high CO_2 content of the Miller oilfield. Anorthite provide a higher CO_2 buffering capacity compared to K-feldspar (van Berk et al., 2009), and consequently, was maybe completely dissolved prior to K-feldspar dissolution. The chemical composition of the original formation water (unaffected by seawater injection) is characterized by high concentrations of barium and strontium. The both elements are known to be often incorporated in other minerals (e.g., K-feldspar) or to substitute calcium in plagioclases and calcite (Puchelt, 1978; Stueber, 1978). This may be the reason why plagioclase has not been detected, and indicates a strong dissolution of K-feldspar, calcite, and even plagioclase (Fu et al., 2012).

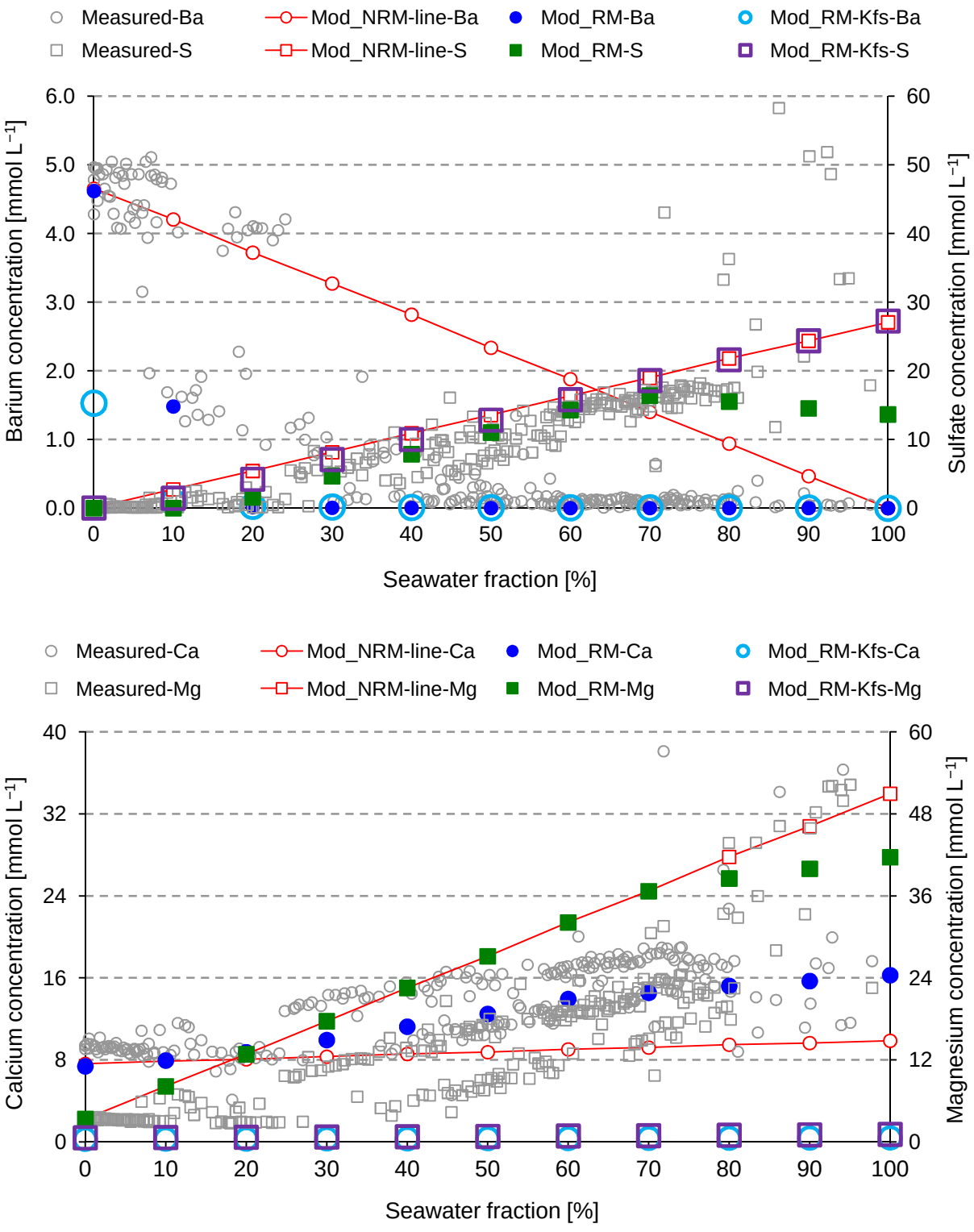

Fig. 11: Measured and modeled concentrations of barium, sulfate, calcium and magnesium from scenarios NRM, RM, and RM-Kfs (modified after Fu et al., 2012). Measured data: Houston (2007); Mod: calculated results; NRM-line: scenario NRM; RM: scenario RM; RM-Kfs: scenario RM-Kfs (additionally considering K-feldspar); Ba, S, Ca, and Mg represent the total concentration of barium, sulfate, calcium and magnesium, respectively.

The calculation of the most probable standard scenario (RM) achieves a reproduction of the measured concentrations. However, the batch model ignores the effect of total pressure on the chemical composition of the produced water. The batch model using the computer code PHREEQC performs calculations only at a total pressure of 1.0 atm. Elevated total pressure conditions influence the solubility constants of minerals and gases and the equilibrium constants of species dissociation and association to a certain degree. A modeling scenario considering solubility constants (RM-Sup), which are calculated by the computer code SUPCRT92 and its data base DPRONS92.dat (Johnson et al., 1992) at elevated temperature and pressure conditions, aims to test the effect of the elevated total pressure. This scenario considering solubility constants, which are calculated by SUPCRT92, is incapable of reproducing the measured concentration development versus seawater fraction, especially the barium and strontium concentrations (Fig. 12). The extremely low witherite solubility, which is calculated by SUPCRT92, causes a removal of barium ions by witherite formation at the seawater fraction of 0% (in other words: prior to seawater breakthrough). Consequently, the low barium activity in the formation water at starting conditions results in formation of Sr-bearing barite with very minor amounts. As a result, the concentrations of strontium and sulfate calculated by scenario RM-Sup deviate from the measured data and the results calculated by scenario RM. The minor amount of Sr-bearing barite newly formed is counter to the statement provided by Wylde et al. (2005) that barite dominates in the scale mineral assemblage.

The Wateq4f.dat database (Parkhurst and Appelo, 1999) defines a log K (25 °C/1.0 atm) of –8.562 for witherite, which is in good agreement with the values presented by Millero et al. (1984; log K = –8.56 ±0.04, at infinite dilution) as well as by Busenberg and Plummer (1986; log K = –8.5617) for the standard condition (25 °C/1.0 atm). All log K values of witherite discussed here refers to the following reaction: $BaCO_{3(s)} \leftrightarrow Ba^{2+} + CO_3^{2-}$. These equilibrium solubility constants of witherite provide a significant difference compared to the constant calculated by SUPCRT92 and DPRONS92.dat (log K = –13.325 for 25 °C and 1.0 atm). Calculating solubility constants by SUPCRT92 for an elevated temperature and pressure condition is based on the solubility constants at 25 °C and 1.0 atm. Thus, this comparison demonstrates that the failure to reproduce the measured data with consideration of the effect of elevated temperature pressure conditions (scenario RM-Sup) is caused by the SUPCRT's incorrect solubility constant for witherite (Fu et al., 2012). As a result, the incorrect solubility constant for witherite causes significant deviations of the modeled concentration of other components from scenario RM_Sup from the measured data, because barium and carbonate species bound to witherite are parts of a complex web of interconnected hydrogeochemical processes.

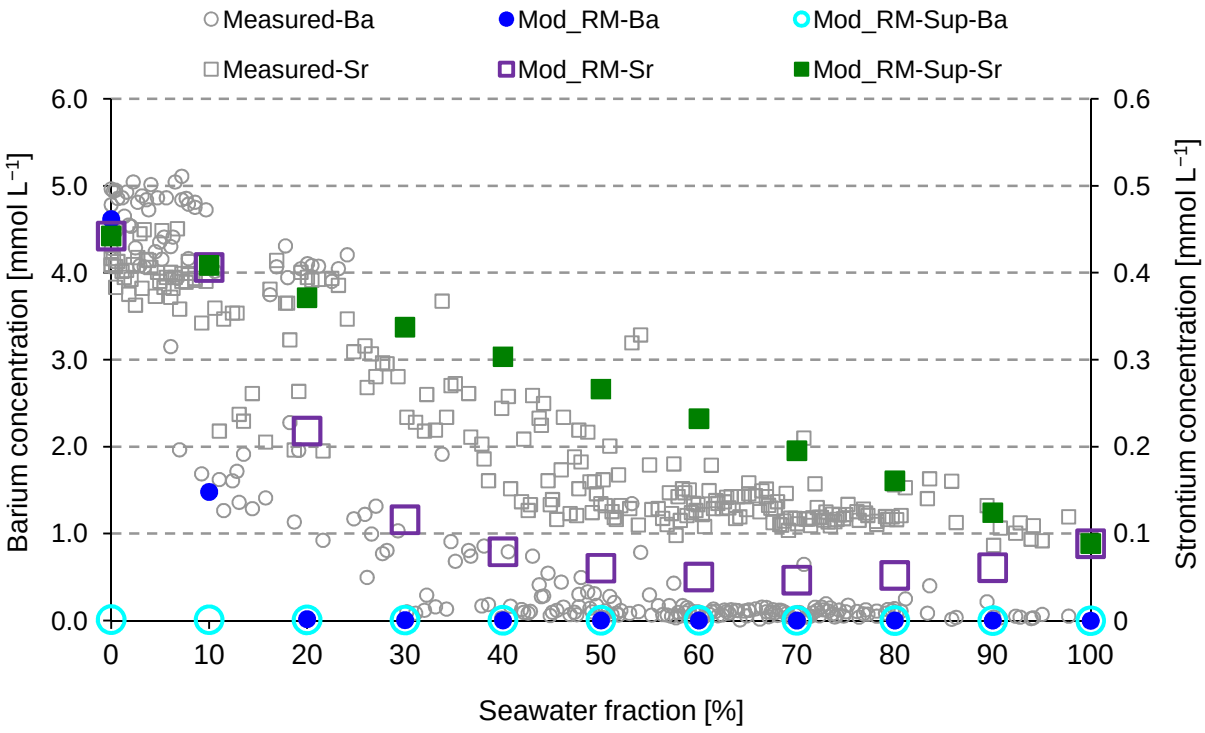

Fig. 12: Measured data and modeled concentrations of barium and strontium from scenarios RM and RM-Sup (modified according to Fu et al., 2012). Measured data: Houston (2007); RM: scenario RM based on the Wateq4f.dat database; RM-Sup: scenario RM-Sup using the solubility constants calculated by SUPCRT92 and its database DPRONS92 at 120 °C and 500 atm; Ba and Sr represent the total concentration of barium and strontium, respectively.

Wesolowski et al. (2004) stated that the majority of isocoulombic homogenous actions are commonly insensitive to pressure changes at a constant temperature, provided that the temperature is lower than 250 °C. Based on the following two examples, Fu et al. (2012) illustrated the effects of increased pressure on solubility constants of minerals. García (2005) calculated that 1.1×10^{-4} mol kgw^{-1} barite dissolves in 0.2 molal NaCl solution at 120 °C and 500 atm (corresponding to the Miller oilfield's reservoir conditions). 8.2×10^{-5} mol kgw^{-1} barite dissolves in 0.2 molal NaCl solution by using PHREEQC and its Wateq4f.dat database for the same temperature and pressure conditions. A difference of 2.8×10^{-5} mol kgw^{-1} is the range of tolerable analytical inaccuracy. The quartz solubility was investigated at 100 °C for 50 and 500 atm by Azaroual et al. (1997). The difference in aqueous silica activities in equilibrium with quartz between these two pressures is only ca. 10% of the equilibrium activity at 500 atm. In comparison to pressure, changes in temperature more strongly affect the solubility constant of minerals.

All alternative modeling scenarios are incapable of providing a reproduction of the measured magnesium concentrations. The mismatch between the measured and modeled magnesium concentrations reveals that the batch model excludes the hydrogeochemical processes controlling the magnesium concentrations.

3.2.4 Conclusions of batch modeling

In summary, the modeling approach developed by Fu et al. (2012) considers all hydrogeochemical processes potentially occurring in the Miller oilfield, and also includes dissolution of primary minerals. The modeling approach aims to quantify the hydrogeochemical processes characterizing the chemical composition of the produced water measured in the Miller oilfield by comparing the modeling results with the measured data. A fairly good accordance between the measured and modeling results confirms the validity of the batch model, even allowing for several modeling limitations (see section 3.2.3). The modeling results of the batch modeling indicate:

(1) that mixing of seawater and formation water induce precipitation of Sr–bearing barite solid solutions, dolomite, and potentially also of anhydrite in the Miller oilfield,

(2) that calcite and microcrystalline quartz dissolve,

(3) that the composition and the amount of the mineral assemblage including scale minerals depend on the seawater fraction, and more importantly,

(4) that the formation water-seawater mixtures quickly achieved near-equilibrium conditions with respect to the abovementioned hydrogeochemical processes.

This achievement of equilibrium conditions is the prerequisite for any modeling approach based on chemical thermodynamics to quantitatively predict the mass conversion of hydrogeochemical processes without any kinetic aspect, provided that the residence time of aqueous solutions under the reservoir conditions is more than two years.

Varying different parameters of the batch model and comparing the modeling results with the measured data can help us (1) to conclude on which hydrogeochemical processes occurred and (2) to identify the temperature and pressure conditions (including $pCO_{2(g)}$ level) at which such processes occurred. For instance, the modeling results suggest that the K-feldspar is not involved in the complex web of the interconnected hydrogeochemical processes in the Miller oilfield. Testing different temperature and pCO_2 conditions and comparing the modeling results with the measured data indicate that the pCO_2 prevailing in the mixing zone during seawater injection into the Miller oilfield is in the range of 30 atm at the reservoir temperature of 120 °C to 60 atm at a temperature of 140 °C.

A batch modeling exercise using the PHREEQC computer code (Parkhurst and Appelo, 1999) considers an admixture of the injected seawater to the original formation water measured in the Miller oilfield at various mixing factors (for details, see Table 2). Similar to such approaches selecting specific minerals, this separate PHREEQC exercise only allows formation of barite, celestite and anhydrite due to the chemical incompatibility of the both water types (for details of the input file of this PHREEQC exercise, see Appendix A1). The calculated results of this separate exercise show that barite is the single mineral phase newly formed from the formation water-seawater mixtures at any mixing ratio, whereas anhydrite only forms at higher seawater fractions (>90%; Table 3).

Additionally, the amount of barite calculated by this separate exercise differs from the amount of Sr-bearing barite from scenario RM (considering all relevant hydrogeochemical processes). This comparison of these two modeling scenarios reveals that the selected hydrogeochemical processes affect not only the type of minerals precipitated or dissolved but also their intensity. Therefore, a model, which aims to represent the reality, must involve all hydrogeochemical processes of aqueous species, mineral phases and gas phase in this system. This is because all hydrogeochemical processes affect each other. A model, which isolates certain processes (e.g., considering only barite formation) from the entire system, can merely lead to a wrong calculated mass conversion (e.g., the amount of barite precipitated due to seawater injection). Consequently, a "reasonable" model must consider all hydrogeochemical processes potentially occurring in this system.

Table 3: Calculated amount of sulfate minerals newly formed (units: mmol per one liter of formation water-seawater mixtures) in the batch model and in the separate exercise for various seawater fractions.

		Seawater fraction [%]								
		10	20	30	40	50	60	70	80	90
Batch model	Sr-barite	2.91	4.15	3.74	3.24	2.72	2.20	1.66	1.12	0.57
Separate exercise	Barite	2.92	4.0	3.5	3.01	2.50	2.00	1.50	1.00	0.50
	Celestite	0.0	0.0	0.0	0.0	0.0	0.0	0.0	0.0	0.0
	Anhydrite	0.0	0.0	0.0	0.0	0.0	0.0	0.0	0.0	0.13

The application of the batch model developed by Fu et al. (2012) is unrestricted to a siliciclastic oil reservoir. Adapting variable input parameters of this modeling approach to a case specific reservoir broadens its applications. For instance, scale formation in a carbonate reservoir can be reproduced by changing the primary mineral assemblage. Modeling scale formation, which results from sulfate reduction or $H_2S_{(g)}$ from the reservoir gas, can also be modeled by addition of reducing agents or H_2S to the batch model.

The calculated mass conversion of minerals precipitated or dissolved refers to one liter of formation water-seawater mixtures for a given mixing ratio. It is still unknown whether such modeling results could be linearly extrapolated to cases of much larger volumes of produced water (several orders of magnitude). Although a batch model considers all relevant hydrogeochemical processes that potentially occur in reservoirs, it is still incapable of correctly quantitatively evaluating such processes (including scale formation). This is due to the fact that modeling results of a batch model, just like the measured chemical composition of the produced water, are an integrated signal of all hydrogeochemical processes in reservoirs. Additionally, batch models exclude any temporal and spatial aspects. Thus, batch modeling is incapable of providing any information about when and where scale minerals form. Effects of hydraulic processes (water flow; e.g., dispersive-advection in

combination with diffusion) on hydrogeochemical processes cannot be integrated into any batch modeling. Consequently, a 1D hydrogeochemical reactive transport modeling should be developed to more exactly identify hydrogeochemical processes and to quantify their intensity. In comparison to batch modeling, temporal and spatial aspects are integrated into a 1D transport model. The 1D transport model is capable of investigating the effects of the simultaneously occurring hydraulic processes (fluid flow) on the thereby coupled hydrogeochemical processes (water-rock-gas interactions). Nevertheless, a reasonable hydrogeochemical batch model is one of basic prerequisites for building up a plausible 1D and even 3D reactive transport model.

3.3 One-dimensional reactive transport modeling

Forecasting hydrogeochemical processes in time and space, for instance production-interfering scale formation, is high on the agenda for successful reservoir engineering and finally for efficient and sustainable technical measures in oil reservoirs. So far, useful tools, which satisfy such requirements of reservoir engineering, are lacking. The applicability of batch modeling approaches (e.g., developed by Houston, 2007, and by Fu et al., 2012) is restricted to defined starting conditions which are oversimplified compared to the real reservoir conditions constantly developing in time and space. In addition, such batch modeling approaches are based solely on two water analyses − unchanged formation water and injected seawater. Sorbie and Mackay (2000) proposed that intense admixture of injected seawater to formation water occurs in or near production wells. On the contrary, local deposition of scale minerals caused by seawater injection within reservoir aquifers would be insignificant (Sorbie and Mackay, 2000). However, seawater can react with the formation water and the reactive reservoir rocks within the reservoir aquifer, before it reaches production wells. Such hydrogeochemical processes occurring along the flow path of formation water-mixtures continuously modify the chemical composition of the seawater water. Consequently, the seawater, which reaches the production well and results in scale formation there, does not keep its same chemical composition compared to its composition during injection. Therefore, any batch model approach is incapable of providing a reproduction of such an ongoing and dynamic system, for instance the oil reservoir undergoing seawater injection.

The shortcomings of the batch model developed by Fu et al. (2012; or see section 3.2) promote an extension of a batch model to a one-dimensional hydrogeochemical transport (1DHT) model based on thermodynamic equilibrium. In the following, reference is mainly made to Fu et al. (2013b) unless otherwise indicated. Their publication involves the modeling setup of the 1DHT transport model, the corresponding modeling results, discussion of the modeling results and conclusions. Developing a 1DHT model aims to more exactly quantify hydrogeochemical processes, as well as to identify their temporal and spatial evolution. Similarly to the batch model (Fu et al., 2012; or for details, see section 3.2), the developed 1DHT model uses the PHREEQC computer code (Parkhurst and Appelo, 1999),

which includes the capacities to model chemical equilibrium reactions and to simulate 1D reactive mass-transport including dispersion and diffusion. The direct way to verify the validity of a model is to check whether the measured data (signals or proxies of real processes) match the modeled data. To test the validity of this 1DHT model, the Miller oilfield is chosen as the test site, because it has undergone water injection for 10 a (Houston et al., 2007). Additionally, its accessible measured data are characterized by the hydrogeochemical processes driven by water injection and are of high quality.

3.3.1 Modeling setup

The developed 1D hydrogeochemical transport model comprises a geohydraulic and hydrogeochemical model part. The geohydraulic model part calculates different transport processes, such as dispersive-advection and diffusion. Due to its 1D feature, a 1DHT model is incapable of simulating transversal dispersion. The hydrogeochemical part calculates the chemical reactions among mineral phases, pore water and gas phase. Thus, a 1DHT model simplifies a flow field and couples fluid flow to the hydrogeochemical processes. Several assumptions and simplification of the flow field of the Miller oilfield must be made in this study owing to the lack of data (e.g., hydraulic head, number of production and injection wells, their spatial configuration). The 1DHT model considers this simplified flow field (Fig. 13) and aims to semi-generically reproduce the simultaneously occurring and coupled hydraulic (water flow) and hydrogeochemical processes (water-rock-gas interactions).

(1) Geohydraulic model part

Figure 13 schematically illustrates a generic flow field triggered by one seawater injection and by one production well. This generic flow field is calculated by the computer code PHAST (Parkhurst et al., 2010) based on assumed hydraulic data (e.g., injection- and production rate, reservoir permeability and dispersivity). The migration of injected seawater through the reservoir aquifer is markedly characterized by the temporal and spatial development of the chloride concentration of pore water (Fig. 13). Injected seawater flows through the reservoir aquifer towards the production wells and stepwise substitutes the formation water filling the aquifer along the flow path of the seawater. At any time, the reservoir aquifer can be divided into three different aquifer types depending on the pore water filling the aquifer: (1) seawater with a lowest chloride concentration, (2) formation water with highest chloride concentration, and (3) formation water-seawater mixtures along the flow path from the injection well to the production well (Fig. 13). The water mixtures result from longitudinal dispersion. It leads to the mixing of the both water types at the front, which is located between the erstwhile seawater and the original formation water (Fig. 13). In addition to dispersion, hydrogeochemical processes among minerals, pore water and gas phase modify the composition of the injected water, as it migrates through the reservoir aquifer. Subsequently, the composition of the

seawater, which reaches the production well and results in scale formation there, deviates from its original composition during injection.

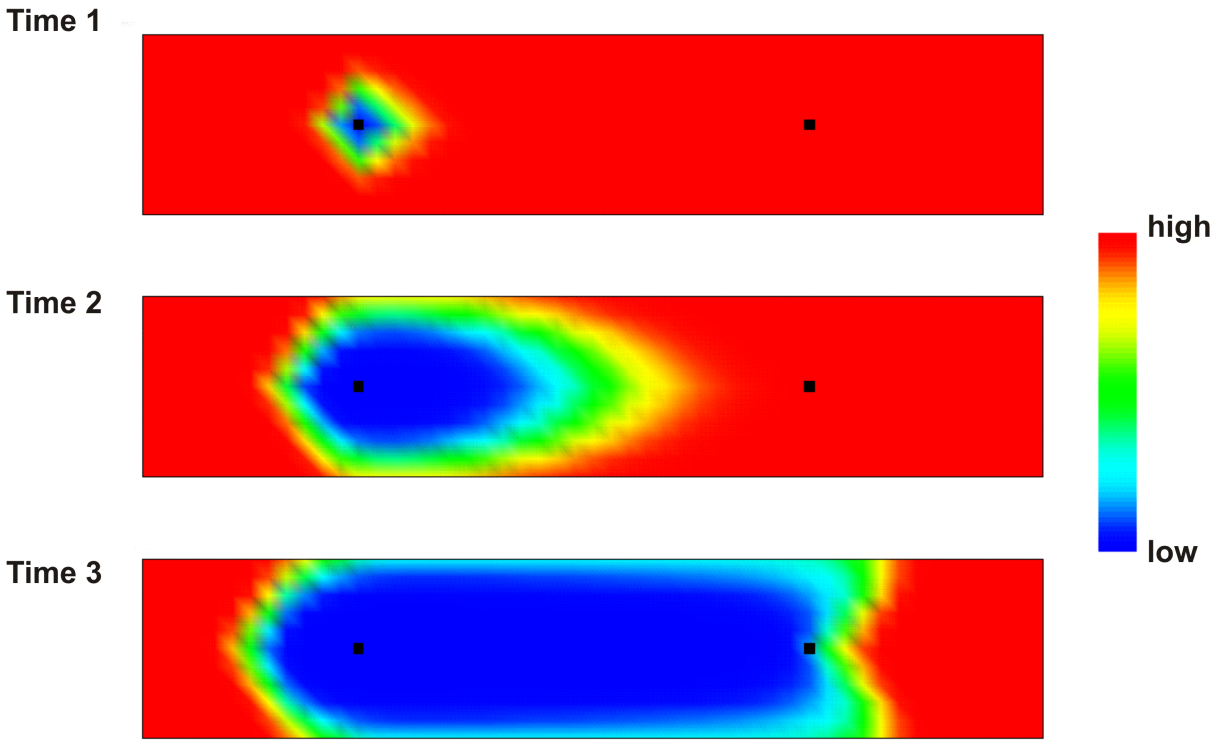

Fig. 13: Schematic of the two-dimensional migration of injected seawater through the reservoir aquifer characterized by the development of chloride concentration at three different time steps; Black squares: injection (left) and production (right) wells; Color bar: relative chloride concentration; Red: highest chloride concentration in formation water; Blue: lowest chloride concentration in injected seawater; the migration is calculated by PHAST (Parkhurst et al., 2010) based on assumed hydraulic data.

Conceptually, a flow field can be simplified and represented by multiple 1D stream tubes (Fig. 14). Sorbie and Mackay (2000) stated that intense mixing of seawater and formation occurs almost near or in production wells. Thus, only the 1D stream tubes, which end in production wells, are of great importance for predicting scale formation. The other stream tubes are ignored in this mode. One additional compartment is set up and represents as production well behind the end of all 1D stream tubes ending in the production well. Water leaving of the last cell of all stream tubes is mixed in the production well (Fig. 14). Hydraulic conditions (e.g., the injection and production rates, the number of injection and production wells, and their spatial configuration) determine the fraction of water which leaves each stream tube and subsequently flows in the production water. If all hydraulic relevant data are available, a 2D or 3D flow model can be built. Such models provide a reproduction of the hydraulic conditions and the temporal development of the mixing ratio of water from all stream tubes. Adapting corresponding variable input parameters (e.g., number and length of cells, time step) to case-

specific oilfields allow applications of this 1DHT model for other oilfields exposed to seawater injection. The validity of this 1DHT model is tested in the Miller oilfield test site.

A reproduction of the hydraulic flow field in the Miller field is prevented due to lacking hydraulic field data. As a result, the flow field of the Miller oilfield is simplified in this 1DHT geohydraulic model part. The geohydraulic model part consists of only one stream tube that represents all stream tubes starting at the injection well and ending at the production well (Fig. 14). At any time, the flow field can be roughly divided into two parts that both are filled with erstwhile seawater and formation water, respectively (Fig. 14). The produced water is composed exclusively of the original formation water, before the front arrives at the production well. The erstwhile seawater is mixed with the formation water in the production well only after seawater breakthrough. The variation of the mixing factors of the both water types in the production well represents different length of the flow paths, different arrival times of seawater from different stream tubes, and even changes in hydraulic conditions (e.g., caused by changed injection and production rates). The mixing ratios of water from each stream tube can be provided by 2D or 3D flow modeling. In the case of the lack of the hydraulic field data and of the simplification of the flow field of the Miller oilfield, the 1DHT model for the Miller oilfield is only of semi-generic nature. The mixing ratios of the water from the two parts (filled by erstwhile seawater and by formation water) are specified by calibration in view of the measured chloride concentrations, in other words: adapted to the measured temporal development of the chloride concentration in the produced water. Chloride can be considered to be non-reactive tracer because of its inert chemical properties. Additionally, its concentration in the seawater is lower than the formation water and remains almost unchanged in the both water types. Thus, the chloride concentration in the produced water characterizes the seawater fraction (Houston et al., 2007; Fu et al., 2012). The temporal development of chloride concentrations provided by Houston et al. (2007) indicates that the injected seawater reaches the production well after ca. 611 days. In the Miller field, one typical production well is located ca. 2.5 km away from an injection well (Houston et al., 2007). This distance is treated as the mean flow path length. As a result, the calculated mean apparent flow velocity of formation water-seawater mixtures is 4.1 m day^{-1} in the 1DHT model for the Miller oilfield test site. The total simulation period is assumed for 1833 days, because the chloride concentration was almost daily measured within this production time. A 2.5 km long 1D stream tube consists of 25 cells (each 100 m in length). One modeling time step can be calculated for 24.44 days on the base of the mean apparent flow velocity of 4.1 m day^{-1} and a flow distance (cell length) of 100 m. In total, the calculation is performed for 75 modeling time steps. Although such a discretization is rough, this study does not test the effects of temporal and spatial discretization on the modeling results. For other applications of the 1DHT for case-specific oilfields, a reasonable and suitable discretization should be chosen.

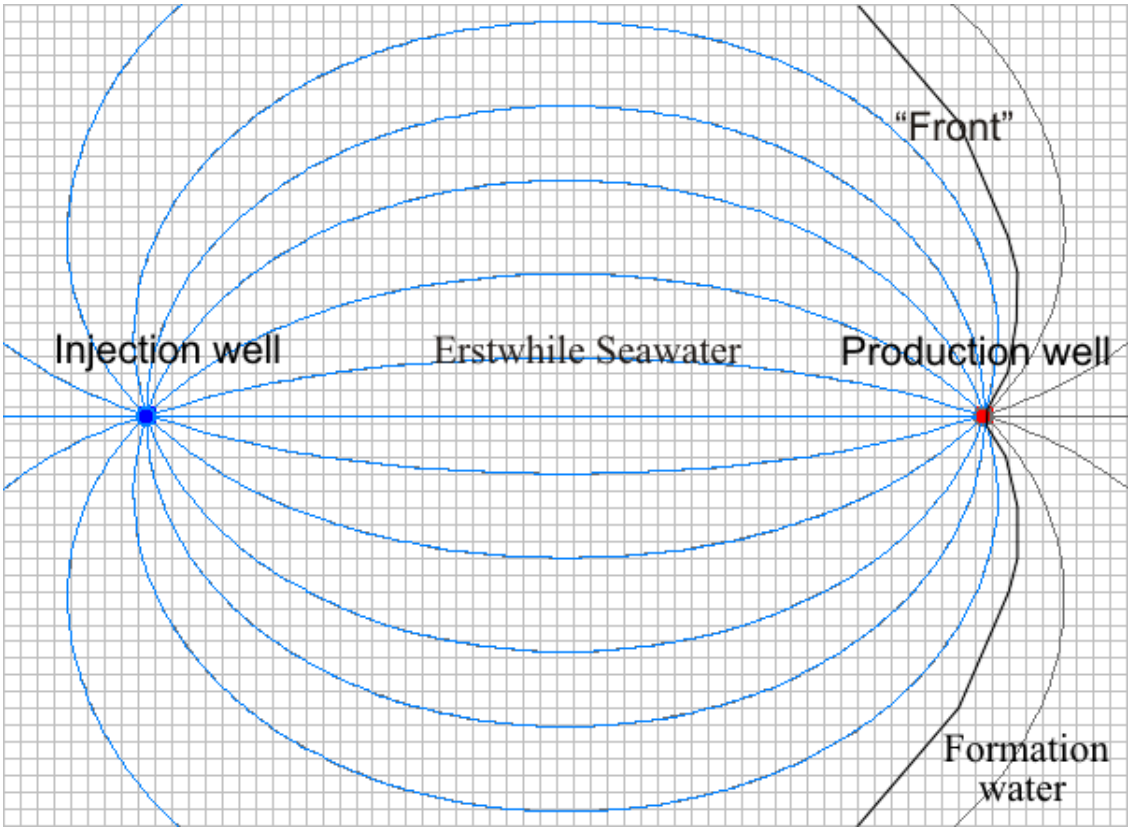

Fig. 14: Schematic of the simplified flow field triggered by seawater injection at a given time step and division of this flow field into multiple 1D stream tubes (modified after Fu et al., 2013b); Blue lines: representing the stream tubes filled by erstwhile seawater; Black line: representing the stream tubes filled by formation water; Bold black line: illustrating the front resulting from dispersion.

At starting conditions prior to seawater injection, one liter of the original formation water fills the pore space of each cell. At each modeling time step, one liter of the injected original seawater flows into the first cell, and consequently, forces a movement of the original pore water by advective flow from the first cell to the second cell (Fig. 15). This displaced pore water flows 100 m into the second cell. Simultaneously, one liter of pore water (in the temporal order of appearance: original formation water, formation water-seawater mixtures resulting from dispersion, erstwhile seawater after breakthrough) flows out from the last (the 25th) cell of the stream tube, is admixed into the original formation water in the compartment (cell 26; representing the production well), and is pumped as produced water.

Dispersion leads to the formation of the formation water-seawater mixtures. Their intensity depends on longitudinal dispersivity (transversal dispersion is ignored in this study). Depending on flow path length, a strong variation of longitudinal dispersivity was observed (Kinzelbach and Rausch, 1995, and references therein). For a flow path of 100 m in length (the cell length), the observed dispersivity varies from ca. 1 up to 100 m. The 1DHT model considers a pre-assigned dispersivity of 10 m. Diffusion is excluded from the transport calculation due to the high velocity (4.1 m day^{-1}). The

voluminous PHREEQC input file of the standard 1DRM and the calibrated mixing factors were documented in the appendix provided by Fu et al. (2013b).

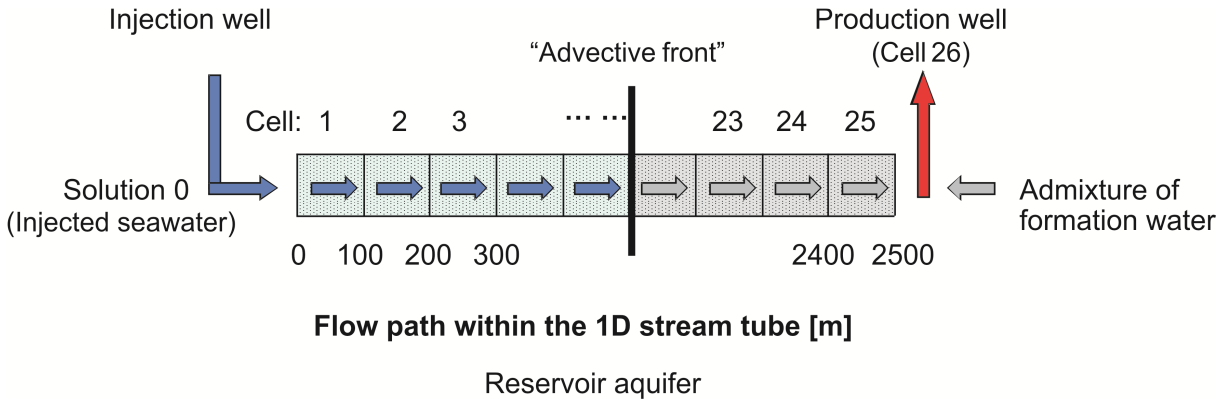

Fig. 15: Schematic of the conceptual 1D stream tube representing the simplified flow field (modified according to Fu et al., 2013b).

(2) Hydrogeochemical model part

In the 1DHT model, the hydrogeochemical model part defines (1) the chemical composition of injected seawater and formation water, (2) the mineralogical composition of the reservoir aquifer rock, and (3) the chemical composition of the gas phase, if it prevails in the reservoir. Wider applications of the 1DHT can be achieved by adapting such parameters to a case-specific reservoir or by changing their homogenous distribution to a heterogeneous distribution in order to identify hydrogeochemical consequences of water injection into other oil reservoirs.

For the Miller oilfield test site, several basic assumptions are made. Firstly, the 1DHT stream tube display a homogeneous distribution of hydrogeochemical properties with respect to the mineralogical composition of the reservoir aquifer rocks and porosity. Secondly, the pore space of each cell is filled with the same formation water at starting conditions. Thirdly, the chemical composition of the injected seawater and of the original formation water admixed in the production well remains unchanged during the 75 modeling time steps. Additionally, neither dissolution nor precipitation of chloride-bearing mineral phases occurred in the Miller oilfield.

Each cell represents one liter of pore volume and a total volume of 7.1 liters, and contains the primary mineral assemblages that have been used in the batch model (for details, see section 3.2 or Fu et al., 2013b). The results of the batch modeling demonstrate that the formation water-seawater mixtures did not equilibrate with the reactive K-feldspar (Fu et al., 2012; section 3.2). Thus, K-feldspar is excluded from the primary assemblage. Additionally, the batch modeling results (Fu et al., 2012; section 3.2) suggest that the produced water of the Miller field equilibrated with a easier soluble

$SiO_{2(s)}$ phase compared to the microquartz investigated by Azaroual et al. (1997). In the Wateq4f.dat database, the chalcedony is defined by a higher solubility compared to the microquartz's solubility at 120 °C. In consequence, chalcedony is chosen as the reactive $SiO_{2(s)}$ phase equilibrating with the formation water-seawater mixtures used in most modeling scenarios instead of the microquartz. Nevertheless, an additional scenario 1DRM-MQ uses the solubility of the microquartz investigated by Azaroual et al. (1997) to test how intensively the modeling results depend on the type of $SiO_{2(s)}$ phase. In summary, the primary mineral assemblage contains calcite, chalcedony and kaolinite in most modeling scenarios (Table 4).

Mixing of the chemically incompatible injected seawater and formation water in the production well or driven by dispersion within the reservoir aquifer lead to a new equilibrium state of the species distribution among $minerals_{(s)}$, aqueous $species_{(aq)}$ and $gas_{(g)}$. In consequence, secondary mineral phases can form at their saturation. The batch modeling results unravel the most hydrogeochemical processes occurring in the Miller oilfield except for the formation of calcium sulfate phase. Similar to the batch model, the secondary mineral assemblage of the standard scenario 1DRM includes barite, celestite, their solid solutions, witherite, celestite, strontianite, dolomite, gypsum (Table 4). Two scenarios 1DRM and 1DRM-An consider gypsum and anhydrite as secondary calcium sulfate phase, respectively, and aim to identify which phase actually forms.

At elevated temperature and pressure conditions, the injected seawater is undersaturated regarding to several primary reservoir aquifer minerals. The thereby induced re-equilibration between the injected seawater and the reservoir aquifer minerals changes the chemical composition of the injected seawater. Thus, the seawater, which reaches the production well later, does not keep its chemical composition compared to its original composition during injection. In this study, the corresponding solubility constants and their temperature dependence are defined in the Wateq4f.dat database (Parkhurst and Appelo, 1999).

Prior to seawater injection, the primary phase assemblage is equilibrated with the original formation water and the CO_2 gas phase at starting conditions. Another important gas component methane is ignore in the batch model, because no publication mentioned the significant effects of sulfate reduction or sulfur-bearing scale formation in the Miller oilfield. The results of the batch model (Fu et al, 2012; section 3.2) suggest that all relevant hydrogeochemical processes reached their equilibrium conditions at a reservoir temperature of 120°C that is used in all modeling scenarios in this study. The calcium concentration in the original formation water, which is calculated in equilibrium with calcite at a $pCO_{2(g)}$ level of ca. 30 bar (suggested by Fu et al., 2012) prior to seawater breakthrough, are slightly lower than the measured data. A good agreement between the equilibrium calcium concentration and the measured data requires a $pCO_{2(g)}$ level of 40 bar that is applied to all modeling scenarios in this study. Due to low clay contents in the Miller oilfield (Lu et al., 2011), the effect of cation exchange on the calculated mass conversion and on the chemical composition of the

produced water can be considered to be minor. However, an alternative modeling scenario includes cation exchange and tests its effects (Table 4). Iron(III) hydrous oxides have not been mentioned as major components of the reservoir mineral assemblage. Consequently, surface complexation on such iron(III) hydrous oxides is bypassed due to their potential limited effectds. Fu et al. (2012) discussed the effect of the total pressure (differing from 1 atm) on the equilibrium constants (1) of the solubility of minerals and gases, as well as (2) of dissociation and association of species in detail. They stated that this effect may be minor. Consequently, the pressure effect on all reactions is neglected in this study.

3.3.2 Modeling scenarios

Lacking data (e.g., aqueous dispersivity, the type of $SiO_{2(s)}$ and of calcium sulfate phase equilibrating with the reservoir fluids, etc.) results in calculations of several alternative modeling scenarios (Table 4). Such modeling scenarios with different processes or parameter values are needed to cover a broad range of the possible reservoir conditions. Additionally, several modeling scenarios aim to approach to the reality of supposed processes, such as formation of anhydrite or of gypsum. Table 4 summarizes all tested parameter values and processes in this study: (1) different mineral types (anhydrite displaces gypsum; microquartz substitutes chalcedony), (2) cation exchange, (3) dispersivity, (4) sampling effects (only $CO_{2(g)}$ outgassing here), (5) the method for calculating activity coefficients (alternatively using Pitzer parameters), and (6) sampling effects (CO_2 outgassing in this study). Moreover, a modeling scenario 1DNRM (1D transport model with Non-Reactive Mixing) exclusively considers pure dilution of formation water in the production well by seawater without any heterogeneous reactions. This means that this scenario suppresses all chemical reactions among minerals, pore water and gas phase. However, scenario 1DNRM takes dissociation and association of species into account. It aims to compare its results with the modeling results of other scenarios considering reactive mixing. Furthermore, this comparison should highlight how intensively hydrogeochemical processes influence the chemical composition of the produced water and the mass transfers of mineral phases precipitated or dissolved.

The calculated concentrations of all aqueous components are given in molal units in PHREEQC. To directly compare the measured data with the calculated data, the concentrations of aqueous components are re-converted from mol kgw^{-1} to mol L^{-1} by specified factors with consideration of the aqueous solution's density (Fu et al., 2012, 2013b).

Table 4: Modeling scenarios of the 1D hydrogeochemical transport model (modified according to Fu et al., 2013b).

	Model type		Data base		Mineral assemblage												CE	Dispersivity (m per 100 m flow path)			*p*CO2 Drop
					Si-bearing minerals			Carbonates				Sulfates									
	NRM	RM	W	P	Ch	MQ	Kao	Cc	Do	St	Wi	Ba	Ce	Sr-Ba	Gy	An		1	10	100	
1DNRM	x		x																x		
1DRM		x	x		x		x	x	x	x	x	x	x	x	x	x			x		
1DRM-An		x	x		x		x	x	x	x	x	x	x	x	x	x			x		
1DRM-MQ		x	x			x	x	x	x	x	x	x	x	x	x	x			x		
1DRM-Ex		x	x		x		x	x	x	x	x	x	x	x	x	x	x		x		
1DRM-Dis1		x	x		x		x	x	x	x	x	x	x	x	x	x		x			
1DRM-Dis100		x	x		x		x	x	x	x	x	x	x	x	x	x				x	
1DRM-Drop		x	x		x		x	x	x	x	x	x	x	x	x	x					x
1DRM-Pi		x		x	x		x	x	x	x	x	x	x	x	x	x					

1DNRM: non reactive mixing (hydrogeochemical heterogeneous interactions are unconsidered); 1DRM: reactive mixing (hydrogeochemical heterogeneous interactions are included); W: Wateq4f database (Parkhurst and Appelo, 1999); Pi: Pitzer database developed by Bozau (2013); Ch: Chalcedony; MQ: microquartz characterized by the solubility investigated by Azaroual et al. (1997); Kao: kaolinite; Cc: calcite; Do: dolomite; St: strontianite; Wi: witherite; Ba: barite; Ce: celestite; Sr-Ba: Sr-Barite; Gy: gypsum; An: anhydrite; CE: cation exchange; x: present as mineral phase or process included in modeling scenario.

3.3.3 Modeling results

The modeling results (especially scenarios 1DNRM and RM) are described in detail in this chapter. The detailed description of the modeling results (especially the compositional development of the produced water) aims to identify the mechanisms of hydrogeochemical processes including scaling, because the concentration of a certain aqueous component can be affected by different processes. Moreover, all hydrogeochemical processes of any system are interconnected and affect each other. For instance, the sulfate concentration could be potentially controlled by mixing of the injected seawater and the formation water. Another control can be precipitation of Sr-bearing barite and of calcium sulfate minerals (anhydrite or gypsum) in a system that undergoes seawater injection and that is rich in sulfate, calcium, and strontium ions. Consequently, a detailed description of the modeling results from different modeling scenarios could help to better understand such a complex web of water-rock-gas interactions. The results of alternative scenarios are briefly discussed in section 3.3.4 and their complete results can be found in the Appendices.

(1) Non-reactive mixing scenario 1DNRM

Scenario 1DNRM suppresses all heterogeneous chemical equilibrium reactions among minerals, pore water and gas phase. The temporal development of measured and calculated (calibrated) chloride concentrations ($c_{tot}Cl^-$) reveal that the injected seawater arrived at the production well after ca. 611 days and that its fraction in the produced water continuously increases up to 1176 days followed by a slight decrease (Fig. 16). A similar tendency is reflected by the modeled sodium concentrations (1DNRM) which temporal development is in good accordance with the measured data. On the other hand, the modeled pH remains almost constant (ranging from 5.2 to 5.3; Fig. 16). On the contrary, the modeled concentrations of barium, sulfate and magnesium ($c_{modeled} > c_{measured}$) and of calcium and dissolved silica ($c_{modeled} < c_{measured}$) clearly deviate from the measured data (Figs. 16 to 18).

(2) Reactive mixing scenario 1DRM

Any sodium-bearing mineral is unconsidered in the primary or secondary mineral assemblage. Hence, no difference of modeled sodium concentrations ($c_{tot}Na^+$) occurs between scenarios 1DNRM and 1DRM. A constant $pCO_{2(g)}$ of 40 bar and coupled fluid-rock interactions within 1DRM lead to an almost constant modeled pH level between 5.0 and 5.2, which is slightly lower than scenario 1DNRM (Fig. 16).

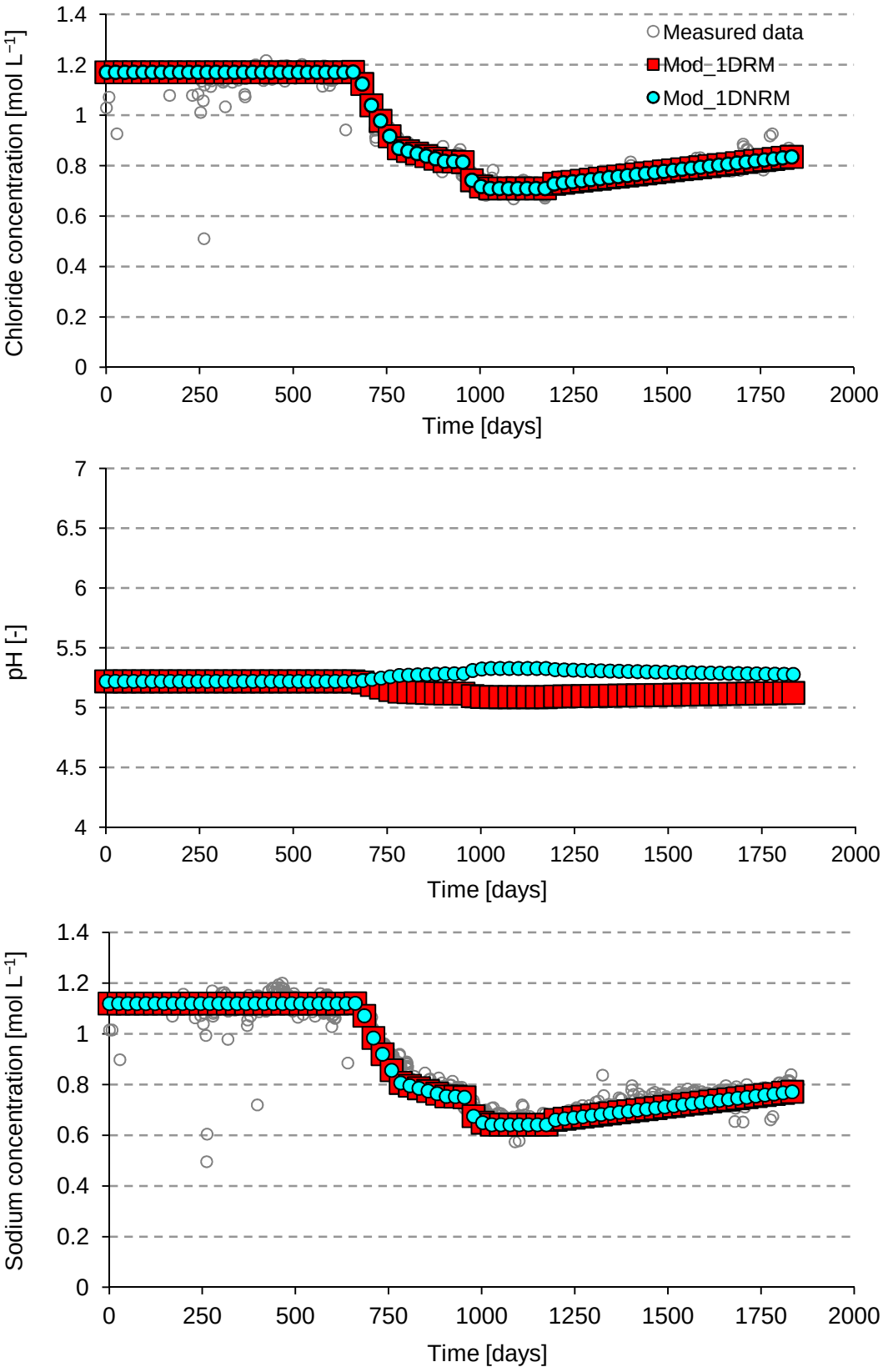

Fig. 16: Measured data and modeled pH (no measured data available) as well as concentrations of chloride and sodium from scenarios 1DNRM and 1DRM (modified after Fu et al., 2013b); Measured data: according to Houston (2007).

After the seawater breakthrough, the total dissolved barium concentrations ($c_{tot}Ba^{2+}$) in the produced water modeled by scenario RM abruptly decline from 4.6 mmol L^{-1} to low concentrations (<0.1 mmol L^{-1}). The modeled $c_{tot}Ba^{2+}$ indicate Sr-barite formation and are in good temporal agreement with the measured concentrations (Figs. 17 to 19). Within the reservoir aquifer, the modeled $c_{tot}Ba^{2+}$ increase from cell 1 to 25, before the front arrives at the production well (Fig. 20). This indicates that the chemical composition of the erstwhile injected seawater characterized by the lowest chloride concentration develops in time and space. Within the aquifer (cells 1 to 25 of the 1D stream tube), less Sr-barite forms (in average 0.7 mmol $cell^{-1}$). The Sr-barite precipitated within reservoir aquifer is heterogeneously dispersed and reaches a maximal amount of 4 mmol per one cell that is filled by 7.1 kg of solids (cell 3; partly presented in Fig 19). Massive Sr-Barite formation in the production well starts after seawater breakthrough and reaches a maximum after 1833 days (105 mmol per total produced water volume of 75 liters; Fig. 19). Barite scale formation in the production well is negligible before seawater breakthrough ($<2 \times 10^{-5}$ mmol) and consists of pure $BaSO_{4(s)}$. The strontium proportion in the sulfate solid solutions increases up to 7.2 mol% ($Ba_{0.928}Sr_{0.072}SO_4$; Fig. 19).

Sr-Barite formation causes a negative deviation of the calculated sulfate concentrations (c_{tot}sulfate) in the produced water in scenario 1DRM compared to scenario 1DNRM (Fig. 17). The modeled trend and absolute level of c_{tot}sulfate in the produced water cover the range of the measured data. Differences in the $c_{tot}Ba^{2+}$ of the produced water calculated by the two 1DRM and 1DNRM scenarios (ca. 2 mmol L^{-1}; Fig. 17) are in the same order compared to the differences in c_{tot}sulfate of the both scenarios at the same modeling time step. It follows that Sr-Barite is the exclusive secondary sulfate phase. This conclusion is supported by the following modeling results: all modeled formation water-seawater mixtures display undersaturation with regard to gypsum in this modeling scenario (for anhydrite see scenario 1DRM-An in Fig. 22 and Appendix A3). The modeled c_{tot}sulfate within the aquifer decrease from cell 1 to 25 prior to seawater breakthrough (Fig. 20).

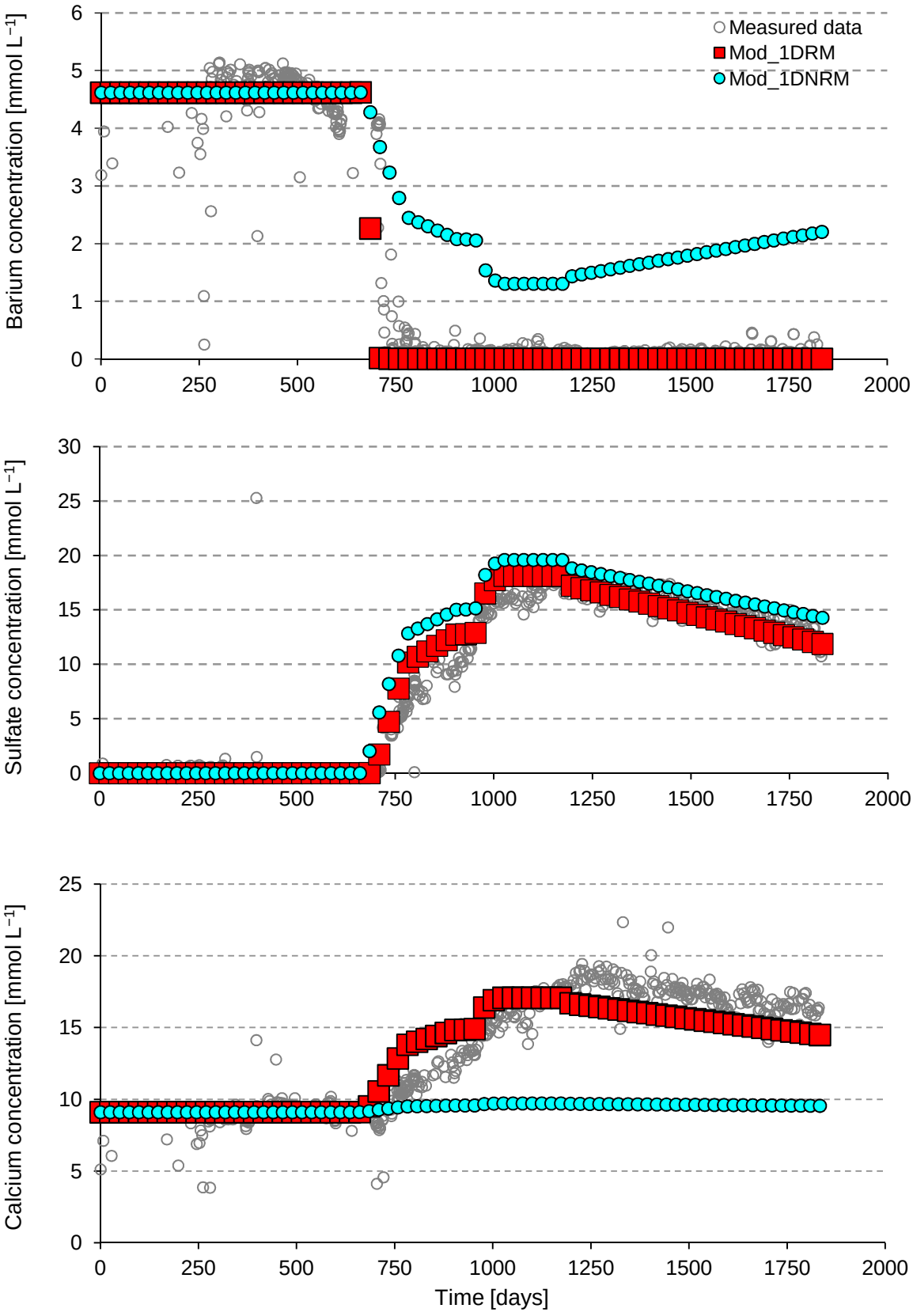

Fig. 17: Measured and modeled concentrations of barium, sulfate and calcium from scenarios 1DNRM and 1DRM (modified after Fu et al., 2013b); Measured data: according to Houston (2007).

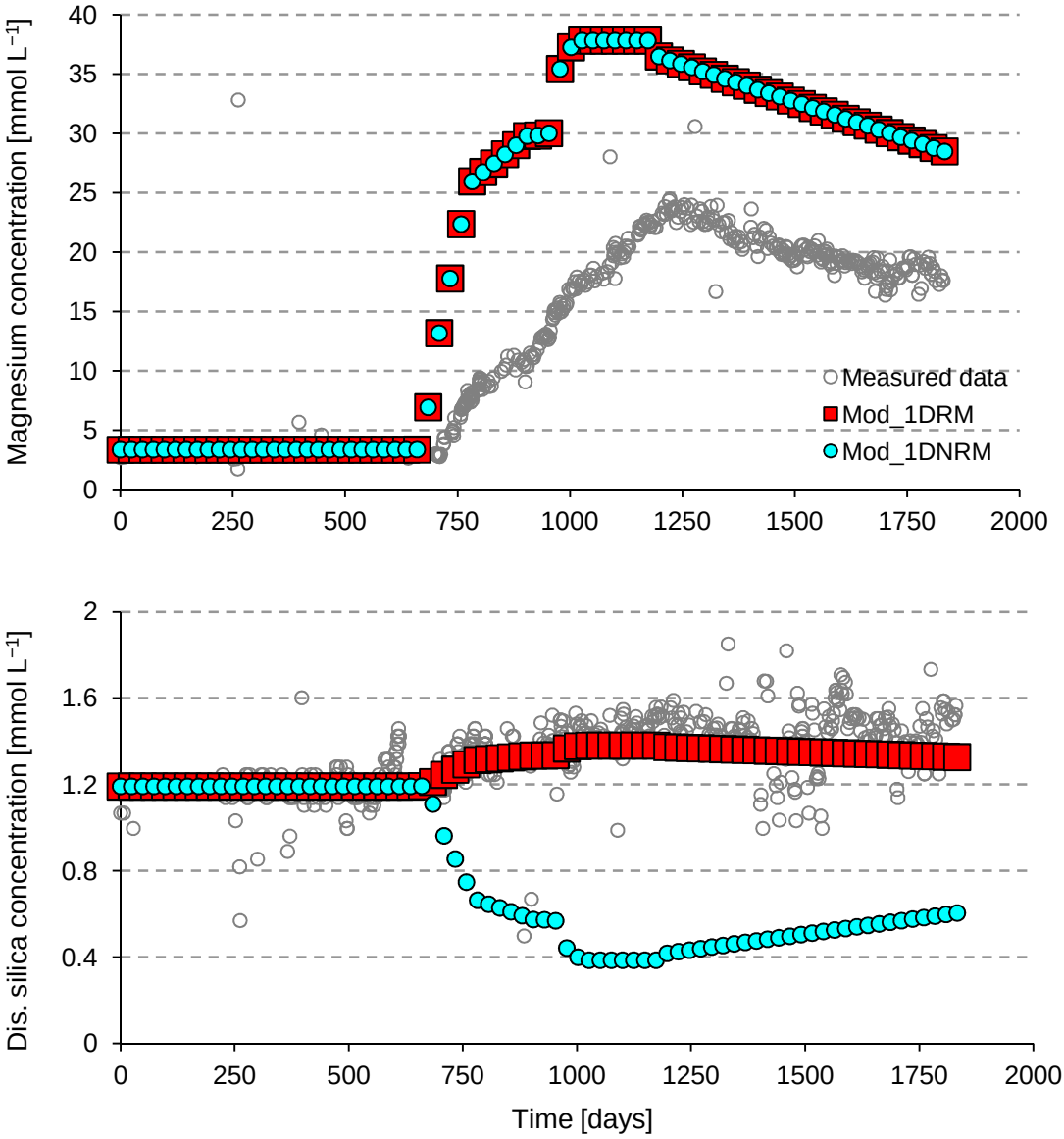

Fig. 18: Measured and modeled concentrations of magnesium and dissolved silica from scenarios 1DNRM and 1DRM (modified after Fu et al., 2013b); Measured data: taken from Houston (2007); Dis.: dissolved.

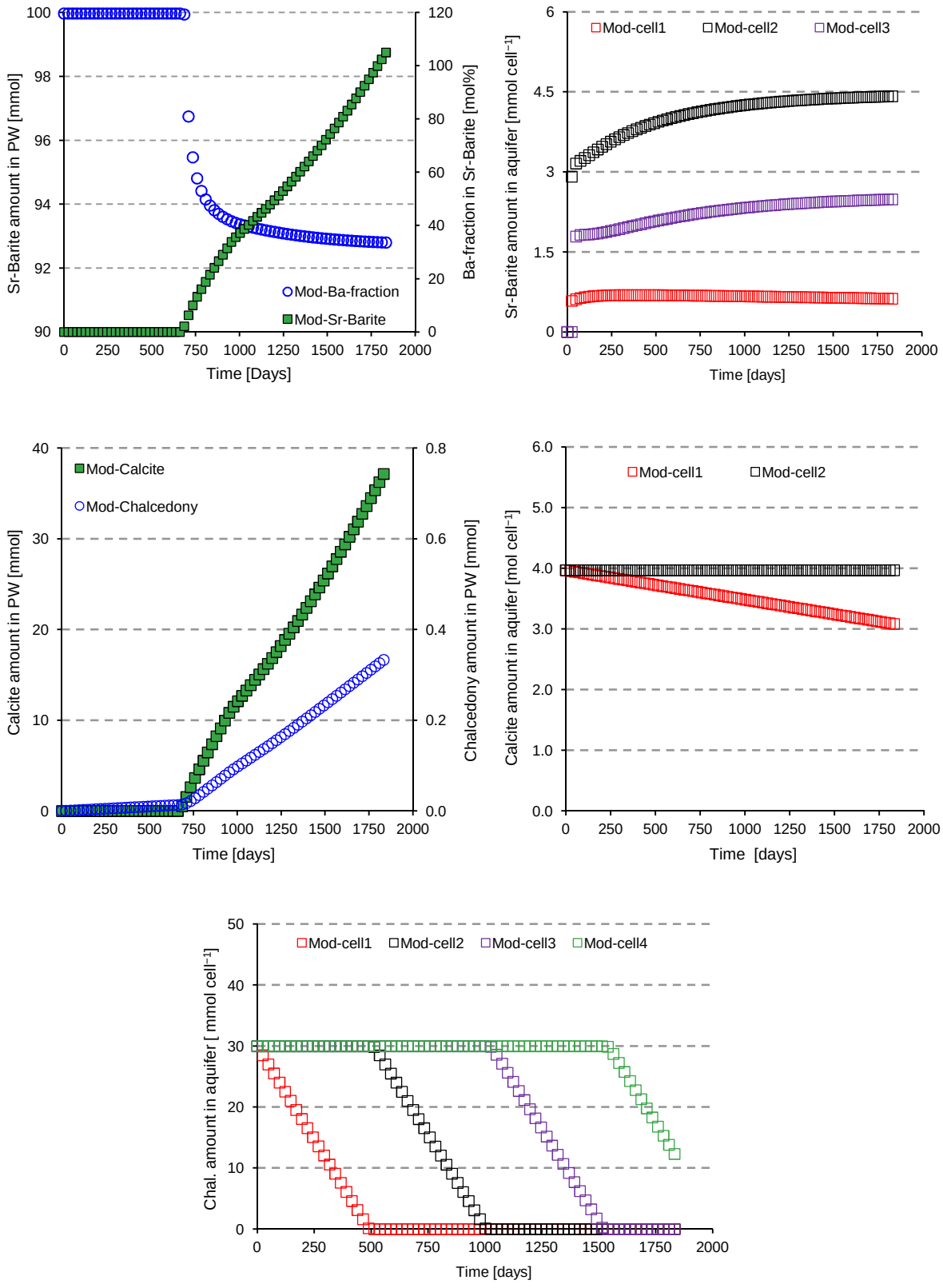

Fig. 19: Modeled mineral conversions in the production well and/or within the reservoir aquifer per 75 liters of produced water from scenario 1DRM (modified according to Fu et al., 2013b); PW: production well; Chal.: chalcedony.

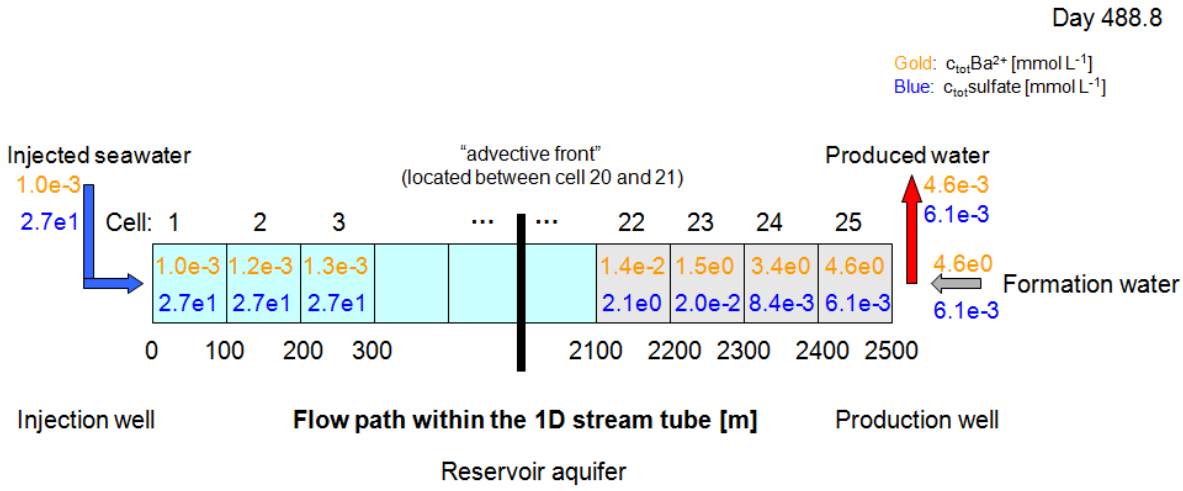

Fig. 20: Modeled concentrations of barium (gold) and sulfate (blue) in the injection and production wells, as well as within the reservoir aquifer (cell 1 to 25) at the modeling step of day 488.8 (modified after Fu et al., 2013b).

The modeled total dissolved calcium concentrations ($c_{tot}Ca^{2+}$) in scenario 1DRM resemble the measured data (Fig. 17). The modeled $c_{tot}Ca^{2+}$ are slightly higher than the measured data between 684 and 928 days, and slightly lower between 1198 and 1833 days. Dissolution of primary calcite within the aquifer (Fig. 19) causes in a positive deviation of the modeled $c_{tot}Ca^{2+}$ in scenario 1DRM from those in scenario 1DNRM (Fig. 17). The amount of calcite in the aquifer cell 1 continuously decreases during production (Fig. 19), because the injected seawater is undersaturated with regard to calcite under the reservoir conditions. Owing to the presence of calcite in aquifer cell 1 even after 1833 days, the amount of calcite in cells 2 to 25 remains unchanged compared to the starting conditions (partly presented in Fig. 19). In contrast to its dissolution occurring near the injection well, calcite is precipitated in the production well. Scaling intensity of calcite is weaker than Sr-barite; at maximum 37 mmoles calcite per 75 liters of the produced water (Fig. 19).

During the 75 modeling steps, all aqueous solutions display an undersaturation with regard to dolomite. Thus, the calculated magnesium concentrations in scenario 1DRM follow the results calculated by scenario 1DNRM and are clearly higher than the measured data (Fig. 18).

After seawater breakthrough, the calculated concentrations of dissolved silica ($c_{tot}SiO_{2(aq)}$) in scenario RM (at equilibrium with chalcedony) are ca. 0.6 mmol L^{-1} higher than for scenario 1DNRM (Fig. 18). The modeled $c_{tot}SiO_{2(aq)}$ of scenario 1DRM slightly increase during production and are similar to the measured data. In analogy to calcite dissolution in the aquifer, the undersaturation of the injected seawater with regard to chalcedony under reservoir conditions causes dissolution of primary chalcedony within the aquifer (Fig. 19). After 1613 days, chalcedony in cells 1 to 3 is completely consumed. In contrast, the conversion of silica-bearing kaolinite is low (less than 10^{-6} mole per cell after 1833 days in all scenarios). Further dissolution of chalcedony is restricted to cell 4. As for calcite,

chalcedony scale formation of 0.33 mmole per 75 liters of produced water occurs in the production well (Fig. 19).

3.4 Discussion of modeling results

The modeling results of scenario 1DRM are in good agreement with the measured compositional development of the produced water (presented by Houston (2007)) and with the observed composition of the scale mineral assemblage formed in the production well (stated by Wylde et al. (2006)). This good match demonstrates that the developed 1DHT model can reproduce the relevant hydrogeochemical processes in the Miller oilfield. Therefore, this reproduction of such processes confirms the validity of the 1DHT model.

Strontium-bearing barite dominates in the assemblage of the scale minerals newly formed in the production well. Production of 75 liters water result in scale formation with 27.9 g (composed of 86.6 wt.-% Sr-barite, 13.3 wt.-% calcite and 0.1 wt.-% chalcedony calculated by scenario 1DRM). Roughly 1.9×10^{11} liters of produced water were pumped from all production wells (Houston et al., 2007). In total, 7.1×10^{10} g of scale minerals form in and close to the production well in the aquifer by linear extrapolation in scenario 1DRM. 17,100 m^3 scale minerals could form under the assumptions that the density of Sr-barite, chalcedony and calcite account for 4.5, 2.648 and 2.711 kg L^{-1}, respectively (for detail, see Fu et al., 2013b).

Lacking data (e.g., dispersivity, the type of $SiO_{2(s)}$ equilibrating with the reservoir fluids, etc.) results in a large number of the modeling scenarios. In several scenarios, only one parameter is changed compared to the standard scenario (1DRM). These scenarios provide possibilities to test single parameters and their influence on the chemical composition of the produced water and on the mass conversion of minerals especially of scale minerals precipitated. The type of $SiO_{2(s)}$ equilibrating with the reservoir fluids (either microquartz solubility characterized by the Azaroual et al. (1997) or chalcedony included in the Wateq4f.dat database from Parkhurst and Appelo, 1999) shows no effect on other parameters (see Appendix A2), but minor effects on the silica concentration and on the mineral conversion of the $SiO_{2(s)}$ (Fig. 21). This is because $H_4SiO_{4(aq)}$ species dominate at a pH level of 5.2 and precipitation of $SiO_{2(s)}$ does not involve any H^+-transfer reaction. The comparison of the model results of the both scenarios suggests that the produced water of the Miller oilfield equilibrated with a SiO_2 solid phase, which display a similar solubility to chalcedony defined in the Wateq4f.dat database (provided by Parkhurst and Appelo, 1999).

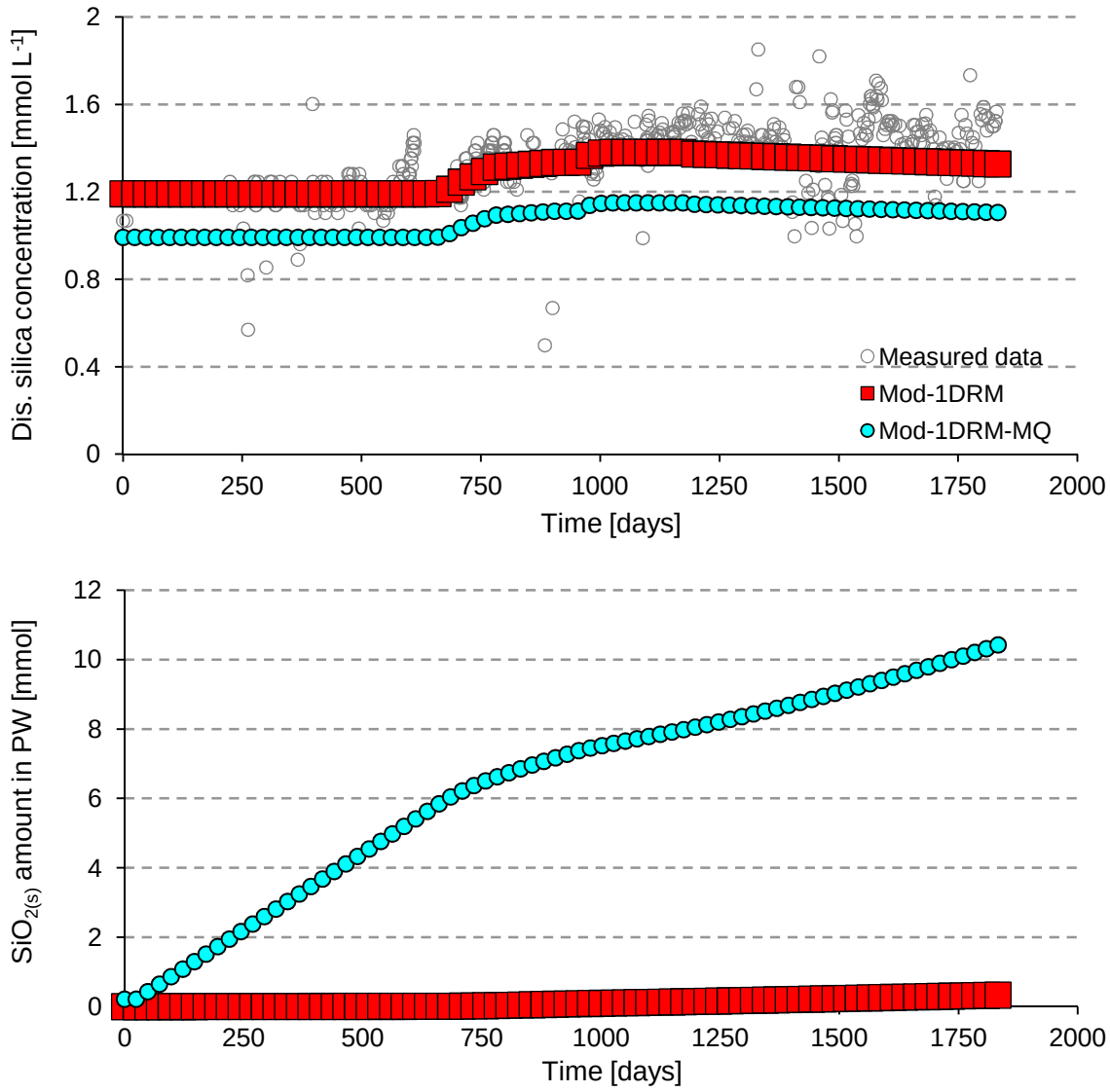

Fig. 21: Measured and modeled concentrations of dissolved silica in the produced water, as well as the modeled amount of $SiO_{2(s)}$ newly formed in the production well (per 75 liters of produced water) from scenario 1DRM and 1DRM-MQ (modified according to Fu et al., 2013b); Measured data: taken from Houston (2007); Dis.: dissolved; PW: production well.

The injection of sulfate-rich seawater into reservoirs, which formation water contains calcium ions, could cause gypsum or anhydrite oversaturation depending on the activity of calcium and sulfate ions. Scenarios 1DRM and 1DRM-An consider gypsum and anhydrite as potential secondary sulfate phase besides Sr-barite, respectively. Anhydrite formation leads to much lower calculated $c_{tot}Ca^{2+}$ and c_{tot}sulfate compared to the measured data (scenario 1DRM-An; Fig. 22). The concentrations of calcium and sulfate calculated by scenario RM fairly well match the measured data, whereas the produced water is undersaturated with respect to gypsum (Fig. 17). This indicates that no calcium sulfate phase forms in the Miller field, although Fu et al. (2012) suggested that anhydrite formation may have occurred in view of their previous batch modeling results. The concentrations of other

parameters calculated by scenario 1DRM-An show similar trend compared to scenario 1DRM (Appendix A3).

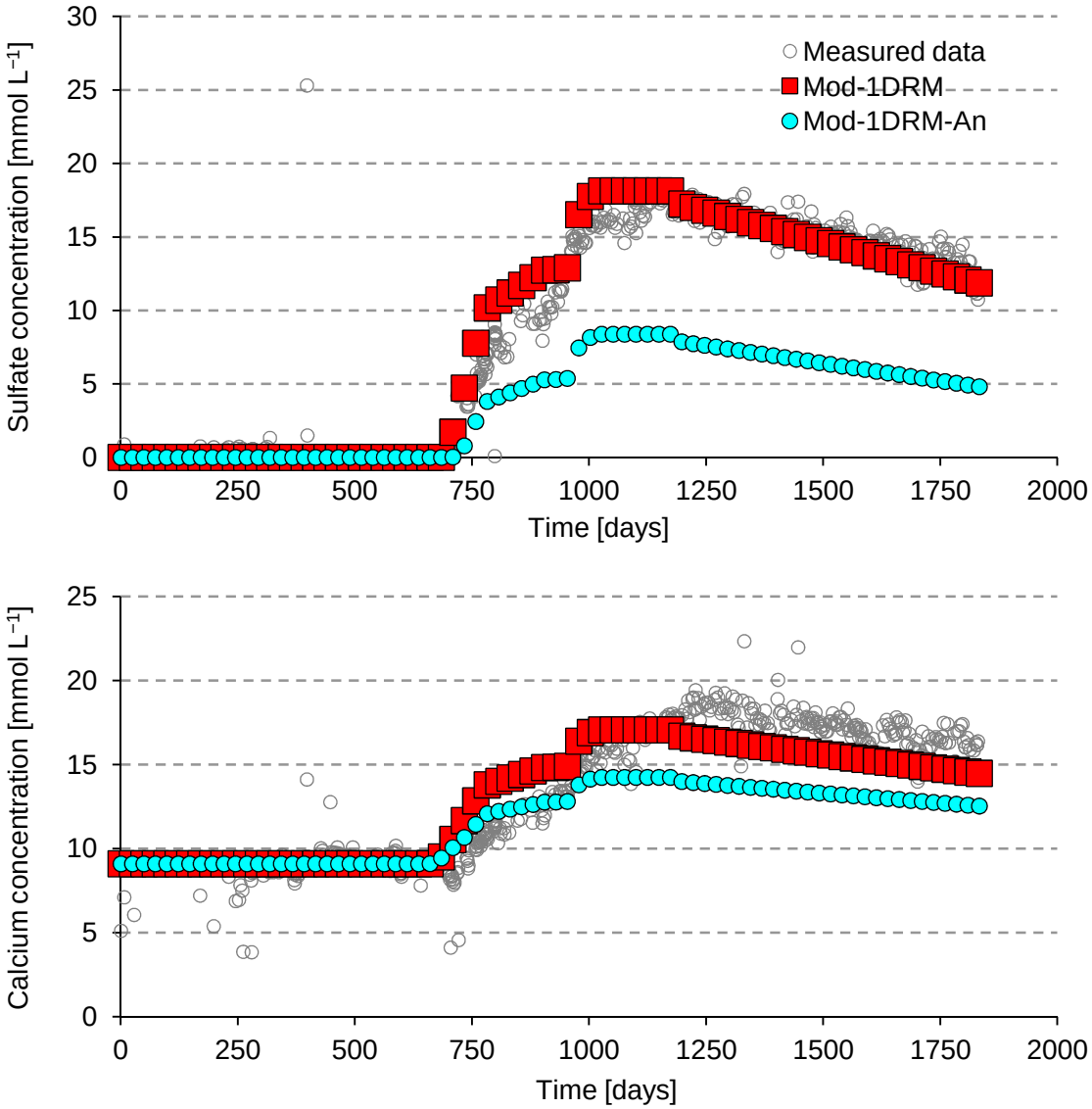

Fig. 22: Measured and modeled concentrations of sulfate and calcium in the produced water from scenario 1DRM and 1DRM-An; Measured data: taken from Houston (2007).

Cation exchange is another process that can affect the chemical composition of aqueous solution and the mineral assemblage. However, the total exchange capacity of the Miller field's aquifer rocks is restricted due to low clay contents (Lu et al., 2010). An assumed cation exchange capacity of 0.1 equivalent per 7.1 kg of solid leads to minor changes in the concentrations of Na^+, Ca^{2+} and Mg^{2+} and in a negligible effect on the mineral conversions. Nevertheless, the modeled $c_{tot}Mg^{2+}$ are still much higher than the measured concentrations (Fig. 23; Appendix A4).

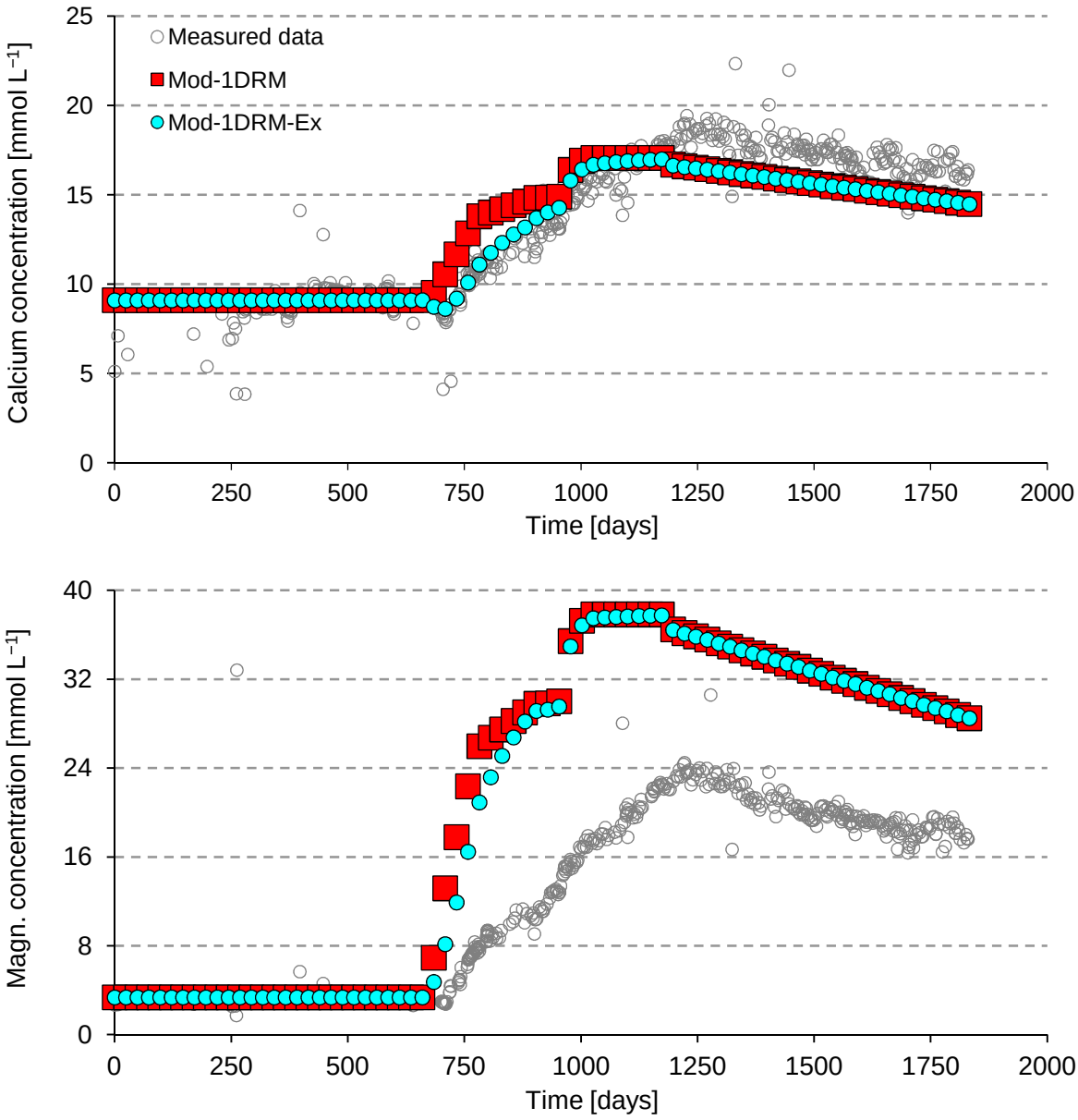

Fig. 23: Measured and modeled concentrations of sulfate and calcium in the produced water from scenario 1DRM and 1DRM-Ex; Measured data: taken from Houston (2007); Magn.: Magnesium.

Two alternative scenarios consider a dispersivity of 1 and 100 m per 100 m long cell length, respectively, in order to test the effects of varying dispersivity on the calculated resutls. Despite a broad range of the tested dispersivity (1, 10, 100 m per 100 m long cell length), differences in most of the parameters occur, but are minor (Appendix A5).

Due to the high ionic strength of the formation water, scenario 1RDM-Pi uses the thermodynamic database Pitzer.dat (Parkhurst and Appelo, 1999), which is extended by Bozau (2013). The comparison between scenarios 1RDM and 1DRM-Pi reveals that most parameters (e.g., the sulfate and barium concentrations, the amount of Sr-bearing barite scale) are virtually independent on which method is used to calculate activity coefficients (Appendix A6). Although the method for

calculating activity coefficients slightly affects the calculated amount of calcite scale, $c_{tot}Ca^{2+}$, and $c_{tot}SiO_{2(aq)}$, the $c_{tot}Ca^{2+}$, and $c_{tot}SiO_{2(aq)}$ calculated by scenario 1DRM-Pi are still in the variation range of the measured data.

Insofar as, all scenarios exclude any artificial effects from their model setup, such as changes in temperature and pressure in production wells. Such changes result in a new state of equilibrium of the species distribution. Subsequently, the thereby induced hydrogeochemical processes could furthermore cause scale formation (Hassane and Mackay, 2012). Pressure drop can induce CO_2 outgassing in the produced water. CO_2 outgassing alters the carbonate species distribution and can additionally cause carbonate scale formation. Kan and Tomson, (2010) claimed that pressure drop accompanying production generally cause calcite formation. Such artificial effects are difficult to quantify. Scenario 1DRM-Drop arbitrarily pre-assigns a pCO_2 drop from 100 bar within the reservoir aquifer to 40 bar in the production well. The calculated results from scenario 1DRM-Drop even considering such a strong pCO_2 drop show a virtual identity with the results without consideration of pressure drop effects (for details, see Fu et al., 2013b). This identity even applies to $c_{tot}Ca^{2+}$ which is generally very sensitive to pCO_2 changes. Nevertheless, this pre-assigned pCO_2 drop results in the dominance of calcite (457 mmoles per 75 liters of produced water) over Sr-bearing barite in the assemblage of the scale minerals newly formed in the production well. A higher $pCO_{2(g)}$ level prevailing in the reservoir aquifer increases the equilibrium concentration of calcium ions which are bound to calcite in the production well due to the pH increase caused by $pCO_{2(g)}$ drop.

3.5 Limitations of modeling

The extension of the batch model presented by Fu et al. (2012) to the 1DHT model presented by Fu et al. (2013b) is incapable of reproducing the hydrogeochemical processes, which occurred in the Miller oilfield and controlled the magnesium concentration of the produced water, such as absorption of magnesium ions on the surface of calcite crystals (e.g., proposed by Chen et al., 2006).

The geohydraulic model part is simplified by only one stream tube due to the lacking of the hydraulic data. As a result, this 1DHT model excludes transversal dispersion which additionally causes the complex interplay between different stream tubes. In consequence, the 1DHT model could on the one hand underestimate the mass conversions of hydrogeochemical processes occurring within the reservoir aquifer, and on the other hand overestimate them in production well. In addition, the 1DHT model predicts the scaling intensity based on minor volumes of produced water. It is unknown whether a linear extrapolation of these calculated results could be applied for the real cases characterized by much larger volumes of produced water.

The ambiguous character of the calculated results of the 1DHT model allows for a rough estimation. The reason is that the conditions, under which hydrogeochemical processes occurred, are unspecified. Such conditions strongly alter the measured compositional development of the produced water. This development is the key signal to reproduce hydrogeochemical processes, but integrates all processes that occurred within the reservoir aquifer, in production well and even during sampling and analyzing. In other words, the measured data are the final state of a complex process chain. In consequence, this ambiguous character of the 1DHT model could be weaken by specifying the initial reservoir conditions (e.g., measuring $pCO_{2(g)}$).

3.6 Conclusions

Fu et al. (2013b) developed a one-dimensional hydrogeochemical transport model into which the temporal and spatial aspects are integrated. This 1DHT model was tested in the hydrogeochemical dynamical system − the Miller field. The validity of the 1DHT model is confirmed by (1) a fairly good agreement between the measured and calculated the temporal development of the produce water's composition (concentration of sodium, calcium, sulfate, barium and dissolved silica) in combination with (2) the consistency of the modeled composition of the scale mineral assemblage newly formed in the production well with the observed composition. The good match demonstrates that the developed 1DHT model can reproduce the coupled hydraulic and hydrogeochemical processes despite some modeling limitations. Wider applications of this model can be extended by changing different parameters which are adjusted to other case-specific reservoirs. Such hydrogeochemical transport modeling could provide a reasonable method of resolution for investigating and forecasting such hydrogeochemical processes in time and space. The following comparison between the developed 1DHT model and other modeling approaches, which are commonly applied for reservoir engineering, could highlight their differences and the significant advantages of the 1DHT model for predicting scale formation.

(1) Several publications presented modeling approaches for assessing scaling risk due to seawater injection. Some of these studies are based also on reactive transport models and represented their corresponding modeling results (e.g., Mackay et al., 2012). However, no plausibility tests of these modeling approaches were performed. On the contrary, the developed 1DHT model was tested for plausibility by comparing the modeling results with the measured data from the Miller field test site. The good agreement of the modeled and measured compositional development of the produced water demonstrates that our 1DHT model can reproduce the simultaneously occurring and coupled hydraulic (fluid flow) and hydrogeochemical processes (water-gas-rock interactions), even allowing some modeling limitations. Consequently, the plausible 1DHT model can be applied for other oilfields undergoing seawater injection by changing certain variable input parameters.

(2) Calculation of saturation indices and the establishment of equilibrium conditions of selected minerals using one formation water analysis at varying seawater fractions are the two modeling approaches (e.g., DownHole SAT^{TM} (French Creek Software, 2012)) commonly applied for predicting scale formation in reservoir engineering. To prove their plausibility, a separate modeling exercise also using PHREEQC considers an admixture of the original injected seawater to the original formation water from the Miller field. This separate exercise focuses on the calculation of saturation indices of selected mineral phases that are considered by a commercial modeling tool (DownHole SAT^{TM} provided by French Creek Software (2012)) to predict scale formation. For this exercise, various mixing factors are selected to prepare a mixture of the original injected seawater and the original formation water under the Miller field's reservoir conditions. The PHREEQC modeling results represent oversaturation of formation water-seawater mixtures with regard to anhydrite, aragonite, barite, brucite, calcite, dolomite, magnesite, strontianite and witherite for at least one of the selected seawater fractions (10, 16.67, 33.33, 50, 66.67, 83.33 and 90%). At all the selected seawater fractions, the modeled water mixtures are undersaturated regarding to celestite. In contrast, the good agreement between the measured data and the calculated results of the 1D hydrogeochemical transport model indicates: (1) that Sr-bearing barite ($Ba_{0.928}Sr_{0.072}SO_4$) forms, although the calculated saturation indices suggest a celestite undersaturation and a strontianite oversaturation, (2) that witherite does not form despite its calculated oversaturation, (3) that no calcite sulfate phase forms in the Miller oilfield despite an positive saturation indices with respect to anhydrite, and (4) that calcite which is present near the injection well dissolves despite a calculated calcite oversaturation. Consequently, the comparison of the modeling results calculated by saturation indices using two water analyses and by 1DHT model indicates that calculation of saturation indices is unsuitable for exactly predicting scale formation.

(3) The establishment of equilibrium conditions of selected minerals using one formation water analysis at varying seawater fractions (e.g., the batch modeling presented by Fu et al., 2012) is incapable of exactly concluding on the resulting hydrogeochemical processes. The reason for this is that the water (especially the injected seawater), which results in scale formation in the production well, does not keep its chemical composition compared to its original composition during injection. The chemical composition of the injected water develops in time and space due to mineral precipitation and dissolution along the flow path within the reservoir aquifer, before it reaches the production well. This was proven by the 1DHT modeling (e.g., Fig. 20). However, this approach (the establishment of equilibrium conditions of selected minerals using one formation water analysis at varying seawater fractions) provides a first insight into the system evaluation.

(4) The 1DHT model aims to quantitatively retrace hydrogeochemical processes in combination with their corresponding mass conversions, as well as to determine where they occur in the reservoir. The modeling results indicate that scale minerals (e.g., Sr-bearing barite) can be dispersively

distributed within the reservoir aquifer. Consequently, modeling approaches, which exclude dispersion (and diffusion depending on flow velocity), would cause an overestimation of scaling intensity that might occur in the production wells. Moreover, such modeling approaches probably neglect changes in the porosity-permeability properties within the reservoir aquifer, specifically close to the injection wells.

(5) The modeling results reveal that undersaturation of the injected seawater at elevated reservoir temperature and pressure conditions results in dissolution of several primary minerals (calcite and chalcedony in the Miller field test site) near the injection well within the reservoir aquifer. On the other hand, such minerals could form as scale minerals in the production well due to changes in hydrogeochemical conditions. Therefore, the scaling intensity in production wells could be increased compared to the modeling results calculated for especially selected processes. Consequently, it is incorrect to isolate some (and arbitrarily predefined) hydrogeochemical processes (e.g., exclusively including barite formation from barium and sulfate free ions) from the entire systems. Instead, all relevant hydrogeochemical processes including dissociation and association of species should be integrated into the model to exactly assess the type of scaling and its intensity.

In summary, hydrogeochemical modeling based on thermodynamics of chemical equilibrium helps us to identify the exact mechanisms of hydrogeochemical processes. Quantifying the intensity of such processes by using such hydrogeochemical modeling necessitates that the hydrogeochemical processes achieve their equilibrium state. Fu et al. (2012, 2013b) demonstrated by using hydrogeochemical modeling that hydrogeochemical water-rock-gas interactions in the Miller oilfield study case reached equilibrium conditions under the reservoir conditions within less two years despite several modeling limitations. This highlights that kinetic inhibition of many reactions under the reservoir conditions (at elevated temperature and pressure conditions) can be neglected within a short simulation period (e.g., of more than two years). The modeling results provided by Fu et al. (2013b) reveal that batch modeling approaches and calculation of mineral saturation indices are incapable for exactly predicting and quantify hydrogeochemical processes in a dynamic system. The simultaneously occurring hydraulic processes (fluid flow) are coupled to the hydrogeochemical processes. Nevertheless, calculations of saturation indices and batch modeling approaches provide important elements for a first system evaluation despite their restricted applicability. Moreover, the setup of a plausible 1D or even 3D hydrogeochemical transport model needs a reasonable hydrogeochemical batch model. The 1DHT model tested in the Miller oilfield is incapable of providing a reproduction of the Miller oilfield' flow field owing to the lack of hydraulic data. For applications of the 1DHT model for other oilfields, the 1DHT model should be extended to contain multiple stream tubes. Nevertheless, the extended 1DHT models cannot simulate transversal dispersion that causes interactions between stream tubes within the reservoir aquifer. Thus, the mass conversion within the reservoir aquifer could be underestimated. To keep and to overcome the pros and cons of the

aforementioned approaches, respectively, a 3D hydrogeochemical transport model should be developed to predict the temporal and spatial consequences of simultaneously occurring and coupled hydraulic and hydrogeochemical processes.

4. Case study – Siri oilfield

Hydrogeochemical modeling (batch and 1D transport modeling) is applied to reproduce the hydrogeochemical processes in the Miller oilfield based on the measured composition of its produced water (see section 3). On the other hand, hydrogeochemical processes can mark their diagenetic features in sediments. Thus, such diagenetic features can be also used as a key factor to retrace hydrogeochemical processes by numerical modeling. Several investigations on the Siri oilfield located in the Danish North Sea (e.g., Kazerouni et al., 2010; Schovsbo, 2009 (pers. com.); Stokkendal, 2009; Weibel et al., 2010) clearly reveal that several diagenetic features characterize the Siri oilfield's reservoir sandstones, such as formation of secondary quartz, berthierine and calcite. Dense formation of berthierine and calcite strongly blocks the pore space and reduce the permeability (Kazerouni et al., 2010; Schovsbo, 2009 (pers. com.); Stokkendal, 2009). A good understanding of the formation mechanisms of such minerals is a prerequisite for quantitatively predicting where and when a decrease in porosity induced by mineral precipitation could occur. Correspondingly, the temporal and spatial development of the reservoir permeability can be qualitatively estimated. Such forecast is important and basic for successful reservoir engineering. Investigating hydrogeochemical processes in such deep subsurface petroleum systems is by far not as straight forward as it would seem because of their complexity and of the restrictions on their accessible measured data (e.g., resulting from the difficulty in obtaining samples and from the limited number of representative samples). The following study aims to fill the gap in investigation of such deep subsurface processes with a multidisciplinary approach at multi-scale. For this, this study chooses the Siri oilfield as case study. To this end, the study investigates the Siri oilfield's diagenetic features by analytical methods (petrographic microscope, XRD, XRF, SEM, HRTEM) and to identify which mechanisms result in such features by means of hydrogeochemical modeling. In this way, this study aims to provide a method of resolution for identifying and quantifying hydrogeochemical processes in deep subsurface petroleum systems by such a multidisciplinary approach at multi-scale.

4.1 Introduction

The Siri oilfield is a part of the Siri Canyon which is located in the Central Graben of the North Sea (Ohm et al., 2006). The Siri Canyon continues along the Danish-Norwegian North Sea border and extends over a large area (Ohm et al., 2006; Weibel et al., 2010). The sandstones in the Siri Canyon Fairway were deposited at roughly 66-55 Ma (Ohm et al., 2006). The underlying deep marine marl and the overlying shale embed the reservoir sandstones (Ohm et al., 2006; Stokkendal et al., 2009; e.g., Fig. 24). The marls, which are characterized by multiple thin interbedded sandstone layers, resulted from the sandy mass flows and sandy turbidites (Weibel et al., 2010, and references therein; e.g., Fig. 24). Ohm et al. (2006) claimed that the seal of the Siri oilfield was established through

Eocene (55-53 Ma). Such marls and shales encase these sandstones (e.g., a typical well Siri A from the Siri oilfield in Fig. 24; Fig. 4 in Ohm et al., 2006). Therefore, the mudstones form barriers and prevent a local vertical petroleum migration to the Siri oilfield's reservoir sandstones (Ohm et al., 2006). The results of the geochemical analysis of oil in the Siri oilfield suggest that oil was generated in the Central Graben from different organic-rich Formations and migrated through the intervening Cretaceous Chalk succession into the Siri traps (Ohm et al., 2006). A regional tilt induced by the Fennoscandian uplift caused petroleum remigration from the Siri traps and establishment of a new OWC (Ohm et al., 2006).

The glauconitic sand of the Siri oilfields may have originated from the Stavanger Platform (Weibel et al., 2010, and references therein). The sandstones of the Siri oilfields is strongly glauconitic, fine-grained, well sorted but not well rounded (Stokkendal et al., 2009; see section 4.3). The reservoir sandstones exhibit a high porosity of ca. 30% (Stokkendal et al., 2009; see section 4.3). The reservoir temperature is slightly lower than 80 °C (Ohm et al., 2006). Nice et al. (2000) measured the reservoir pressure and temperature accounting for 230 bar and 78 °C, respectively, whereas the measurement provided by Weibel et al. (2010) indicates a bottom hole temperature of 65 °C in the well Siri 4. Formation of specific minerals is responsible for the observed large variation in permeability within the ca. 30 m thick reservoir sandstones (e.g., wells Siri 4 and 5; ranging from 1 to 450 mD, Stokkendal et al., 2009).

The well Siri A was drilled in 1995 and its oil is unsaturated (GEUS, 1996). A series of wells drilled in the Siri Canyon discovered petroleum (filled with gas, oil or gas and oil), such as the wells Francisca 1, Siri 3, Siri 2 (Ohm et al., 2006). However, several wells drilled in the Siri Canyon are dry wells. The structural complexity of the Siri Canyon and the connectivity among its individual traps result in slight differences in their properties of the sandstones, their character of oil, their chemical composition of gas phase (Ohm et al., 2006). For instance, the trap of the Siri 3 is filled with undersaturated oil, whereas the trap of the Siri 2 is characterized by a gas cap (Ohm et al., 2006).

In the Siri oilfields, tectonic instability and regional uplift resulted in major submarine erosion of the chalk deposits and in a new establishment of the recent oil-water contact (OWC), which is located above the palaeo OWC (Hamberg et al., 2005; Ohm et al., 2006, and references therein). As a result, the present live oil column for wells Siri 1, 2 and 3 is strongly shortened by 5, 13.5 and 14 m, respectively (Ohm et al., 2006). Simultaneous water and gas injection into the Siri oilfield has been applied for a successful improved oil recovery since 1999 (Berge et al., 2002).

Fig. 24: Core image of the well Siri A taken from the upper shales (a-b), the reservoir sandstones (c-d) and the lower marls (e-f).

4.2 Aims

Hydrogeochemical processes in oil reservoirs lead to compositional alterations of pore water and of oil, as well as to restructuring of in-pore interfaces. Furthermore, theses processes trigger dissolution of primary minerals and precipitation of authigenic minerals, and consequently, cause changes in the reservoir porosity-permeability properties which can strongly obstruct oil production. A number of research works on the Siri oilfield have been undertaken and concern various aspects, such as geological history (e.g., Ohm et al., 2006), quartz morphologies (Weibel et al., 2010), elemental geochemical study (Friis et al., 2007), permeability variation depending on specified diagenetic features (Stokkendal et al., 2009). Several of the diagenetic features observed in the Siri oilfield, on the one hand, occur across the entire thickness of the reservoir sandstones. On the other hand, some of the observed features are restricted to specific positions in the reservoirs (see section 4.3). For instance, formation of secondary $SiO_{2(s)}$ and berthierine is commonly observed in the Siri wells (Stokkendal et al., 2009; Weibel et al., 2010). Berthierine formation in the water leg results in very low permeability (Stokkendal et al., 2009). In analogy, calcite cementation observed in specific positions is responsible for the extremely low porosity and permeability (Schovsbo, 2009 (pers. com.); Stokkendal et al., 2009). Thus, it is substantial for successful reservoir engineering to identify such hydrogeochemical processes, to determine their mechanisms inducing their occurrence, and to predict their consequences.

The following study presents a multidisciplinary approach at multi-scale and focuses on the well Siri A to investigate the major hydrogeochemical processes in the Siri oilfield's reservoir sandstones. The reservoir sandstones were investigated by various analytical methods (e.g., XRF, XRD, petrographic microscope; for details, see section 4.3) to identify the hydrogeochemical processes which triggered the observed diagenetic features. The Siri oilfield is characterized by the comparable reservoir conditions as the Miller oilfield: 230 bar and 78 °C in the Siri oilfield (Nice et al., 2000); 500 bar and 120°C in the Miller oilfield (Rooksby, 1991). It thus follows that the hydrogeochemical processes in the Siri oilfield achieved equilibrium conditions. Additionally, aqueous species in oilfield formation water may achieve metastable equilibrium conditions with hydrocarbons and with minerals in reservoir rocks at oil-water contacts (Helgeson et al., 1993). Consequently, hydrogeochemical (batch, 1D and 3D) models, which are based on thermodynamics of chemical equilibrium, are stepwise built to retrace the Siri oilfield's hydrogeochemical processes based on the results from all analytical methods. Slight reduction in porosity could result in significant decrease in permeability (Vaughan, 1987). The batch model consequently aims to provide first insights which minerals tend to dissolve and form in the Siri oilfield's reservoir sandstones. The 1D and 3D reactive transport models aim to couple the simultaneously occurring hydraulic processes (fluid flow including advection, dispersion and diffusion during mass transport) to the hydrogeochemical processes in order to investigate the temporal and spatial development of hydrogeochemical processes. This could help to

conclude on the temporal and spatial modifications to the porosity-permeability properties of the reservoir aquifers.

4.3 Investigating the Siri oilfield's reservoir rocks

Hydrogeochemical processes are reflected by the compositional development of pore water and mark diagenetic features in sediment. The case study on the Miller oilfield is based on the measured compositional development of the produced water to investigate the hydrogeochemical processes. The good agreement between the measured and modeled data confirms by means of hydrogeochemical modeling which hydrogeochemical processes occurred in the Miller oilfield (section 3). In contrast, the investigations on the hydrogeochemical processes in the Siri oilfield are based on the observed diagenetic features. Thus, a series of reservoir rock samples are taken from the well Siri A and from the Sandra A (a dry well) of the Siri Canyon. In total, 37 core samples are taken from the well Siri A compared to 15 core samples from Sandra A (Figs. 25 and 26). The reservoir sandstones of the well Siri A are investigated in detail, whereas the samples taken from the well Sandra A are analyzed as reference to compare with the Siri A. To identify the reservoir rock matrix alterations, the core samples are investigated by various analytical methods: petrographic microscope, X-ray fluorescence (XRF), X-ray powder diffraction (XRD), scanning electron microscopy (SEM) and high-resolution transmission electron microscopy (HRTEM). The results investigated for the well Siri A are described in detail in the following.

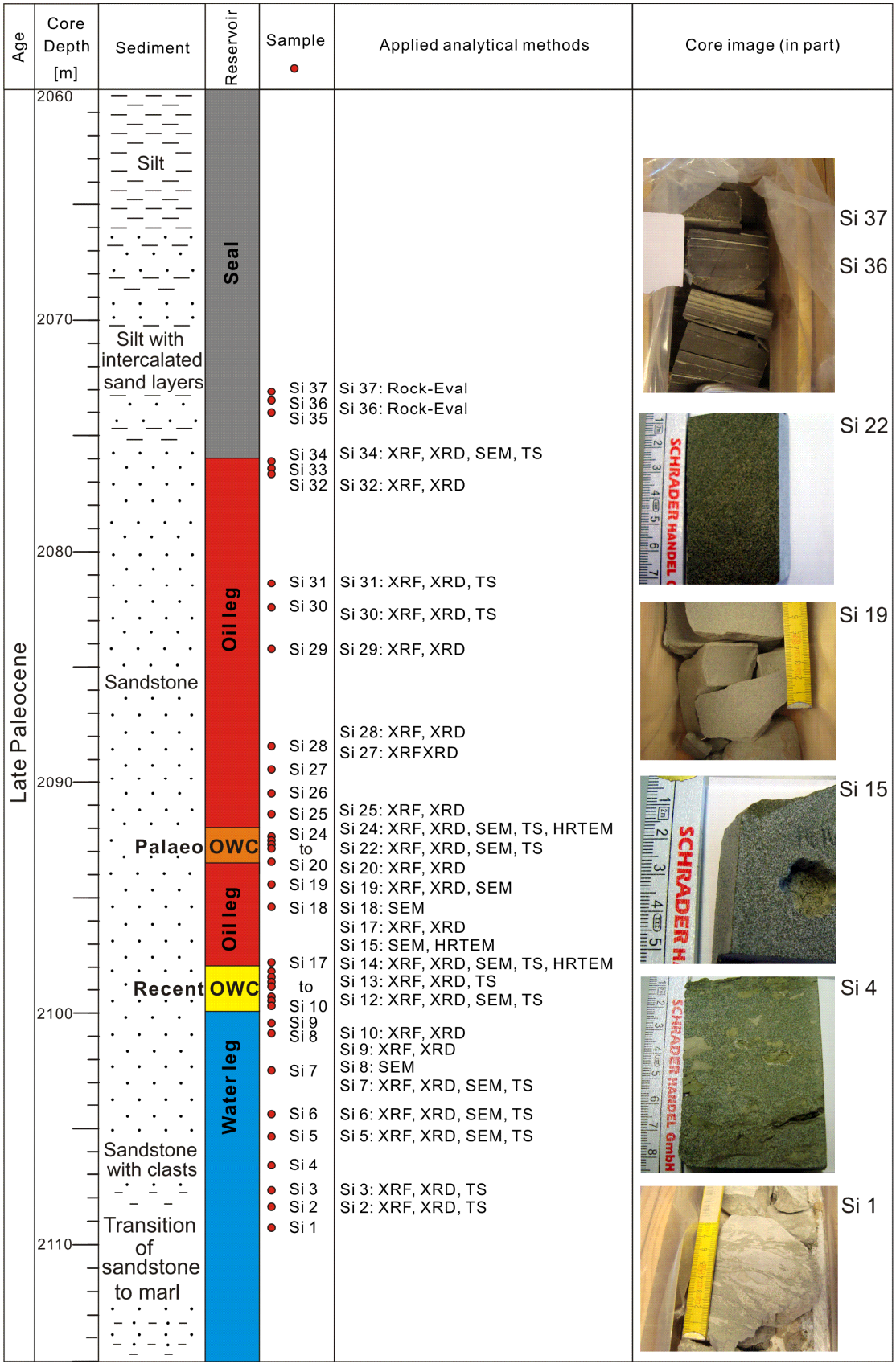

Fig. 25: Sample positions of the well Siri A and the applied analytical methods. OWC: Oil-water contact; XRF: X-ray fluorescence; XRD: X-ray powder diffraction; SEM: scanning electron microscopy; TS: petrographic investigation in thin section; HRTEM: high-resolution transmission electron microscopy.

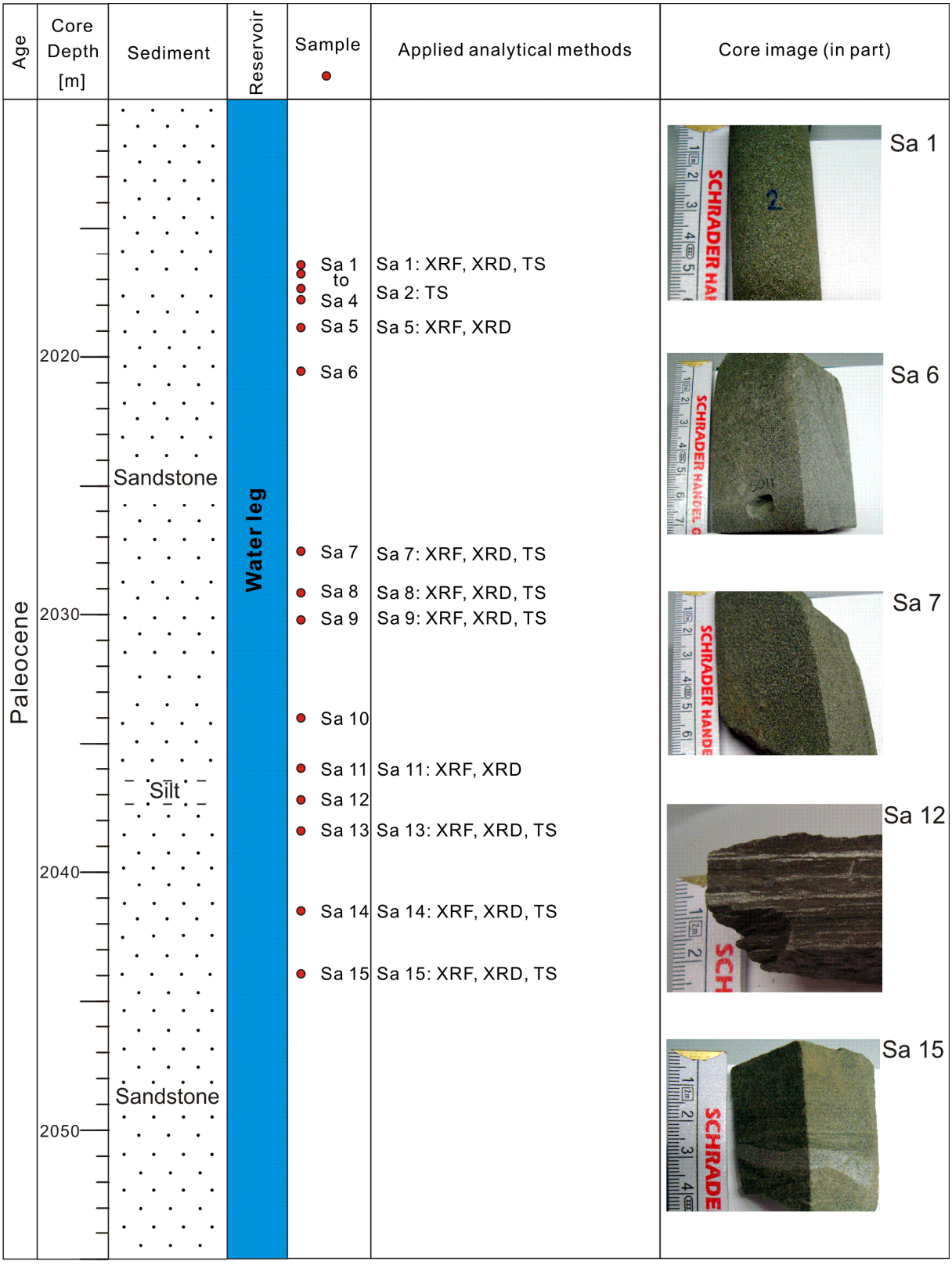

Fig. 26: Sample positions of the well Sandra A (dry well) and the applied analytical methods. XRF: X-ray fluorescence; XRD: X-ray powder diffraction; TS: petrographic investigation in thin section.

4.3.1 Mineralogical composition

Ohm et al. (2006) stated (1) that the Fennoscandian uplift caused the tilt of the Siri traps, (2) that oil re-migrated from the Siri traps, (3) and that the palaeo OWC is consequently observed below the recent OWC there. However, the horizon in the well Siri A, which is located at the depth of ca. 2093 m (Fig. 25), is named as the palaeo OWC in this study. This is because that this horizon (at the depth of 2093 m) cemented by calcite displays identical properties with the recent OWC in terms of mineralogical composition, diagenetic features (for detail, see sections 4.3.1, 4.3.2 and 4.3.4). To investigate the mineralogical composition of the reservoir rock matrix of the well Siri A, XRD was performed on 23 of 37 core samples taken from different reservoir parts: the upper seal, the oil and water legs, as well as the palaeo and the recent OWCs (Fig. 25; 9 core samples in the well Sandra A). The first petrographic investigations show that quartz and glauconite dominate in the Siri oilfield's reservoir sandstones (their sum amount >80 wt.-% based on the observations of petrographic microcopy; for detail, see section 4.3.2). However, only XRD analysis of the bulk mineralogy was carried out in powdered samples in this study. Thus, this makes it impossible to exactly identify the mineralogical composition of the rock matrix. This difficulty in particular applies for investigating the clay fraction by using XRD under room conditions.

Figures 27 to 29 displays the X-ray diffraction patterns of the main minerals measured in samples from the oil leg (Si 31), the palaeo and the recent OWCs (Si 22 and 14, respectively), the water leg (Si 7) and the sandstone with clasts (Si 2) in the well Siri A. Figure 30 summarizes the mineralogical composition of the investigated core samples of the well Siri A by means of XRD. The measured X-ray diffraction patterns of the main minerals in other samples are not presented here. The XRD analysis results of the bulk mineralogical composition represent minor variations (Figs. 27 to 30). The most of the core samples show the similar mineralogical composition: quartz, glauconite, potassium feldspar, albite and muscovite. Pure calcium plagioclase (anorthite) is absent in the most samples. However, calcian albite exists in several samples. Evaporation of pore water with high salinity leads to formation of halite and sylvite. Calcite or calcium carbonate containing trace amounts of magnesium occurs only in specified reservoir parts of the well Siri A: directly underneath the upper seal, at the palaeo and the recent OWCs, in the sandstone containing clasts. In comparison to calcite, siderite was detected in only one sample taken from the sandstone with carbonate clasts. Pyrite was proven in only one sample, maybe due to its low amount in the reservoir rock matrix (Fig. 30). However, SEM observations show that pyrite occurs in several samples in which XRD analysis does not prove its presence (Fig. 41). Additionally, the mineral assemblage of the reservoir rocks could contain trace amounts of hematite.

The mineralogical composition of the reservoir mineral assemblage in the well Sandra A show similar results compared to the well Siri A, although the well Sandra A is not filled with oil (partly documented in Appendix 7). Calcite was proven only in three core samples of the well Sandra A.

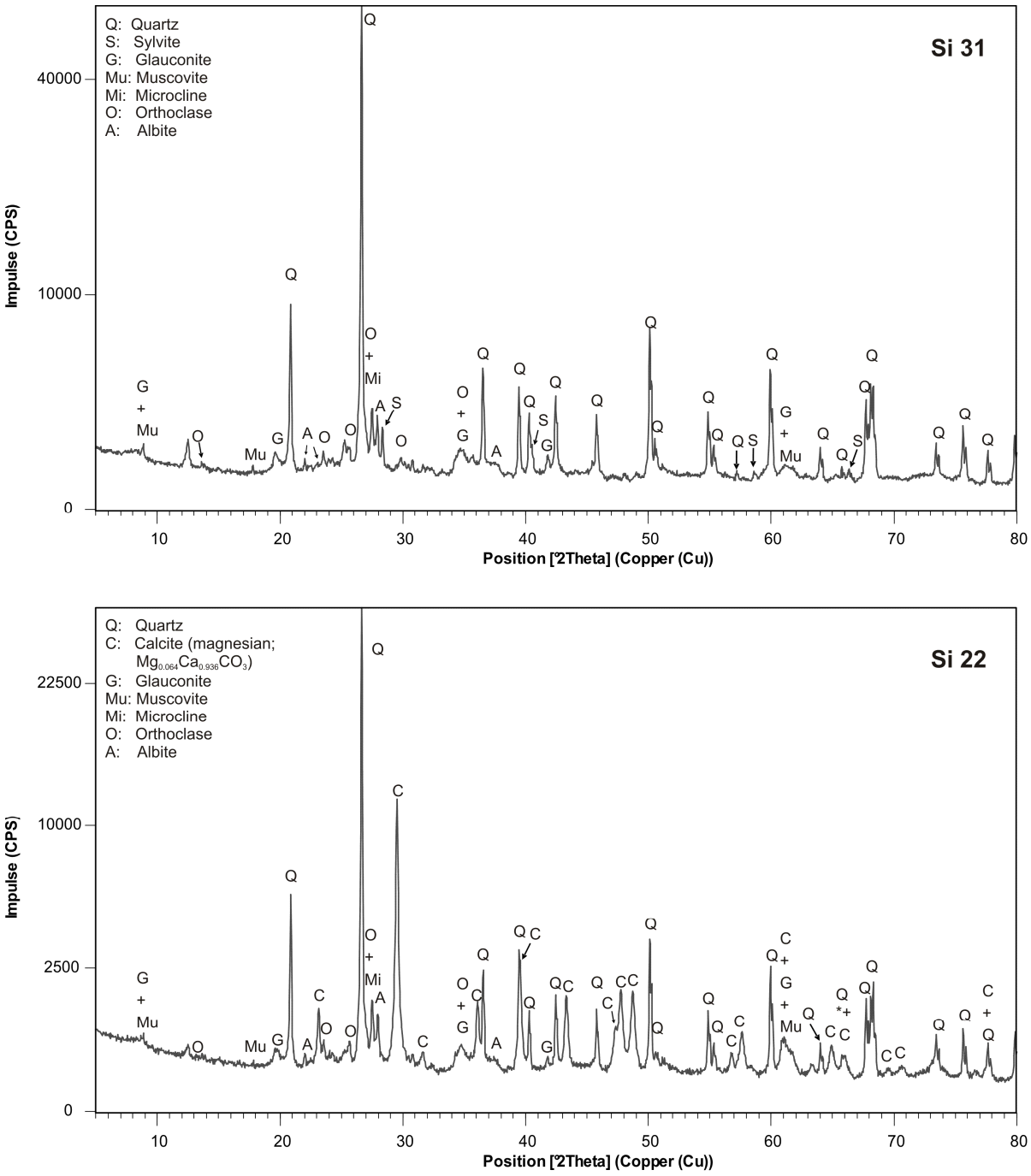

Fig. 27: Measured X-ray diffraction patterns of the bulk samples Si 31 (oil leg) and Si 22 (oil leg) from the well Siri A.

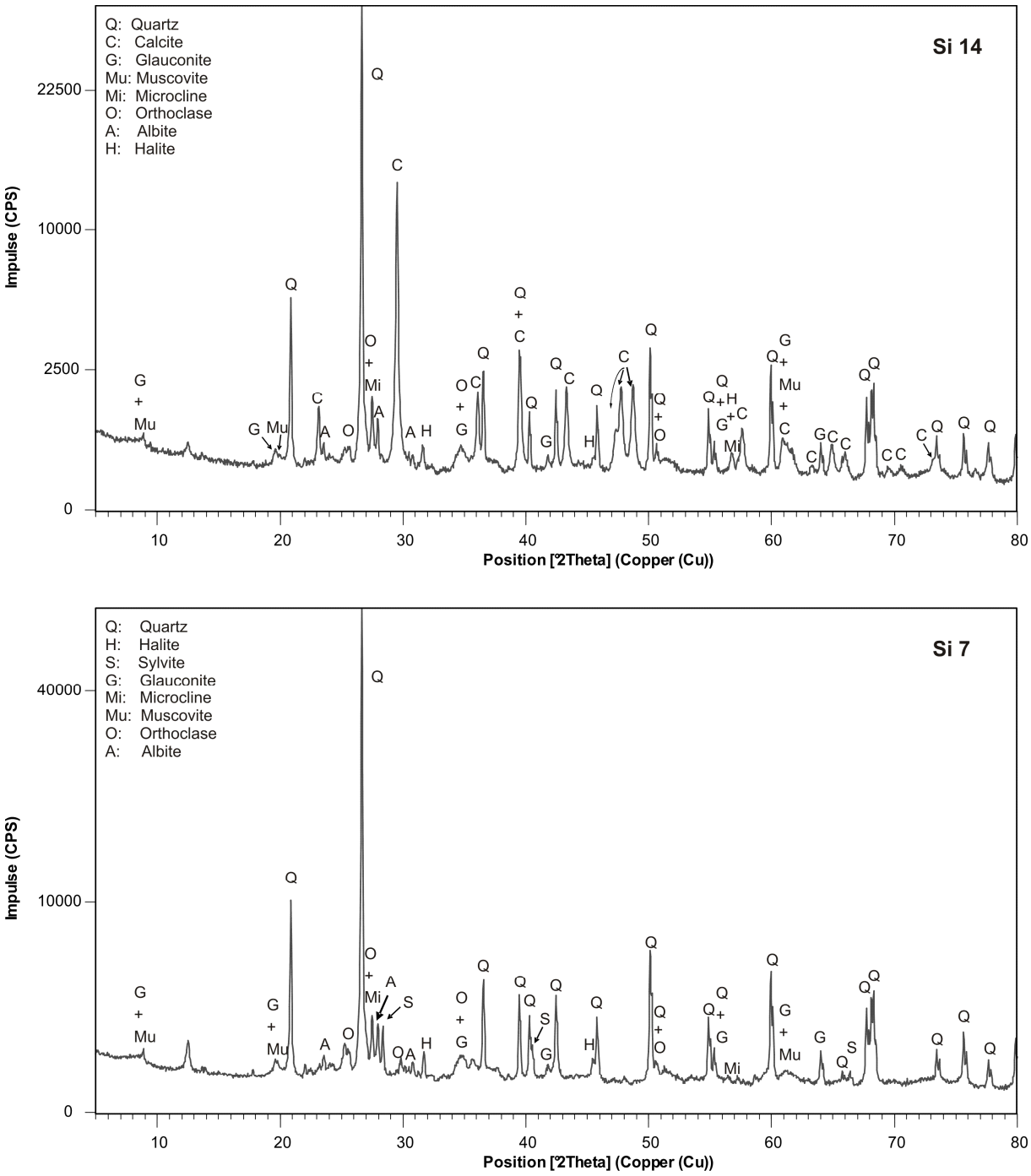

Fig. 28: Measured X-ray diffraction patterns of the bulk samples Si 14 (recent oil-water contact) and Si 7 (water leg) from the well Siri A.

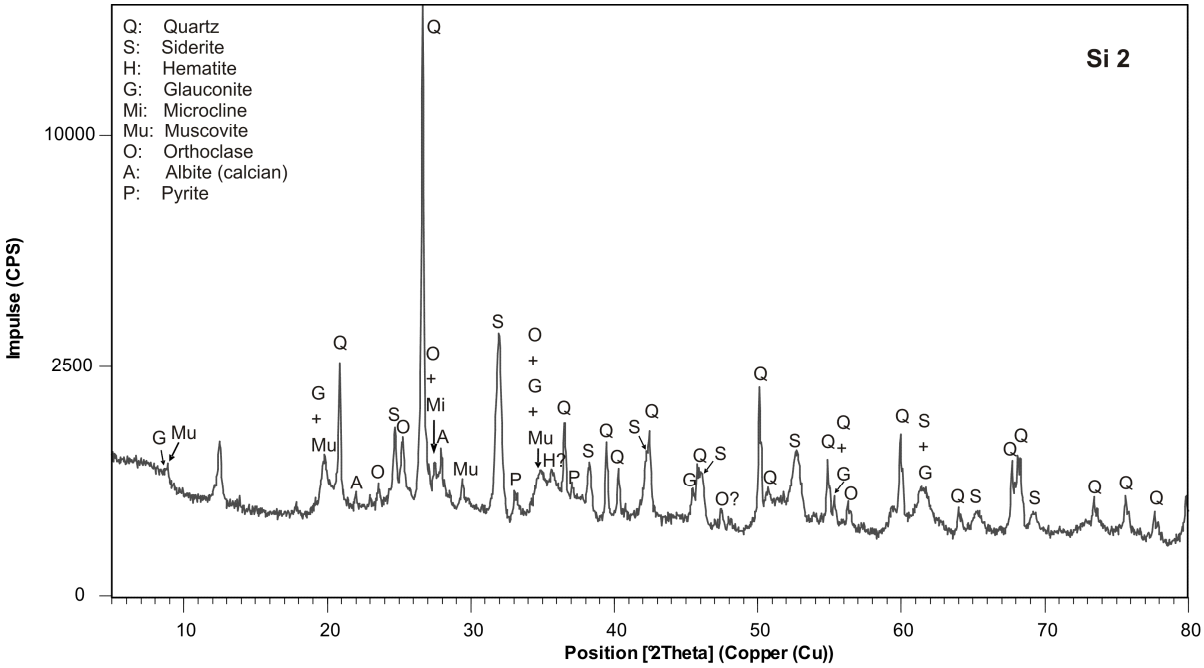

Fig. 29: Measured X-ray diffraction pattern of the bulk sample Si 2 (in the sandstone containing clasts) from the well Siri A.

The reflection at ca. 7.2 Å (2-theta: ca. 12.5 °) is proven in all samples, indicating the presence of a clay mineral (Figs. 27 to 29). Additionally, the reflection at 3.6 Å (2-theta: ca. 25 °) seems to be assigned to this unidentified clay mineral. The intensity of this reflection suggests its low amount compared to other major minerals in the bulk samples. Moreover, glauconite, muscovite and feldspars, which make a significant contribution to the reservoir rock mineral assemblage besides quartz, display their several reflections in the range of the 2-theta from 5 to 30 °. Thus, this complicates the identification of this unknown clay mineral only by performing XRD on the bulk samples. In addition, several minerals (e.g., kaolinite, chlorite, berthierine) share their major reflection at ca. 7.2 Å and several additional XRD lines with each other. Stokkendal et al. (2009) consequently performed XRD on the clay fraction of the samples under different conditions until the mineral characterized by the reflection at 7.2 Å was identified as berthierine. Therefore, application of XRD on the bulk sample at normal conditions is incapable of identifying this clay mineral. In addition, XRD investigation only provides an overview about the constituent reservoir minerals, but no indications for the diagenetic evolution on which this study focuses. However, XRD results also establish the basis for the other methods. Thus, other analytical methods must be performed.

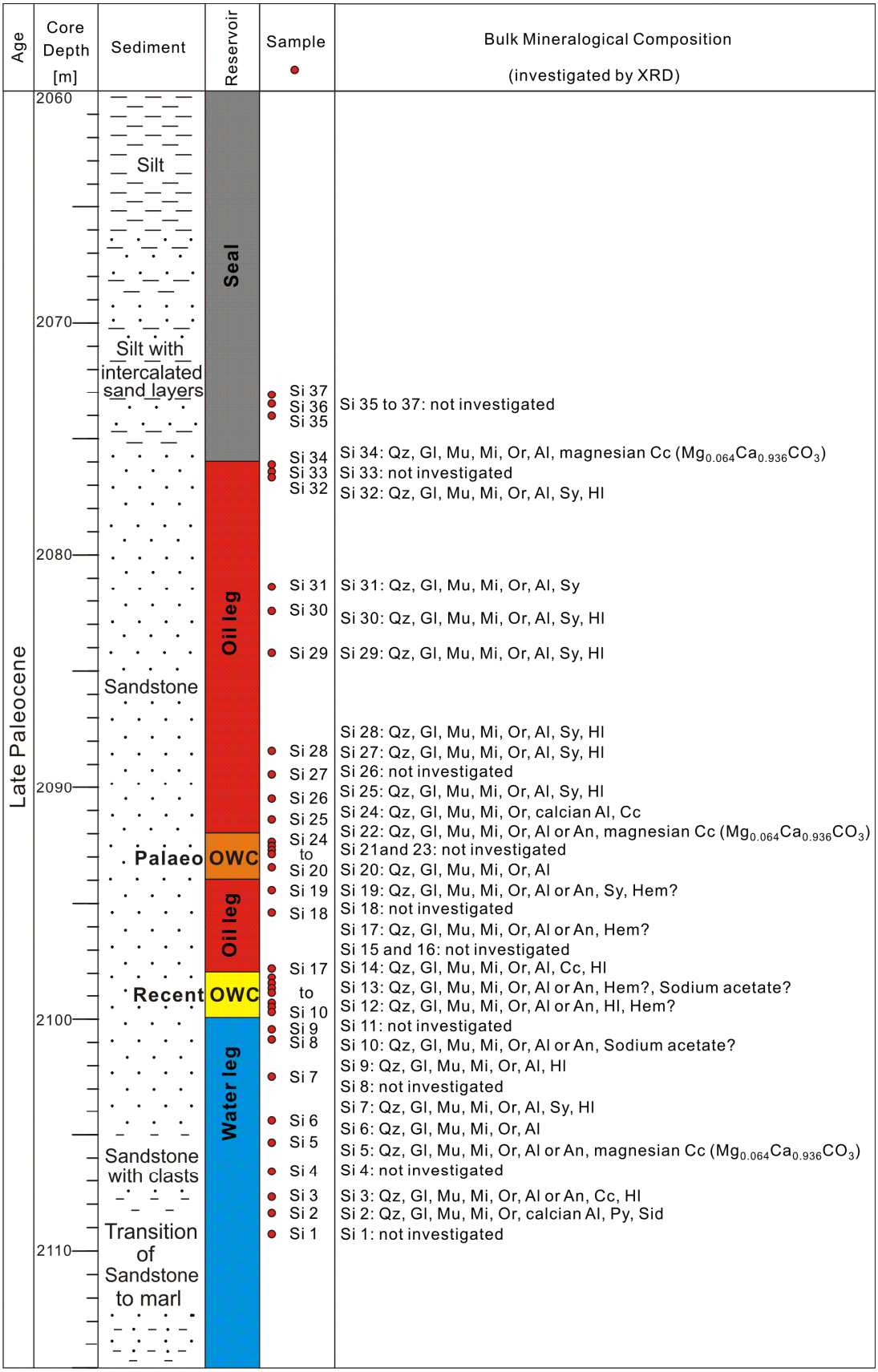

Fig. 30: Summary of the mineralogical composition of the well Sir A investigated by XRD.OWC: oil-water contact; Qz: Quartz; Gl: Glauconite; Mu: Muscovite; Mi: Microcline; Or: Orthoclase; Al: Albite; An: Anorthite; Sy: Sylvite; Hl: Halite; Cc: calcite; Hem: Hematite; Py: Pyrite; Sid: Siderite; ?: not clearly determinable.

4.3.2 Diagenetic features

Hydrogeochemical processes characterize the diagenetic evolution in the reservoir rock matrix. XRD results provide an overview about the constituent reservoir minerals which could have participated in the hydrogeochemical reaction chain. Petrographic investigations aim to establish the diagenetic evolution in 12 polished thin sections under petrographic microscope from the well Siri A (8 thin sections from the well Sandra A; Figs. 25 and 26). To complement petrographic investigations at multi-scale, SEM was performed on 12 samples taken from different reservoir parts in the well Siri A (from the oil and water legs, as well as the palaeo and the recent OWCs; Fig. 25). Combining the both methods aims to identify the primary and authigenic minerals, their morphology and their sequential relations. Based on such investigations, working hypotheses about hydrogeochemical processes which result in the observed diagenetic features can be developed.

The sandstone of the reservoir Siri oilfield exhibits a high porosity of 33 % (Fig. 31). The reservoir mineral assemblage is dominated by quartz (ca. 65 wt.-%; assumed by petrographic microscopy, as well as for other minerals; Fig. 31). All core samples are fine-grained sand display a grain size of detrital quartz ranging from 60 to 130 µm (Fig. 31). The detrital quartz grains are almost irregular and less rounded (Fig. 31), indicating a short-range transport from Stavanger Platform. It can thus follow that hydrogeochemical processes induced by weathering may be insufficiently. Additionally, it can be assumed that the diagenetic features observed in the samples may have been primarily characterized by the hydrogeochemical processes proceeding after the reservoir deposition. However, it is incapable of concluding that all diagenetic features observed must have occurred in the reservoir after the reservoir deposition.

The sandstones contain less abundant glauconite (ca. 20 wt.-%) compared to quartz (65 wt.-%). Feldspars comprise 1 wt.-% of the bulk rock. Detrital clays account for ca. 8 wt.-%. The amount of muscovite is low (ca. 9 wt.-%). Pyrite occurs in minor or to trace amounts in the sandstones. The abovementioned mineralogical composition of the Siri oilfield's reservoir rocks is assumed on the basis of the observations of the petrographic microscopy.

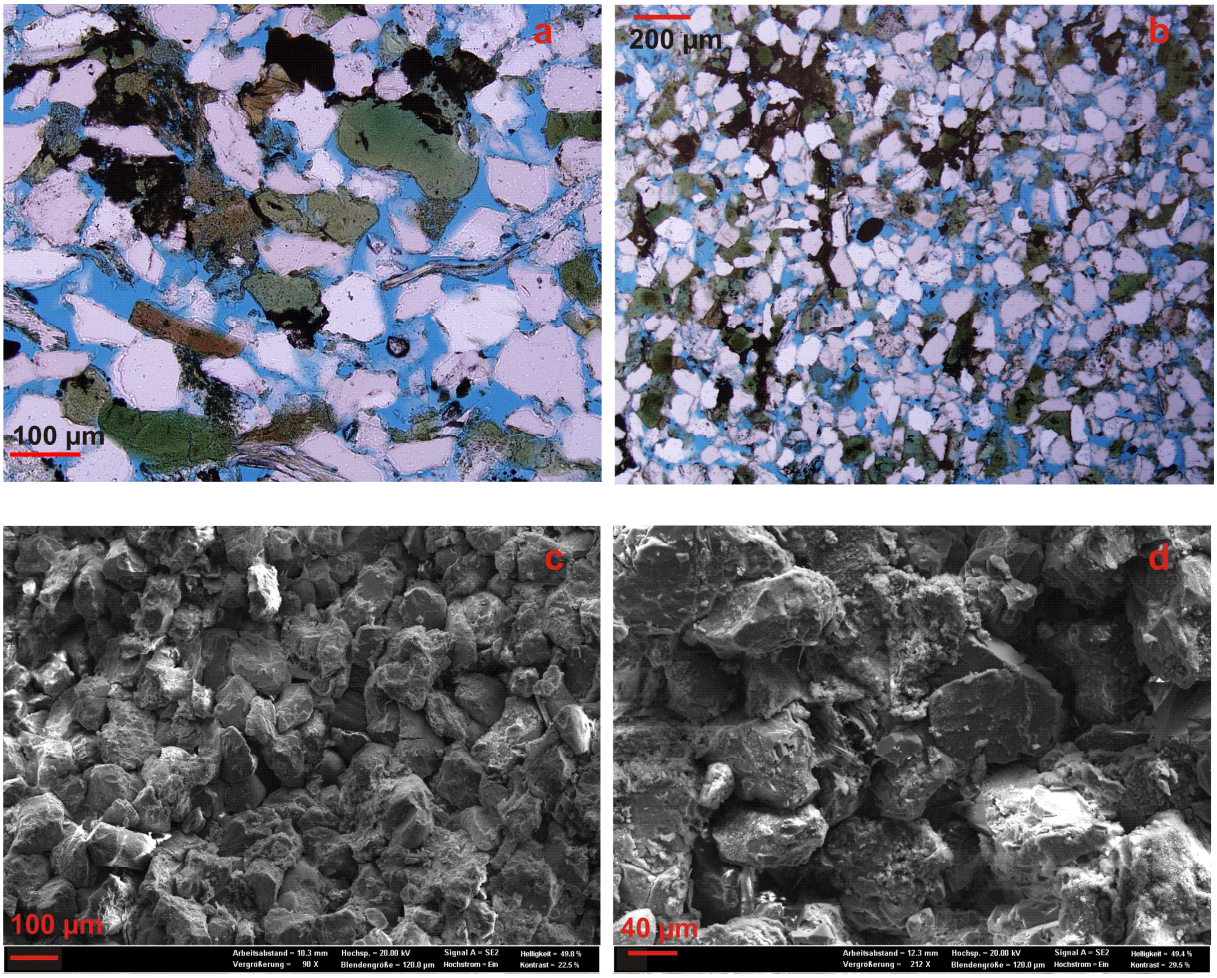

Fig. 31: Thin-section photomicrographs and SEM images of the samples of the well Siri A. a and c: from the oil leg (Si 20 and 19, respectively); b and d: from the water leg (Si 6); porosity in blue.

Several samples, which are located in specific reservoir parts (directly underneath the upper seal, at the palaeo and the recent OWCs), are strongly cemented by carbonate (Fig. 32). The carbonate cement almost occupies the entire pore space (Fig. 32). Free pore space still exists between the fibrous structures of secondary minerals (b in Fig. 32 and Fig. 40; free pore space marked in blue). Consequently, the measured permeability at the OWCs dramatically decreases compared to the data measured in the oil and water legs (Schovsbo, 2009, pers. com.). The sandstones located between 2105 and 2109 contain calcite clasts. The deposition of clasts may have resulted from geological processes and did not participate in the hydrogeochemical reaction chain on which this study focuses. Thus, applications of other analytical methods and hydrogeochemical modeling are not performed to investigate the mechanisms of the clast formation in the following study.

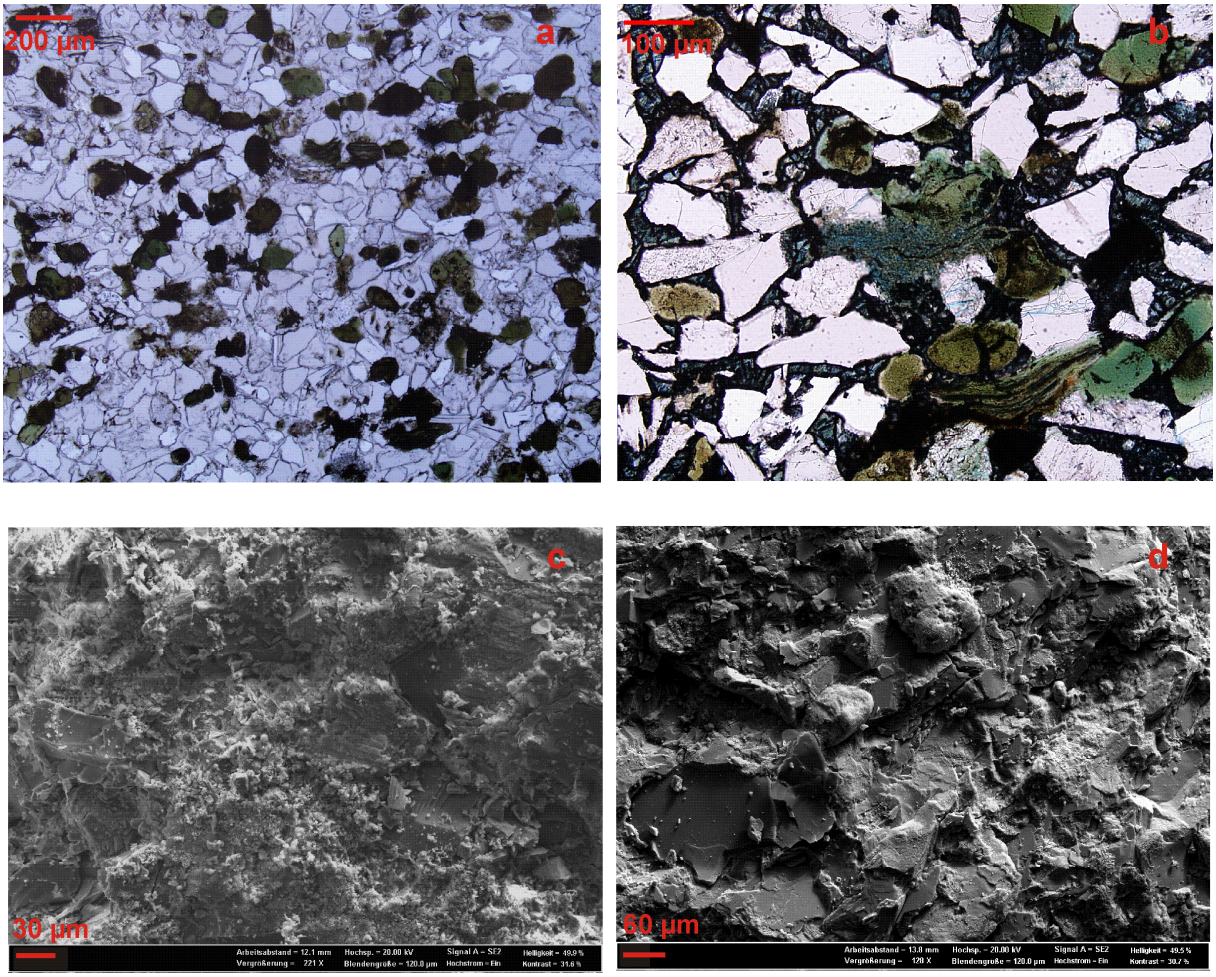

Fig. 32: Thin-section photomicrographs and SEM images of the samples of the well Siri A. a and c: from the palaeo oil-water contact (Si 22); b and d: from the recent oil-water contact (Si 14).

Petrographic microcopy and SEM are used to determine diagenetic features observed in the Siri oilfield's reservoir rock. Six major diagenetic processes were identified and are described below (Depletion and enrichment of elements are described and discussed in detail in section 4.3.4). Table 5 summarizes these diagenetic processes and their occurrence positions.

(1) Formation of authigenic quartz

Primary quartz grains dominate in the reservoir mineral assemblages. The detrital quartz grains are almost characterized by an irregular shape and are less rounded. Secondary fine quartz grains can be observed in a number of samples taken from different reservoir parts. Fine quartz grains are characterized by a grain (crystal) size of ca. 20 µm and form directly adjacent to altered feldspars (Fig. 33). Additionally, secondary quartz occurs as overgrowth in almost all samples (Fig. 33). In the gap between quartz overgrowths, an iron-rich clay mineral forms. This iron-rich mineral comprises bladed platelets and is surrounded by newly formed quartz (Fig. 33). This suggests that formation of

authigenic quartz is accompanied by formation of this iron-rich mineral. Additionally, this observation could mean that precipitation of the both minerals result from a same hydrogeochemical process. Microcrystalline quartz with a crystal size <5µm are also observed in the samples (d in Fig. 34).

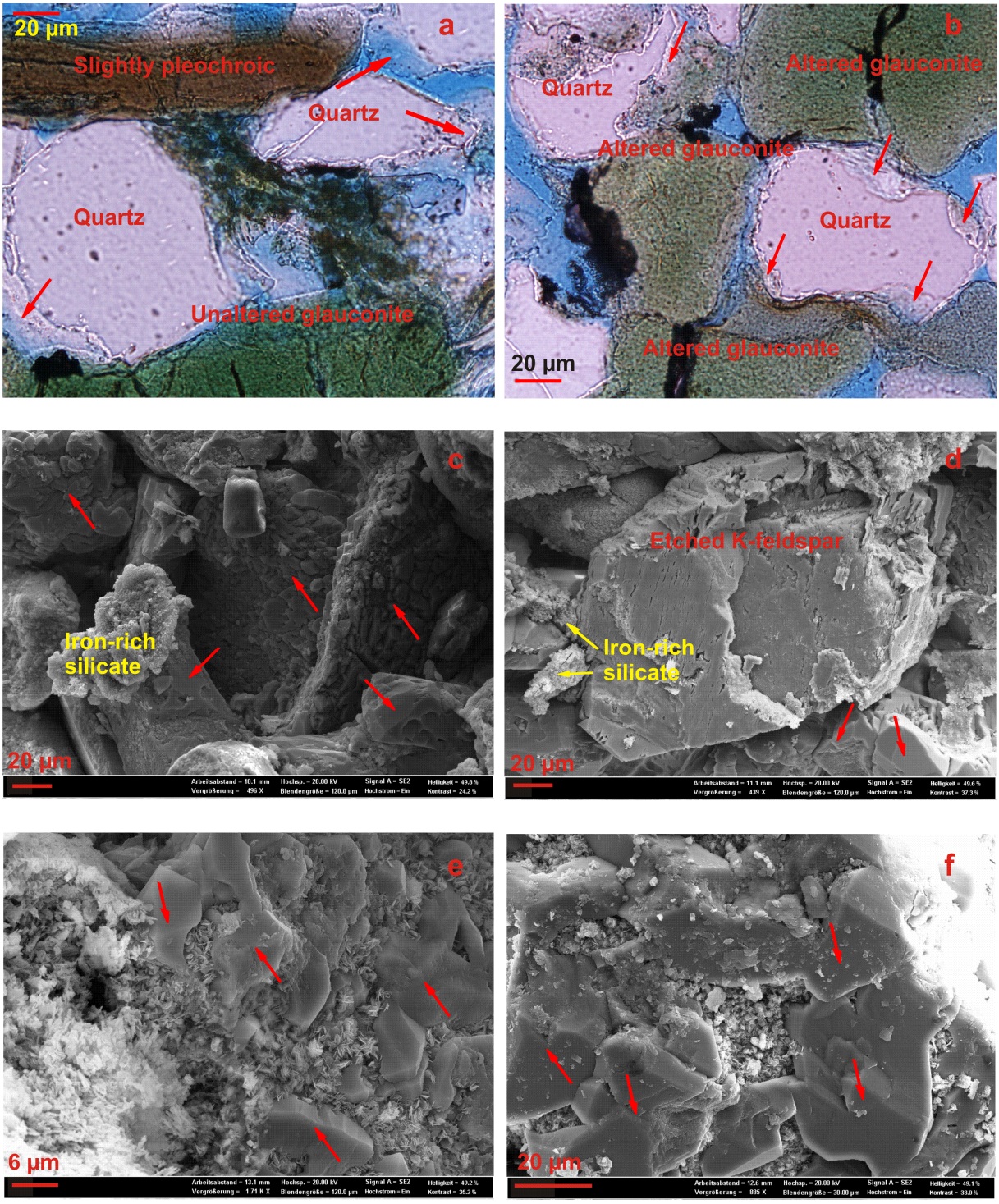

Fig. 33: Thin-section photomicrographs and SEM images of newly formed quartz in the well Siri A. a, c and e: taken from the oil leg (Si 20, 19, 18, respectively); b, d and f: taken from the water leg (Si 7, 8 and 7, respectively); red arrows: secondary quartz; porosity in blue.

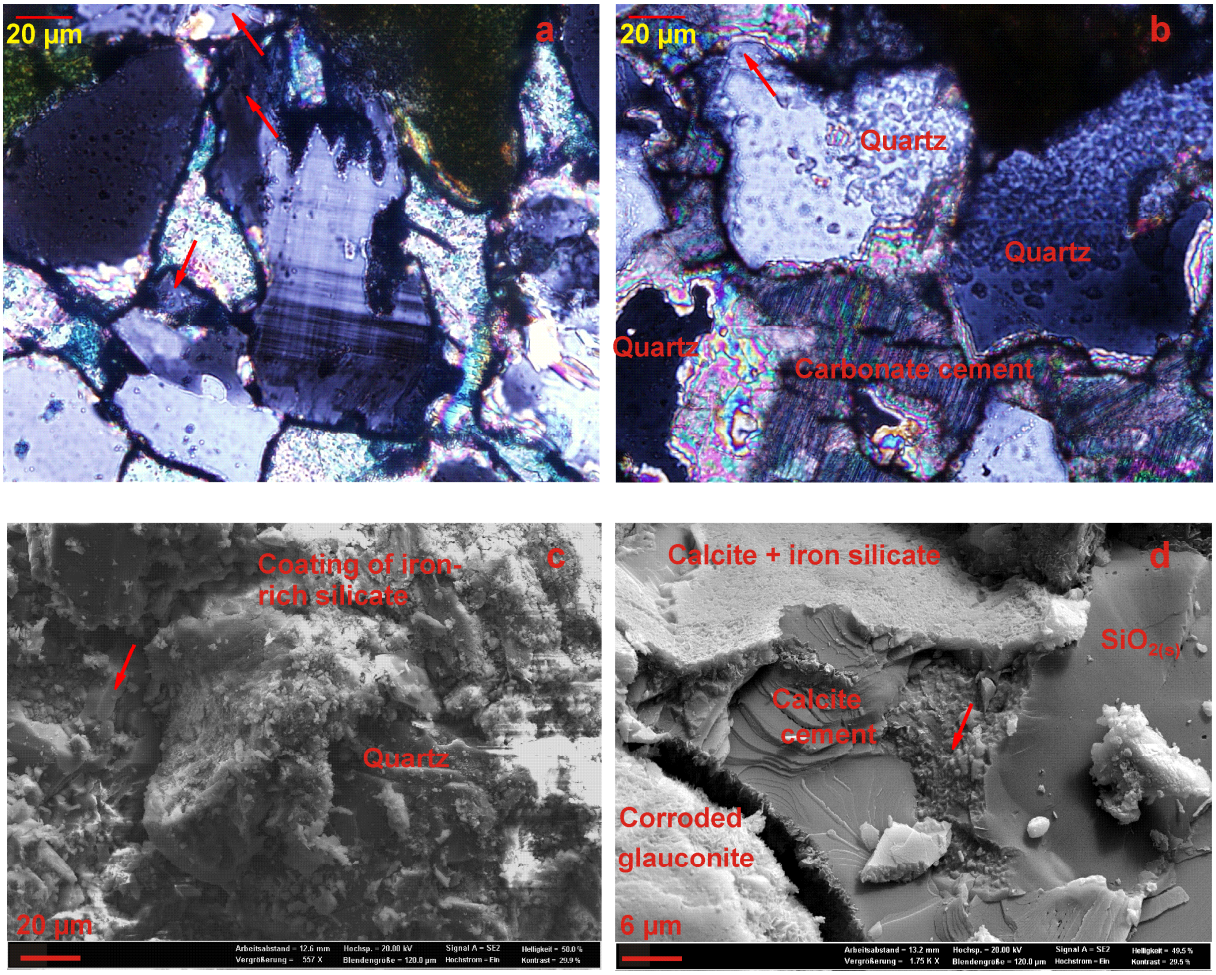

Fig. 34: Thin-section photomicrographs and SEM images of newly formed quartz at the oil-water contacts in the well Siri A. a and c: taken from the palaeo oil-water contacts (Si 22); b and d: taken from the recent oil-water contact (Si 14); red arrows: secondary quartz.

Table 5: Summary of diagenetic features observed in different reservoir parts of the well Siri A.

	Oil leg	OWCs[a]	Water leg
(Microcrystalline) quartz formation	x[b]	x	x
Glauconite alteration	x	x	x
Corrosion of feldspars	x	x	x
Formation of iron-rich silicate	x	x	x
Strong calcite cementation	–[c]	x	–
Formation of muscovite	x	x	x
Impoverishment /enrichment of elements[d]	–	x	–

[a] Palaeo and recent oil-water contacts;
[b] observed by petrographic microscopy and/or SEM;
[c] Not observed;
[d] investigated by XRF and discussed in section 4.3.4 (not presented in this section).

(2) Alteration of glauconite

Glauconite is the subdominant mineral in the reservoir mineral assemblages. It commonly occurs as pellets and shows a (dark) green color in thin section with transmitted light (a in Figs. 33 and 35). The petrographic observations show that the primary glauconite grains in the Siri oilfield are characterized by different degrees of alterations (Fig. 35 to 37). In thin section under crossed nicols, unaltered glauconite grains display a homogeneous structure and low birefringence (b in Fig. 35). A number of the glauconite grains keep their original colors and their crystal textures. However, changes in the features, (e.g., in optical features and in crystal textures) of glauconite grains indicate their alteration (Fig. 35). Glauconite alteration can be observed in different the reservoir parts (Figs. 35 to 37). Unaltered glauconite grains differ in color and in refraction index from unaltered glauconite (Figs. 35 and 36). Figure 35 (e and f) reveals that a half of a glauconite grain displays a slightly yellow-green color differing from the other half (dark green). This half yellow-green glauconite grain possesses shows a less homogeneous structure compared to the other half grain in thin section under crossed nicols. In Figure 36 (c and d), partial alterations of the glauconite grain and its transformation to another mineral are characterized (1) by a change in color to a grey-green color on the edge of the glauconite grain, (2) by a higher interference color, and (3) by a noticeable cleavage structure compared to the central part of this glauconite grain.

At higher magnifications, glauconite can be simply detected by its typical crystal habitus (rounded, commonly occurring as pellets; Fig. 37). SEM investigations display that glauconite alteration is characterized by different degrees and is observed in different reservoir parts (Fig. 37). In general, glauconite surface is coated by its transformation product, which shows a similar crystal texture to chlorite (b, and f in Fig. 37). Additionally, this chlorite-shaped mineral also grows in the free pore space (e in Fig. 37), which could have negative impacts on the reservoir permeability. The EDX analysis of SEM shows that the glauconite deposited in the Siri oilfield consists of potassium, iron, magnesium, aluminum and silica as major component, as well as maybe contains trace amounts of sodium and titanium (Fig. 38).

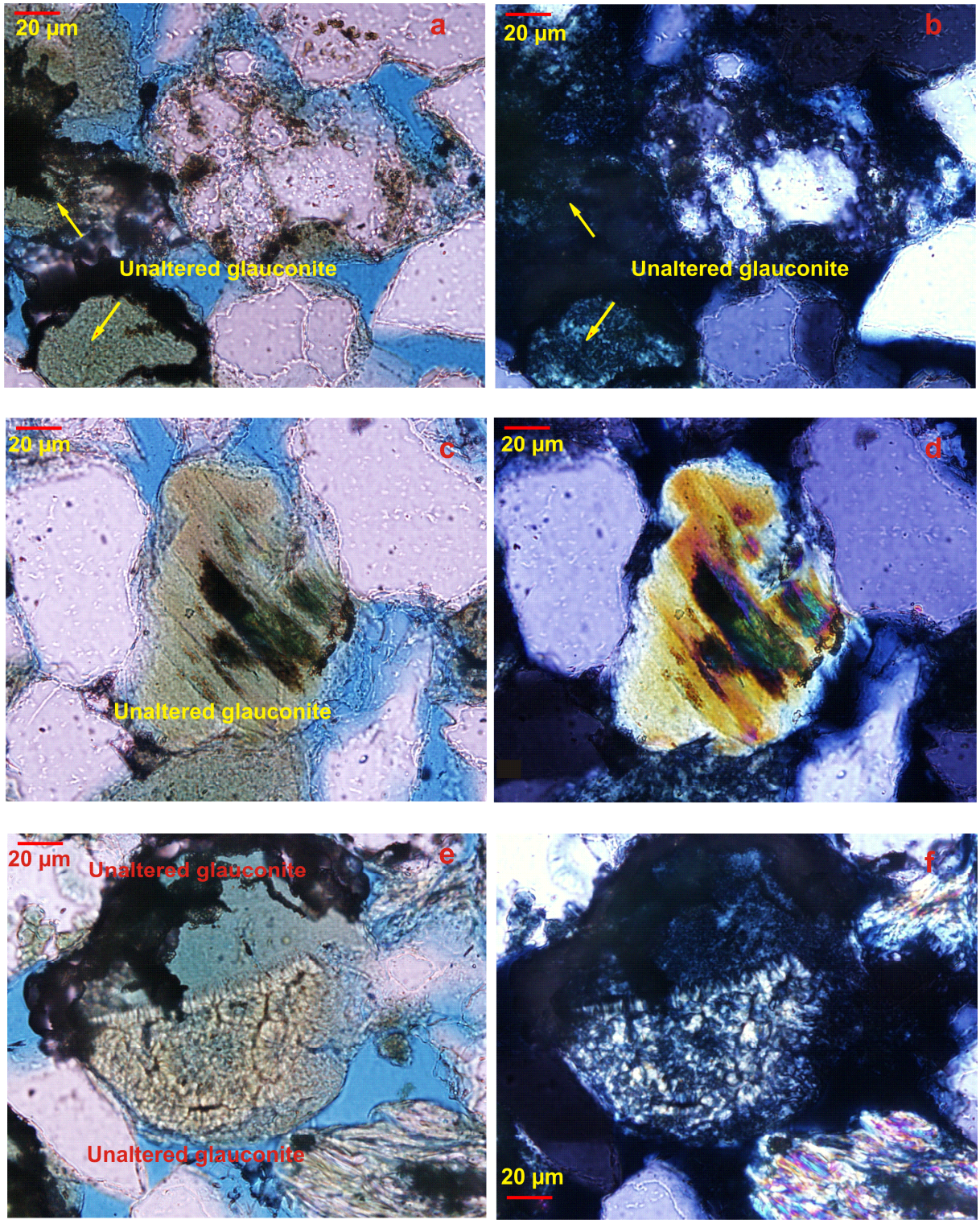

Fig. 35: Thin-section photomicrographs of the sample (Si 20) taken from the oil leg of the well Siri A; porosity in blue.

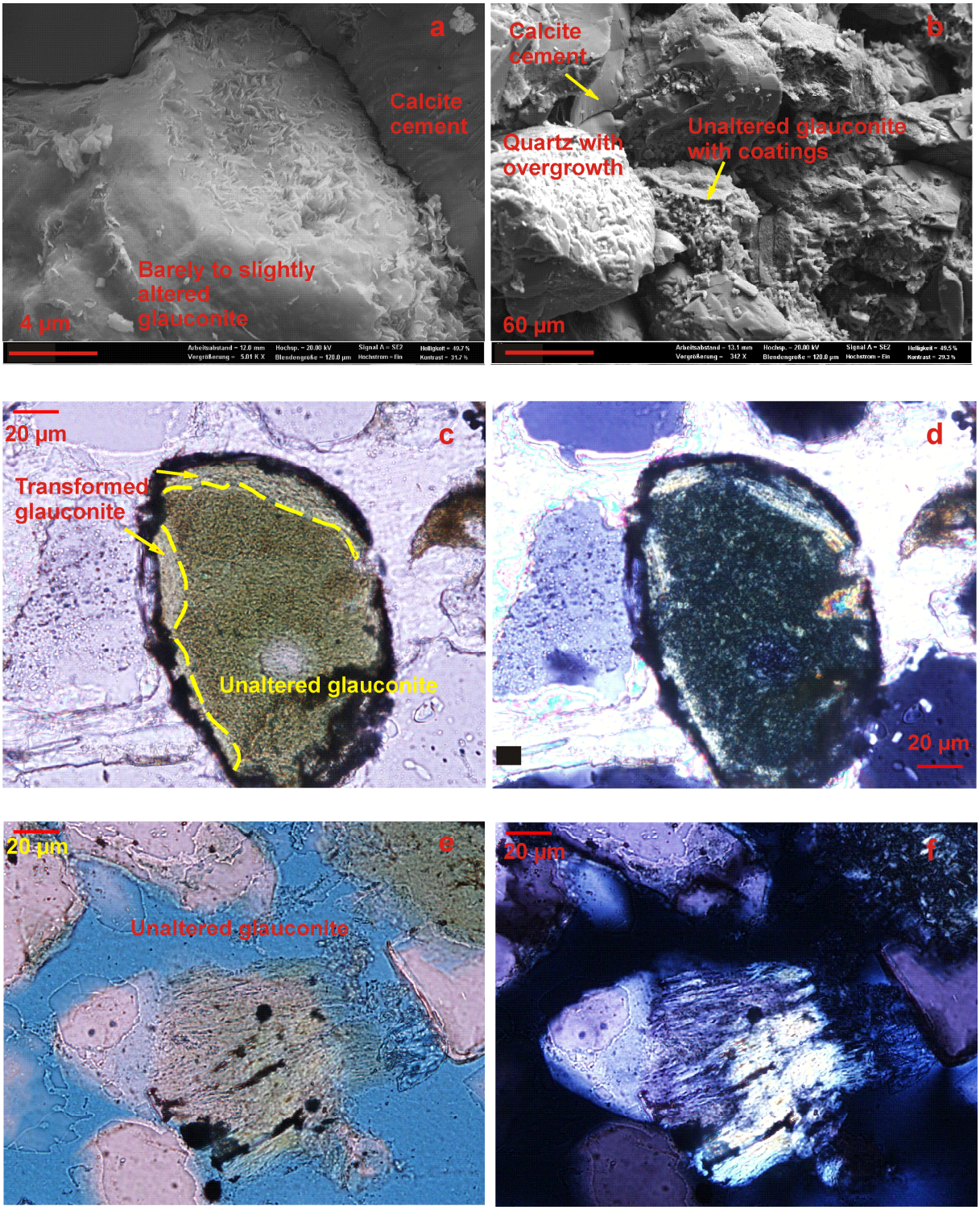

Fig. 36: Thin-section photomicrographs of the samples taken from the well Siri A. a and b: from the palaeo oil-water contact (Si 22); c and d: from the recent oil-water contact (Si 14); e and f: from the water leg (Si 7); porosity in blue.

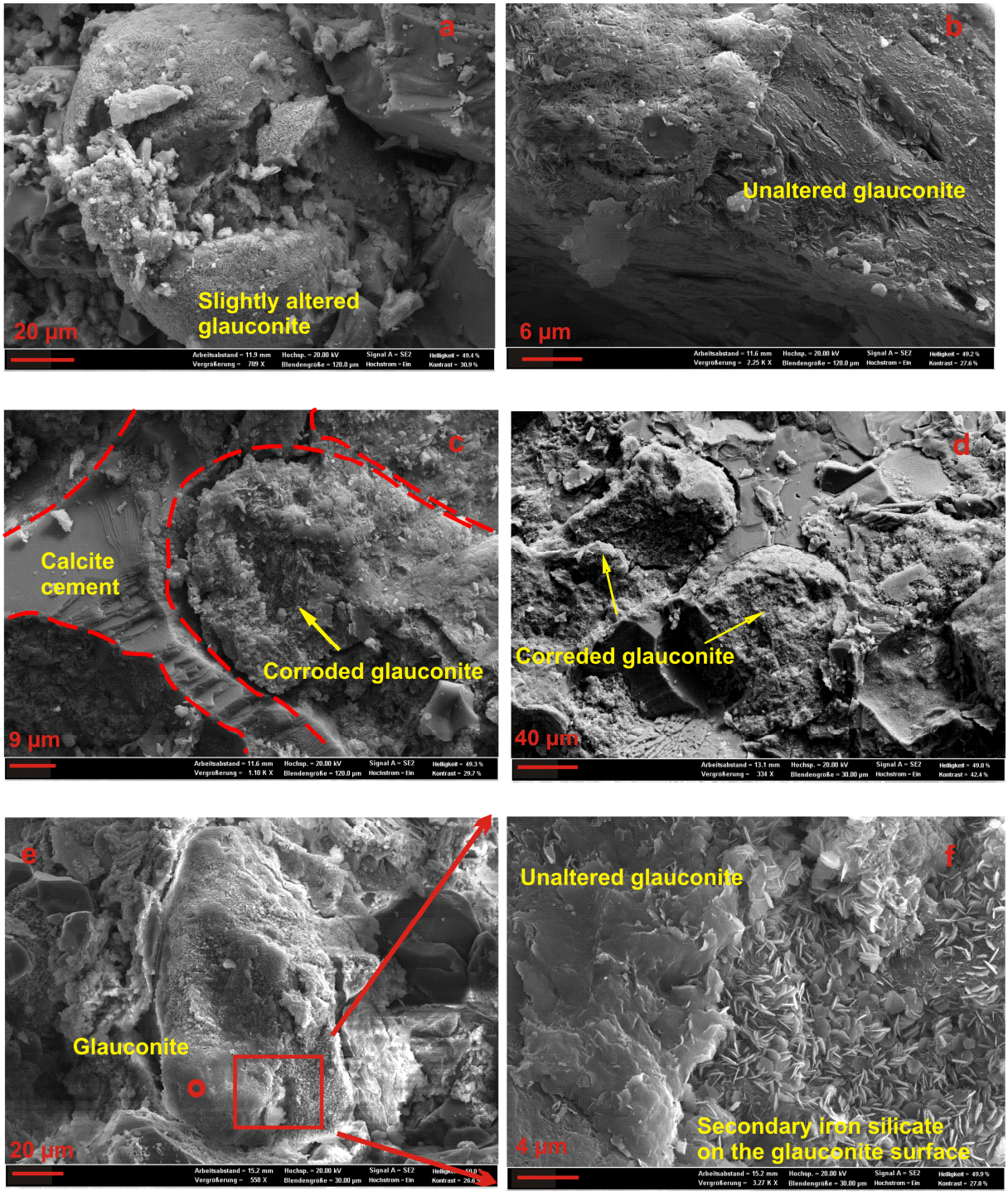

Fig. 37: SEM image of glauconite and its transformation observed in the well Siri A. a and b: from the palaeo oil-water contact (Si 24); c and d: from the recent oil-water contact (Si 14); e and f: from the water leg (Si 7).

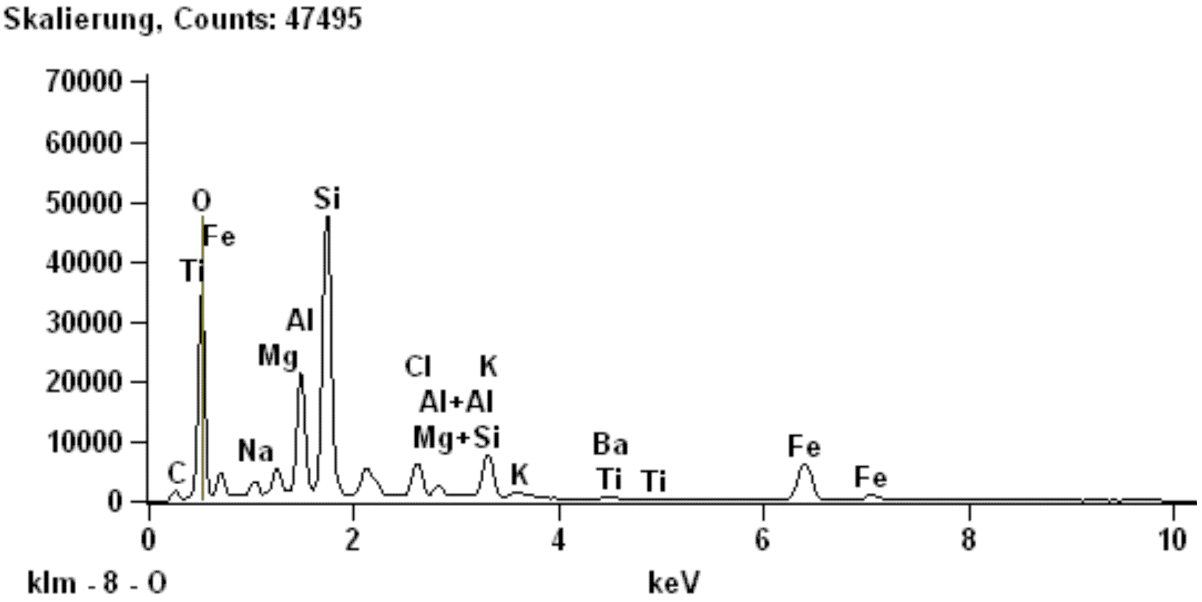

Fig. 38: Energy dispersive X-ray spectrum (EDX) of glauconite. The measuring spot is marked by a red circle in e of Fig. 37.

(3) Precipitation of an olive-brown mineral

Around altered primary glauconite grains, an olive-brown or brown secondary mineral is commonly observed (Fig. 39). This mineral shows an olive-brown color or still more or less keeps the original color of the glauconite grains. This suggests that the secondary mineral, which is observed as coatings of glauconite grains by SEM, can be allocated to the mineral characterized by an olive-brown color in the thin section with transmitted light. Formation of the olive-brown mineral is identified in all samples (Fig. 39). The unknown olive-brown mineral is preliminarily named as clay X prior to its identification. Clay X is characterized by a medium refraction index and a low birefringence (b in Fig. 39). Additionally, it is slightly pleochroic and has a higher interference color compared to glauconite grains (b in Fig. 39). Between its fibrous structures or on its surface, residual oil can be commonly observed (Figs. 39 and 40). This may indicate that formation of clay X formed after oil charging and clay X may be well capable of absorbing oil. Furthermore, the fibrous structures of clay X could dramatically reduce reservoir permeability, although several pore spaces still remain among these structures (Fig. 40).

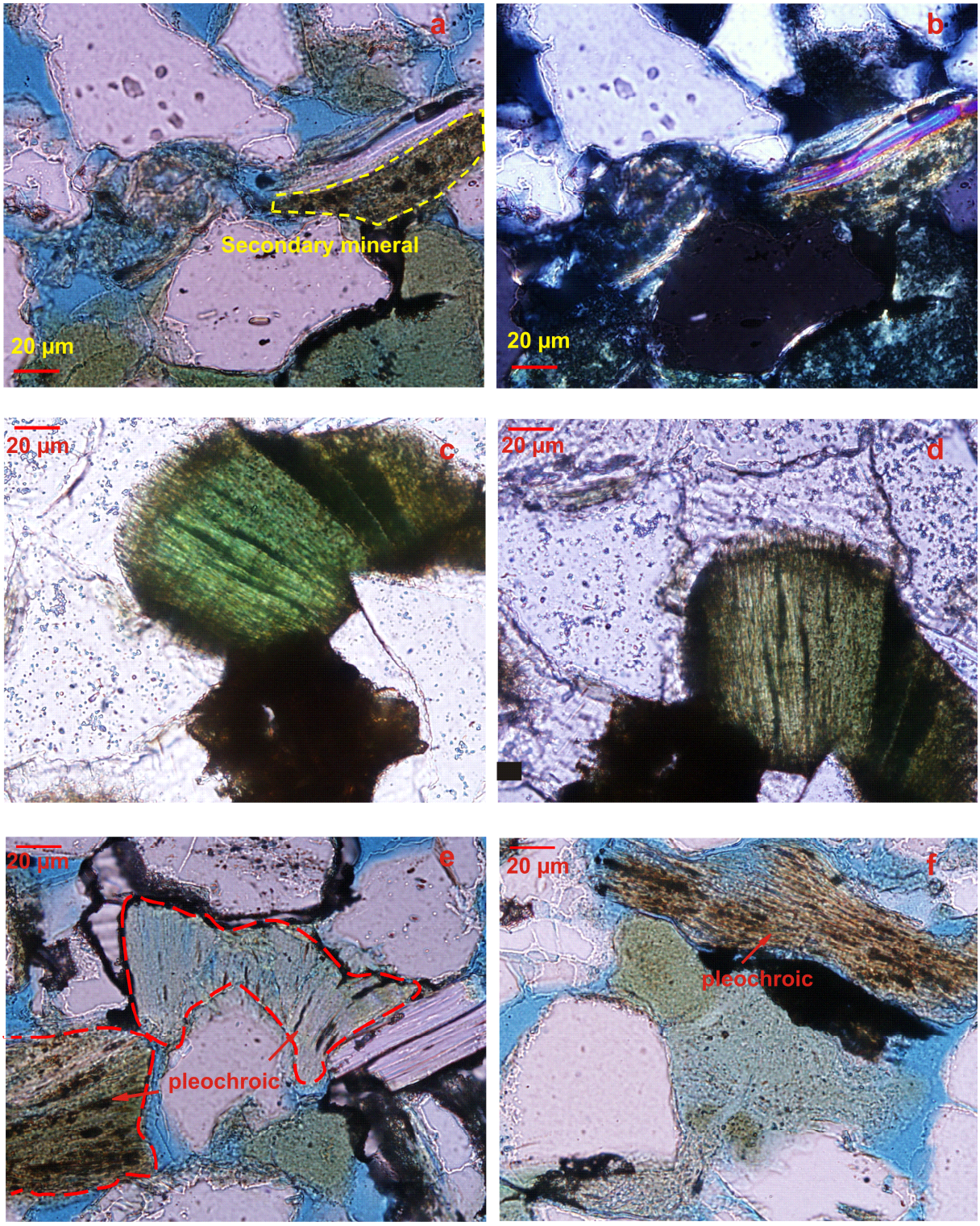

Fig. 39: Thin-section photomicrographs of the secondary mineral transformed from glauconite in the well Siri A. a and b: transmitted light image and image under crossed nicols (oil leg, Si 20); c and d: transmitted light image (from the recent oil-water contact, Si 14); e and f: from the water leg (Si 7); porosity in blue.

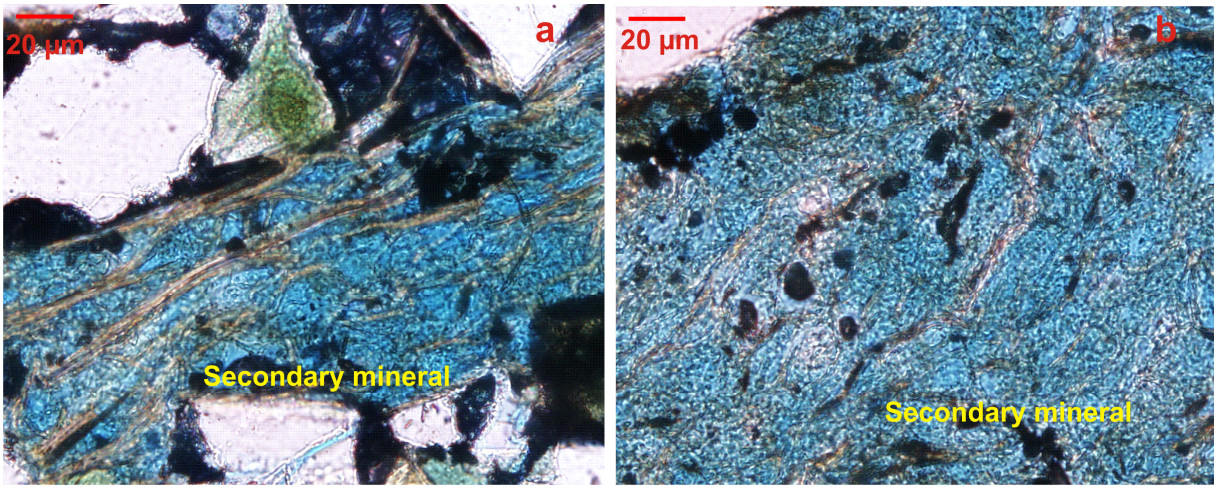

Fig. 40: Thin-section photomicrographs of the unknown secondary mineral in the well Siri A. a and b: from the recent oil-water contact, Si 14); porosity in blue.

At higher magnifications, the morphology of clay X comprises bladed platelets and is similar to chlorite (f in Fig. 37 and Fig. 41). Formation of clay X is unrestricted to a selected part of the reservoir. It is present in all samples taken from the oil and water legs as well as from the OWCs (Fig. 41). This mineral shows pore-lining occurrences as coatings of glauconite grains, where it extends into free pore space and is absent at gain contacts (e in Fig. 37). Additionally, it forms on the surface of glauconite (f in Fig. 37). Sometimes, clay X could build a thin coating over a large area (b in Fig. 41). It also forms on the surface of corroded K-feldspar (c in Fig. 41). Moreover, it can be surrounded by newly formed quartz (d in Fig. 41). In several samples clay X has striking structures (e and f in Fig. 41).

The EDX chemical analysis was performed on the unaltered glauconite and on the clay X coating of the glauconite in two different samples (Si 7 and 24 in Fig. 42 and Table 6). Due to the thin coating of clay X, the analysis performed on the clay X coating provides a mixed result comprising the chemical compositions of glauconite and clay X. Thus, comparing the chemical compositions measured in the area with coating and without coating indicates the difference in the chemical composition between clay X and glauconite. The element mapping of iron provided by the EDX analysis reveals that clay X coating is iron-richer than glauconite (b in Fig. 42). Table 6 also shows this enrichment of iron in clay X compared to glauconite. In general, the contents of potassium and sodium in clay X are lower than in glauconite (except for the measuring spot 1 for potassium and spot 3 for sodium in sample Si 7). Additionally, the measured chemical composition of the both minerals displays an impoverishment of silica in clay X (Table 6). Moreover, clay X in sample 24 contains more magnesium, whereas clay X in sample 7 displays a comparable magnesium content compared to glauconite.

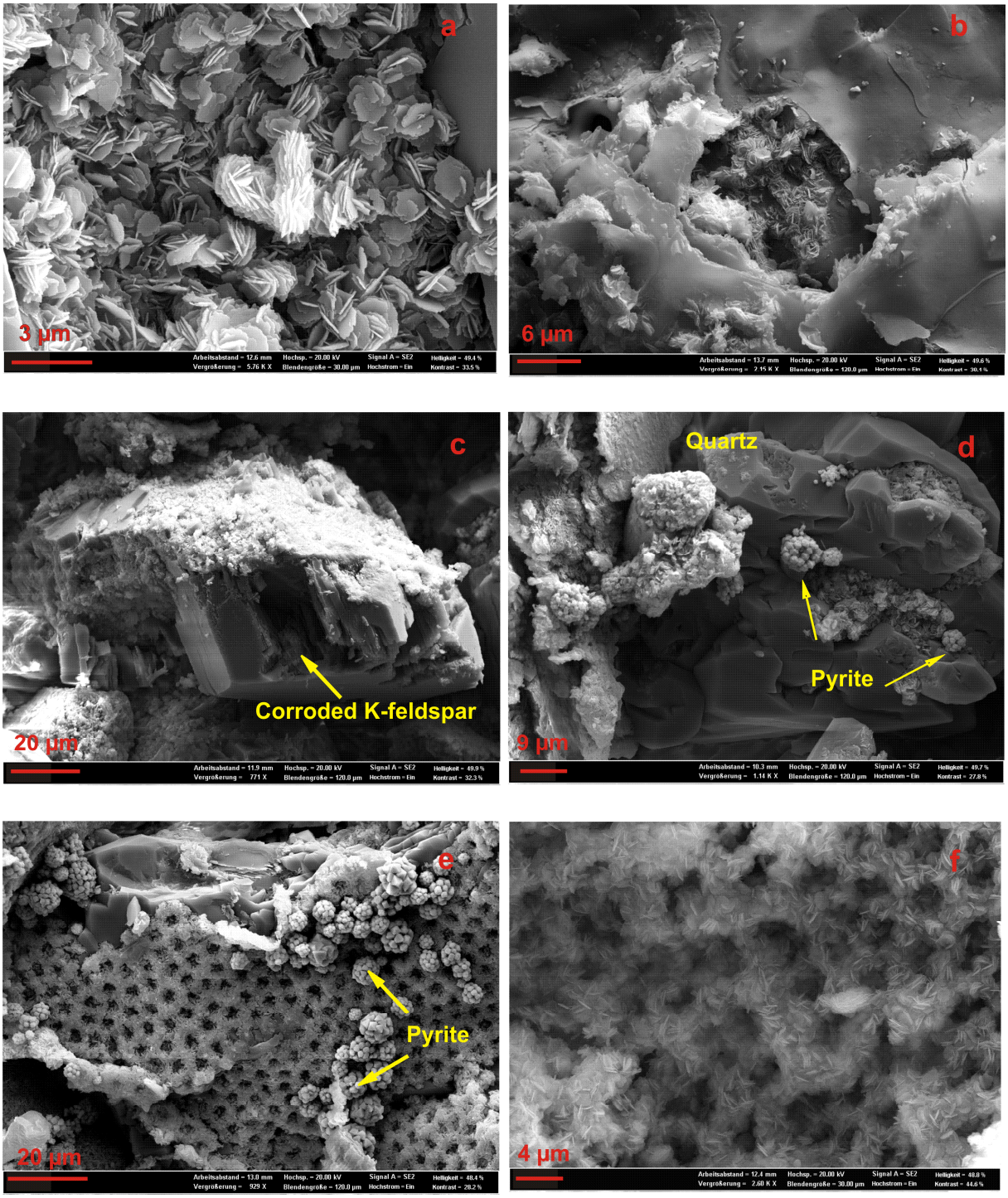

Fig. 41: SEM images of the secondary mineral X in the well Siri A. a, c and f: from the water leg (Si 7, 12 and 6, respectively); b: from the recent oil-water contact (Si 14); d and e: from the oil leg (Si 19 and 18; respectively).

Table 6: The chemical composition of the measuring spots analyzed by EDX.

		Measuring spot[a]	Atom [mol%]												
			C	O	Na	Mg	Al	Si	Cl	K	Ca	Ti	Fe	Ni	Br	Ba
Sample Si 24		1	8.6	63.2	0.5	0.9	8.9	12.1		1.4	0.2	0.1	4.2			
	with coating	2	7.3	63.0	0.5	1.1	8.5	12.7		1.4	0.2	0.1	5.3			
		3	8.2	63.0	0.7	1.5	8.4	11.4		0.8	0.1	0.1	5.9	0.02		
		4	7.4	63.1	0.7	0.5	9.4	14.4		2.2		0.1	2.2			
	without coating	5	4.7	62.6	0.8	0.8	9.6	16.0	0.3	2.3		0.1	2.8			
		6	5.0	62.6	0.8	0.7	9.9	15.3		2.4		0.1	3.1			
Sample Si 7		1	3.2	62.0	0.4	1.3	4.5	18.1	0.8	3.4		0.1	6.2			
	with coating	2	5.1	61.9	1.1	1.7	6.7	14.8	0.8	2.1		0.1	5.9			
		3	4.4	61.2	1.6	1.7	6.4	15.8	1.4	2.6			5.0			0.1
		4	5.3	61.7	1.3	1.7	5.4	17.0	1.4	2.7		0.2	3.3			
	without coating	5	5.9	62.5	0.4	1.8	5.1	16.9	0.6	3.0		0.1	3.9			
		6	6.6	62.5		1.6	3.4	18.0	0.4	2.8		0.1	3.3		1.3	

[a] measuring spots are marked by red circles in Figure 42.

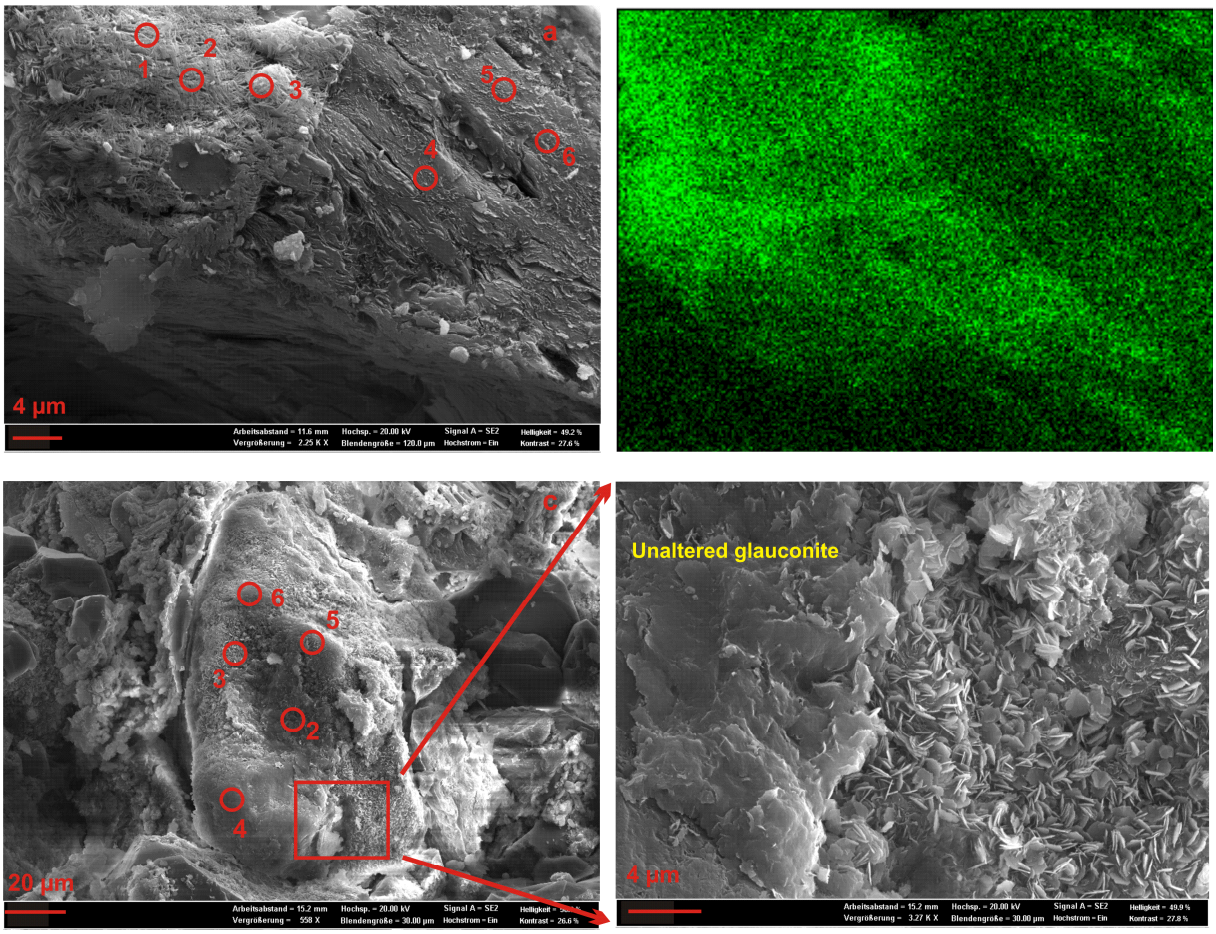

Fig. 42: SEM images of the positions of the measuring spots (a, c and d) and the element mapping of iron analyzed by EDX (b). a and b: sample Si 24; c and d: sample Si 7.

(4) Corrosion of feldspar

Corrosion of feldspar (K-feldspar and albite) is seen in a number of samples taken from different reservoir parts: the water leg, the OWCs and the oil leg (d in Fig. 33 and Fig. 43). Dissolution of feldspar is commonly accompanied by widespread formation of quartz. Thick quartz coatings formed on the surface of corroded feldspar (f in Fig. 43), suggesting that dissolution of feldspar could have resulted in quartz formation. Calcium-containing plagioclase is not observed in all analyzed samples.

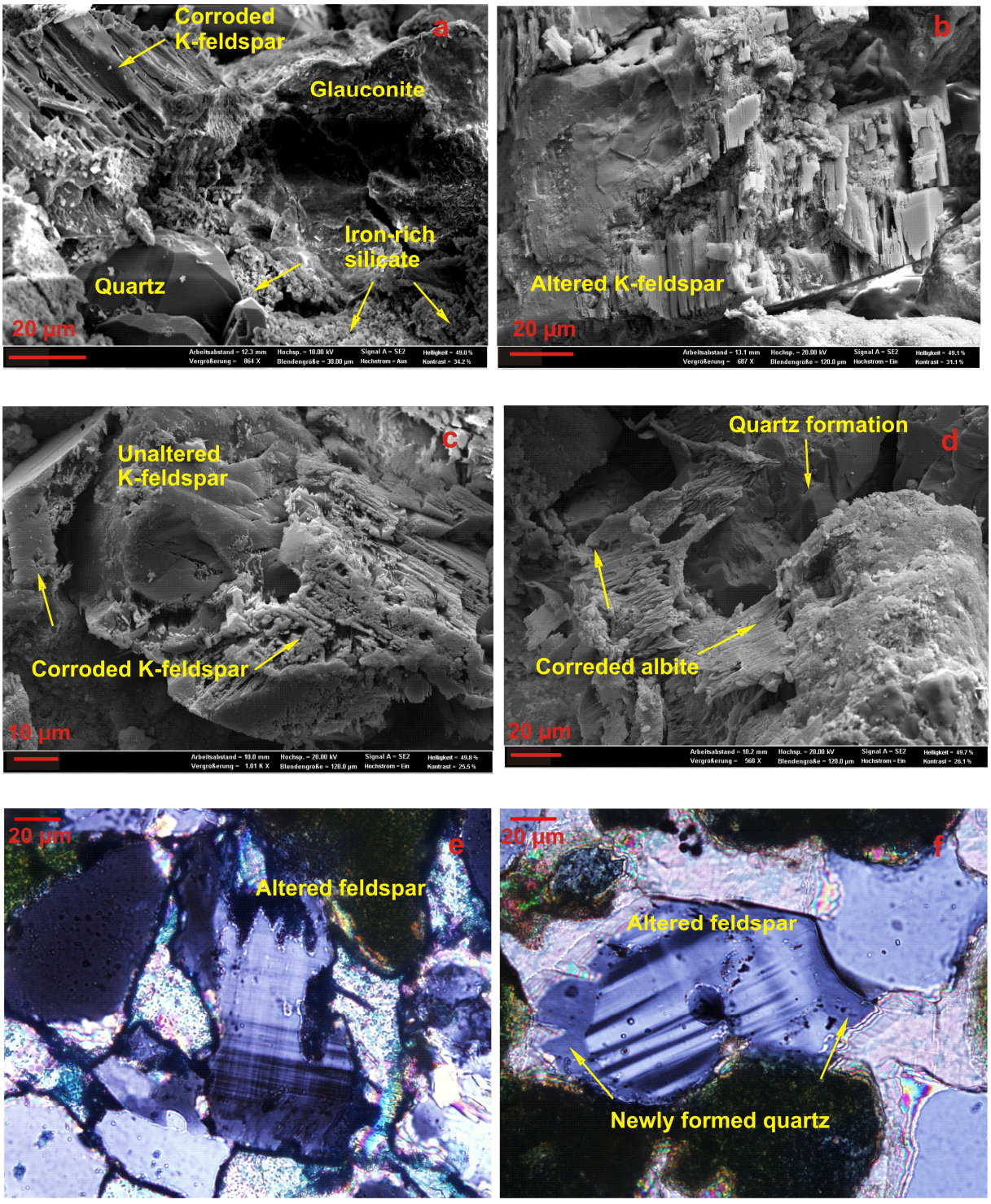

Fig. 43: SEM images and thin-section photomicrographs of feldspar dissolution in the well Siri A. a: from the water leg (Si 7); b to d: from the oil leg (Si 18, 19, and 19, respectively); e: from the palaeo oil-water contact (Si 22); f: from the recent oil-water contact (Si 14).

(5) Formation of muscovite

Combining petrographic microcopy and SEM indicates that primary and secondary muscovite coexists in the reservoir sandstones. Primary muscovite is identified in thin section by its cleavage plane structure, extinction along its cleavage plane structure and its morphology (a and b in Fig. 44). In comparison, formation of secondary muscovite is more difficult to identify in thin section due to its small grain size. However, its typical cleavage plane structure and optical properties help to prove its formation. In an altered glauconite grain, the plate-like mineral clearly shows cleavage structure (c and d in Fig. 44). It more or less keeps the color of the primary glauconite. This secondary mineral is characterized by a low to medium birefringence and by extinction along its cleavage plane structure. All these observed optical properties are consistent with those of muscovite, and consequently, confirm the formation of secondary muscovite in the reservoir sandstones. Additionally, secondary muscovite also formed together with the brown iron-rich mineral (a in Fig. 40). Such observations suggest that alteration of glauconite could have induced muscovite precipitation including formation of the olive to brown and iron-rich clay mineral X.

(6) Carbonate cementation

Carbonate cementation is observed in a limited number of core samples: directly underneath the upper seal as well as at the palaeo and the recent OWCs (Figs. 27, 28 and 30). In these zones, carbonate almost occupies the entire pore space (Figs. 32, 34, 36 and 37). Consequently, the permeability dramatically decreases in these horizons (Schovsbo, 2009; pers. com.). Thus, it is important and basic for successful reservoir engineering to identify which hydrogeochemical processes induce the carbonate cementation in these specified horizons of the reservoir sandstones. The chemical composition of this carbonate cement must be analyzed at first.

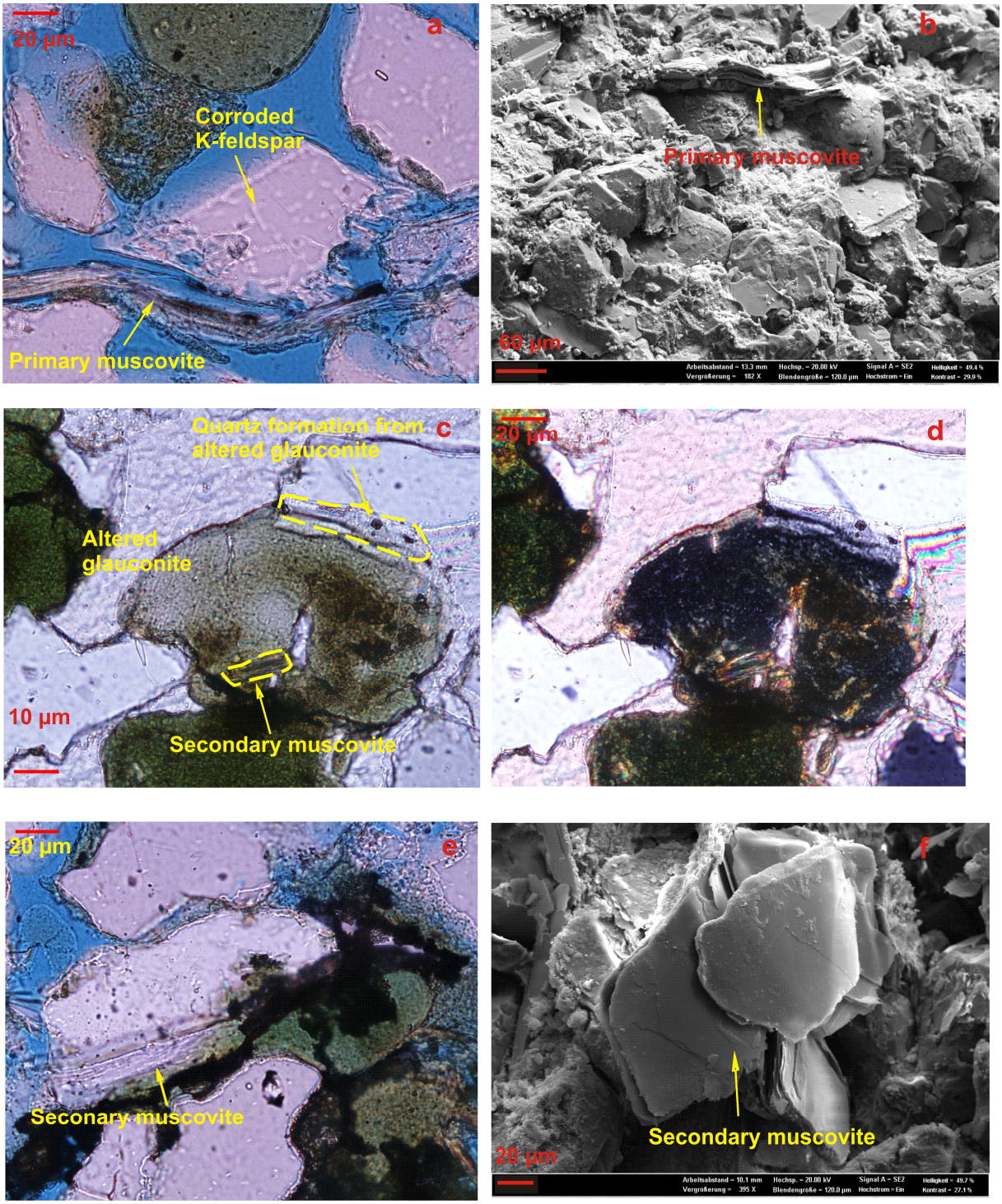

Fig. 44: Thin-section photomicrographs and SEM images of primary and secondary muscovite in the well Siri A. a: from the oil leg (Si 20); b: from the palaeo oil-water contact (Si 24); c and d: transmitted light and with cross nicols (Si 14); e and f: from the oil leg (Si 20 and 19, respectively); porosity in blue.

Alizarin red S combined with potassium ferricyanide was used as stains for distinguishing carbonate minerals in the cemented samples. All of these stained carbonate samples display a mauve to blue color in thin sections (e.g., Fig. 34). This suggests that the carbonate cement contains iron with

trace amounts but without magnesium (Ayan, 1965; Dickson, 1965). The results of XRD and SEM investigations indicate that the carbonate cement is made up of almost pure calcite. However, the XRD results of the sample Si 22 taken from the cemented palaeo oil-water contact show that the carbonate cement contains trace amounts of magnesium (Fig. 27). The results provided by HRTEM confirm that calcite dominates in the carbonate cement. Additionally, the cement contains trace amounts of manganese (in average 2.5 mol%). It is incomprehensible that the carbonate cement is magnesium-free and lacks sufficient amounts of iron, although the reservoir mineral assemblage is rich in magnesium and also in iron which are bound to glauconite. In addition, glauconite dissolution proven by petrographic microscopy and SEM must have released considerable amounts of magnesium and iron ions into the pore water. This suggests that formation of another or other minerals comprising iron and magnesium can more efficiently remove aqueous magnesium and iron species compared to precipitation of iron- or magnesium containing carbonates. In addition, two spot analyses of HRTEM reveal that this calcite-dominated cement contains trace amounts of phosphorus (accounting for 0.1 mol%).

Besides the six major diagenetic processes described above, there are several diagenetic processes that petrographic microscopy is incapable of verifying. However, they are established in a few samples by using SEM. SEM observations indicate that secondary pyrite formed on the surface of secondary quartz and clay X (d and e in Fig. 41, and a in Fig. 45). It suggests that pyrite could also have formed at the late-stage diagenesis in the Siri oilfield reservoir sandstone. Nevertheless, pyrite is incapable of being proven by using XRD in the same samples, maybe due to its low content in bulk samples. Titanium is bound to glauconite with trace amounts, proven by EDX analysis (Fig. 38 and Table 6). Identification of the single crystal as titanium oxide is based on the SEM-EDX analysis which only shows titanium as the major element. The abundance of calcium and phosphorus with trace amounts of fluorine in the SEM-EDX spectrum indicates the presence of (fluor-) apatite (Fig. 45).

The petrographic observations provided by petrographic microscopy and SEM clearly show (1) which primary minerals are corroded and which secondary minerals form. They also indicate into which secondary minerals the primary minerals are converted based on the texture of minerals. Note that such observations are incapable of correctly delivering significant information about the temporal succession of such processes. The aim of this study is not to reproduce the entire geological diagenetic development of the Siri oilfield by means of hydrogeochemical modeling. The developed model is restricted to investigate the specific geological period. Thus, several discordances between the observed and modeled diagenetic features do not mean the invalidity of the model. The petrographic observations demonstrate that an olive to brown and iron-rich clay mineral X formed from glauconite alteration, but are incapable of identifying it. Thus, a combination of various analytical methods aims to identify it in the following study.

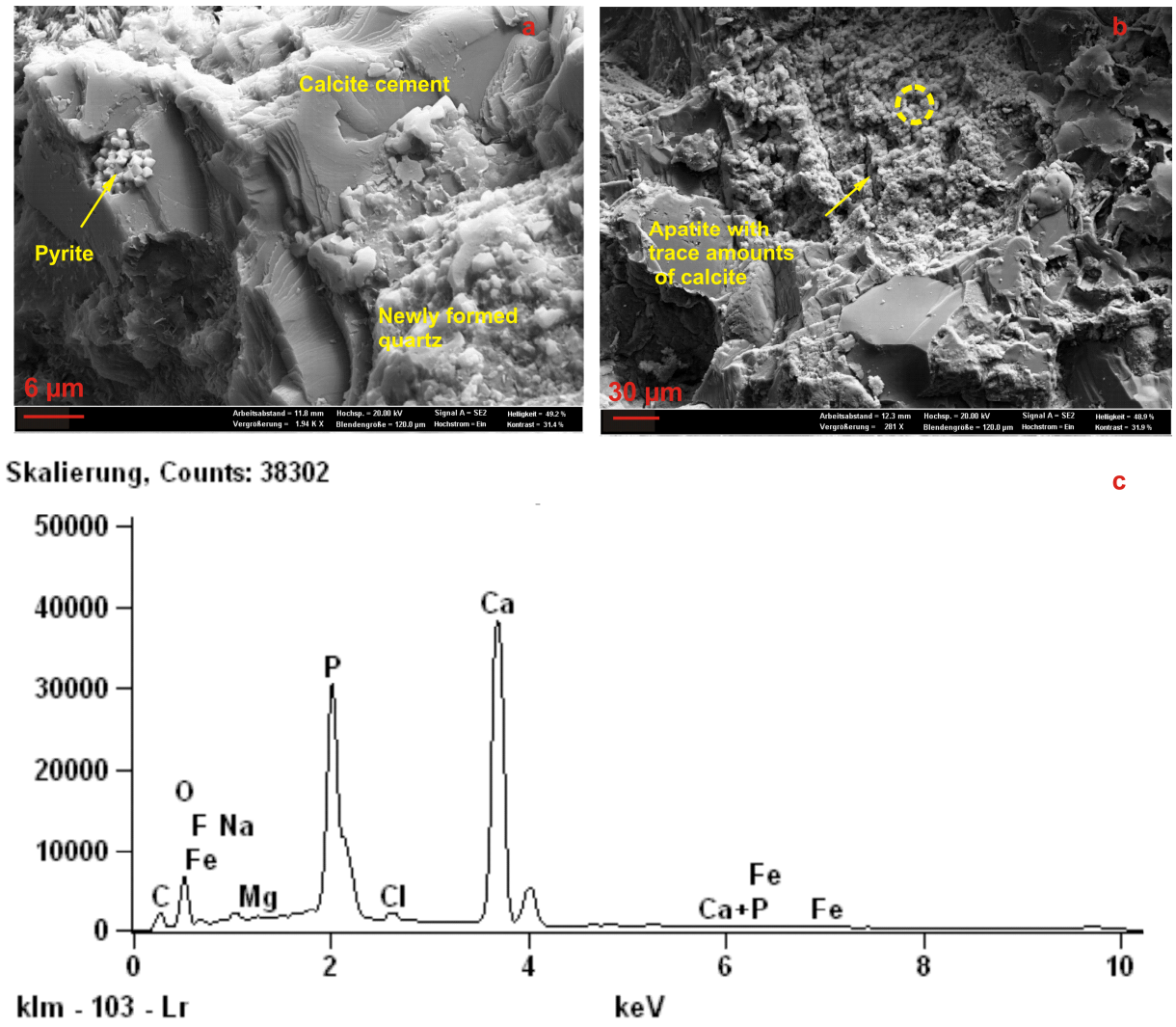

Fig. 45: SEM images and SEM-EDX spectrum of secondary pyrite and apatite in the sample Si 15 taken from the palaeo oil-water contact of the well Siri A. c: analysis spot is marked in Fig. b by a yellow circle.

4.3.3 Identification of authigenic clay mineral X

Compositional and structural similarities among a variety of clay minerals prevent an exact identification by using only one analytical method. This applies in particular for determination of clay minerals, when the clay mineral to be identified is not a main component in the mineral assemblage. For instance, bulk XRD analysis could result in misidentification of clay minerals, when the identification is based merely on the XRD spectra criteria performed under normal measurement conditions (e.g., without a stepwise increase in measurement temperature or ethylene glycollated treatment for the separated clay fraction).

Petrographic analysis provides a preliminary overview of the mineralogical quantity of the Siri oilfield's reservoir sandstone assemblage: (1) dominance of quartz and glauconite; (2) intensive calcite formation within the specified horizons; (3) slight formation of micas; and (4) precipitation of an olive-brown to brown authigenic clay mineral (preliminarily named as clay X) as a minor component. The low content of this unknown authigenic clay X leads to difficulties in its identification. XRD analysis of all bulk samples from the Siri oilfield reveals a major reflection at ca. 7.2 Å (Figs. 27 to 29). This could suggest that the clay X can be attributed to the serpentine-chlorite group. In comparison to other mineral groups characterized by relatively simple structures (e.g., quartz and calcite), silicates have much more XRD reflections owing to their complicate structures. Additionally, variation in chemical composition of silicates (e.g., chlorite consisting of different end-members) could proliferate the XRD spectra criteria of one mineral. These three reasons mentioned above complicate the identification of clay X only based on the measured XRD-ray diffraction pattern of the bulk samples. Nevertheless, XRD analysis results provide indications of the mineral group to which clay X is attributed. Therefore, combining a series of analytical methods working at "mm-scale" (XRD and petrographic studies by optical microscopy) to "micro-scale" (SEM and HRTEM) aims to enable its identification. Table 7 summarizes all features of the clay X provided by these analytical methods.

Petrographic observations show that an olive brown secondary mineral X appears to be precipitated due to glauconite alteration, as it commonly formed around glauconite grains and sometimes still more or less keeps the original color of its ambient glauconite grains (e.g., Fig. 39). The fibrous structure of clay X may strongly decrease the permeability of the reservoir, although some pore spaces still exist among its fibrous structures (Fig. 40). Clay X displays slight pleochroism, as well as is characterized by a medium to high refraction index and a low birefringence (Figs. 39 and 40; Table 7).

At higher magnifications, SEM investigations reveal that clay X displays a crystal texture comprising bladed platelets (e.g., Figs. 33 and 41). The chemical analysis provided by SEM-EDX indicates that clay X contains iron, magnesium, aluminum and silicon as major elements and maybe with trace amounts of potassium, sodium, titanium, carbon and chloride. The chemical composition of clay X provided by SEM-EDX is semi-quantitative, because the results from this method can be interfered by several factors. Sodium and chloride may be contaminants from halite formed owing to evaporation of high saline formation water. Due to the absence of calcium and to the crystal texture of clay X, the occurrence of carbon could represent the contamination of residual hydrocarbons adsorbed on the surface of clay X. Additionally, SEM-EDX analysis could deliver a mixing result from several minerals which overlap each other.

High-resolution transmission electron microscopy (HRTEM) was applied to more precisely determine the chemical composition of clay X and its crystal structure. Figure 46 shows at different magnifications that clay X formed in the pore space which is located between two quartz grains and

which is filled with oil. The observations provided by HRTEM analysis demonstrate that flakes of clay X are randomly distributed in the pore space (c in Fig. 46). The EDX analysis yields a spectrum containing iron, magnesium, aluminum and silicon with an absence of potassium and sodium (d in Fig. 46) compared to the chemical composition provided by SEM (the measured composition of the clay X coating in Table 6). Additionally, HRTEM investigations reveal that this authigenic iron-rich clay X is characterized by a basal spacing of 7.0 Å (Fig. 46). Moreover, this clay X shows a remarkably high iron content which is higher than the silica content (Fe : Mg : Al : Si = 1.1 : 0.19 : 0.94 : 1.0 on average).

The oil phase filling the pore space between the two quartz grains displays a striking netlike structure that is characterized by voids of 1 µm at maximum in length under HRTEM (b in Fig. 46). It follows that these voids must have been filled with pore water to withstand the elevated reservoir pressure of ca. 230 atm, because the reservoir of the well Siri A is filled with undersaturated oil. Thus, such foamy structures consisting of pore water and oil phase in emulsion can be described as oil-water contacts at a micro-scale. EDX analyses investigated the chemical composition of the oil phase located between the both quartz grains at different sites: oil with and without the netlike structures. The measured results show that the oil phase located at the "micro" OWCs (in other words: near the voids) contains more sulfur compared to the oil phase in which surroundings no oil-water foam was observed. This observation provides another indication that the oil of the Siri oilfield was degraded. The measured high concentration of organic acids in the formation water and the potential consumption of hydrogen produced by oil degradation (due to the redox-reactions with ferric iron ions; Eq. 13) additionally indicate the oil degradation in the Siri oilfield.

The measured results provided by SEM and HRTEM suggest that the unidentified clay mineral X is a silicate containing iron, magnesium and aluminum and shows clear iron dominance over magnesium (Fig. 46). The XRD results suggest that clay X may belong to the serpentine or chlorite group. There are four typical aluminum silicate hydroxide minerals, which major constituent elements accord with this unidentified clay mineral except for primary glauconite: berthierine, biotite, chamosite and odinite. These four minerals more or less have similar properties regarding to their chemical composition, petrographic features, crystal texture, or mineralogical structure, which are summarized in Table 7 (for the corresponding references, see the following text).

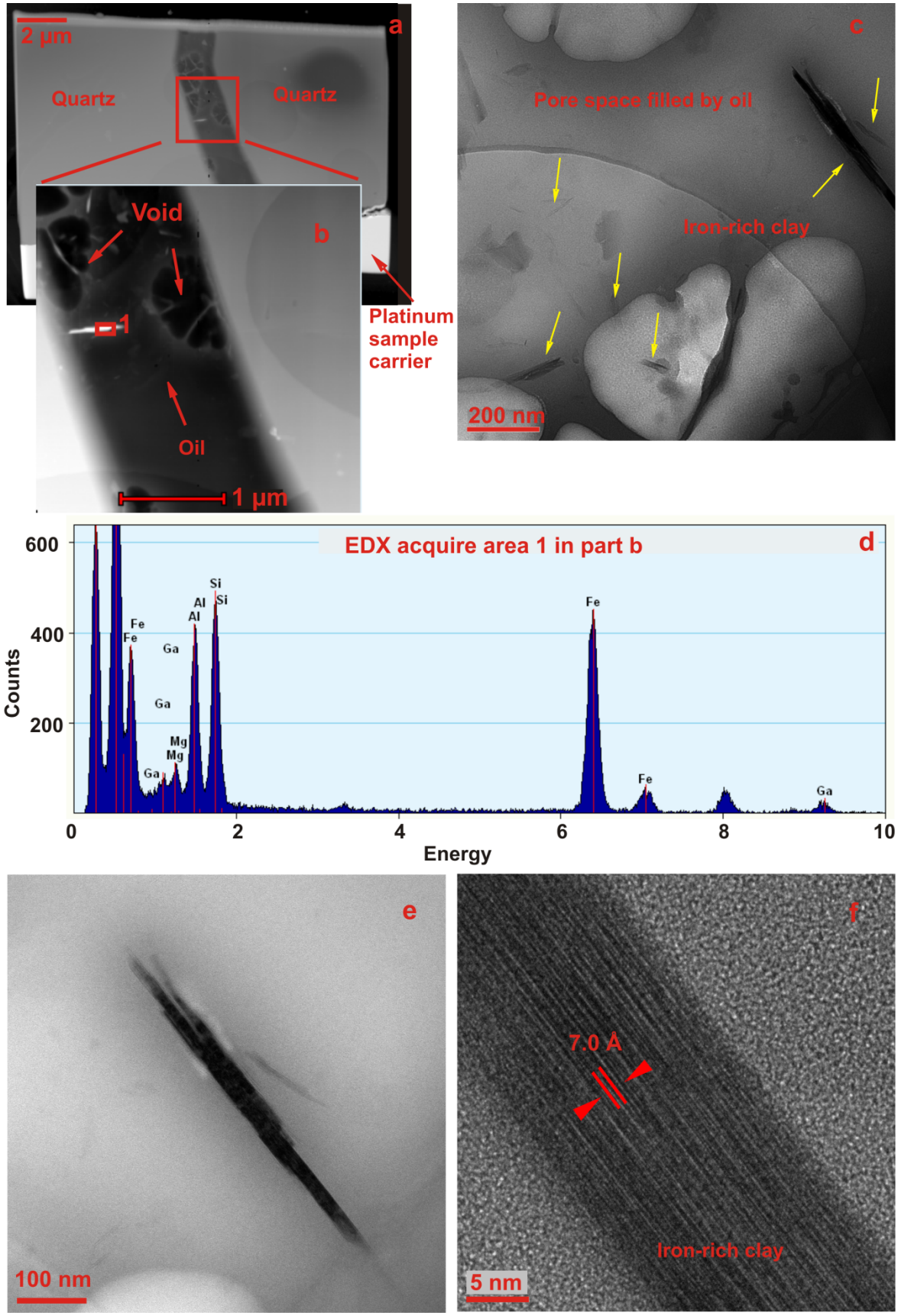

Fig. 46: HRTEM images and EDX spectrum of authigenic iron-rich clay X in sample Si 15 of the well Siri A. c: distribution of iron-rich clay X (marked by yellow arrows) in oil; d: EDX spectrum of the analyzed area 1 marked by a red box in part a.

Table 7: Summary of the features of the unidentified mineral and of similar minerals[a].

	Features/properties (in thin section)					Texture	Major constituent	Basal
	Color	Pleochroismus	Refraction index	Birefringence	Special features	(observed by SEM)	elements[c]	Spacing
Unknown[b]	olive brown	slight to medium	high	low		bladed platelets	Fe, Mg	7 Å
Berthierine	various	medium	high	low		bladed platelets or thick rims	Fe, Mg	7 Å
Biotite	various	strong	medium	high	"bird's eyes"	cleavage planes	K, Fe, Mg	10 Å
Chamosite	various	slight	high	low		platelets, rosette pattern	Fe, Mg	14 Å
Odinite	green	-[d]	-	-	dominance of ferric iron	-	Fe, Mg	7 Å

[a] References used in Table 7 are mentioned in the text;
[b] Unknown mineral to be identified;
[c] besides aluminum, silicon, oxygen and hydrogen;
[d] no available data.

Berthierine commonly occurs in marine sedimentary environment (Iijima and Matsumoto, 1982; Hornibrook and Longstaffe, 1996). However, its occurrence has been also reported in fresh- and brackish-water sediments (Hornibrook and Longstaffe, 1996), Canadian Arctic desert soils (Kodama and Foscolos, 1981), in coalfields (Iijima and Matsumoto, 1982), and its intergrowths with chlorite-group minerals in low-temperature metamorphic and hydrothermally altered rocks (Xu and Veblen, 1996, and references therein). It is a ferrous iron-dominant clay mineral that is structurally similar to serpentine: trioctahedral 1:1 layer silicate having a basal spacing of 7 Å (Kodama and Foscolos, 1981; Brindley, 1982; Bhattacharyya, 1983). Berthierine considerably shows pleochroismus (Rivas-Sanchez et al., 2006). In view of its chemical composition, berthierine resembles the iron-rich chlorite chamosite, with which berthierine shares a significant number of XRD lines (Bhattacharyya, 1983; Hornibrook and Longstaffe., 1996). Stokkendal et al. (2009) investigated the reservoir sandstones taken from the Siri oilfield by using XRD. They performed measurements for the separated clay fraction under the following various conditions to exactly distinguish berthierine and chlorite, which reveal a major reflection at ca. 7 Å: (1) air dried and heated to 500 °C, (2) ethylene glycollated and heated to 500 °C, and (3) stepwise heated from 450 to 625 °C with a temperature increase of 20 °C. The presence of berthierine was proven, as the reflection of the 7.3 Å peak weakens and almost disappears at 625 °C (Stockkendal et al., 2009). Berthierine formation necessitates reducing conditions in combination with a corresponding pH condition, a reasonable chemical composition of aqueous solutions (Bhattacharyya, 1983; Fritz and Toth, 1997). Newly formed berthierine is unstable in the presence of O_2 and is converted into other minerals depending on the pH-pe conditions (Rivard et al., 2013). In thin section, berthierine is characterized by the similar features to chlorite, which thus results in misidentification based on petrographic criteria alone (Slack et al., 1992). Berthierine displays dark green, yellowish green, or brown color with a variety of its crystal structure (from crypto- to microcrystalline to amorphous shape; Iijima and Matsumoto, 1982; Rivas-Sanchez et al., 2006). Berthierine possesses a high refraction index and a very low to null birefringence (Rivas-Sanchez et al., 2006). Scanning electron images illustrate that berthierine can show different types of morphology, even as it formed in a same well: laths (Horinbrook and Longstaffe, 1996); thick rims with smooth surfaces which cover surface of others grains and bladed shape in the Siri oilfield (Stokkendal et al., 2009).

Biotite is present in a wide variety of igneous and metamorphic rocks (Gilkes et al., 1972). The chemical formula $[(K_{0.91}Na_{0.01})(Mg_{0.4}Fe_{2.07}Mn_{0.05}Al_{0.14}Ti_{0.19})(Si_{2.82}Al_{1.18})O_{10}\ (OH)_2]$ of fresh biotite determined by Murakami et al. (2003) clearly displays the dominance of potassium in biotite over other cations (besides iron, silica and aluminum). Thus, biotite may become a major source of potassium, magnesium, zinc and manganese to plants as it is weathered in the root zone (Gilkes et al., 1972; Wallander and Wickman, 1999). The crystal structure of unaltered biotite is characterized by a basal spacing of 10 Å (Adomo and Violante, 2000; Murakami et al., 2003). In thin section, biotite

displays various colors (brown, yellowish brown, reddish brown, olive green or green) depending on its occurrence and chemical composition (Pichler and Schmitt-Riegraf, 1993). It has a medium refraction index and a birefringence, and is characterized by golden yellow pleochroismus (Pichler and Schmitt-Riegraf, 1993). Additionally, biotite can be well distinguished by its typical "bird's eyes" structure in thin section. The morphology of biotite is similar to other micas, which are commonly characterized by cleavage planes or flakes (Welton, 1984).

In comparison with berthierine, chamosite also is an iron-rich silicate and contains magnesium in the octahedral sites. Both minerals coincide in refraction index and birefringence (Rivas-Sanchez et al., 2006). However, chamosite can be distinguished from berthierine by optical features and crystal structures. Chamosite is the ferrous iron-end member of the chlorite group (Brindley, 1982). It displays a variety of colors depending on its iron amount: green (Rivas-Sanchez et al., 2006), brown green and yellow green (Pichler and Schmitt-Riegraf, 1993). In thin section chamosite is characterized by slight pleochroisms (Pichler and Schmitt-Riegraf, 1993). Ferrous iron and magnesium dominate as cations in chamosite (besides silicon and aluminum), which can be represented by a measured formula $(Fe^{2+}_{2.8}Mg_{1.91}Al_{1.28})(Al_{1.28}Si_{2.72}O_{10})(OH)_8$ (Wiewióra et al., 1998). Additionally, it is a 2:1 layered silicate with a basal spacing of 14 Å (Ryan and Hillier, 2002; Rivas-Sanchez et al., 2006). Chamosite rims consist of small euhedral, pseudohexagonal crytals which are oriented on edge with faces and which are often arranged in a rosette pattern (Welton, 1984). Chamosite commonly forms in marine mudstone (Brindle, 1951) and sediments (Arundhathi et al., 2010), as well as in metamorphic environment characterized by a low to medium degree (Rivas-Sanchez et al., 2006). High temperature (above 90 °C) could result in compositional and structural changes of such similar iron-rich silicates, which include transformation of 7 Å berthierine-like layers to 14 Å chamosite-like layers (Ryan and Hillier, 2002).

Odinite, a green clay mineral, belongs to the serpentine group with a basal spacing of 7 Å and is chemically and structurally similar to iron chlorite (Bailey, 1988; Ryan and Reynolds Jr., 1996). Thus, it shares many of the same XRD compared to berthierine (Hornibrook and Longstaffe, 1996). The investigations performed by Bailey (1988) demonstrated that ferric iron shows absolute dominance over ferrous iron. Odinite occurs as pellets and infillings in tropical reef lagoonal areas (Bailey, 1988; Hornibrook and Longstaffe, 1996, and references therein). Additionally, it forms in tropical shallow marine sediment (Ryan and Reynolds Jr., 1996), or just at or below the seawater-sediment interface in semi-confined geochemical environments, but in shallower water (Humphreys, et al. 1989). Worden and Morad (2003) claimed that odinite occurs only in recent sediments. Bailey (1988) found that odinite is unstable in geochemical conditions which differ from its restricted environment of formation. Due to its formation environment, odinite possesses more magnesium, more silica, and markedly ferric iron compared to berthierine containing merely ferrous iron (Bailey, 1988). Therefore,

odinite cannot be precipitated from aqueous solutions under reducing conditions. It is reduced to berthierine in the iron-reduction zone (Pe-Piper and Weir-Murphy, 2008).

In comparison of other three silicate containing iron and magnesium, the investigated features of the unidentified iron-rich clay X are well consistent with berthierine (Table 7). This agreement confirms the formation of secondary berthierine in the Siri oilfield's reservoir sandstone.

4.3.4 Elemental variation

X-ray fluorescence (XRF) is used to investigate the geochemical composition of the bulk samples taken from the reservoir sandstones of the wells Siri A and Sandra A. The total inorganic carbon (TIC) content is measured in the purging gas from acid treatment. The geochemical data on major element distribution of the well Siri A are presented in Figures 47 to 49 (measured data of trace elements of the well Siri A and of the well Sandra A, see Appendix A8). The measured data illustrate a systematic variation in the content of Na_2O, K_2O, SiO_2, Al_2O_3, Fe_2O_3, MgO, CaO, MnO, Sr and total inorganic carbon (TIC), which correlates with the observed distribution of carbonate formation in the vertical direction. The different correlations with the carbonate distribution can divide the above-mentioned geochemical parameters in two groups:

(1) elements are impoverished where carbonate cementation is observed, for example sodium, potassium, silica, aluminum, iron and magnesium (Figs. 47 and 48). The measured contents of these elements remain almost constant and are higher in the oil and water legs than the measured data in the horizons characterized by carbonate cementation; and

(2) elements are enriched at depths where carbonate cement almost occupies the entire pore space, for example calcium, total inorganic carbon, manganese and strontium (Fig. 49). The measured contents of these elements remain almost constant and are much lower in the samples taken from the oil and water legs than the measured data in the horizons where carbonate cementation occurs.

In the oil and water legs which sandstones are not cemented by carbonate, the Na_2O content remains almost constant (ca. 1.1 wt.-%; Fig. 47). In contrast, the measured Na_2O content decreases to 0.5 wt.-% at the palaeo and the recent OWCs, as well as in the horizon containing carbonate clasts. A similar trend can be observed in the measured K_2O content (Fig. 47). Petrographic microscopy and SEM investigations reveal that K-feldspar and albite partly dissolved (Figs. 41 and 43). Dissolution of potassium- and sodium-bearing feldspars can liberate sodium and potassium from the sandstone to aqueous solutions, and consequently, reduces the content of sodium and potassium. However, dissolution of feldspar was observed in all samples taken from different reservoir part (oil leg, water leg and sandstones cemented by carbonate). Consequently, it follows that dissolution of sodium- and

potassium-bearing feldspar is incapable of explaining the impoverishment of the both elements at the OWCs.

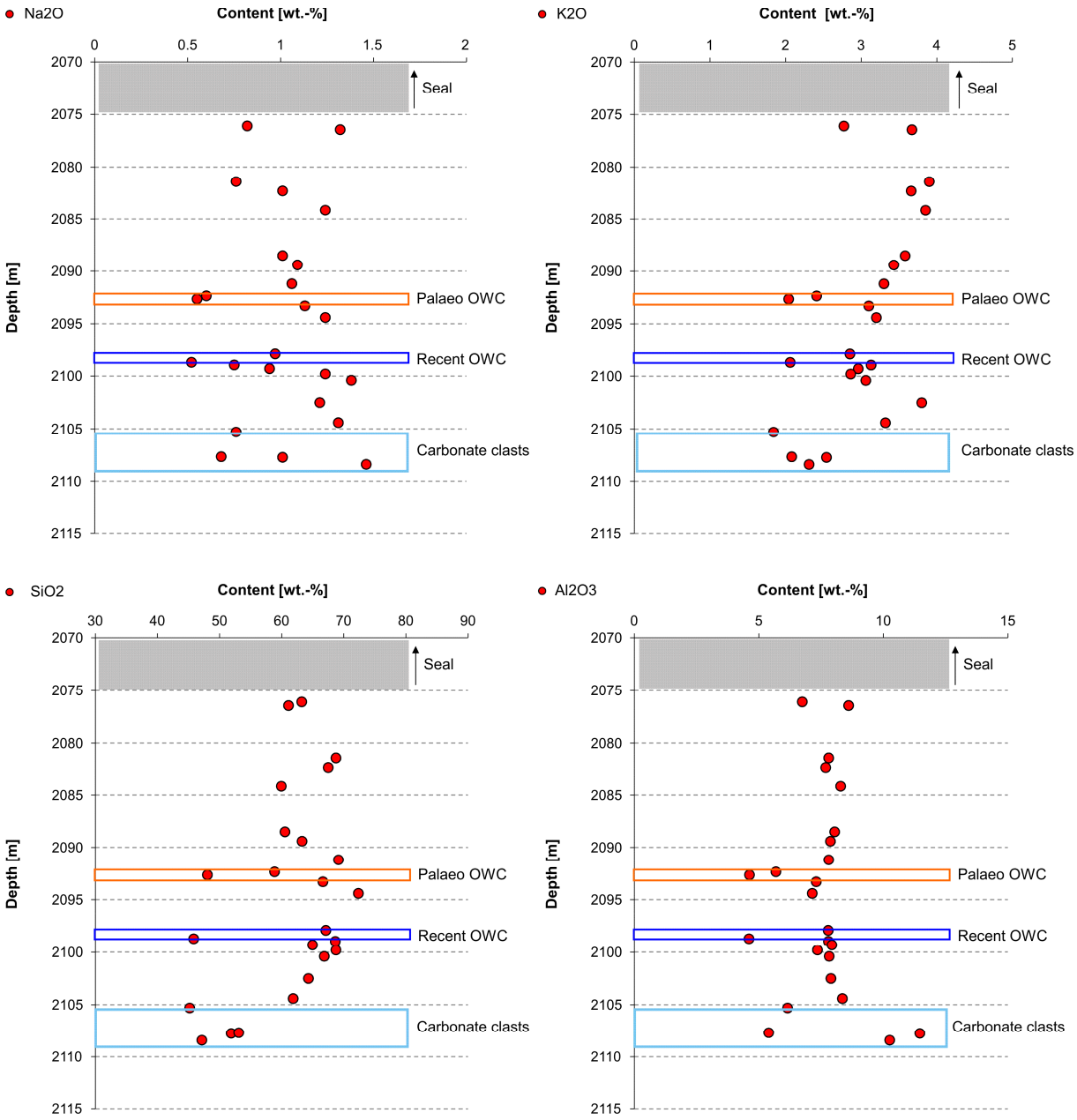

Fig. 47: Geochemical composition (content of sodium, potassium, silica and aluminum) of the bulk rock samples taken from the well Siri A and measured by XRF.

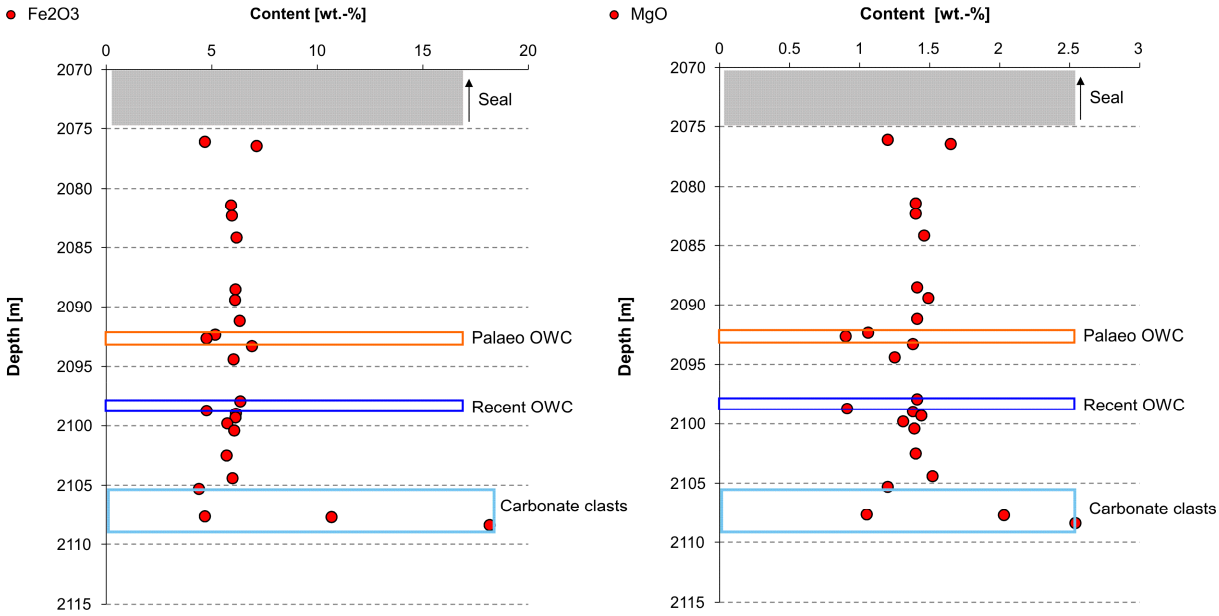

Fig. 48: Geochemical composition (content of iron and magnesium) of the bulk rock samples taken from the well Siri A and measured by XRF.

Figure 48 displays a decrease in the measured SiO_2 content in the cemented horizons by ca. 21 wt.-% (from 66 to 45 wt.-%) compared to the non-cemented horizons. Silica is a less mobile component in sediment. Dissolved silica concentration in pore water generally remains low due to establishment of equilibria among aqueous solution and minerals containing silica (e.g., quartz and clay minerals). Many silica-bearing minerals newly formed exhibit a low solubility in pore water. This leads to the less mobile character of the silica and can keep the SiO_2-content in sediment on an almost constant level, even if several silica-bearing primary minerals dissolve. This transformation among different silicate minerals (e.g., dissolution of glauconite and feldspar and precipitation of secondary quartz) merely results in a silica re-distribution in sediment, but is incapable of causing the observed impoverishment of silica. In analogy to silica, the Al_2O_3 content decreases from ca. 7.8 wt.-% in the non-cemented horizons to ca. 4.6 wt.-% in the cemented horizons. Generally, equilibration among aqueous solutions and aluminum hydroxides or aluminum silicates in the neutral pH range holds the total concentration of aluminum species in pore water on a very low level despite a great aluminum mass conversion. Thus, combining dissolution and precipitation of aluminum minerals causes insufficient aluminum loss in a closed system. The existence in the oil column and the impermeable marl formation underlying prevent effective mass transport processes. It follows that the strong impoverishment of aluminum and silica at the OWCs must have resulted from other processes in which the both components did not participate.

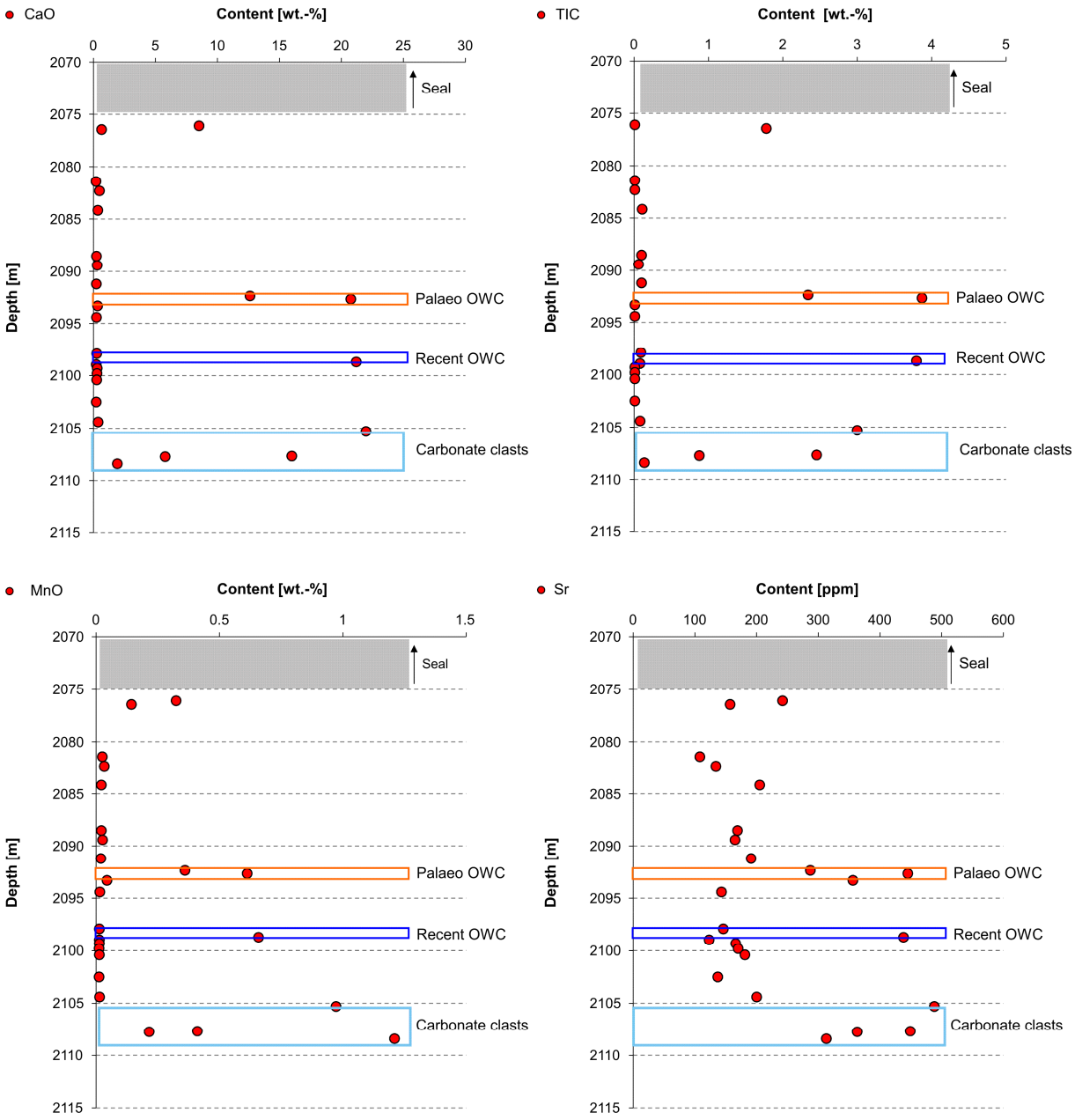

Fig. 49: Geochemical composition (content of calcium, total inorganic carbon (TIC), manganese and strontium) of the bulk rock samples taken from the well Siri A and measured by XRF.

Iron is a main element bound to glauconite and berthierine, which was proven by a combination of XRD, SEM and HRTEM. The results of XRD, SEM and HRTEM measurements show that carbonate occupying the pore space at the OWCs consists of almost pure calcite. However, iron and magnesium are commonly found as important major components of carbonate solid solutions. In comparison with other parameters (content of sodium, potassium, silica and aluminum), the Fe_2O_3 and MgO contents show a similar trend (Fig. 48). The measured Fe_2O_3 content ranges from 6.3 wt.-% in the non-cemented horizons to 4.4 wt.-% in the cemented horizons with the exception of two samples that are located in the clast horizon. These both samples additionally contain hematite and

consequently show an extremely high iron content. The measured data show a decrease in the MgO content from 1.4 wt.-% on average to 0.9 wt.-%.

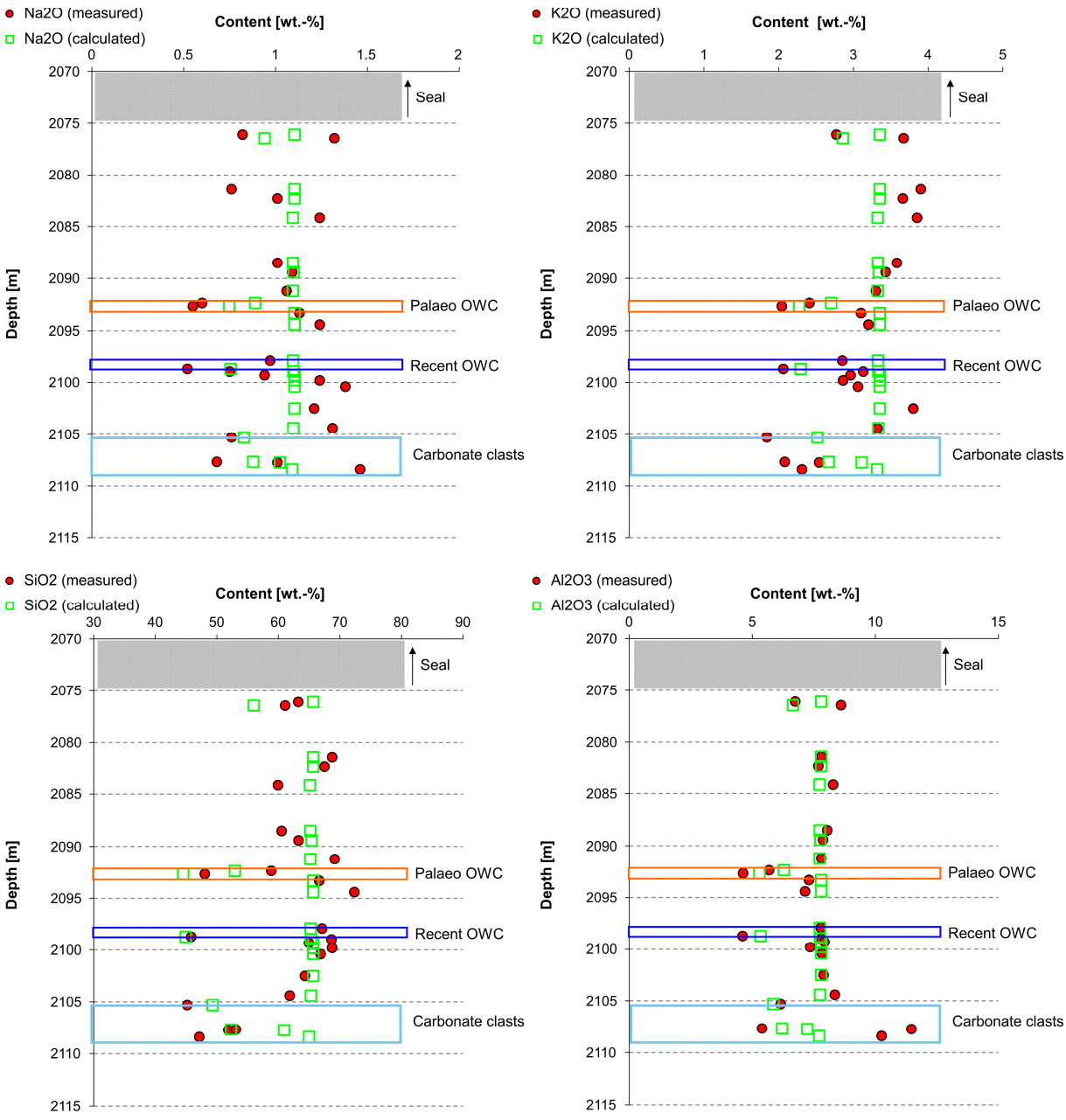

Fig. 50: Comparison between the measured contents of sodium, potassium silica, and aluminum in the well Siri A and their calculated contents with consideration of the carbonate “dilution” effect.

The measured contents of TIC, CaO, MnO and Sr provide a reverse behavior depending on the cement positions compared to the above-mentioned parameters (e.g., contents of Na_2O, K_2O): (1) enrichment in the cemented horizons, and (2) low and almost constant contents in the non-cemented horizons. The content of TIC and CaO shows the strongest enrichment at the OWCs, increasing from

<0.5 wt.-% in the non-cemented horizons to 3.9 wt.-% and 22 wt.-% in the cemented horizons, respectively (Fig. 49).

It is striking that many major components of the reservoir sandstones (e.g., SiO_2, Na_2O) are impoverished in the reservoir sandstones which pore space is completely occupied by carbonates. In comparison with such components, the four components (inorganic carbon, calcium, manganese and strontium), which are commonly bound to carbonates, display a reverse behavior. It could be assumed that the reservoir sandstones display a homogeneous distribution with respect to the mineralogical composition, as it deposited. This is because the reservoir sandstones display a limited thickness of 40 m and resulted from turbidities. The two groups of the vertical elemental distribution depending on the cement positions lead to an interest issue which processes developed the two reverse trends of the components. Carbonates formed in the reservoir rocks as cement. Neither thin section nor SEM identified any primary carbonate (except for the calcite clasts).

Precipitation of carbonate in the pore space increases the total mass of the reservoir sandstones in a given volume compared to the non-cemented sandstone. Accordingly, the addition of the carbonate cement results in a "dilution" effect on the content of the other components (e.g., SiO_2, Na_2O) that are not involved in the newly formed cement occupying the pore space (Eqs. 3 to 6; as example of the SiO_2 content). Consequently, the content of the other components must decrease. On the contrary, the content of calcium, inorganic carbon and manganese theoretically has to increase.

Prior to carbonate cementation[2]:

Measured SiO_2 wt.-% = $m(SiO_2) \times m_{tot}^{-1} \times 100\%$ (Eq. 3)

After carbonate cementation:

(Calculated) SiO_2 wt.-% = $m(SiO_2) \times [m_{tot} + m(carbonate)]^{-1} \times 100\%$ (Eq. 4)

Measured carbonate wt.-% = $m(carbonate) \times [m_{tot} + m(carbonate)]^{-1} \times 100\%$ (Eq. 5)

In consequence, after carbonate cementation:

(Calculated) SiO_2 wt.-% =

measured SiO_2 wt.-% x (1 − measured carbonate wt.-%) (Eq. 6)

Simple calculations were performed to prove the argument that the carbonate "dilution" effect is responsible for the observed variation of the component contents depending on the carbonate positions. Firstly, it is assumed that the reservoir sandstones display a homogenous distribution across prior to calcite cementation. This means that the porosity of the reservoir rocks and its mineralogical composition are independent on the sediment depth. Thus, all component contents remain constant across the main reservoir sandstone. An average content for each major component in the reservoir

[2] $m(SiO_2)$: the total SiO_2 mass (in g; bound to quartz, glauconite, and so on) in the sample prior to calcite cementation; m_{tot}: the total mass of the specified sample (in g) prior to calcite cementation; m(carbonate): the mass of calcite-dominate carbonate cement (in g).

mineral assemblage was calculated from the data measured by XRF in the water and oil legs, because the component contents slightly vary. These average component contents (e.g., m(SiO_2) in Eq. 3) were used as the initial value prior to carbonate cementation. In view of Eqs. 3 to 6, another important parameter −the mass of carbonate (m(carbonate) in the equations)− can be re-calculated from the measured TIC content and the chemical composition of the carbonate cement (97.5 mol% calcite and 2.5 mol% rhodochrosite). Other hydrogeochemical processes, which can lead to dissolution of primary minerals and which accordingly alter the component contents, are excluded in this calculation.

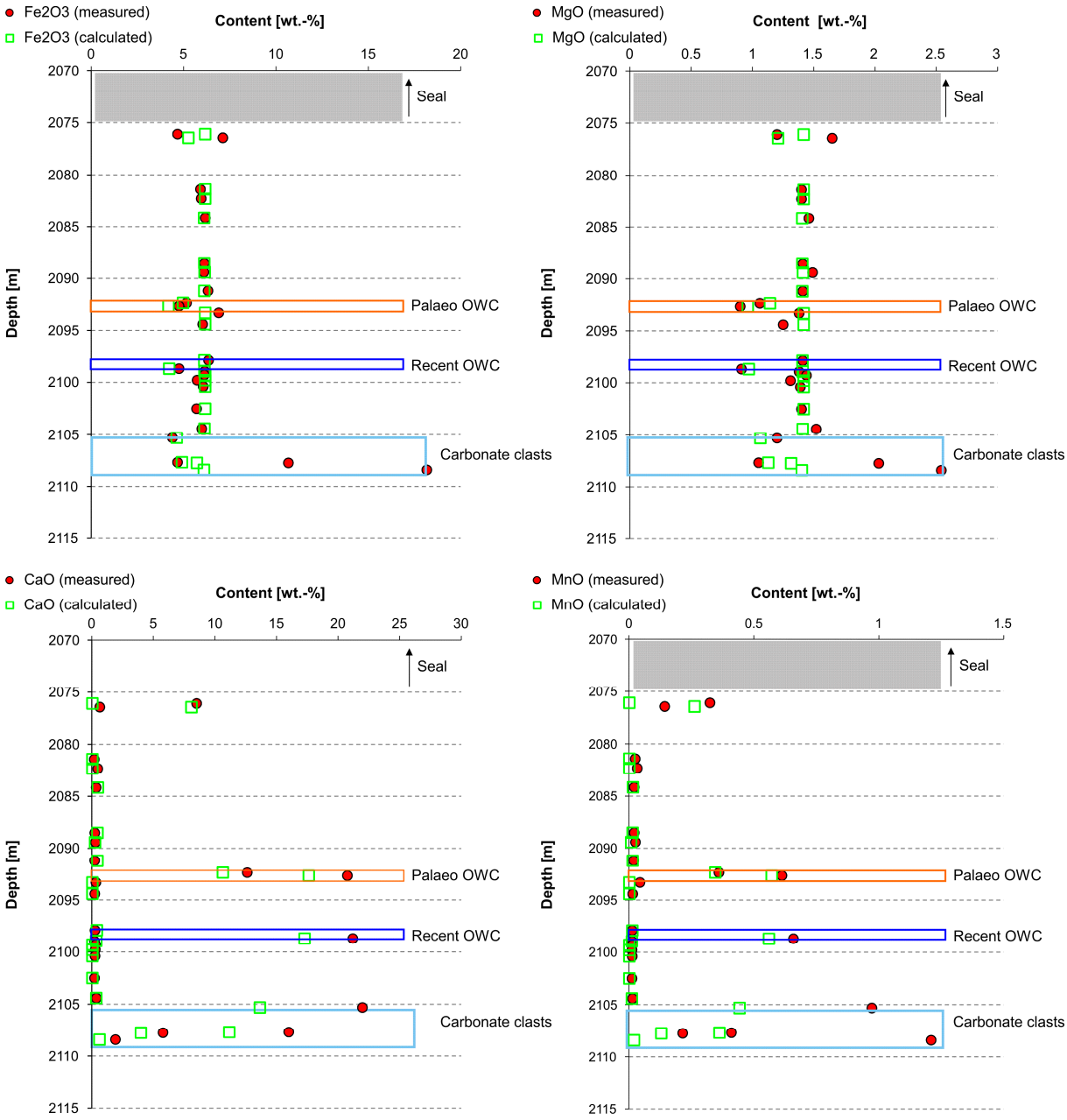

Fig. 51: Comparison between the measured contents of iron, magnesium, calcium and manganese in the well Siri A and their calculated contents with consideration of the carbonate “dilution” effect.

Figures 50 and 51 represent the calculated component contents with consideration of the pure dilution effect caused by carbonate cementation in comparison with the measured data. The most calculated contents of all major components (e.g., SiO_2, Al_2O_3, Na_2O, K_2O, Fe_2O_3, MgO, CaO and MnO) well coincide with the measured contents. The slight difference between the calculated and measured data could result (1) from a slight difference between the real component content and the assumed value prior to calcite cementation, or (2) from hydrogeochemical processes releasing components from mineral assemblage into pore water (dissolution of albite and K-feldspar observed by thin section and SEM). The calculated component contents of the clast horizon do not agree with the measured data. The samples taken from the clast horizon contain hematite. The chemical composition of the carbonate in the clast horizon was hardly measured by SEM-EDX analysis. The pore space is so strongly occupied by carbonates that no mineral grain can be recognized (Fig. 52). Consequently, the EDX analysis of the sample taken from this horizon always yields a spectrum that contains many elements with atypical peak heights. This indicates a mixing chemical composition of several minerals. Thus, these may be the reasons for the deviation from the measured component contents to the calculated values in the clast horizon.

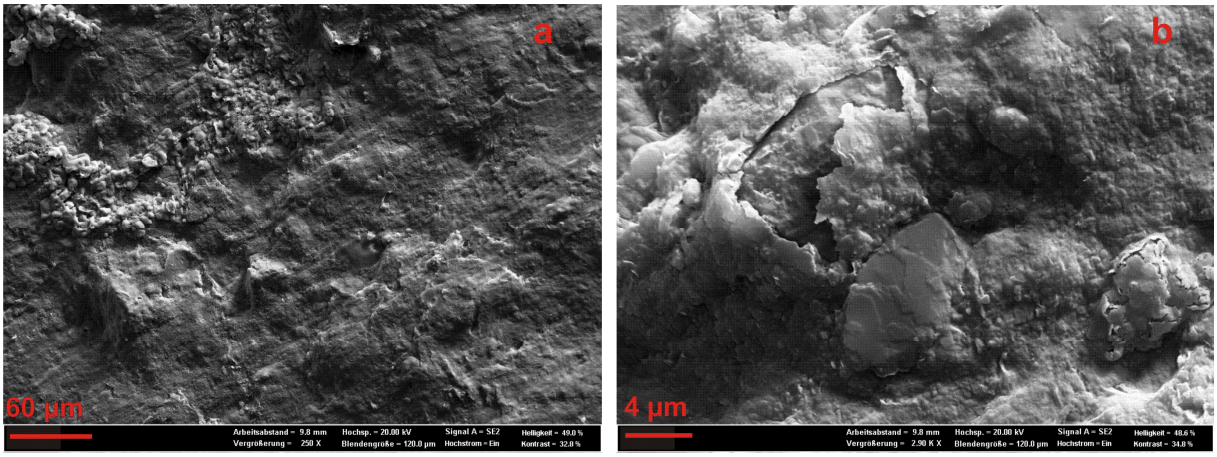

Fig. 52: SEM images of the sample (Si 5) taken from the clast horizon.

In summary, this simple calculation can prove that the decrease in content of several components in the cemented zone (the OWCs and the clast horizon) does not result from mineral dissolution. Calcite cementation causes the observed elemental variation (the enrichment and impoverishment of specific elements) correlating the positions of the calcite cement. This observed elemental variation deserves additional considerations which processes result in such animations as "their" traces in the specified reservoir parts.

5. Hydrogeochemical modeling of processes evolving in the Siri oilfield

5.1 Working hypothesis about hydrogeochemical processes

Most rock matrices of oil reservoirs can be considered to be chemically reactive. A complex hydrogeochemical reaction chain among minerals, water, oil-derived aqueous hydrocarbons and gas can be induced by a number of processes (e.g., oil degradation; seawater injection and inflow of external water by seismic pumping). Such hydrogeochemical reaction chains cause dissolution of primary minerals, precipitation of authigenic minerals, compositional alteration of pore water, and finally restructuring in-pore interfaces. By means of a series of analytical methods, the investigation results of the core samples reveal that several hydrogeochemical processes in the Siri oilfield are reflected by diagenetic alterations of different minerals: dissolution of glauconite and feldspar, as well as formation of berthierine, potassium mica, microcrystalline quartz and calcite (section 4.3.2). Dissolution of glauconite and feldspar could create secondary porosity and therefore increase the reservoir permeability. In contrast, precipitation of authigenic minerals could negatively impact the reservoir's porosity-permeability properties. Particularly, this applies to the formation of clay minerals (e.g., berthierine in this study case). Berthierine formation results in very low permeability in the Siri oilfield (Stokkendal et al., 2009). To correctly evaluate such hydrogeochemical processes and their consequences on reservoir properties, it is necessary:

(1) to specify whether any mineral can form or dissolve in the given diagenetic environments, and if so, which type and which amount of them can form or dissolve;

(2) to identify which mechanisms induce their formation or dissolution;

(3) to investigate under which specific reservoir conditions they remain stable;

(4) to predict their subsequent behavior under changed conditions; and

(5) to make plausible predictions of the spatial and temporal distribution of mineral formation and dissolution in the reservoir.

Hydrogeochemical modeling can fulfill such demands of evaluating hydrogeochemical processes of a complex water-rock-gas chemical reaction chain. Relevant hydrogeochemical processes are selected as working hypotheses based on the main the diagenetic evolution observed in the Siri oilfield's sandstones, considered as geochemical reactions, and finally, added to a hydrogeochemical model.

5.1.1 Release of methane, carbon dioxide and hydrogen

Gas formation concurs with oil formation in hydrocarbon-bearing sedimentary basins, although its mechanisms may be rather different. Generally, methane (CH_4) is the major component of gas occurrences and is partially dissolved in oil. In addition to methane, carbon dioxide (CO_2), another

common constituent of a gas phase prevailing in petroleum reservoirs, could be generated in various stages of the evolution of organic matters or originate from several inorganic interactions. The major mechanisms of gas formation in sedimentary rocks can be attributed to:

(1) early diagenetic re-mineralization of degradable organic matter (modeled by Arning et al., 2011);

(2) thermal maturation of kerogen, due to which CH_4 is a subordinate to large quantities of CO_2 (Tissot and Welte, 1987);

(3) cracking at greater depths, which causes the catagenetic stage of gas formation (CH_4 is predominant), which leads to the metagenetic stage of dry gas generation (where only CH_4 is generated; Tissot and Welte, 1987); and

(4) methanogenic hydrocarbon degradation driving formation of CH_4 and CO_2 (Jones et al., 2008).

At a relatively late step of the petroleum history, different gases can be also generated, namely when hydrocarbon is degraded by bacterial activity or by irreversible hydrolytic disproportionation (Tissot and Welte, 1987; Helgeson et al., 1993; Seewald, 2003). In comparison with static hydrocarbon systems, irreversible hydrolytic disproportionation of light paraffins in combination with maturation of crude oil preferentially occurs in young dynamic basins (Helgeson et al., 1993). In such dynamic systems, such as in flow channels and reservoirs, fluid flow consists of oil, water and gas so extensively spreads that these three components can be in pervasive contact (Helgeson, et al. 1993). A number of experiments demonstrated that hydrocarbons dissolved in aqueous solutions are of high reactivity (Seewald, 2001; Meier 2012, and references therein). The Seewald's (2003) overall reaction describes the hydrolytic disproportionation of aqueous *n*-alkanes at elevated temperature and pressure conditions (Eq. 7a). The hydrolytic disproportionation of aqueous *n*-alkanes at an elevated temperature and pressure proceeds in five steps according to Seewald (2003):

(1) dehydrogenation, which converts aqueous *n*-alkanes to aqueous *n*-alkenes;

(2) hydration, which produces 2-alkanol from the *n*-alkenes released from the first step;

(3) transformation from 2-alkanol to 2-alkanon;

(4) oxidation, which results in formation of carboxylic acids from 2-alkanon;

(5) decarboxylation, which produces *n*-alkenes characterized by a short chain, CH_4, H_2 and CO_2.

Dehydrogenation is rate determining and needs a catalyst as well as elevated temperatures (Meier et al., 2012). Seewald (2003) stated that the reactions from the first to the third step achieve a metastable thermodynamic equilibrium state of aqueous species. H_2 is involved as reaction product during the first and third reaction steps (Seewald, 2003). The activity of aqueous H_2 is of great significance and controls the concentrations of aqueous alkenes, ketones and alcohols (Seewald,

2003). On the other hand, the activity of aqueous H_2 is regulated by iron-bearing mineral assemblages (Seewald, 2003), for instance hematite used as catalyst in the experiments performed by Meier (2012). Seewald (2003) stated that the exchange of hydrogen and oxygen among aqueous alkanes, alkenes, alcohols, ketones, water and minerals rapidly proceeds with minimal kinetic barriers. Meier (2012) carried out experiments with hexadecane, deionized water, and Rotliegende sandstones (or hematite sticks) in evacuated glass tubes at 200 °C to investigate the reactions of *n*-alkanes with hematite. All intermediate oil degradation products were proven already after a short reaction time of 25 hours, such as alkenes, alcohols, aldehydes, ketones, shorter n-alkanes, carbon oxide, and carboxylic acids as iron-carboxylate (Meier, 2012). As intermediates of hydrolytic disproportionation, organic acids are commonly produced in petroleum reservoirs regardless of reservoir temperature (Barth, 1991; Helgeson et al., 1993). The water analysis results provided by Nice et al. (2000) show a high concentration of organic acids of 320 mg L^{-1} in the formation water of the Siri oilfield. Additionally, the reservoir rock mineral assemblage of the Siri oilfield is very rich in (ferric) iron-bearing mineral due to the high content of glauconite (ca. 20 wt.-% of the bulk sandstone). Consumption of hydrogen, which results from the redox-reaction with ferric iron species released by glauconite corrosion, supports the continuous progress of the entire reaction (steps 1 to 5; Meier, 2012). The both aspects, (1) the high concentration of organic acids measured in the formation water and (2) potential redox-reaction between $H_{2(aq)}$ and ferric iron species, show that oil degradation proceeded in the Siri oilfield.

Oil degradation could have triggered a series of organic-inorganic interactions which altered the chemical composition of reservoir rock assemblage, pore water, oil and gas phase (if a gas phase develops). In general, acetic acid (CH_3COOH; abbreviated as HAc) dominates. Decarboxylation of acetic acid results in additional formation of CH_4 and CO_2. In comparison to geologic time scales, this process can be considered to be slow. Thus, the acetic acid can be always proven in petroleum formation water. Equation 7a can be transferred to Equation 7b under an assumption that 2% acetic acid remains undegraded.

$$RCH_2CH_2CH_3 + 4H_2O \rightarrow R + 2CO_2 + CH_4 + 5H_2 \quad \text{(Eq. 7a)}$$

$$RCH_2CH_2CH_3 + 4H_2O \rightarrow R + 1.98CO_2 + 0.02HAc + 0.98CH_4 + 5H_2 \quad \text{(Eq. 7b)}$$

This irreversible conversion of aqueous *n*-alkanes to CO_2 and H_2 provides an additional pathway of methane formation (Eq. 8). In addition to acting as reactant of methanogenesis, carbon dioxide can provide proton and cause a decrease in pH of aqueous solutions (Eqs. 9 to 11).

$$CO_2 + 4H_2 \rightarrow CH_4 + 2H_2O \quad \text{(Eq. 8)}$$

$$CO_2 + H_2O \leftrightarrow H_2CO_3 \quad \text{(Eq. 9)}$$

$$H_2CO_3 \leftrightarrow H^+ + HCO_3^- \quad \text{(Eq. 10)}$$

$$HCO_3^- \leftrightarrow H^+ + CO_3^{2-} \quad \text{(Eq. 11)}$$

The different mechanisms mentioned above release CO_2, CH_4 and H_2, which can dissolve in water and/or oil and which could contribute to build a coexisting gas phase. The hydrogeochemical model developed in this study is incapable of distinguishing the concrete reason for the generation of CO_2, and CH_4 and H_2 which triggered a series of hydrogeochemical processes observed in the Siri oilfield. Thus, it is assumed that the reactive CO_2, and CH_4 and H_2, which are responsible for the observed diagenetic features, were conceptually generated by oil degradation. Diffusive mass transport can distribute CO_2, and CH_4 and H_2 (regarded as Oil Degradation Products; abbreviated as ODP) into formation water. Consequently, this disequilibrates the former thermodynamic equilibrium state prevailing in reservoirs preferentially by means of (1) pH-controlling H^+-transfer reactions (Eqs. 9 to 11) and (2) redox-controlling electron-transfer reactions (owing to the presence of CH_4 and H_2). Dissolution of primary and unstable minerals and precipitation of secondary and stable minerals follow these reactions until a new state of chemical equilibrium is established among minerals, pore water and gas phase.

5.1.2 Alteration of glauconite

Glauconite is the subdominant mineral in the sandstones of the Siri oilfield. Glauconite, a green mineral, is generally attributed to the mica group and exclusively forms in marine sedimentary sequences (Amouric and Parron, 1988; Mackenzie et al., 1988). The chemical composition of glauconite has been often reported in the literature and is characterized by high iron content (McRae, 1972; Thompson and However, 1975; Amouric and Parron, 1985; Mackenzie et al., 1988; and references therein). Chemical investigations of glauconite show that ferric iron shows great dominance over ferrous iron. For instance, a measured average formula for glauconite analyzed by Amouric and Parron (1985; samples taken from the eastern part of the sedimentary basin of the Ivory Coast)

$$K_{0.709}Na_{0.084}Ca_{0.043}(Al_{0.427}Fe^{3+}_{0.869}Fe^{2+}_{0.176}Mg_{0.521})(Si_{3.793}Al_{0.207})O_{10}(OH)_2$$

displays that the investigated glauconite is very rich in iron and its total iron content is even higher than its aluminum content. Additionally, more than 83 mol% of the total iron exist as ferric iron in the glauconite investigated by Amouric and Parron (1985). Besides ferric and ferrous iron, magnesium partially substitutes aluminum in octahedral sheets of glauconite. Potassium and sodium with trace amounts of calcium are embedded in the interlayer of glauconite to balance the negative charge, which is resulted from substitution (1) of silicon by aluminum in tetrahedral sheet and (2) of aluminum or ferric iron by ferrous iron and/or magnesium in octahedral sheets.

Aqueous carbon dioxide, which is produced by different pathways of organic-inorganic interactions (for detail, see section 5.5.1), can produce free H^+-ions via dissociation of carbonic acid and result in pH decrease (Eqs. 9 to 11). This change in pH disequilibrates the thermodynamic

equilibrium states formerly prevailing in the reservoir. Different mineral phases (e.g., micas, feldspars, carbonates and hydroxides) are sensitive to the change in pH and can consequently dissolve depending on their pH buffering level. For instance, the pH decrease triggered by CO_2 release can be buffered by alteration of glauconite. In the Siri oilfield, glauconite dissolution is one of widespread diagenetic mineral alterations observed by petrographic investigations in all core samples of the wells Siri A and Sandra A (in the water and the oil leg and at OWCs; for details, see section 4.3). As a result, cations (potassium, sodium, calcium, magnesium, ferric and ferrous iron), hydrated aluminum species ($Al(OH)_4^-$) and dissolved silica species (H_4SiO_4) can be released in aqueous solutions (Eq. 12 as an example for an assumed chemical composition of glauconite in the reservoir sandstone).

$$K_{0.709}Na_{0.084}Ca_{0.066}Mg_{0.521}Al_{0.634}Fe_{1.045}Si_{3.793}O_{10}(OH)_2 + 10H_2O \leftrightarrow$$
$$0.709K^+ + 0.084Na^+ + 0.066Ca^{2+} + 0.521Mg^{2+} + 0.634Al(OH)_4^- + 0.869Fe^{3+} + 0.176Fe^{2+} + 3.793H_4SiO_4 + 4.292OH^- \quad \text{(Eq. 12)}$$

$$8Fe^{3+} + CH_{4(aq)} + 2H_2O \rightarrow 8Fe^{2+} + CO_{2(aq)} + 8H^+ \quad \text{(Eq. 13)}$$

Under unaltered redox-conditions of the hydrogeochemical environment, in other words, without addition of any oxidizing or reducing agents, the activity of ferric iron could be more or less controlled by precipitation of ferric iron hydroxides in a neutral pH rang. If this is the case, ferric iron species in aqueous solutions are incapable of being efficiently consumed; in other words, the activity of ferric iron cannot be properly reduced. Thus, dissociation of glauconite (Eq. 12) will be quickly subdued and even stopped. Nevertheless, another oil degradation product methane can reduce the ferric iron ions and be converted into carbon dioxide (Eq. 13). This redox-reaction, on the one hand, consumes the ferric iron species, on the other hand, can deliver additional CO_2 besides the CO_2 generated from organic matter. Ultimately, this process can strongly drive glauconite alteration compared to oxidized conditions. In summary, reduction of ferric iron to ferrous iron is of crucial relevance and even is indispensable to prove a detectable intensity of glauconite alteration by using analytical methods. This consideration will be checked for plausibility by hydrogeochemical modeling based on chemical equilibrium of thermodynamics (see section 5.2).

5.1.3 Corrosion of feldspar

Besides glauconite, feldspar provides a significant contribution to the primary mineral assemblage in the Siri oilfield's rock matrix. The primary mineral is defined in this study as mineral that is present in the reservoir mineral assemblage prior to organic-inorganic interactions. Different feldspar types are proven by XRD, including K-feldspar, albite and low-calcium albite (for details, see section 4.3). Van Berk et al. (2009) stated by using hydrogeochemical modeling that anorthite provides a high pH buffering level compared to albite and K-feldspar. The pH level resulting from

acidity production by interactions between $CO_{2(aq)}$ and water (Eqs. 9 to 11) can be controlled by equilibrium reactions of feldspar at temperatures <110−140 °C (van Berk et al., 2009; Eqs. 14 to 16). The hydrogeochemical modeling results from van Berk et al. (2009, 2013) demonstrate that different feldspars provide different pH buffering capacities to control pCO_2 level in siliciclastic hydrocarbon reservoirs. Anorthite will firstly dissolve, which concur with a stability of K-feldspar (van Berk et al., 2013). After anorthite depletion, ongoing supply of CO_2 (regardless its origins) will induce massive dissolution of albite, and finally dissolution of K-feldspar (van Berk et al., 2009).

$$CaAl_2Si_2O_{8(anorthite)} + 8H_2O \leftrightarrow Ca^{2+} + 2Al(OH)_4^- + 2H_4SiO_4 \quad \text{(Eq. 14)}$$

$$NaAlSi_3O_{8(albite)} + 8H_2O \leftrightarrow Na^+ + Al(OH)_4^- + 3H_4SiO_4 \quad \text{(Eq. 15)}$$

$$KAlSi_3O_{8(K\text{-}feldspar)} + 8H_2O \leftrightarrow K^+ + Al(OH)_4^- + 3H_4SiO_4 \quad \text{(Eq. 16)}$$

Petrographic observations of the core samples of the well Siri A demonstrate strong dissolution of albite and K-feldspar (see section 4.3). Thus, it is reasonable to argue that anorthite was present in the Siri oilfield's reservoir sandstones and its available part completely dissolved by chemical reactions. Dissolution of feldspar play an important role of a complex web of hydrogeochemical interactions in the Siri oilfield, and consequently, has to be integrated in a hydrogeochemical model.

5.1.4 Formation of berthierine

Petrographic and SEM investigations clearly display that glauconite alteration was observed in all core samples. Alteration of glauconite releases aqueous ferric iron, magnesium, aluminum and silica species into the formation water owing to CO_2 provided by oil degradation. Additionally, the oil degradation products CH_4 and H_2 can reduce ferric iron species to ferrous iron species. Additional silica and aluminum species can be released by dissolution of feldspar, which was proven by petrographic microscopy and SEM. This enrichment of various aqueous species in pore water could lead to an oversaturation regarding to other minerals, for instance to berthierine. This oversaturation allows berthierine formation in the reservoir sandstone. Petrographic and SEM investigations reveal that glauconite alteration is always accompanied by formation of an olive to brown iron-rich mineral. This mineral is identified as berthierine by combination of different analytical methods (for details see section 4.3.3). The morphological relations provided by petrographic observations between the primary glauconite grains and the authigenic berthierine crystals suggest that berthierine formation results from glauconite alteration. Therefore, berthierine is chosen as a potential secondary mineral in the mineral assemblages, when the co-existing aqueous solution achieves saturation regarding to berthierine.

Berthierine is a mixture of the magnesium- and the ferrous iron-end member of the serpentine group. The chemical composition of berthierine depends on its depositional environment which is hydrogeochemically characterized by pH-E_H conditions as well as the aqueous activities of ferrous iron, magnesium, aluminum and silica of the aqueous solution. Additionally, berthierine is commonly considered as the solid solutions consisting of the pure ferrous iron and magnesium serpentine mineral end members. Therefore, berthierine displays a variable composition. By using electron microprobe, Stokkendal et al. (2009) analyzed the chemical composition of berthierine which formed in the wells Siri 3 and 4. Their measurements reveal that the chemical composition of berthierine precipitated in the glauconitic sandstones reservoir approximates $Fe_{1.738}Mg_{0.417}Al_{0.95}Si_{1.71}O_5(OH)_4$. In this study HRTEM was used to determine the chemical composition of berthierine and its basal space. HRTEM investigated berthierine in the sample Si 15 taken from the recent OWC. EDX analyses of HRTEM shows that the newly formed berthierine is characterized by the following chemical composition: $Fe_{1.639}Mg_{0.283}Al_{1.4}Si_{1.489}O_5(OH)_4$. This chemical composition of the berthierine investigated in the sample Si 15 slightly deviates from the data provided by Stokkendal et al. (2009). Nevertheless, these measurements display that ferrous iron shows dominance in the newly formed berthierine and even over silica. Due to the limited number of the measured chemical composition of berthierine from the well Siri A, the chemical composition of berthierine investigated by Stokkendal et al. (2009) is used as the composition of berthierine for hydrogeochemical modeling. An alternative scenario considering the chemical composition of berthierine measured in the well Siri A will test whether the chemical composition of berthierine used in the hydrogeochemical modeling affects the calculated mineral behaviors and mineral conversion, and if so, how intensively.

Berthierine precipitation results from glauconite dissolution. Thus, when one mole of glauconite ($K_{0.489}Na_{0.045}Mg_{0.281}Al_{1.387}Fe_{1.183}Si_{3.327}O_{10}(OH)_2$; the average chemical composition analyzed by SEM in the well Siri A) completely dissolve, all ferrous iron ions (including ferrous irons originating from the reduction of ferric iron ions by methane) can be removed from aqueous solutions by berthierine formation owing to its low solubility (see sections 5.2.2 and 5.2.3). Correspondingly, ca. 0.68 mole berthierine, which is characterized by the composition measured by Stockkendal et al. (2009), can form. Consequently, the formation of 0.68 mole berthierine consumes 1.16 moles silica species, 0.28 mole magnesium ions, and 0.65 mole aluminum ions. Therefore, this berthierine formation results in an excess of potassium, sodium, aluminum and silica species in aqueous solutions (Table 8). This excess alters the chemical composition of aqueous solutions, and consequently, leads to establish a new equilibrium state among the aqueous solution and other minerals. Thus, additional hydrogeochemical processes will be induced.

Table 8: Mass transfer of components due to glauconite dissolution and berthierine formation.

	Release of components due to 1.0 mole glauconite dissolution [mol]	Consumption of components due 0.68 mole berthierine formation [mol]	Balance of components [mol]
K	0.489	0.000	0.489
Na	0.045	0.000	0.045
Fe	1.183	1.183	0.000
Mg	0.281	0.284	-0.003
Al	1.387	0.647	0.740
Si	3.327	1.164	2.163
O	12.000	6.126	5.874
H	2.000	2.723	-0.723

5.1.5 Formation of microcrystalline quartz

Several hydrogeochemical processes, including dissolution of glauconite and feldspar, intensively release aqueous H_4SiO_4 species in aqueous solutions (Eqs. 12, and 14 to 16). Mass balances show a silica excess in aqueous solutions caused by these processes, although a part of silica species can be consumed by berthierine formation (Table. 8). Thus, the aqueous silica concentration ($c_{tot}SiO_{2(aq)}$) will increase. Various hydrogeochemical processes involving silica-containing minerals can control the level of $c_{tot}SiO_{2(aq)}$. One of the common pathways is precipitation of secondary silica minerals ($SiO_{2(s)}$) which was proven by analytical methods in the Siri oilfield (see section. 4.3.2; Eq. 17).

$$2H2O + SiO_{2(s)} \leftrightarrow H_4SiO_4 \qquad \text{(Eq. 17)}$$

Silica-rich aqueous solutions undergo different diagenetic environments and cause formation of $SiO_{2(s)}$ minerals, which are distinguished by different crystal structures and characterized by various “crystal” size. Thus, such $SiO_{2(s)}$ minerals show different solubilities. Under conditions of 25 °C and 1 atm, quartz has a lower solubility (log K = −3.98; according to the thermodynamic database Phreeqc.dat provided by Parkhurst and Appelo, 2013) compared to chalcedony (log K= −3.55 according the Phreeqc.dat database from Parkhurst and Appelo, 2013) and microcrystalline quartz characterized by a grain size of 0.1 µm (log K = −3.857; investigated by Azaroual et al., 1997). The solubility constant of a mineral phase determines its mass conversion due to precipitation. SEM investigations display that the secondary $SiO_{2(s)}$ mineral forms in the well Siri 1 with various “crystal textures” and is characterized by different grain sizes: from quartz overgrowth to fine quartz crystals. The secondary fine quartz crystals can have a grain size from <0.5 to ca. 3.0 µm (section 4.3.2). Larger quartz crystals could show a grain size up to 10 µm. The hydrogeochemical model uses the

$SiO_{2(s)}$ mineral with an average grain size of 5 µm as secondary mineral, which can be attributed to chalcedony (Lee, www.geos.ed.ac.uk/homes/s0789516/ microsilica.pdf).

5.1.6 Formation of muscovite

Muscovite ($KAl_3Si_3O_{10}(OH)_2$) can form at low temperature conditions (Dapples, 1967). Muscovite preferentially forms in glauconite sandstones and establishes equilibrium with glauconite, which may be results of potassium-containing in the lattice of micas (Dapples, 1967). Results from petrographic investigations of the core samples (well Siri A) are consistent with the observations provided by Dapples (1967) that local patches of newly formed muscovite occur within glauconite grains (Fig. 44).

Dissolution of glauconite and potassium feldspar is capable of delivering different species to the pore water (potassium, aluminum, silica and iron with trace amounts of sodium; Eq. 12). These components can be partially removed from the pore water by precipitation of berthierine and $SiO_{2(s)}$. However, the high potassium activity and the excess of aluminum and silica species, which are not incorporated to berthierine and $SiO_{2(s)}$, could lead to an oversaturation of the pore water with respect to muscovite. Muscovite formation can control the concentrations of potassium, aluminum and silica, as well as pH (Eq. 18). Consequently, this process additionally triggers glauconite alteration and dissolution of feldspar depending on pH-E_H conditions, until the formation water establishes a new equilibrium state among all minerals and pore water. In combination with the petrographic observations, this suggests that muscovite should be allowed to precipitate as secondary mineral in the hydrogeochemical model, when its saturation is achieved.

$$K^+ + 3Al^{3+} + 3H4SiO_4 \leftrightarrow KAl_3Si_3O_{10}(OH)_{2(muscovite)} + 10H^+ \qquad \text{(Eq. 18)}$$

5.1.7 Calcite cementation

Calcium ions can be released in aqueous solutions by dissolution of glauconite and calcium-bearing plagioclase (anorthite). The continuous supply of carbonate species (CO_3^{2-}), produced by buffering of carbonic acid due to dissolution of glauconite and feldspar, could cause oversaturation with regard to calcite. Subsequently, calcite can form (Eq. 19). Calcite-dominating carbonate has been proven in the several samples from the well Siri A by analytical methods, but its distribution is restricted to the specific reservoir parts (section 4.3.2). Strong calcite cementation was observed at the recent and palaeo OWCs. Thus, the hydrogeochemical model considers calcite as secondary mineral phase. Although magnesium and iron can be partially removed by berthierine formation, the release of magnesium and iron ions induced by glauconite alteration could lead to an oversaturation in the pore

water with regard to siderite and dolomite (Eqs. 20 and 21). Consequently, the both carbonate minerals are also chosen as potential secondary mineral in the model. Nevertheless, calcite is the single carbonate mineral that has been proven in the specific horizon of the well Siri A. Manganese was proven in glauconite and in carbonate with trace amounts. However, the glauconite used as primary mineral in the hydrogeochemical model does not contain manganses. Additionally, pore water and any other minerals in the model are free of manganese. Consequently, rhodochrosite ($MnCO_3$) is excluded from the list of the secondary minerals.

$$Ca^{2+} + CO_3^{2-} \leftrightarrow CaCO_{3(s,\ calcite)} \quad \text{(Eq. 19)}$$

$$Ca^{2+} + Mg^{2+} + 2CO_3^{2-} \leftrightarrow CaMg(CO_3)_{2(s,\ dolomite)} \quad \text{(Eq. 20)}$$

$$Fe^{2+} + CO_3^{2-} \leftrightarrow FeCO_{3(s,\ siderite)} \quad \text{(Eq. 21)}$$

In summary, all hydrogeochemical processes mentioned in section 5.1 in combination with dissociations of all aqueous complexes of involved components build up a complex hydrogeochemical reaction chain in which all processes influence each other. Thus, all of them should be integrated in any hydrogeochemical model to correctly reproduce such hydrogeochemical processes.

5.2 Zero-dimensional hydrogeochemical modeling

A zero-dimensional hydrogeochemical model (batch-reaction model) consists of only one individual hydrogeochemical reactor. In this reactor, a specified driving force induces hydrogeochemical processes among pore water, mineral phases of the porous rock matrix and a co-existing gas phase at clearly defined starting conditions, until a new equilibrium state is established. The batch-reaction model developed in this study is based on thermodynamics of chemical equilibrium without consideration of any temporal, spatial and kinetic aspects. Consequently, it is not the aim of the batch-reaction modeling to correctly quantitatively reproduce the mineral conversions investigated by petrographic microscope und SEM. Indeed, a batch-reaction modeling should demonstrate:

(1) which reaction mechanism causes dissolution of primary minerals,

(2) which secondary minerals can be consequently precipitated, and

(3) under which specified pH-E_H conditions.

Understanding the hydrogeochemical processes is one of indispensable prerequisites for the setup of a plausible 1D or even a 3D hydrogeochemical transport model.

5.2.1 Conceptual model

Berthierine formation is one of most important diagenetic features observed in the Siri oilfield's reservoir sandstone. Stokkendal et al. (2009) suggested that inflow of an iron-rich brine into the glauconitic Siri oilfield's rock matrix was a significant contributor to an enrichment in ferrous iron needed for berthierine formation. However, they presented no further information regarding the chemical composition of this iron-rich brine. The petrographic observations clearly show that berthierine is precipitated in all samples of the wells Siri A and Sandra A. Thus, it can follow that berthierine formation is not restricted to a specific depth or region of the Siri oilfield's reservoir sandstones. On the contrary, it is a common diagenetic feature spreading over the entire reservoir sandstones. This therefore indicates that it is not likely that inflow of such an iron-rich brine caused the spreading berthierine formation in an open system. The mineral assemblage of the Siri oilfield's reservoir sandstones is rich in iron, magnesium, aluminum and silica which are the necessary components of berthierine. Consequently, it should deserve to consider whether berthierine formation occurred *in situ* due to mineral transformation in such a system. Therefore, a zero-dimensional hydrogeochemical model is developed in this study to test this working hypothesis.

The hydrogeochemical behavior of glauconite depending on the pH-E_H conditions and the hydrogeochemical consequences of glauconite dissolution are still unclear. The petrographic observations indicate that glauconite dissolution may lead to precipitation of berthierine and muscovite (section 4.3.2). Thus, the batch modeling exclusively aims to qualitatively identify the hydrogeochemical mechanisms that cause berthierine formation in glauconitic sandstones. Correspondingly, the batch model simplifies the Siri oilfield's reservoir rock matrix and only considers glauconite as the primary mineral for berthierine formation. This is because glauconite is the only primary mineral in the reservoir rocks that contains iron and magnesium. One alternative modeling scenario includes anorthite as an additional primary mineral phase besides glauconite. This scenario aims to test whether dissolution of glauconite and anorthite observed in the Siri oilfield's reservoir sandstones is responsible for the massive calcite cementation observed at the OWCs.

The behavior of other primary minerals (e.g., albite, K-feldspar) in petroleum systems was well investigated by other research studies. Van Berk et al. (2009, 2013) showed by using hydrogeochemical modeling that albite dissolves due to dissolution of $CO_{2(g)}$ in aqueous solution prior to K-feldspar. Feldspar dissolution leads to formation of secondary $SiO_{2(g)}$, to precipitation of different carbonates depending on the primary minerals and on the $pCO_{2(g)}$ level, and to kaolinite formation (van Berk et al., 2009, 2010 and 2013). Thus, the equilibration of such primary minerals (e.g., K-feldspar, albite) with the pore water is suppressed in the batch modeling. Fu et al. (2013b) stated that any reasonable hydrogeochemical model should not isolate processes specifically selected, but integrate all relevant processes. Consequently, the hydrogeochemical behavior of other primary

minerals and their consequence will be investigated in the 1D hydrogeochemical transport modeling in addition to glauconite and anorthite (section 5.3).

Glauconite contains OH-groups and ferric iron. Therefore, glauconite dissolution can be induced by proton- and/or electron transfer reactions according to pH-E_H conditions. In consequence, it can deliver the necessary components for berthierine formation. A broad range of the pH-E_H conditions are established by stepwise addition of two groups of different substances to the reactor. In the first modeling scenario, hydrochloric acid (HCl) is added in the pore water of the reactor, although no natural mechanism can add HCl in an oil reservoir. This artificial addition of HCl aims to create an acidic-oxidizing condition to test whether such a hydrogeochemical condition can lead to the observed significant glauconite dissolution (ca. 30% of the primary glauconite; assumed from petrographic investigations; see sections 4.3.2 and 5.2.2). The oxidizing condition is established by release of ferric iron due to glauconite dissolution, although no other individual oxidants are added in the pore water. In the other modeling scenarios, CO_2, CH_4 and H_2 (and HAc) are typical reactants produced in a petroleum system by various pathways. One typical pathway is the hydrolytic disproportionation of aqueous *n*-alkanes at elevated temperature and pressure conditions according to Seewald (2003; Eq. 7). Dissolution of CH_4 and H_2 in the pore water establishes reducing conditions. Reduction of ferric iron bound to glauconite by methane can release free H^+-ions and carbonic acid (Eq. 13). Thus, no addition of other acids is needed in this scenario. Addition of different substances in the pore water results in establishment of a new equilibrium state, and consequently in dissolution of primary minerals and/or in precipitation of secondary minerals.

5.2.2 Mineral assemblage

Sandstones in the Siri oilfield exhibit a high content of primary quartz (ca. 65 wt.-% of the bulk rock assumed on the basis of the results of petrographic microscopy; this also applies to the amount of other minerals). Primary quartz is allowed exclusively to dissolve. Secondary $SiO_{2(s)}$ is considered as chalcedony which display a higher solubility compared to quartz at the same temperature and pressure conditions. Unaltered glauconite is the subdominant mineral in the reservoir mineral assemblage and comprises ca. 25 wt.-% of the bulk rock prior to any organic-inorganic interaction. The petrographic observations demonstrate that primary glauconite grains of the Siri oilfield's rock matrix display different degrees of alteration: hardly altered, less altered, strongly transformed, and almost completely dissolved (for detail, see section 4.3.2). This indicates that not all primary glauconite grains are chemically reactive. Therefore, it is assumed that 30% of the total primary glauconite is available for the mineral transformation within the pore water reactor. Moreover, the primary mineral assemblage comprises all three feldspar types (K-feldspar. albite, anorthite) at starting conditions prior to oil degradation, although only K-feldspar and albite were identified (section 4.3.2). Feldspars are

sensitive to changes in pH of aqueous solutions and can buffer pH due to production of acids (e.g., carbonic acid, acetic acid; van Berk et al., 2009). It is assumed that primary anorthite occurred at starting conditions and its reactive part completely dissolved during the organic-interaction interactions (see section 5.1.3). The content of feldspars at starting conditions is unknown. Most glauconitic sandstones are deposited in marine environments (Pettijohn et al., 1987). The glauconitic sandstones of the Alberta Basin (5% glauconite) comprise ca. 3% feldspars including K-feldspar and plagioclase (Gunter et al., 2000). Thus, it is estimated that the glauconitic reservoir sandstones may contain less feldspar compared to siliciclastic reservoir sandstones. In this model, it is assumed that the primary mineral assemblage comprises 5 wt.-% feldspars including K-feldspar, albite and anorthite at the starting conditions. Primary muscovite occurs in trace amounts (estimated of 1.0 wt.-%), although muscovite potentially forms as secondary mineral (see section 5.1.6). Trace amounts of pyrite, rock fragments and several unidentified minerals are neglected in this study. The batch modeling aims to test whether berthierine can potentially form from glauconite dissolution. Thus, equilibration reactions among other primary minerals (e.g., albite, K-feldspar) and pore water are unconsidered in the batch modeling. The impacts of other primary minerals excluding from the batch modeling are tested in the 1D hydrogeochemical transport model (section 5.3).

The conceptual batch model considers a closed reactor with a pore volume of 1.0 L and a total volume of 3.0 L (33% porosity; assumed from the observations of the petrographic microcopy). The pore volume is filled with a generic one molal sodium chloride solution under the reservoir conditions (78 °C and 230 atm; Nice et al., 2000). A primary mineral phase assemblage occupies the remaining 2.0 L of the total reactor and accounts for 5.3 kg with consideration of the bulk density of 2.65 kg L^{-1}. It is assumed that the primary mineral assemblage comprises 7.5 wt.-% reactive glauconite and 5.0 wt.-% feldspars. Additionally, these 5 wt.-% feldspars are assumed to consist only of anorthite in the batch modeling to amplify the effects of anorthite dissolution on formation of secondary calcite. This is because the amount of anorthite at starting conditions prior to oil degradation is unknown. On the other hand, the batch modeling aims to demonstrate whether dissolution of the only calcium source term anorthite (besides the trace amounts of calcium bound to glauconite) is responsible for calcite formation observed at the OWCs. The effects of the correct mineralogical composition (e.g., K-feldspar and albite) on the hydrogeochemical reaction chain are tested in the one-dimensional transport modeling (see section 5.3). Correspondingly, the reactor contains ca. 0.95 mole glauconite (slightly depending on the chemical composition of the tested glauconite) or additionally with 0.76 mole anorthite (depending on the modeling scenarios). The other minerals are considered as non-reactive mineral phases. They are thus excluded from the hydrogeochemical reaction chain evolving in this reactor. This primary mineral assemblage equilibrates with the pore water (one molal NaCl-solution) prior to any processes. Several secondary minerals do not exist in the reactor at starting conditions, but are allowed to form, as addition of substances alters the chemical composition of the

pore water and triggers additional processes (Table 9). The PHREEQCI input file for scenario Gl1_ODP is documented in Appendix A9 as example.

Addition of different substances breaks the original equilibrium state developing among the primary minerals and the pore water. Consequently, secondary mineral phases can be allowed to precipitate. Dissolution of glauconite and anorthite releases species of potassium, sodium, ferric and ferrous iron, magnesium, aluminum and silica into the pore water. Moreover, addition of CO_2 and CH_4 produces carbonate species ($CH_{4(aq)}$, $CO_{2(aq)}$, HCO_3^-, and/or CO_3^{2-} depending on the pH-E_H conditions). Consequently, the thereby triggered changes in the chemical composition of the aqueous solution can potentially lead to an oversaturation with regard to berthierine, muscovite, chalcedony, kaolinite, $Fe(OH)_{3(a)}$, calcite, siderite, and dolomite (Table 9). Additionally, increasing the amount of CO_2 and CH_4 could results in development of a gas phase coexisting in the reactor.

Table 9: Pre-assigned reactive primary minerals, secondary minerals and addition of different substances controlling pH-E_H conditions in different scenarios of the batch modeling at starting conditions.

	Mineral assemblage														Addition of	
	Primary minerals			Secondary minerals												
	Gl1	Gl2	Ano	Be	Be2	Mu	Ch	Ka	FO	Cc	Si	Do	Ma	Chl	HCl	ODP
Gl1_HCl	x			x		x	x	x	x					x	x	
Gl1_ODP	x			x		x	x	x	x	x	x	x	x	x		x
Gl1_ODP_HAc	x			x		x	x	x	x	x	x	x	x	x		x+HAc
Gl2_ODP		x		x		x	x	x	x	x	x	x	x	x		x
Gl1_Be2_ODP	x				x	x	x	x	x	x	x	x	x	x		x
Gl1_Ano_ODP	x		x	x		x	x	x	x	x	x	x	x	x		x

x indicating mineral phase included in the scenario or the substance added in the pore water; Gl: glauconite; 1 and 2: two different chemical compositions of glauconite or berthierine; Ano: anorthite; Be: berthierine; Mu: muscovite; Ch: chalcedony; Ka: kaolinite; FO: $Fe(OH)_{3(a)}$; Cc: calcite; Si: siderite; Do: dolomite; Ma: magnesite; Chl: chlorite7A; ODP: oil degradation products: CH_4, CO_2 and H_2; HAc: Acetic acid.

The computer code PHREEQCI (Parkhurst and Appelo, 2013) is the modeling tool to calculate the equilibrium of species distribution among aqueous solutions, minerals, and gas phase based on the chemical equilibrium of thermodynamics. The thermodynamic database Phreeqc.dat (Parkhurst and Appelo, 2013) includes the equilibrium constants of species dissociation and/or association, as well as the solubility constants of gas and of minerals except for berthierine and glauconite. It additionally involves the temperature dependence of the constants of such chemical reactions. Moreover, molar volumes of solids and parameters for defining the specific volume of aqueous species were entered in PHREEQCI as a function of temperature, pressure, and ionic strength with the Redlich-type equation (Parkhurst and Appelo, 2013). Thus, PHREEQCI can calculate the pressure effects on chemical

reactions and on the density of aqueous solutions (Parkhurst and Appelo, 2013). Implementation of the Peng-Robinson equation of state achieves calculations of the solubility of gases at high pressure conditions (Parkhurst and Appelo, 2013).

The thermodynamic data of berthierine and glauconite, which are not involved in the database Phreeqc.dat, must be defined in the input file. Berthierine is not characterized by an identical chemical composition. Thus, its solubility constant and the corresponding temperature dependence slightly vary in its chemical composition. This also applies to glauconite. The solubility constant (log K) of minerals at the standard conditions (25 °C and 1 atm) can be calculated from the change in the Gibbs free energy (ΔG) of their corresponding reactions. The van't Hoff expression with consideration of the standard enthalpy of reaction (ΔH) can calculate temperature effects on the solubility constants. The Gibbs free energy (G_f^0) and enthalpy (H_f^0) from elements for berthierine and glauconite are needed to calculate ΔG and ΔH of the equilibration reactions of the both minerals. In this study, G_f^0 and H_f^0 for berthierine and glauconite are calculated by a predictive model for estimating the enthalpies and the Gibbs free energy of phyllosilicates based on their chemical composition and crystal structures (Vieillard, 2007; Vieillard and Mathieu, 2009; Vieillard et al., 2011; and references therein). In analogy to carbonate or sulfate solid solutions ($Ca_xMg_yFe_{(1-x-y)}CO_3$ and $Ba_xSr_{(1-x)}SO_4$), berthierine can be considered as solid solutions consisting of pure iron- and magnesium serpentine end-members. In general, the chemical composition of such solid solutions develops with the alteration of the chemical composition of the pore water. However, it is assumed that the chemical composition of newly formed berthierine in the model remains unchanged regardless of the compositional development of the pore water. The average chemical composition of berthierine measured by Stokkendal et al. (2009) is use as the composition of newly formed berthierine in the model (Eq. 21). The results of SEM investigations show that most glauconite grains more or less display alteration intensity or are coated by secondary berthierine. Glauconite provides a cation exchange capacity commonly measured in the range of 10 to 40 milliequivalents per 100 gram glauconite (Manghnant and Hower, 1964; and references therein). Such processes make an exact determination of the chemical composition of glauconite difficult. Thus, the batch modeling considers two different chemical composition of reactive primary glauconite in different modeling scenarios (Table 9). This aims to test how intensively the chemical composition of glauconite affects the hydrogeochemical reaction chain evolving in the modeling reactor. One chemical composition of glauconite was taken from the measured data provided by Amouric and Parron (1985; Eq. 24). The other chemical composition of glauconite is assumed based on the data measured by SEM in the well Siri A's core samples. Several proven components, which display trace amounts (manganese) and are not typical components of glauconite (e.g., carbon), are replaced by the glauconite's common components due to charge balance (Eq. 23; Table 10). This assumed chemical composition of glauconite fairly agrees with the chemical composition of altered glauconite measured by HRTEM in the sample Si 14 (Cl : K: Si :Al : Mg: =0.6 : 9.7 :18.2 : 53.1 : 15 : 3.4; in mole).

Moreover, the crystal structure of the glauconite and berthierine is also assumed for calculating G_f^0 and enthalpy H_f^0 of the both minerals. The EDX analysis of HRTEM investigated the chemical composition of berthierine on only one measuring spot of the sample Si 15 ($Fe_{1.639}Mg_{0.283}Al_{1.4}Si_{1.489}O_5(OH)_4$). This measured composition of berthierine slightly differs from the data provided by Stokkendal et al. (2009). Thus, scenario Gl1_Be2_ODP aims to test how intensively the chemical composition of berthierine affects the alteration of the mineral assemblage driven by ODP addition.

Based (1) on the methods for estimating G_f^0 and enthalpy H_f^0 of phyllosilicates (Vieillard, 2007; Vieillard and Mathieu, 2009; Vieillard et al., 2011; and references therein) and (2) on the assumed chemical composition and crystal structures of the glauconite and berthierine, the G_f^0 and H_f^0 of the both minerals are calculated for the standard condition (25 °C and 1 atm; Table 10). The log K value of a chemical reaction is calculated from the change in the Gibbs free energy (ΔG) of this reaction[3]. Data about the G_f^0 and H_f^0 of other reactants and reaction products are taken from Wagman et al. (1982). Calculations of the temperature dependence of the solubility constant (log K) can be achieved by using the van't Hoff expression with consideration of the standard enthalpy of the reaction (ΔH in kcal). Pressure effects on chemical reactions can be calculated by entering molar volumes (Vm in cm^3 mol^{-1}) of minerals. The mol mass of elements for calculating Vm was taken from the PHREEQC.dat (Parkhurst and Appelo, 2013).

Table 10: Calculated Gibbs free energy (G_f^0) and enthalpy (H_f^0) from elements for berthierine and glauconite based on their assumed chemical composition and crystal structure at the standard conditions (25 °C and 1 atm).

	Chemical composition	G_f^0 (kJ mol^{-1})	H_f^0 (kJ mol^{-1})	Vm (cm^3 mol^{-1})
Berthierine	$Fe_{1.738}Mg_{0.417}Al_{0.95}Si_{1.71}O_5(OH)_4$	−3459.44	−3730.5	109.63
Glauconite1	$K_{0.489}Na_{0.045}Mg_{0.281}Al_{1.387}Fe_{1.183}Si_{3.327}O_{10}(OH)_2$	−5013.76	−5340.0	154.79
Glauconite2	$K_{0.709}Na_{0.084}Ca_{0.066}Mg_{0.521}Al_{0.634}Fe_{1.045}Si_{3.793}O_{10}(OH)_2$	−5042.61	−5405.53	155.92
Berthierine2	$Fe_{1.639}Mg_{0.283}Al_{1.4}Si_{1.489}O_5(OH)_4$	−3523.28	−3784.76-	108.68

Berthierine:

$$Fe_{1.738}Mg_{0.417}Al_{0.95}Si_{1.71}O_5(OH)_4 + 7.16H^+ \leftrightarrow 1.738Fe^{2+} + 0.417Mg^{2+} + 0.95Al^{3+} + 1.71H_4SiO_4 + 2.16H_2O \quad \text{(Eq. 22)}$$

log K = 16.059; ΔH = −60.27.

[3] log K = − ΔG x (2.303 x R x T)$^{-1}$; ΔG: J mol^{-1}; R: gas constant; T: 298. 15 K.

Glauconite1:

$K_{0.489}Na_{0.045}Mg_{0.281}Al_{0.634}Fe_{1.045}Si_{3.793}O_{10}(OH)_2 + 10H_2O \leftrightarrow$

$0.709K^+ + 0.084Na^+ + 0.066Ca^{2+} + 0.521Mg^{2+} + 0.634Al(OH)_4^- + 0.869Fe^{3+} + 0.176Fe^{2+} + 3.793H_4SiO_4 + 4.292OH^-$ (Eq. 23)

$\log K = -71.43$; $\Delta H = 42.492$

Glauconite2:

$K_{0.709}Na_{0.084}Ca_{0.066}Mg_{0.521}Al_{0.634}Fe_{1.045}Si_{3.793}O_{10}(OH)_2 + 10H_2O \leftrightarrow$

$0.709K^+ + 0.084Na^+ + 0.066Ca^{2+} + 0.521Mg^{2+} + 0.634Al(OH)_4^- + 0.869Fe^{3+} + 0.176Fe^{2+} + 3.793H_4SiO_4 + 4.292OH^-$ (Eq. 24)

$\log K = -70.645$; $\Delta H = 52.035$

Berthierine2:

$Fe_{1.639}Mg_{0.283}Al_{1.4}Si_{1.489}O_5(OH)_4 + 8.044H+ \leftrightarrow 1.639Fe^{2+} + 0.283Mg^{2+} + 1.4Al^{3+} + 1.489H_4SiO_4 + 3.044H_2O$ (Eq. 25)

$\log K = 16.814$; $\Delta H = -70.17$.

5.2.3 Modeling results

The batch modeling results (pH-E_H conditions and alteration of mineral assemblage) are shown as a function of the amount of the added reactants (HCl, ODP, or ODP+HAc). The modeled pCO_2 is presented, if a gas phase develops. Different scenarios aim (1) to specify the pH-E_H conditions under which glauconite can dissolve to the observed alteration degree, (2) to determine which secondary minerals can form as a result of glauconite dissolution, (3) to prove the hypotheses working based on the petrographic observations whether berthierine can form *in situ* due to glauconite dissolution, and (4) to identify why almost pure calcium carbonate forms (without siderite, dolomite or magnesite) in such an iron- and magnesium-rich system (due to glauconite dissolution).

(1) Gl1_HCl

Within scenario Gl1_HCl, stepwise addition of HCl in the pore water which equilibrates with the glauconite characterized by a chemical composition provided by SEM investigations. Addition of HCl slightly triggers glauconite dissolution (Fig. 53). Glauconite dissolution releases ferric iron species in the pore water. Such ferric iron species react with water molecules and produce ferric iron hydroxide complexes (e.g., $FeOH^{2+}$, $Fe(OH)_2^+$). This process additionally decreases the model pH. The

calculated extremely low pH result in an undersaturation with respect to $Fe(OH)_{3(a)}$, although the pore water displays a very high iron total concentration (13 mmol kgw^{-1} at maximum) under strong oxidizing conditions (E_H = ca. 640 mV).

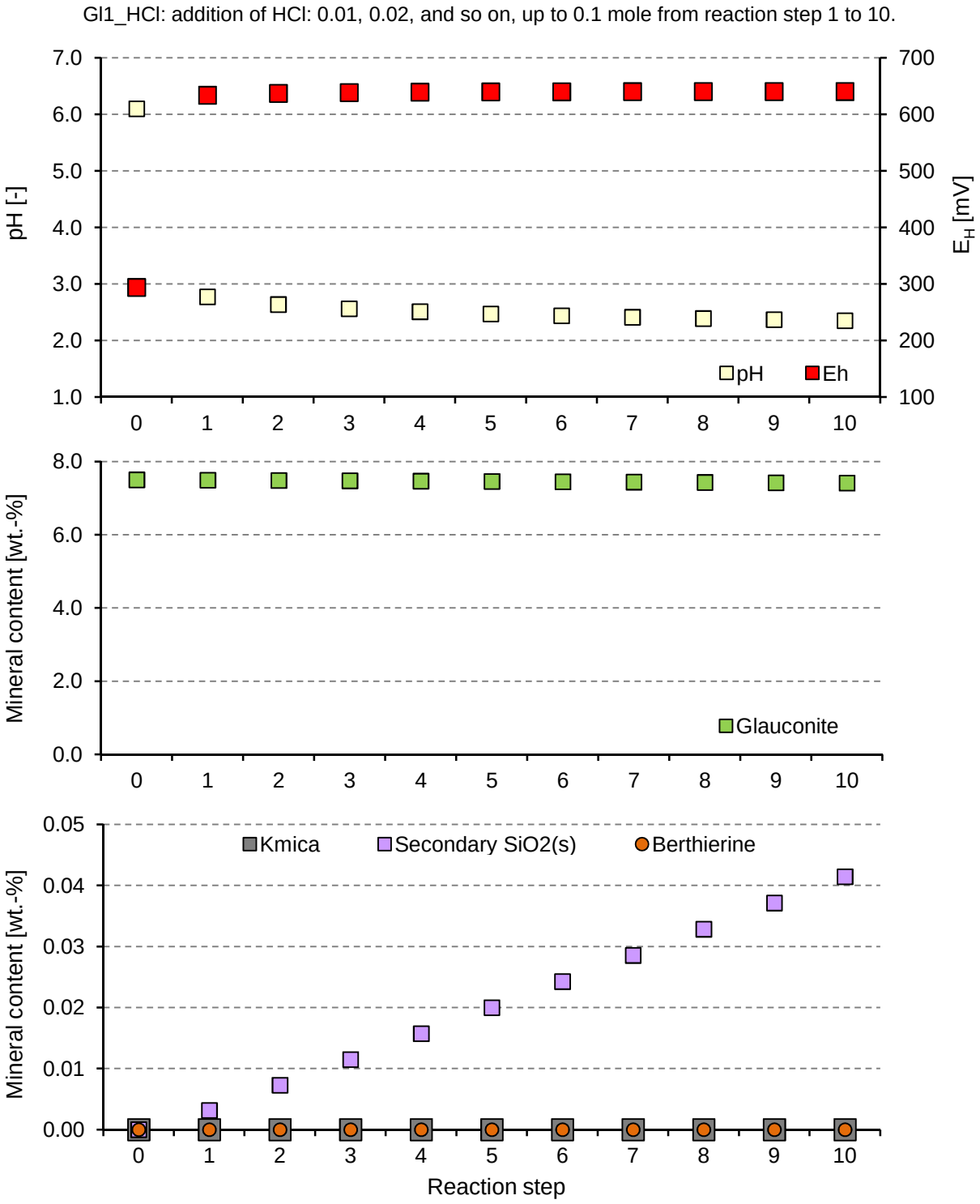

Fig. 53: Modeled pH-E_H conditions and alteration of the mineral assemblage of scenario Gl1_HCl.

The conversion of dissolved glauconite achieves a maximum level of ca. 10 mmoles per one liter of pore water at the final reaction step. Such a mass conversion corresponds only to 0.09 wt.-% of the total masse of the reactor. This limited conversion is inconsistent with the degree of glauconite alteration observed by petrographic investigations (see section 4.3.2). Secondary $SiO_{2(s)}$ (chalcedony in the model) is the single mineral newly formed with trace amounts (Fig. 53). The calculated low pH lead to an undersaturation with regard to berthierine and muscovite (K-mica in the model). In summary, glauconite dissolution is incapable of resulting in formation of berthierine and muscovite, if glauconite dissolves merely due to changes in pH of aqueous solutions.

(2) Gl1_ODP

Stepwise addition of CH_4, CO_2, and H_2 in the pore water establishes reducing conditions in the reactor. Correspondingly, the modeled E_H decrease down to ca. −380 mV (Fig. 54). Berthierine formation strongly consumes free H^+-ions which are produced by the reduction of ferric iron to ferrous iron (Eq. 13) or by dissociation of carbonic acid (Eqs. 9 to 11). Consequently, such processes keep the modeled pH on a high level (ca. 8.0; Fig. 54). Redox-reactions triggered by addition of CH_4 and H_2 result in much stronger glauconite dissolution (Fig. 54). At the final reaction step, the pre-assigned reactive primary glauconite completely dissolves. As a result, berthierine formation occurs (up to 4 wt.-% in the reactor). In addition to berthierine, another iron-bearing mineral siderite also forms but only with trace amounts (0.03 wt.-% at maximum) which are hardly proven by analytical methods (Fig. 54). Combining precipitation of the both iron-bearing minerals keeps the modeled total iron concentration of the pore water on a low level (8.4×10^{-7} mol kgw^{-1}). The excess of silica species, which are produced by glauconite dissolution and which are not completely removed by berthierine formation, causes chalcedony formation. In comparison to chalcedony, primary quartz displays a lower solubility at the same temperature and pressure conditions. Primary quartz is allowed to dissolve. Quartz dissolution is not induced due to chalcedony formation. Thus, the mass conversion of primary quartz remains unchanged and is not discussed here (also not for other scenarios). Additionally, the high potassium activity resulting from glauconite alteration results in K-mica precipitation. A very strong oil degradation (characterized by a large amount of ODP) could lead to development of a gas phase at the final reaction step (Fig. 54).

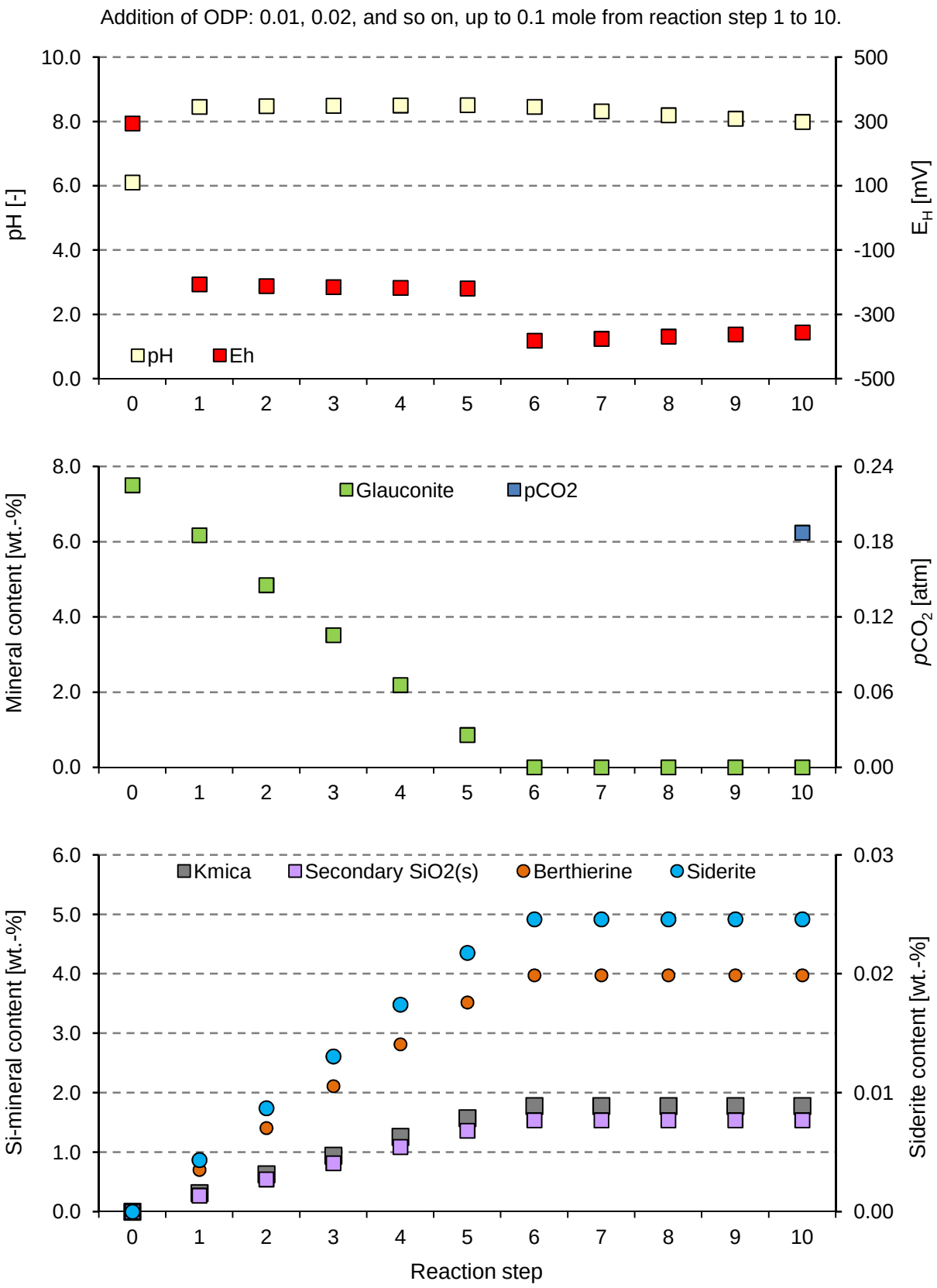

Fig. 54: Modeled pH-E_H conditions and alteration of the mineral assemblage of scenario Gl1_ODP and $pCO_{2(g)}$. 1 mole ODP: including CH_4, CO_2 and H_2 with amounts of 1, 2, and 5 moles, respectively.

The modeling results presented by Xu et al. (2004) show that glauconite can completely dissolve due to the presence of kerogen. Sass et al. (2002) performed experiments to verify the capability of CO_2 trapping for glauconite. Their experiment results show that no siderite was observed. Such modeling results and observations well agree with the modeling results of scenario Gl1_ODP. The modeled results of scenarios Gl1_HCl and Gl1_ODP clearly reveal that noticeable glauconite dissolution (detectable by analytical methods) requires reducing conditions in aqueous solutions. On the contrary, solutions, which even display an extremely low pH under oxidizing conditions, are incapable of achieving a sufficient mass conversion of glauconite. Moreover, the modeling results reveal that berthierine formation can form *in situ* in a glauconitic environment in expense of glauconite, provided that reducing conditions prevail in the system. In summary, the modeling results can qualitatively reproduce several main diagenetic features, showing (1) dissolution of reactive glauconite, (2) berthierine precipitation, (3) formation of secondary $SiO_{2(s)}$, and (4) muscovite formation. Only siderite formation was not observed in the Siri oilfield, which may be due to its minor amount or to a lower oil degradation degree in the Siri oilfield compared to the modeled degree.

(3) Gl1_ODP+HAc

In comparison to scenario Gl1_ODP, scenario Gl1_ODP+HAc assumes that 2% acetic acid remains undegraded to CH_4 and CO_2. The modeling results of the both scenarios aim to show how intensively this process affects the modeled alteration of mineral assemblage. The equilibrium constants of dissociation of acetate complex (e.g., acetic acid (HAc), sodium acetate) were taken from the thermodynamic database minteq.dat (Parkhurst and Appelo, 2013) and additionally defined in the input file.

With ongoing addition of ODP and acetic acid, the alteration of mineral assemblage calculated by scenario Gl1_ODP+HAc develops similarly to scenario Gl1_ODP. The results of the both scenarios slightly differ exclusively in the absolute level of the mineral amounts at the same reaction steps. Partial replacement of CH_4 and CO_2 by acetic acid does not lead to the development of a gas phase within scenario Gl1_ODP+HAc. It follows that trace amounts of acetic acid produced during oil degradation show a limited to negligible effect on the mineral mass conversion and $pCO_{2(g)}$.

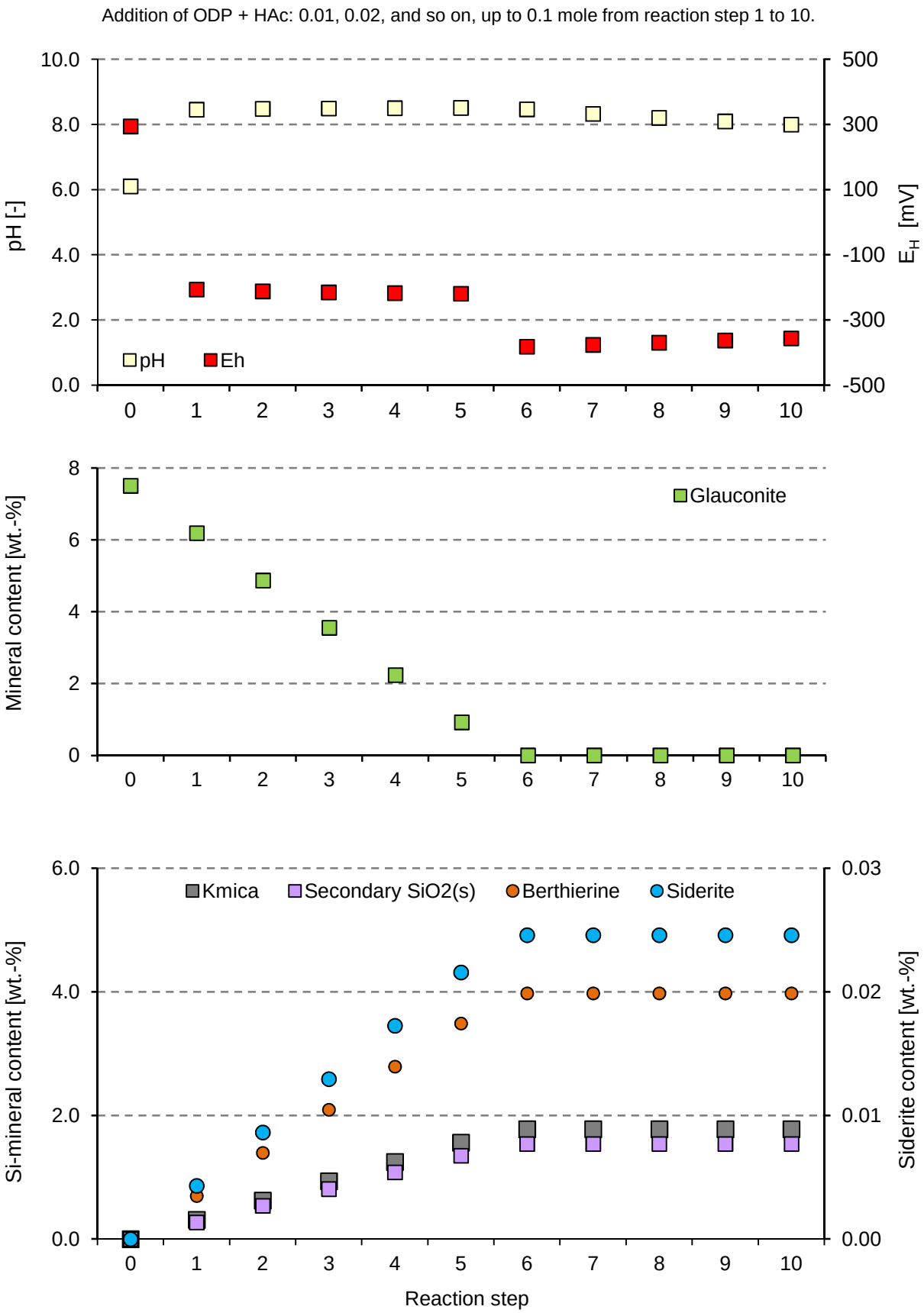

Fig. 55: Modeled pH-E_H conditions and alteration of the mineral assemblage within scenario Gl1_ODP+HAc. 1 mole (ODP + HAc): including CH_4, CO_2, H_2, and acetic acid (HAc) with amounts of 0.98, 1.98, 5.0 and 0.02 moles, respectively.

(4) Gl2_ODP

In this study, the exact chemical composition of altered glauconite composition is hard to determine. The chemical composition of glauconite abbreviated as Gl1 is based on the results measured in the Siri A's reservoir sandstones provided by SEM analysis. Scenario Gl2_ODP considers the glauconite analyzed by Amouric and Parron (1985; abbreviated as Gl2) as the primary unaltered glauconite in the reactor. This scenario aims to test how intensively the chemical composition of glauconite affects the modeling results.

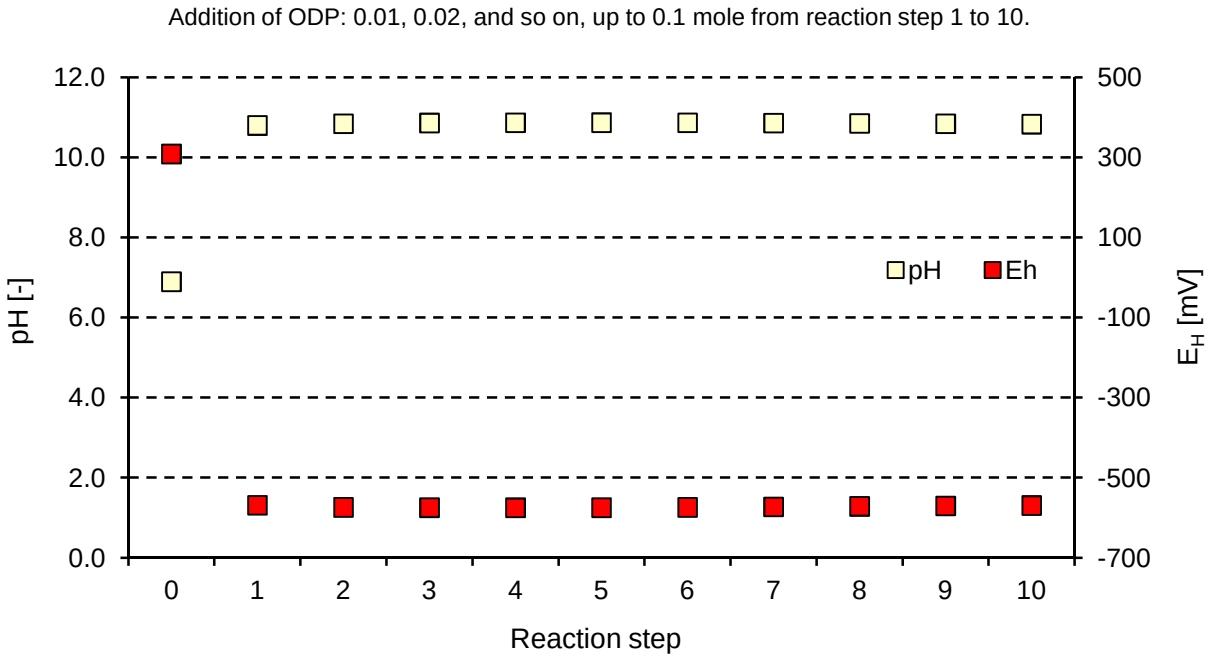

Fig. 56: Modeled pH-E_H conditions of scenario Gl2_ODP. 1 mole ODP: including CH_4, CO_2, and H_2 with amounts of 1, 2 and 5 moles, respectively.

The pH and E_H calculated by scenario Gl2_ODP are higher and lower than those modeled within scenario Gl1_ODP, respectively (Fig. 56). A gas phase develops with ongoing addition of ODP and consists of almost pure CH_4 (pCO_2 = 2 x 10^{-7} atm at maximum; not presented here).

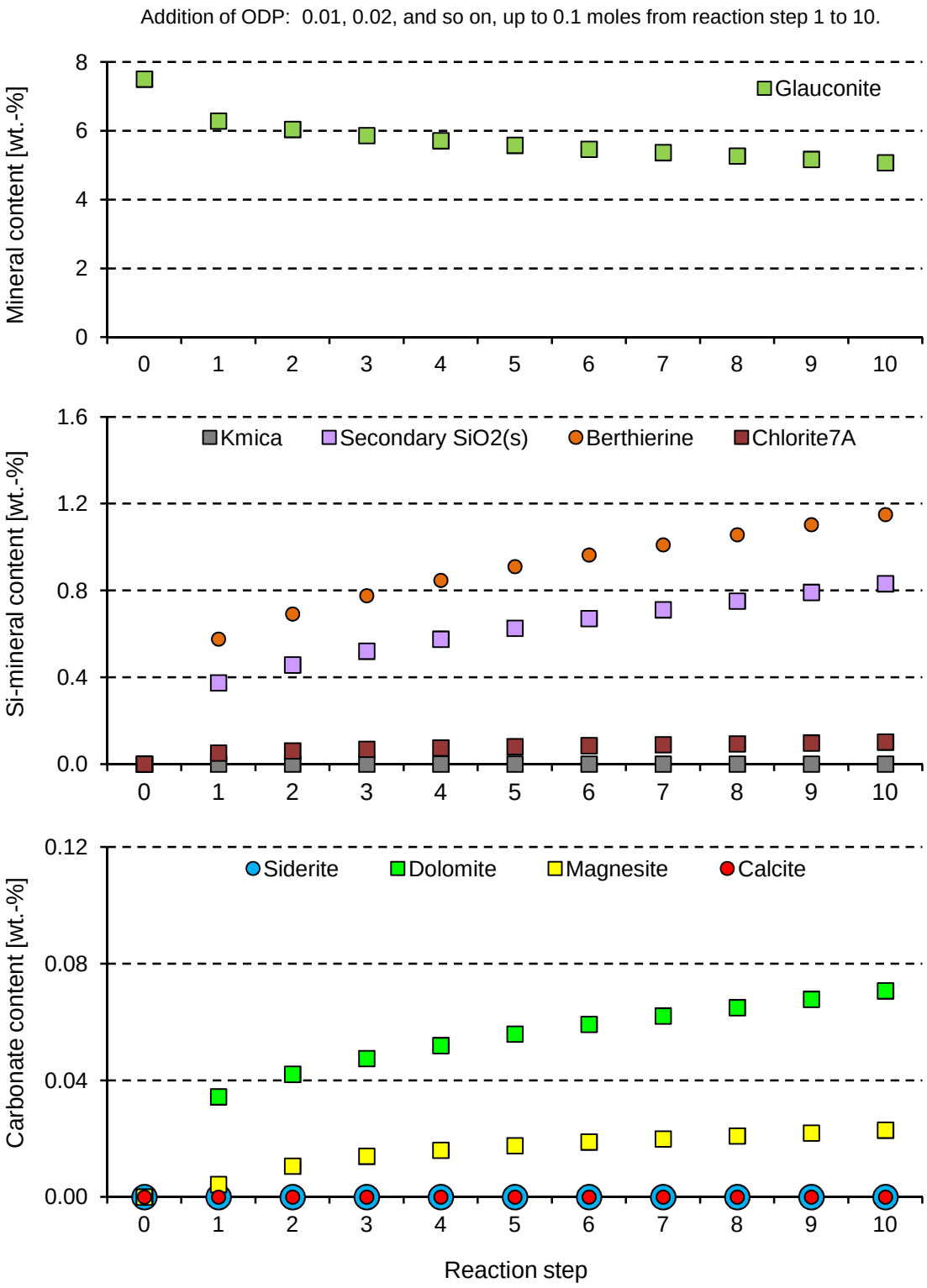

Fig. 57: Modeled alteration of the mineral assemblage within scenario Gl2_ODP. 1 mole ODP: including CH_4, CO_2, and H_2 with amounts of 1, 2 and 5 moles, respectively. Chlorite7A: pure magnesium serpentine with a basal space of 7 Å, which is defined as “Chlorite7A” in the database Phreeqc.dat of PHREEQCI (Parkhurst and Appelo, 2013).

The higher modeled pH lead to a slightly lower mass conversion of glauconite. An undersaturation of the pore water regarding to K-mica results in a very high concentration of aqueous

potassium (0.22 mol kgw^{-1} at the final reaction step). The high potassium concentration prevents glauconite dissolution and is the other reason for the calculated low mass conversion of glauconite within this scenario. The reactive glauconite in the reactor is completely consumed (Fig. 57). Dissolution of the magnesium-rich glauconite (GL2) can cause a high magnesium concentration in the pore water. In consequence, the pore water could be oversaturated regarding to the four following magnesium-bearing minerals and allows their formation at their saturation: berthierine, chlorite7A, dolomite and magnesite. The "chlorite7A" defined in the database Phreeqc.dat is a pure magnesium serpentine with a basal space of 7 Å ($Mg_5Al_2Si_3O_{10}(OH)_8$). It can be described as the pure magnesium serpentine end-member. Within scenario GL2_ODP, the calculated results show that these four magnesium-containing minerals form (berthierine, "chlorite7A", dolomite and magnesite). Actually, berthierine consists of pure iron- and magnesium serpentine end-members. Formation of "chlorite7A" in this modeling scenario indicates that dissolution of a magnesium-rich glauconite can result in formation of a secondary berthierine containing more magnesium. Due to modeling limitations, the process −development of the berthierine's chemical composition depending on the chemical composition of aqueous solutions− cannot be considered. Precipitation of "chlorite7A" removes a part of aqueous magnesium, silica and aluminum species. As a result, the content of berthierine calculated by scenario Gl2_ODP differs from scenario Gl1_ODP (Fig. 57). Additionally, less chalcedony forms within scenario Gl2_ODP compared to scenario Gl1_ODP. Glauconite dissolution releases trace amounts of calcium species in the pore water. These calcium species are bound to dolomite due to the high magnesium concentration in the pore water.

The modeling results calculated by scenarios Gl1_ODP and Gl2_ODP show that glauconite dissolution under reducing conditions can lead to berthierine formation independent on the chemical composition of glauconite. Variation in the chemical composition (especially in the ratio between iron and magnesium) of glauconite can affect the chemical composition of berthierine and the composition of the secondary mineral assemblage. Dissolution of magnesium-rich glauconite results in formation of magnesium-rich berthierine and may cause magnesium-bearing carbonates, when the pore water provides an efficient carbonate activity (aCO_3^{2-}) on an appropriate pH level. In contrast, iron-rich berthierine can form, when the altered primary glauconite contains more iron compared to magnesium. Subsequently, siderite can form instead of magnesite. The modeled iron total concentration remains extremely low ($<5x10^{-7}$ mol kgw^{-1} in the modeled pore water) under reducing conditions due to the low solubility of berthierine. This means that the sink term of iron −berthierine precipitation− efficiently removes the iron species released by glauconite dissolution. Consequently, the ratio of iron to magnesium in glauconite determines whether magnesium- or iron-containing carbonate form. When the primary glauconite displays a similar composition to the measured data from the well Siri A, no siderite or exclusively with trace amounts (ca. 0.03 wt.-% siderite in scenario Gl1_ODP) forms.

(5) Gl1_Be2_ODP

Calculations of scenario Gl1_Be2_ODP aim to test how intensively the chemical composition of berthierine affects the composition of the mineral assemblage. In comparison to scenario Gl1_ODP, the modeling results of scenario Gl1_Be2_ODP show a similar development of the alteration of the mineral assemblage: dissolution of glauconite, formation of chalcedony, berthierine and muscovite (no detailed results here). The alternative chemical composition of berthierine (Be2) leads to formation of pure magnesium serpentine with trace amounts and to different pH-E_H levels compared to Gl_ODP. However, the chemical composition of berthierine shows minor effects on the alteration of the mineral assemblage. Therefore, the chemical composition of berthierine measured by Stokkendal et al. (2009) is used in other hydrogeochemical modeling (1D and 3D model).

(6) Gl1_Ano_ODP

The modeling results of scenario Gl1_ODP provide a qualitative reproduction of the observed diagenetic features except for massive calcite formation. The modeling results from scenario Gl1_ODP indicate that siderite forms with trace amounts (0.03 wt.-% at maximum). EDX analyses of SEM (Table 6) and of HRTEM (section 4.3) show that the glauconite present in the reservoir sandstones of the well Siri A is almost calcium-free. Thus, glauconite dissolution alone is incapable of triggering the proven strong calcite cementation. The albite observed in the well Siri A displays intensive alteration features. Anorthite provides a stronger CO_2 buffering capacity compared to albite (van Berk et al., 2009 and 2013). It can be thus concluded that anorthite has been present in the primary mineral assemblage of the reservoir sandstones and completely dissolved. Scenario Gl1_Ano_ODP considers anorthite as the single reactive feldspar in the batch modeling and correspondingly increases its amount in the primary mineral assemblage. This aims to test whether dissolution of anorthite can cause the observed calcite cementation. In comparison to scenario Gl1_ODP, more ODP are added in the pore water in order to completely dissolve anorthite. In analogy to scenario Gl1_ODP, 0.05 mole ODP is incrementally added to the modeling reactor at the first five reaction steps. At the last five steps, 1.0 moles ODP are incrementally added in the pore water.

Figure 58 shows that the modeled pH from scenario Gl1_Ano_ODP are slightly higher than the values calculated by scenario Gl1_ODP, before glauconite completely dissolves. This is because anorthite in the primary mineral assemblage keeps the pH of aqueous solution on a high level. With ongoing addition of ODP to the reactor, glauconite, anorthite and albite sequentially dissolve, and simultaneously, the modeled pH constantly decrease (Fig. 58 and 59). A gas phase develops from reaction step 6 (Fig. 58). A detectable proportion of $CO_{2(g)}$ occurs in the methane-dominate gas phase at the final reaction step.

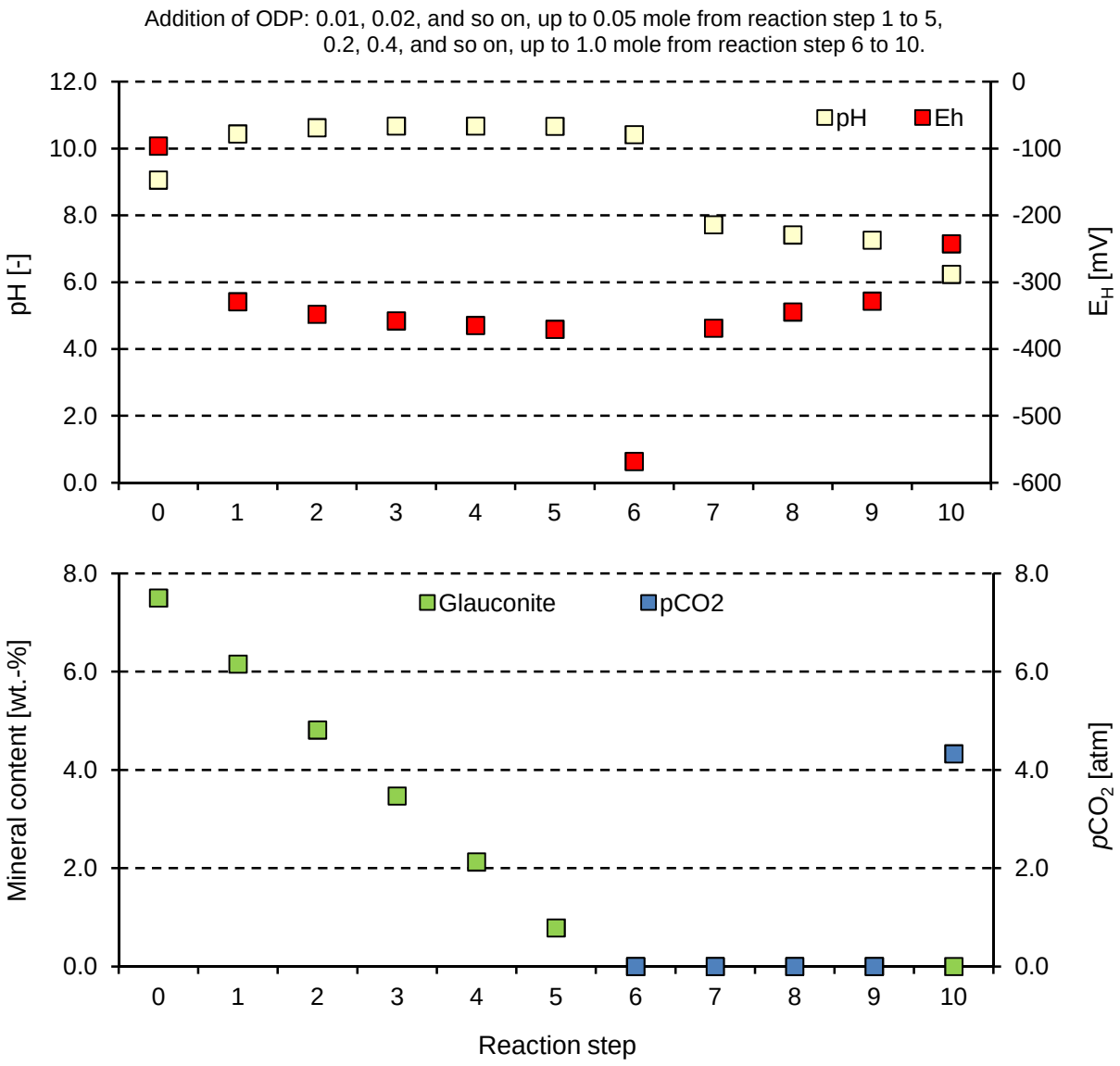

Fig. 58: Modeled pH-E_H conditions, alteration of glauconite and development of $pCO_{2(g)}$ from scenario Gl1_Ano_ODP. 1 mole ODP: including CH_4, CO_2, and H_2 with amounts of 1, 2 and 5 moles, respectively.

The high sodium concentration in the pore water and the high pH buffered by anorthite equilibration induce albitization, until anorthite still exists in the modeling reactor (Fig. 59). The newly formed albite constantly dissolves from reaction step 7 due to addition of ODP. Similar to scenario Gl1_ODP, glauconite dissolution triggers formation of berthierine, muscovite (K-mica in the model) and secondary $SiO_{2(s)}$. Anorthite is an additional source term of aluminum and silica besides glauconite. Thus, more muscovite forms within scenario Gl1_Ano_ODP compared to scenario Gl1_ODP (Figs. 54 and 59). Neither dolomite nor magnesite forms in scenario Gl1_Ano_ODP. Calcite forms due to anorthite dissolution. At the final reaction step, the calcite content in the bulk rock achieves its highest level (1.4 wt.-%). In comparison, the highest modeled siderite content of 0.02 wt.-% in the reactor containing 5.3 kg solids can be ignored (Fig. 59).

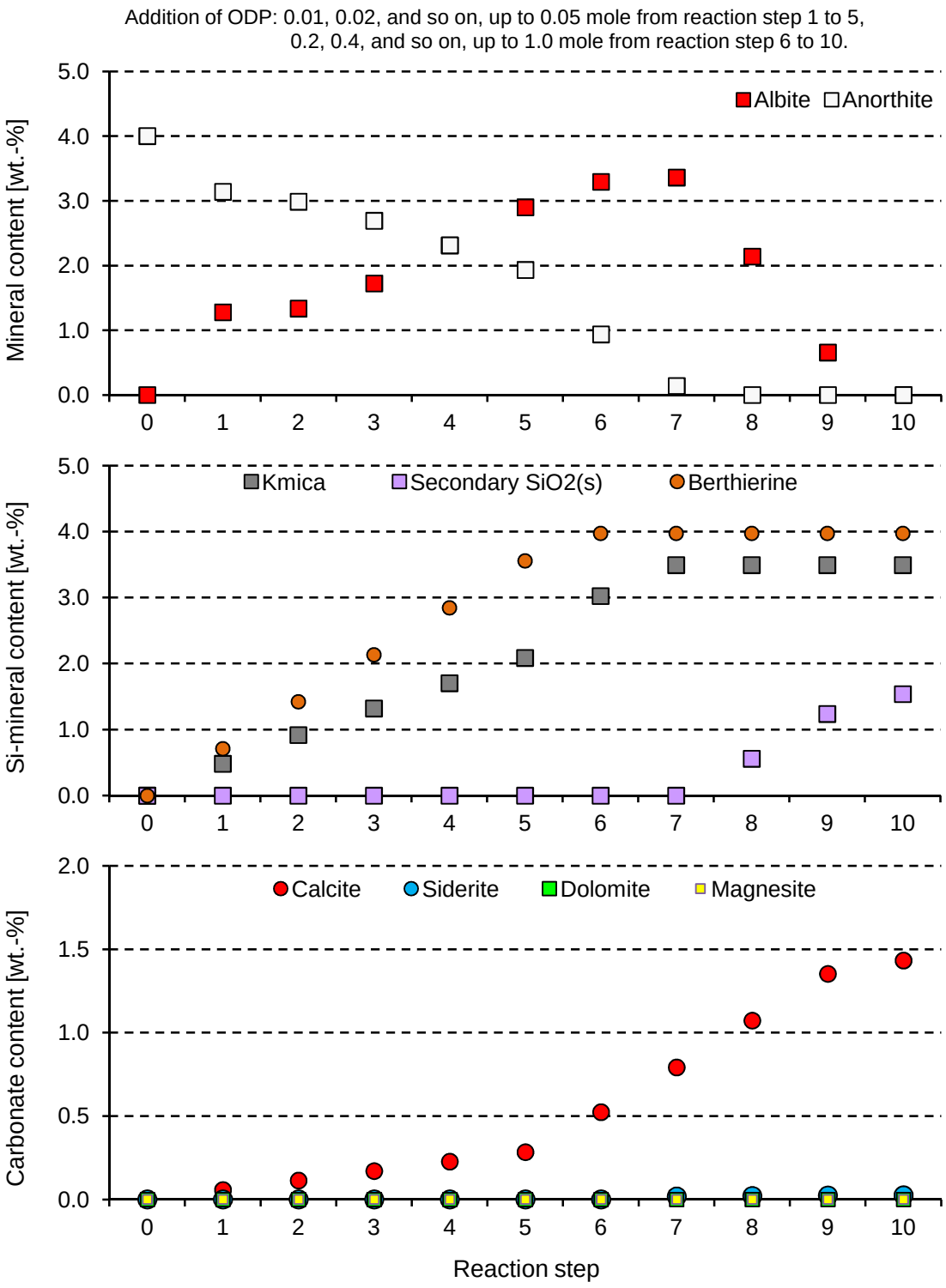

Fig. 59: Modeled alteration of the mineral assemblage from scenario Gl1_Ano_ODP. 1 mole ODP: including CH_4, CO_2, and H_2 with amounts of 1, 2 and 5 moles, respectively.

5.2.4 Conclusions of batch modeling

The calculated results of the six scenarios show that glauconite dissolution under reducing conditions leads to berthierine formation. This indicates that the organic-inorganic interactions caused

the observed diagenetic features. Stokkendal et al. (2009) stated that an iron-rich brine flowed into the reservoir resulted in berthierine formation in the Siri oilfield. An alternative modeling scenario considers a one-dimensional stream tube that represents the reservoir sandstone column. The stream tube contains 30 cells (reactors) each of which is one meter in length. The stream tube is characterized by a homogeneous distribution of geohydraulic and hydrogeochemical properties (e.g., flow velocity, chemical composition of pore water and of mineral assemblage, etc.). The basic properties of each cell (reactor) including the pore volume, the porosity, and the primary mineral assemblage have been used in the batch model (section 5.2.2). The flow velocity of the iron-rich brine is assumed to be 0.91 m per year. A 1.0 molal sodium chloride solution equilibrates with a primary assemblage (containing dolomite and siderite) and several secondary minerals potentially formed under a pCO_2 of 0.003 atm. This calculated solution is considered as the iron-rich brine that flows into the reservoir sandstones (in other words, into the stream tube). The corresponding input file and the detailed modeling results are not presented in this study. Detectable formation of berthierine can be observed only in the first 15 reactors of the stream tube after an inflow lasting for 2.3 Ma. The petrographic investigations in the wells Siri A and Sandra A clearly show that berthierine formation is unrestricted to a specific part of the reservoir sandstone. It forms over the entire reservoir thickness and also in different wells (Siri A, Sandra A; Siri 3, 4 and 5, Stokkendal et al., 2009). Additionally, the observed glauconite dissolution must have released its components in the pore water. Thus, this poses a question in which form such components (magnesium, iron, silica, potassium and aluminum) exist in the system. Aluminum and potassium can be bound to muscovite. Silica can be additionally removed from the pore water by formation of secondary $SiO_{2(s)}$. Except for berthierine, precipitation of any other iron- or magnesium-bearing secondary minerals was not proven, although glauconite is partly strongly altered in this reservoir.

In summary, the batch modeling results provide a reproduction of the most diagenetic features (e.g., glauconite dissolution, formation of berthierine) observed in all reservoir parts. Combining the results of the batch and the simple 1D transport models can demonstrate that berthierine observed in the Siri oilfield formed *in situ* due to glauconite dissolution. Berthierine formation can clarify why pure calcium carbonates form in the Siri oilfield, although the reservoir sandstones are very rich in iron and magnesium. The calcite content calculated by scenario Gl1_Ano_ODP accounts for 1.4 wt.-% at maximum, although anorthite is considered as the single feldspar in the primary mineral assemblage and its content is thereby strongly increased. In comparison, the core samples taken from the OWCs contains ca. 31.7 wt.-% calcite (according to 3.8 wt.-% TIC and 16.7 moles calcite in one reactor containing 5.3 kg solids). Massive calcite cementation is restricted exclusively to the OWCs. It is still unknown which hydrogeochemical processes have driven the massive calcite cementation and why the distribution of the calcite cement is restricted to the specific reservoir parts. Thus, an exact reproduction of calcite newly formed at the OWCs was not successfully integrated in the batch model

by considering anorthite located at the OWCs as primary mineral. Another calcium source term must be responsible for the calcite cementation observed at the OWCs.

Carbon dioxide dissolves in pore water and can produce $CO_3^{2-}{}_{(aq)}$ depending on pH. It can be generated by different pathways, for instance, oil degradation at OWCs, during oil generation, and methane oxidation by glauconite. On the contrary, anorthite is the only calcium-bearing mineral in the batch modeling which dissolution can supply calcium species for calcite cementation. Starting from the assumption that anorthite is the only source term of calcium, the reservoir sandstones should contain ca. 88 wt.-% anorthite. This simple calculation indicates that the primary anorthite in the sandstone of the OWCs is not the main for the calcite formation. An external calcium source is a prerequisite for the calcite cementation at the OWC. In other words, the sandstone at the OWCs is an open system regarding to calcium species. This means that calcite formation at the OWC cannot result from mineral transformation occurring *in situ*. In consequence, calcium aqueous species, which are bound to calcite at the OWCs, must have been transported towards the OWCs. Thus, a hydrogeochemical transport model must be built up to identify which processes resulted in the uncommonly massive calcite cementation.

5.3 One-dimensional hydrogeochemical transport modeling

The petrographic observations indicate that calcite cementation occurred after oil charging in the Siri oilfield (e.g., Fig. 36; for detail, see section 4.3.2). Moreover, several hydrogeochemical processes occurred prior to calcite formation at the OWCs, for instance, transformation from glauconite to berthierine (Fig. 39), muscovite formation (Fig. 44) and precipitation of secondary $SiO_{2(s)}$ (Fig. 43). The development of an oil-water contact can continuously provide inorganic carbon to pore water which can be subsequently removed from the pore water by calcite formation. Thus, sufficient aqueous calcium species are additionally needed for the calcite cementation at the OWCs. The results of the batch modeling demonstrate that aqueous calcium species must have been transported from another part of the rock column towards the OWCs (section 5.2.3).

High petroleum saturation can be considered to effectively cease the advective mass transport of aqueous components through the oil column in the vertical direction (Worden and Morad, 2003). The Siri reservoir sandstones overlie and underlie the impermeable marl and clay seal, respectively. Thus, a vertical fluid flow from the overlying or underlying layers may be prevented. Instead, effective mass transport through the oil column can be achieved by diffusion-driven transport of aqueous components dissolved in the irreducible water of a water-wet sediment column filled with oil, although the systems gradually evolves to stagnant conditions, even more or less to closed conditions by the end (Worden and Morad, 2003). The results of petrographic investigations indicate that the Siri oilfield's reservoir sandstones are characterized by a homogeneous distribution of the primary mineral assemblage. These

sandstones in the oil and water legs also contain anorthite besides the reservoir sandstones at the OWCs. They are water-wet (Stokkendal et al., 2009). In consequence, it can be hypothesized that the anorthite located in the oil and water legs may have provided the calcium species for the calcite cementation at the OWCs. Anorthite equilibrates with the pore water in the water leg or with the irreducible water within the water-wet sediment column filled with oil. This process supplies calcium species dissolved in the pore water and in the irreducible water, which can diffuse from the water or oil leg towards the OWCs, provided that a calcium concentration gradient develops.

Oil degradation at OWCs and the thereby triggered anorthite dissolution at OWCs lead to precipitation of calcite. The removal of calcium species, which are caused by calcite formation, reduces the calcium concentration at OWCs. Therefore, a concentration gradient of calcium develops from the oil and water legs towards the OWCs. In consequence, diffusion-driven transport process is induced. Anorthite dissolution occurring in the water and oil legs constantly delivers calcium species which are transported by diffusion towards the OWCs. In addition, the reservoir sandstones overlie the marl (Fig. 4 in Ohm et al., 2006). In the investigated well Siri A, the sandstones containing many calcite clasts underlie the glauconitic sandstones characterized by a high permeability. If the calcite clasts can dissolve due to production of carbonic acid at OWC, aqueous calcium species released by dissolution of these clasts can also diffuse towards the OWC. Thus, a one-dimensional (1D) diffusion-driven transport model is built up to test whether combining diffusive mass transport and dissolution of calcium-bearing minerals (anorthite in the water and oil legs as well calcite in the clast horizon) could have led to the massive calcite cementation observed at the OWCs.

5.3.1 Conceptual model

Mass transport through oil column can be achieved by diffusive mass transport (Worden and Morad, 2003). Nevertheless, the low content of irreducible water in the water-wet sandstones filled with oil restricts diffusive mass transport. The computer code PHREEQCI (Parkhurst and Appelo, 2013) simulates transport processes exclusively in water-saturated flow systems. Additionally, it includes only one diffusion coefficient for the modeled sediment column. Thus, the 1D diffusion-driven transport model developed in this study considers the oil leg as a water leg. To weaken the effect of the diffusive mass transport in the oil leg, the 1D diffusion-driven transport model considers a 3-m long oil leg, although the well Siri A penetrates ca. 22 m oil column in the reservoir sandstones (Fig. 30). Moreover, the 1D model does not try to provide a reproduction of the real reservoir sediment column. It exclusively aims to investigate whether combining diffusive mass transport and dissolution of anorthite as well as calcite clasts may have led to calcite cementation in a similar magnitude to the observations at the OWCs. Therefore, the 1D diffusion-driven transport model only considers one conceptual oil-water contact at which oil degradation may induce calcite formation.

The modeled sediment column of 14.5 m in length is subdivided into 29 cells (reactors), each 0.5-m thick (Fig. 60). The first six cells represent the three meter long sediment column which is considered as the sandstones filled with oil. Cells 7 and 8, in which *n*-alkanes are degraded to CH_4, CO_2 and H_2, are considered as the recent OWC (Fig. 60). Cells 9 to 28 are defined as the glauconitic sandstones filled with formation water. In addition, cell 29 represents the horizon of the reservoir sandstone containing calcite clasts. The model only simulates the highly permeable reservoir sandstone column and an additional cell that represents the underlying horizon containing carbonate clasts. The core sample taken from the clast horizon has an extremely low permeability (Schovsbo, 2009; pers. com.). Consequently, the upper and lower boundary conditions are defined as a closed boundary with regard to diffusive mass transport.

Within cells 7 and 8, *n*-alkanes are degraded to CH_4, CO_2 and H_2 (Fig. 60). Calcite formation, which results from oil degradation at the OWC and the thereby triggered anorthite dissolution, operates a sink term for calcium species in the pore water at the OWC. Diffusive mass transport is induced. Diffusive exchange of aqueous species takes place between two adjoining cells. This exchange enables a mass transport of calcium species from the water and the oil legs towards the OWC (Fig. 60). The sandstones within cells 47 to 65 are filled with formation water. Cell 66 represents the sandstone containing many carbonate clasts (Fig. 60). The modeling results of the two scenarios Gl1_ODP (without consideration of acetic acid) and Gl1_ODP+HAc (including acetic acid) clearly show that generation of acetic acid has a minor effect on the alteration of the mineral assemblage and on the $pCO_{2(g)}$ (section 5.2.3). Therefore, other common oil degradation products −carboxylic acids− (dominantly acetic acid) are ignored in the 1D diffusion-driven transport model.

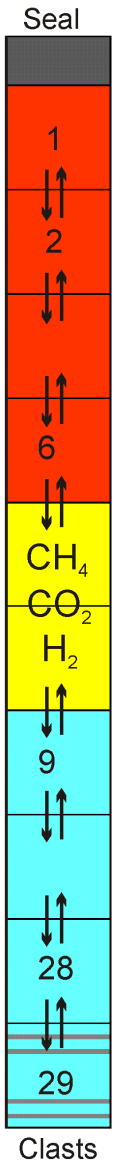

Fig. 60: Schematic of the concept of the 1D diffusion-driven transport model. Diffusive mass transport regulates the exchange of dissolved species between two adjoining cells within the sandstone column; oil degradation occurs at the recent OWC within cells 7 and 8; cells 1 to 6: oil leg; cells 9 to 28: water leg, cell 29: glauconitic sandstone containing carbonate clasts.

The batch modeling (section 5.2) aims (1) to prove the hypotheses based on the petrographic observations whether berthierine can form *in situ* due to glauconite dissolution, and (2) to clarify why almost pure calcium carbonate is precipitated (without siderite, dolomite or magnesite components) in such an iron- and magnesium-rich system due to glauconite dissolution. Thus, the batch model simplifies the primary mineral assemblage of the Siri oilfield's reservoir rocks and considers only glauconite with or without anorthite. In comparison, each cell within the sediment column in the 1D diffusive mass transport model integrates all hydrogeochemical reactions that potentially occurred in the Siri oilfield. In the 1D diffusion-driven transport model, each cell contains one liter of pore water and 5.3 kg of solids ($\varphi = 0.33$; bulk density = 2.65 kg L^{-1}; length : width : height = 0.077 m : 0.077 m : 0.5 m). The sediment column is characterized by a homogeneous distribution of the hydrogeochemical and geochemical properties. Correspondingly, each cell contains K-feldspar, albite and muscovite besides glauconite and anorthite (Table 11). The chemical composition of the primary glauconite used in the 1D transport model was taken from the data measured by SEM-EDX analysis in the well Siri A (corresponding to Glauconite1 in Table 10). Cell 29 representing the clast horizon additionally contains 13 moles calcite compared to the other cells, although the total mass of solids in this cell is greater than 5.3 kg. Consequently, primary calcite sourced from the clast horizon is an additional calcium source besides anorthite in the sediment column. Dissolution of calcite located in the clast horizon may provide additional calcium species which can diffuse towards the OWC and result in calcite cementation there.

Table 11: Pre-assigned assemblage of the primary minerals and their assumed amount in each cell of the 1D diffusive mass transport model at the starting condition prior to oil degradation at the generic oil-water contact.

		Amount	
		(wt.-%)	(mol)
Quartz		65	57.34
Glauconite	(total)[a]	25	3.17
Glauconite	(reactive)	7.5	0.951
Anorthite		2	0.38
Albite		2	0.40
K-feldspar		1	0.19
Muscovite		1	0.13
Pyrite	(non-reactive)[b]	1	0.44
Unidentified minerals	(non-reactive)[c]	3	

[a] 30% of the total primary glauconite is available for calculation of chemical equilibrium.
[b] No oxidizing agents exist in pore water or in mineral phase assemblage. Pyrite is thus removed from the list of the reactive mineral assemblage.
[c] Unidentified minerals (including rock fragments with trace amounts) are considered to be non-reactive for calculation of chemical equilibrium.

Prior to the first step of the diffusive transport modeling, a one molal NaCl solution equilibrates with the primary minerals (the minerals listed in Table 11 without and with primary calcite, respectively) in order to calculate the chemical composition of the pore water within each cell. The computer code PHREEQCI can only simulate water-saturated flow. Consequently, it is incapable of correctly calculating diffusive transport process in the oil leg. The minor content of irreducible water in oil leg can efficiently reduce the effect of solute diffusion. However, the model considers the oil leg a water leg; in other words, the effects of solute diffusion in the oil leg are amplified to test whether diffusive mass transport could have resulted in the strong calcite cementation observed at the OWCs. On the one hand, PHREEQCI can calculate multicomponent diffusion, where aqueous species have individual diffusion coefficients (Parkhurst and Appelo, 2013). On the other hand, these diffusion coefficients are corrected for temperature with consideration of the temperature dependence of the viscosity of water (Parkhurst and Appelo, 2013). Detailed information about calculation of diffusive flux by using PHREEQCI is documented in the PHREEQCI's manual provided by Parkhurst and Appelo (2013). The individual tracer diffusion coefficients of species are defined in the used database Phreeqc.dat (Parkhurst and Appelo, 2013). The species, which tracer diffusion coefficients are not defined in this database, are pre-assigned by a diffusion coefficient of 1.0^{-9} m^2 s^{-1}. The model assumes that the exponent, which is utilized for calculating the pore water diffusion coefficient from the tracer diffusion coefficient, equals to 1.0 (for detail, see Parkhurst and Appelo, 2013). In total, 600 modeling steps are calculated and each step is defined for 1000 years.

The term "oil-water contact" is not restricted to the oil-water interface located between the oil and water legs. It can also widely spread across the entire reservoir thickness: (1) at the interface between oil and irreducible water in the oil leg of a water-wet reservoir and (2) at the interface between pore water and residual oil absorbed on mineral surfaces in the water leg. In the Siri reservoir's sandstones, residual oil was commonly observed on the surface of glauconite grains and is surrounded by berthierine and muscovite (see section 4.3.2). However, oil degradation proceeds in the model only within cells 7 and 8, in which the oil degradation products (CH_4, CO_2 and H_2 with a given ratio according to Seewald, 2003; see Eq. 7a) are constantly released to the pore water.

In the 1D diffusion-driven transport model, it is assumed that the oil degradation rate in the model remains constant over the entire modeled period. The degradation rate in the model is independent on the alterations (1) of the composition of the pore water (e.g., salinity) and (2) of the relative volume of oil leg to water, although the both parameters act as second-order controls on oil degradation rate (Later et al., 2006). Additionally, oil degradation rates depend on many other parameters, such as temperature, nutrient supply and thickness of oil leg (Later et al., 2003, 2006). The effects of such parameters on oil degradation rates are ignored in this model. Later et al. (2003) estimated that biodegradation rate constants are around 10^{-6} to 10^{-7} $year^{-1}$ for hydrocarbons (first order) in the degradation zones. These rate constants are in good agreement with the estimated field-

wide minimum rate constants (10^{-8} kg hydrocarbons per kg oil per year for the whole oil column; Later et al., 2003). For fresh petroleum in clastic reservoirs, degradation "fluxes" vary in the range of 10^{-3} and 10^{-4} kg petroleum m^{-2} OWC $year^{-1}$ (Later et al., 2006)[4]. With increasing temperature from 50 °C, significant oil degradation decreases and may cease around 80 °C (Head et al., 2003). A generic oil phase only consists of the *n*-alkane $C_{10}H_{22}$ fills the conceptual oil leg. It is assumed that the *n*-alkane $C_{10}H_{22}$ is degraded at the conceptual OWC in the model with a relative low rate constant of 5 x 10^{-5} kg $C_{10}H_{22}$ m^{-2} OWC $year^{-1}$, whereas the reservoir temperature accounts for 78 °C. Each cell has a cross sectional area of 0.005929 m^2 (0.077 m in length and wide). As a result, an effective oil-water-area is approximately calculated for 0.00107 m^2 with consideration of porosity (0.005929 x 0.33; 0.33: porosity). Each modeling step is pre-assigned for 1000 years. Therefore, ca. 0.7 mmoles $C_{10}H_{22}$ can be degraded during one modeling step. Additionally, it is assumed that $C_{10}H_{22}$ is completely degraded into CH_4, CO_2 and H_2 according to Seewald (2003; Eq. 7a). Correspondingly, 1 mole $C_{10}H_{22}$ can produce 4 moles CH_4, 6 moles CO_2 and 15 moles H_2. Thus, 2.8 mmoles CH_4, 4.2 mmoles CO_2 and 10.5 mmoles H_2 are added within cells 7 and 8 respectively at each modeling step.

5.3.2 Modeling results

The results of the batch modeling clearly show that calcite cementation at the OWCs cannot result from dissolution of anorthite located at the OWCs. Anorthite is the single source term for calcium in the primary mineral assemblage, whereas glauconite may also contribute calcium but with trace amounts. The developed 1D diffusive transport model aims to test whether combining (1) oil degradation at the conceptual OWC, (2) diffusive mass transport and (3) dissolution of anorthite as well as calcite clasts could have in principle resulted in the calcite cementation observed at the OWCs. Thus, the 1D diffusion-driven model considers only one conceptual OWC that is divided in two cells.

The results calculated by the 1D diffusive transport modeling show that oil degradation produces CH_4 and H_2 at the conceptual OWC. This process establishes reducing conditions and causes complete dissolution of reactive glauconite in the entire sandstone column (Fig. 61). The pre-assigned reactive glauconite of 0.951 mole $cell^{-1}$ completely dissolves after 400,000 years (no details presented here). Consequently, strong reducing conditions, which are characterized by a E_H value of ca. −577 mV, prevail in the modeled sandstone column after 600,000 years (Fig. 61). The hydrogeochemical reaction chain induced by oil degradation at the OWC keeps the modeled pH on a high level of ca. 10.6 at the final modeling step (Fig. 61). The $CH_{4(aq)}$ species dissolved in aqueous solution diffuse from the OWC towards the overlying oil leg and the underlying water leg. The high activity of aqueous ferrous iron, magnesium, aluminum and silica species, which are released by glauconite dissolution into the pore water, leads to an oversaturation regarding to berthierine and allows its

[4] m^{-2} OWC $year^{-1}$: kg of petroleum degraded per square meter of OWC area per year or kg petroleum.

precipitation. Due to the low solubility of berthierine, the iron and magnesium species are almost completely bound *in situ* to berthierine. Therefore, each cell, being independent on its location (at the OWC, or in the water or oil leg), is characterized by a same berthierine amount of 0.64 mol per cell (Fig. 61).

Redox-reactions, which evolve in the Siri oilfield's hydrogeochemical reaction chain, on the one hand reduce ferric ions of glauconite, and on the other hand oxides $CH_{4(aq)}$ to $CO_{2(aq)}$ or other carbonate species (depending on the pH of aqueous solutions). Besides glauconite dissolution, the carbonic acids can also trigger dissolution of anorthite. As a result, the pH of pore water is kept on a high level (Fig. 61). After 600,000 years, most cells contain albite with an amount of ca. one mole (Fig. 61), whereas 0.4 mole albite is pre-assigned in each cell at starting conditions. This indicates that the modeled high pH level and the high salinity of the pore water lead to albitization. After the complete consumption of glauconite and anorthite, albite dissolution buffers the pH of the pore water. On the contrary, the amount of K-feldspar (0.19 mole per cell in Fig. 61) remains unchanged compared to the starting conditions, because albite displays a higher buffering capacity against acids (van Berk et al., 2009, 2013). The 1D diffusion-driven transport model only aims to test whether dissolution of anorthite and calcite clasts could have led to the calcite cementation observed at the OWC. Thus, the calculation of this model is performed up to 600,000 years, as the primary anorthite fully dissolves. This indicates that K-feldspar will dissolve, provided that the oil degradation still proceeds.

The excess of silica and aluminum species, which are not bound to berthierine, causes muscovite formation in combination of the high potassium activity in the pore water (resulting from glauconite dissolution). In addition to glauconite, dissolution of anorthite and albite releases aluminum and silica species into the pore water. In comparison to the extremely low solubility of berthierine, the relatively higher solubility of muscovite (K-mica in the model) results in a slight enrichment of muscovite at the conceptual OWC (Fig. 61). Additionally, chalcedony newly forms to control the silica activity in the pore water (Fig. 61). At the OWC, chalcedony formation occurs most intensively.

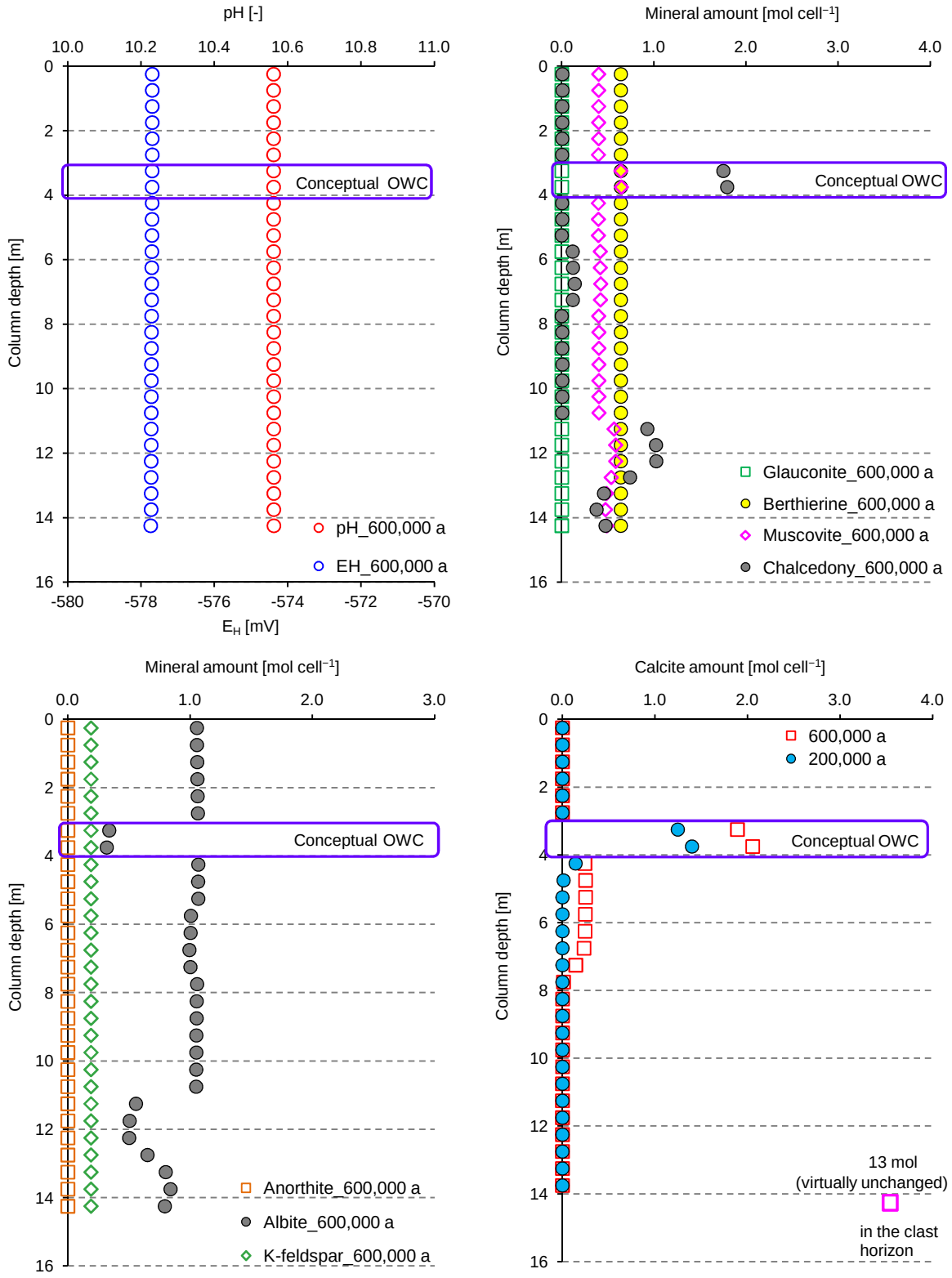

Fig. 61: Modeled pH-E_H conditions and alteration of the mineral assemblage in the sandstone column of the 1D diffusion-driven transport model. Oil column: cells 1 to 6 (0 to 3 m); conceptual OWC: cells 7 to 8 (3 to 4 m); water column: cells 9 to 28 (4 to 14 m); sandstone containing many calcite clasts: cell 29 (14 to 14.5 m); a: years.

Oil degradation at the conceptual OWC operates the source term for the inorganic carbon bound to calcite. The modeled high pH level (ca. 10.6 on average) determines that aqueous CO_3^{2-} ions dominate in the distribution of inorganic carbon. Combining calcium species provided by anorthite dissolution and the high concentration of aqueous CO_3^{2-} ions causes strong calcite formation at the OWC. Calcite formation at OWC operates a calcium sink term and reduces the calcium concentration within cells 7 und 8. Thus, a calcium concentration gradient develops, which induces diffusive mass transport of calcium species. Diffusive mass transport of calcium species towards the OWC triggers a re-equilibration between the pore water and the mineral assemblage in the oil and water legs, where anorthite dissolution continues. Consequently, dissolution of anorthite within cells 1 to 6 and 9 to 29 verifies that diffusive mass transport proceeds in the modeled column (Fig. 61). Due to diffusive mass transport, calcite intensively forms within cells 7 and 8 with a maximum amount of 2.0 moles per 5.3 kg solids (per cell) after 600,000 years (Fig. 61). This corresponds to 0.5 wt.-% TIC in the sandstone. This calculated amount of calcite at the OWC is much lower than the measured data (16.7 moles calcite per 5.3 kg solids; corresponding to 3.8 wt.-% TIC). On the other hand, oil degradation and dissolution of glauconite and feldspar keep the concentration of CO_3^{2-} species at the OWC on a higher level compared to the water and oil legs. Therefore, CO_3^{2-} species can diffuse from the OWC towards the oil and water legs. Consequently, this could lead to a calcite oversaturation of the pore water and allows calcite precipitation in the water and oil legs. Calcite is also precipitated with an average amount of 0.25 mole $cell^{-1}$ within cells 9 to 14 in the water leg after 600,000 years (Fig. 61). Correspondingly, the calculated TIC content within these cells accounts for 0.06 wt.-% of the bulk sandstone. In comparison, the core samples of the well Siri A, which are located directly below the recent and palaeo OWCs, contains much less calcite (0.01 wt.-% TIC of the bulk sandstone).

In addition to anorthite, calcite in the clast horizon is the other primary mineral containing calcium. Thus, its dissolution could also provide calcium species which are bound to the calcite cement at the OWC due to diffusive mass transport. The modeling results clearly show that the primary calcite within cell 29 (representing the sandstone containing calcite clasts) barely dissolve even after 600,000 years (Fig. 61). This is because the carbonic acids produced by oil degradation are consumed in expense of glauconite and feldspar within cells 7 and 8. Consequently, the modeling results demonstrate that calcite clasts are not the calcium source for calcite cementation at the OWC.

The chemical composition of the mineral assemblage is difficult to exactly quantify by petrographic investigations. On the one hand, several primary mineral grains display different intensities of alteration and are transformed into secondary minerals (e.g., Fig. 35). On the other hand, authigenic mineral crystals closely grow (e.g., Fig. 40). The amount of secondary $SiO_{2(s)}$ is difficult to identify by petrographic investigation due to its small grain size and widespread distribution. In addition, authigenic minerals grow partly within the primary mineral crystals (e.g., Figs. 36 and 44). However, on the basis of the observations provided by petrographic microscopy (section 4.3.2), it is

estimated that the reservoir sandstones contain 65 wt.-% quartz, 20 wt.-% glauconite, 9 wt.-% muscovite, 6 wt.-% berthierine, 1 wt.-% feldspars, pyrite and unidentified minerals in trace amounts, and no calcite (except for OWC). The calculated results of the 1D diffusion-driven transport modeling shows that

(1) 4 wt.-%[5] berthierine form, when 30% of the total glauconite as reactive glauconite dissolve (corresponding to 7.5 wt.-% of the bulk sandstone);

(2) muscovite accounts for 4 wt.-% with consideration of the primary muscovite assumed for 2 wt.-%; and

(3) 2.3 wt.-% $SiO_{2(s)}$ are newly formed. Further $SiO_{2(s)}$ can be precipitated, when potential feldspar dissolution continues in the modeling.

The amounts of authigenic minerals modeled for 600,000 years slightly differ from the observed data. This is because the estimated chemical composition of the primary mineral assemblage is based on the observations after organic-inorganic interactions. In other words, the reactive primary mineral assemblage at starting conditions is practically unavailable. Moreover, it is impossible to quantify the total mass transfer of the degraded oil components in a dynamic system, such as the Siri oilfield which is a part of the Siri Fairway. However, it can follow that

(1) more berthierine can continue to form in the model, when more reactive glauconite is available for oil degradation;

(2) the calculated amount of muscovite can increase, (1) when oil degradation induces more intensive dissolution of glauconite and K-feldspar, or (2) if the amount of the primary muscovite used in the model is underestimated compared to the geological reality; and

(3) additional dissolution of glauconite and feldspar can lead to more formation of $SiO_{2(s)}$.

Owing to data deficiency, the modeled composition of the altered mineral assemblage does not exactly coincide with the observed composition of the Siri oilfield's reservoir sandstone. However, (1) the good agreement between the modeled and observed diagenetic features (dissolution of glauconite and feldspar, formation of berthierine, secondary $SiO_{2(s)}$, and muscovite) and (2) the fairly good match between the modeled and observed mineral conversion confirm the validity of the model except for the massive calcite formation.

[5] The calculated mineral amounts in wt.-% refer to the entire reactor, in other words, to 5.3 kg solids.

5.3.3 Conclusions of 1D reactive transport modeling

In summary, a fairly good agreement between the observed and modeled alteration of the mineral assemblage confirms the validity of the hydrogeochemical model developed in this study. Similar to the batch (zero dimension) model, the calculated results of the 1D diffusion-driven transport model can reproduce dissolution of glauconite and feldspars, as well as formation of berthierine, secondary $SiO_{2(S)}$ and muscovite. No magnesium- and iron-bearing carbonate forms in the mineral assemblage of the reservoir sandstone, although the hydrogeochemical system is rich in the both components due to glauconite dissolution. More importantly, the (zero- and one-dimension) hydrogeochemical modeling results reveal that berthierine formation observed in the Siri oilfield's reservoir sandstone results from glauconite alteration, which is induced by organic-inorganic interactions. The results of the 1D diffusion-driven transport model show that diffusive transport processes lead to a calcite enrichment at the OWC. However, the calculated results of the 1D diffusive transport model clearly show that a combination (1) of oil degradation at the conceptual OWC, and (2) of dissolution of calcium-bearing minerals which operate as internal calcium sources (anorthite dissolution occurring over the entire reservoir thickness and the presence of calcite clasts) is not the reason for the massive calcite cementation observed at the OWCs in the well Siri A. It follows that a sufficient supply of aqueous calcium species from external sources must have been more efficiently provided by mass transport processes, just by a flow of a calcium-rich aqueous fluid.

5.4 Three-dimensional hydrogeochemical reactive transport modeling

A combination of the hydrogeochemical batch and 1D diffusive mass transport modeling verifies that berthierine formation is induced by glauconite alteration under reducing conditions. Moreover, this combination of both modeling types clearly demonstrates that dissolution of primary calcium-bearing plagioclase (including in-reservoir alteration of glauconite characterized by trace amounts of calcium) in the reservoir sandstones is not the main reason for the calcite cementation observed at the OWCs. As a result, an exclusion approach leads to the conclusion that three-dimensional hydrogeochemical transport processes involving aqueous calcium species must have occurred after oil charging in the Siri oilfield and are the reason for the strong calcite cementation observed. In the following study, a three-dimensional hydrogeochemical reactive transport model is built to investigate which processes caused the calcite cementation at OWCs.

5.4.1 Conceptual model

The reservoir sandstone of the well Siri A is located between two impermeable layers −the upper seal and the lower marl (Fig. 25). This indicates that a direct vertical fluid flow from the

underlying layer into the reservoir sandstone may be prevented. The role of faults is of great relevance in view of petroleum migration, overpressure development and destruction of petroleum accumulation (Karlsen and Skeie, 2006). There are two main faults that are located ca. 40 km (named as Coffee Soil Fault) and 10 km far away from the Siri oilfields, respectively (Fig. 3 in Andresen et al., 2009). The Siri Canyon Fairway can be described as a dynamic system, because its petroleum has migrated through its Paleocene sandstones for up to 70 km (Ohm et al., 2006). The oil accumulation in the Siri oilfield was soured from the Central Graben (Tail-End Graben or Søgne Basin; Ohm et al., 2006). Ohm et al. (2006) suggested that its migration from the source rocks into the Siri traps occurred around 22−18 Ma. Moreover, this oil migrated along the Coffee Soil Fault and through the Cretaceous chalk underlying the glauconitic reservoir sandstones (Ohm et al., 2006).

Seismic pumping is the main driving-force of hydrocarbon accumulation (Qu et al., 2008). Additionally, it supports migration of hydrocarbon fluids in tectonically active regions (Sibson et al., 1975) and is one of important mechanisms of hydrocarbon migration (Yan et al., 1999) besides buoyancy forces. Hydrocarbon migration induced by seismic pumping is determined by periodic seismic activities and intermittent pulse of fracture extension of the change in stress field (Yan et al., 1999). Moreover, Seismic pumping can result in fluid flow with considerable volumes following seismic faulting (Sibson et al., 1975). For instance, the outpouring of groundwater along faults was induced by seismic pumping due to earthquakes (Sibson et al., 1975, and references therein). Therefore, the “fairway” of the oil migration from the source rocks in the Central Graben along the Coffee Soil fault through the chalk is more efficient for flow of aqueous solutions due to their much lower viscosity. It follows that calcium-bearing solutions sourced from the Cretaceous chalk could have migrated along faults into the overlying glauconitic reservoir sandstone, provided that appropriate pressure gradients have developed.

Disequilibrium compaction and lateral transfer of pressure from the Central Graben in the North Sea along the Siri Canyon fairway could have generated an overpressure and caused the formation of sediment mound above the Siri Canyon during the mid-Miocene (ca. 15 Ma; Andresen et al., 2009, and references therein). Ohm et al. (2006) stated that the Coffee Soli Fault acted as a seal. Fault reactivation during the Fennoscandian uplift was probably coupled to renewed petroleum migration from the source rocks in the Tail-End Graben. Additionally, a regional tilt induced by the Fennoscandian uplift caused petroleum remigration from the Siri traps, and established a new OWC (Ohm et al., 2006). As the Siri oilfield is located in an area of high tectonic activity, widespread and intense fluid expulsion occurred during the mid-Miocene (ca. 15 Ma; Andresen et al. 2009).

In summary, flow of calcium-bearing aqueous solutions sourced from the underlying Cretaceous chalk is believed to have migrated along the Coffee Soil Fault after oil charging in the Siri oilfield into the Siri traps. If this was the case, the calcium-bearing aqueous solutions were in equilibrium with the chalk. These solutions must have moved along the recent oil-water contact due to

the different densities and displaced the pore water which was in equilibrium with the glauconitic sandstone (Fig. 62). The displacement of the aqueous solutions sourced from the chalk (abbreviated as chalk water) at the OWC could have resulted in a new equilibrium state among the minerals and the chalk water. This would have altered the pH and the species distribution of the pore water, and consequently, triggered a series of hydrogeochemical processes. For instance, the thereby induced dissolution of glauconite and/or feldspar could have increased the pH of the chalk water, subsequently enhanced the activity of the carbonate species ($aCO_3^{2-}{}_{(aq)}$) in the chalk water, and finally induced calcite formation. To prove this hypothesis, a 3D hydrogeochemical reactive transport (3DHRT) model is built up.

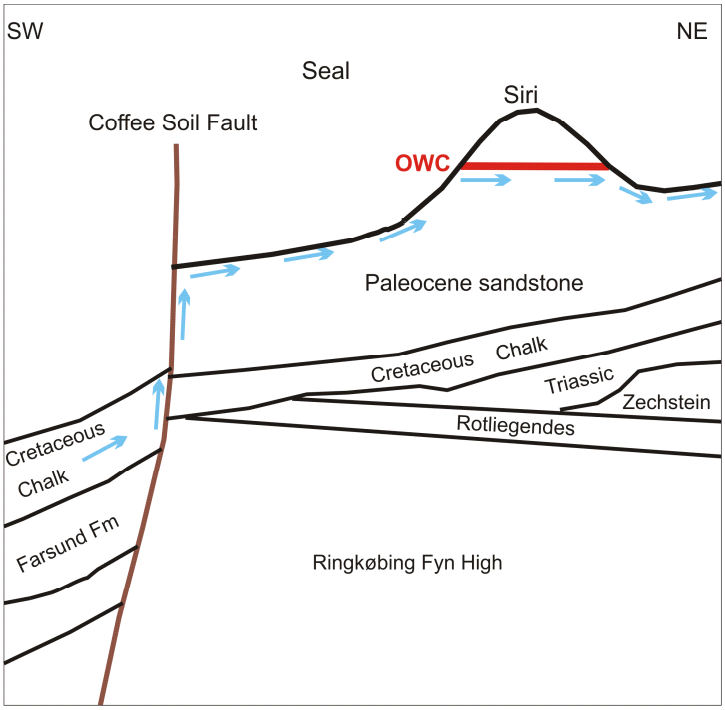

Fig. 62: Schematic (not to scale) of the conceptual model considering inflow of calcium-bearing aqueous solutions along the Coffee Soil Fault into the Siri traps along the oil-water contact (OWC; modified after Ohm et al., 2006).

5.4.2 Modeling setup

It is hypothesized that seismic pumping may have caused inflow of the chalk water along the Coffee Soil Fault into the reservoir sandstones and its further migration along the Siri OWC (section 5.4.1). The three-dimensional hydrogeochemical reactive transport (3DHRT) model aims to identify whether this hypothesis can in principle lead to the massive calcite cementation observed at the OWC. Therefore, the developed 3DHRT model does not try to reproduce the fluid flow from along the Coffee Soil Fault through the Siri Canyon Fairway. It simplifies the complex Siri Canyon Fairway system, and consequently, conceptually focuses on only one Siri trap where the well Siri A is located. Similar to the 1D diffusion-driven transport model (section 5.3), the 3DHRT considers only one conceptual OWC (the recent OWC) to test this hypothesis. If the calculated results of the 3DHRT model could verify this hypothesis, the calcite cement horizon, which is located at the depth of ca.

2093 m and is named as the palaeo OWC in this study, may have also resulted from the inflow of chalk water induced by seismic pumping at an earlier geological time.

The 3DHRT model consists of a geohydraulic and hydrogeochemical model part. On the one hand, the geohydraulic model part calculates different mass transport processes: inflow of the chalk water (calcium-bearing aqueous solutions sourced from the underlying Cretaceous chalk), diffusion transport induced by concentration gradients, dispersive transport on coupled to the inflow of the chalk water. On the other hand, the hydrogeochemical part calculates the equilibrium of species distribution among aqueous solutions, minerals and gases with consideration of oil degradation.

The computer code PHAST (Parkhurst et al., 2010) couples the computer codes PHREEQC and HST3D and is chosen as the modeling tool for calculating the 3D hydrogeochemical transport processes. It provides capacities to simulate multicomponent, reactive mass transport in 3D water-saturated flow systems (Parkhurtst et al., 2010). Thus, PHAST is applied to calculate the simultaneously occurring and coupled hydraulic and hydrogeochemical processes. The thermodynamic database Wateq4f.dat (provided by Parkhurst and Appelo, 1999), in which the equilibrium constants and their corresponding temperature dependence of all equilibrium reactions for involved aqueous species, minerals and gases are defined, is used for the 3DHRT modeling.

(1) Geohydraulic mode part

The 3DHRT model aims (1) to generally reproduce the inflow of calcium-bearing aqueous solution sourced from the Cretaceous chalk into the Siri trap and (2) to test whether this inflow could be responsible for the strong calcite cementation observed at the OWCs. Therefore, a reservoir sandstone analogue (the model) of the conceptual Siri trap A is built up in the 3DHRT model. It is composed of a 1000 m long x 3 m wide x 39 m thick section, which underlies and overlies the impermeable clay seal and marl, respectively (Fig. 63). Each coordinate direction of this section is divided by uniformly spaced nodes with a distance between two adjoining nodes of 100, 1 and 1m for the directions length, width and height, respectively. At the conceptual OWC in the model, the height direction from 28 to 31 m is more adequately discretized by a distance of 0.5 m between two adjoining nodes. The chalk water flows along the OWC in the length direction of the reservoir sandstone analogue. Additionally, it is assumed that no water recharge in the reservoir sandstone and no diffusion-driven mass transport process through the seal and marl occur. The reservoir sandstone analogue can be thus considered to be as a confined reservoir “aquifer”. In the model, the water column is 29 m in height. A 1-m thick oil-water emulsion horizon (from 29 to 30 m in height) is defined as the conceptual oil-water contact in the model. The reservoir sandstone displays the highest column of 9 m in its central part (450 to 550 m in the length). For each 50 m distance away from the central part, the height of the oil column decreases by 1 m (Fig. 63). The difference in density between

water and oil and their immiscibility restrict that the calcium-bearing solution sourced from the chalk mainly flows along the OWC and in the water leg (Figs. 63 and 64). In the model, the chalk water enters the reservoir sandstone from 0 to 0 m in length, 28 to 29 m in height, and 0 to 3 m in width. On the opposite side of the inflow of the chalk water, the same quantity of aqueous solution is simultaneously discharged from the model at the location: from 1000 to 1000 m in length, 28 to 29 m in height, and 0 to 3 m in width. These steady-state flow conditions are assumed to prevail for the entire modeled time.

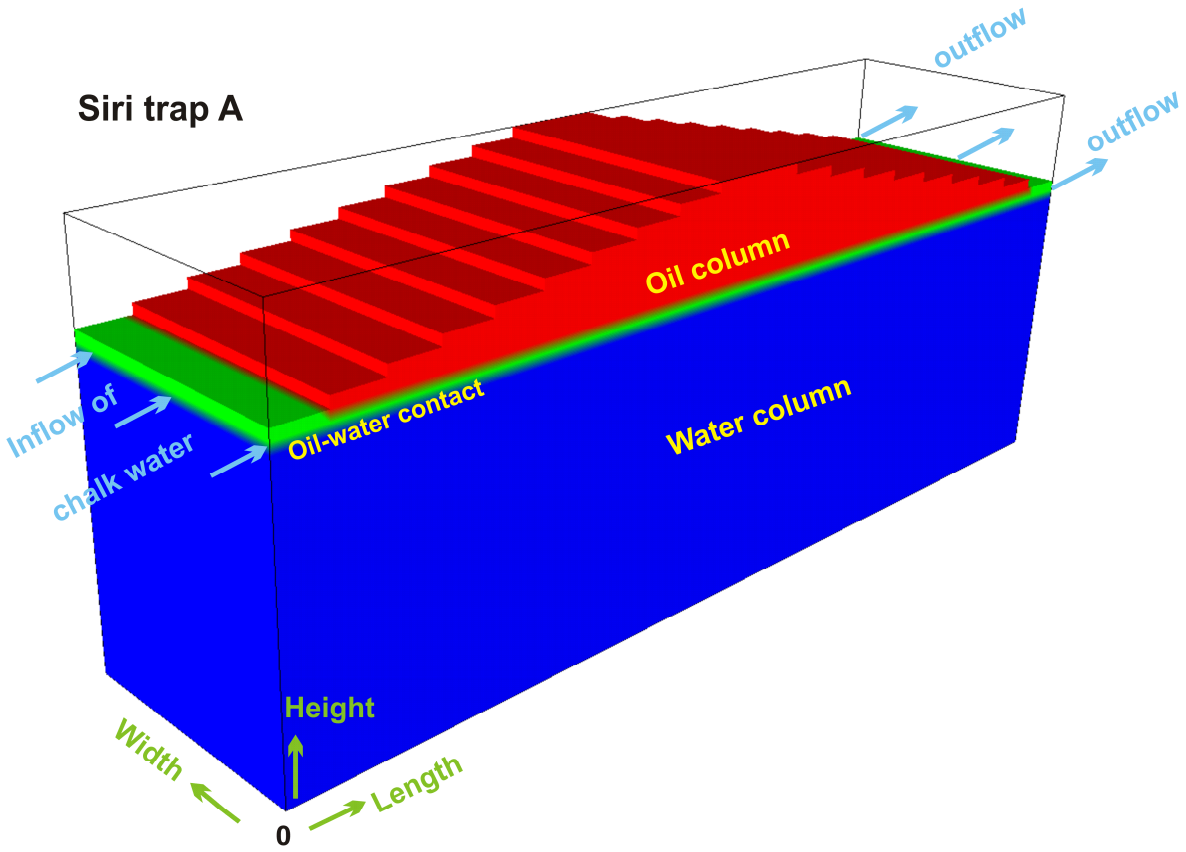

Fig. 63: Schematic (not to scale) of the reservoir sandstone of the conceptual Siri trap A, into which calcium-bearing aqueous solutions flow and along the oil-water contact. Red area: reservoir sandstone filled by oil; green area: oil-water contact; blue area: reservoir sandstone filled by pore water.

The measured permeability of the core samples from the wells Siri 3 and 4 is characterized by a broad range between 1 and 600 mD (Stokkendal et al., 2009). In the model, the reservoir parts (oil-water contact and water column), which display high permeability, have an assumed coefficient of permeability (in flow direction; kfx in Table 12) of 10^{-6} m s^{-1} (corresponding to ca. 100 mD) under reservoir conditions. The coefficients of permeability in the height direction (kfz in Table 12) are assumed to be lower than kfx by one order of magnitude, respectively. Additional hydraulic parameters (e.g., dispersivity, tortuosity) are unavailable. Consequently, they are assumed for calculating the 3DHRT model (Table 12).

The conceptual OWC in the model is defined as a 1-m thick horizon filled by an oil-water emulsion. In comparison to the water column, the presence of oil and berthierine formation induced by oil degradation at the OWC can reduce the hydraulic parameters with ongoing hydrogeochemical modeling, especially the reservoir permeability. The measured results of the experiments performed by Vaughan (1987) and Meier (2012) demonstrate that a slight decrease in porosity can dramatically reduce permeability. The computer code PHAST is incapable of considering the effects of mineral dissolution and precipitation on the thereby changes in porosity and permeability. Moreover, only one value can be defined for several hydraulic parameters in PHAST and applies to the entire modeled time, for instance, for porosity, permeability and dispersivity. The effects of mineral dissolution and precipitation on such hydraulic parameters of the sandstone at the OWC are thus ignored in this study. In consequence, the coefficients of permeability at the OWC are reduced by one order of magnitude (two orders in the height direction) due to mineral precipitation (Table 12).

Similar to the computer codes PHREEQC and PHREEQCI, PHAST can only simulate reactive mass transport processes in water-saturated flow systems. Hydrogeochemical reactions, as oil degradation and the thereby triggered glauconite alteration, can also proceed in the irreducible water of the oil leg. To reproduce hydrogeochemical processes in the oil leg and their consequences, the oil column is treated as a water column in the 3DHRT model. In other word, the oil leg is saturated by pore water in this study. It is characterized by reduced values of different hydraulic properties owing to its low content of irreducible water and to the immiscibility between oil and water (Table 12). Consequently, the hydraulic parameters (e.g., coefficient of permeability kf, effective porosity, dispersivity, tortuosity) in the oil leg are pre-assigned by much lower values compared to those in the water leg.

Table 12: Pre-assigned hydraulic parameters of the oil and water legs as well as of the conceptual oil-water contact (OWC) in the 3DHRT model.

	Oil leg	Oil-water contact	Water leg
kfx ($m\ s^{-1}$)[a]	1.0e−9	1.0e−7	1.0e−6
kfy ($m\ s^{-1}$)[a]	1.0e−9	1.0e−7	1.0e−6
kfz ($m\ s^{-1}$)[a]	1.0e−10	1.0e−9	1.0e−7
Effective porosity	0.03	0.33	0.33
Longitudinal dispersivity (m per 1 m)	0.0	1	1
Horizontal dispersivity (m per 1m)	0.0	0.1	0.1
Vertical dispersivity (m per 1m)	0.0	0.05	0.1
Diffusion coefficient ($m^2\ s^{-1}$)	1.0e−9	1.0e−9	1.0e−9
Tortuosity	0.01	0.05	0.05

[a] the assumed coefficient of permeability (kf) at the reservoir conditions in different directions; x, y and z: length, width and height, respectively.

The intensity of seismic pumping and the thereby triggered pressure gradient regulate the flux of the chalk water into the reservoir sandstone. The frequency of seismic pumping determines whether the chalk water flows into the Siri traps transiently or under steady-state conditions. Such field data are practically unavailable. Thus, a pre-assigned flux (1.0 m $year^{-1}$) is defined for the inflow of the chalk water through a cross sectional area of three m^2 directly below the OWC in the model. A total modeled time is pre-assigned for two Ma in 1000 steps. The values above described are defined in the hydraulic model part of scenario 3DHRT. Alternative modeling scenarios consider different fluxes of the inflow of the chalk water to test how this parameter affects the calculated temporal and spatial distribution of the mineral assemblage, especially of newly formed calcite.

(2) Hydrogeochemical model part

The hydrogeochemical model part defines the used chemical thermodynamic data, the rate of oil degradation at the conceptual OWC, the types of aqueous solutions in different reservoir parts, and the mineral assemblage of the reservoir sandstone.

In comparison to the computer code PHREEQCI, PHAST is incapable of calculating the pressure effects on equilibrium constants of minerals, gases and aqueous species. Wesolowski et al. (2004) claimed that many isocoulombic reactions commonly hardly display any or only very minor pressure dependence of their equilibrium constants at a constant temperature (< ca. 250 °C). The pressure effects on the equilibrium constants of dissociation and association of aqueous species are therefore ignored in the 3DHRT model. The thermodynamic database Wateq4f.dat (provided by Parkhurst and Appelo, 1999) is used to calculate chemical equilibrium and includes all equilibrium constants of species dissociation and association involved in the Siri oilfield's chemical reaction chain. On the contrary, elevated pressure conditions (e.g., 230 atm in the Siri oilfield) could markedly affect the equilibrium constants of minerals and gases involved in the hydrogeochemical reaction chain. The pressure dependence of the equilibrium constants of minerals is considered in the 3DHRT model, as these constants are separately calculated by PHREEQCI for the elevated temperature and pressure conditions and are defined in the input file of the hydrogeochemical model part. Therefore, the equilibrium constants of minerals, which are present in the primary mineral assemblage of the reservoir sandstone Siri A and/oder potentially form, are calculated by PHREEQCI for the reservoir temperature and pressure conditions (78 °C and 230 atm), for instance, glauconite, berthierine, muscovite, and so on (renamed as mineral_78_230; for detail, see Appendix A10).

The Siri oilfield's reservoir sandstones are water-wet (Stokkendal et al., 2009). Oil degradation can thus proceed in three different reservoir parts of the Siri oilfield. Hydrocarbons can partly dissolve in the irreducible water of the oil leg, although the irreducible water content in the oil leg is limited. Consequently, oil can be degraded in the oil leg. Secondly, methanogenic oil degradation occurs as a

primary mechanism at the reactive site "OWC" (Head et al., 2003; Later et al., 2006; van Berk et al., 2013). Oil degradation at OWC induces diffusion of hydrocarbons towards the OWC (Larter et al., 2006). Immiscibility between oil and water develops a concentration gradient of aqueous hydrocarbon components from the irreducible water to the water column. Thus, dissolved hydrocarbons can be constantly transported into the water column where they finally undergo degradation. The computer code PHAST can only simulate mass transport processes in water-saturated flow systems. This means that water is the single fluid phase simulated by this computer code. Due to immiscibility between oil and water, the oil phase can be regarded as an "almost insoluble mineral phase" in the model. A conceptual oil phase exclusively consisting of *n*-hexadecane ($C_{16}H_{34}$) fills the oil column of the modeled Siri trap A (the red part in Fig. 63) and is re-named as "oil" in the input file of the hydrogeochemical model part (Eq. 26). The solubility constant of aqueous *n*-hexadecane species in water, depending on temperature, pressure and salinity of aqueous solutions, is unavailable for the Siri oilfield's reservoir conditions. Consequently, an assumed solubility constant of *n*-hexadecane is used in this study (Eq. 26), which may be differ from its true constant at the same conditions. This assumed solubility constant of *n*-hexadecane under the reservoir conditions results in a concentration of aqueous *n*-hexadecane species of ca. 7.6 x 10^{-4} mol kgw^{-1} in the pore water of the oil leg and at the OWC (Table 13). The petrographic observations in thin section of the core samples taken from the water leg show that residual oil is absorbed on the surface of minerals and can be also degraded (Figs. 33 and 36). To reproduce degradation of oil components in the water leg, the pore water filling the water column is defined to contain 7.6 x 10^{-5} mol kgw^{-1} aqueous *n*-hexadecane species (Table 13).

PHASES (Eq. 26)
Oil
Hexadecane = Hexadecane
    log_K -3

Later et al. (2003) estimated that biodegradation rate constants are around 10^{-6} to 10^{-7} $year^{-1}$ for hydrocarbons (first order) in the degradation zones. Correspondingly, a biodegradation rate constant of 10^{-14} $second^{-1}$ for aqueous *n*-hexadecane species is estimated at the OWC in the 3DHRT model, which depends on the concentration of aqueous *n*-hexadecane species. Due to the high ratio of water to oil and their large contact area in the water column, the degradation rate constant of aqueous hexadecane species is pre-assigned by the same value as at the OWC. In comparison, it is assumed that oil degradation proceeds slower in the oil column (10^{-15} $second^{-1}$) due to the low irreducible water content.

It is assumed that the reservoir sandstones (in the oil and water leg, as well as at the OWC) display a homogeneous distribution of the mineral assemblage. Under the assumption of a porosity of 33%, one liter of pore water fills the pore space of a reactor which remaining volume is occupied by

the primary mineral assemblage used in the 1D diffusion-driven transport model (section 5.3; Table 11). Oil degradation and inflow of chalk water disequilibrate the equilibrium state among the primary minerals and the pore water, and therefore, can trigger formation of secondary minerals (e.g., calcite, berthierine; muscovite, dolomite, chlorite7A, siderite). In comparison to the batch and 1D diffusion-driven transport models, the 3DHRT model replaces chalcedony by quartz as secondary $SiO_{2(s)}$. On the one hand, chalcedony displays a higher solubility than quartz at the same temperature and pressure conditions (see the database Wateq4f.dat). On the other hand, the chalk water, which is assumed to flow into the Siri trap, is strongly undersaturated with regard to any silicate. This chalk water is pre-assigned to equilibrate exclusively with calcite of the Cretaceous chalk, whereas the exact chemical composition of the Cretaceous chalk underlying the glauconitic reservoir sandstone is unknown. Consequently, the higher solubility of chalcedony and the strong undersaturation of the chalk water regarding to silicate could be incapable of inducing formation of secondary $SiO_{2(s)}$ in the 3DHRT model. Thus, the 3DHRT model considers quartz as secondary $SiO_{2(s)}$ mineral to avoid such effects and aims to in principle reproduce precipitation of secondary $SiO_{2(s)}$.

The pore water filling the sandstone and the chalk water are separately calculated by the computer code PHREEQCI for the elevated temperature and pressure conditions, because the computer code PHAST is incapable of considering the pressure dependence of the equilibrium constants. The pore water in the different reservoir parts (oil and water column, as well as OWC) displays a same chemical composition except for the concentration of aqueous *n*-hexadecane species (Table 13). A one molal NaCl solution equilibrates with the primary minerals (listed in Table 11) under the reservoir conditions (78 °C and 230 atm) to calculate the composition of the pore water at starting conditions by using PHREEQCI.

The Siri traps are located ca. 1500 m above the Cretaceous chalk (assumed from Fig. 4 in Ohm et al., 2006). It is estimated that the aqueous solutions in the Siri traps differ from those in the Cretaceous chalk in temperature and pressure conditions of 45 °C and 150 bar, respectively. One liter of 0.5 molal NaCl aqueous solution equilibrates with calcite at the temperature and pressure conditions of 123 °C and 380 atm in a reactor to calculate the chemical composition of the chalk water. It is assumed that a pCO_2 level of 20 atm prevails in this reactor. This composition of the chalk water is calculated by PHREEQCI and defined as the calcium-bearing aqueous solution migrating into the conceptual Siri A trap (Table 13).

The reservoir sandstone of the well Siri A penetrates unsaturated oil (Ohm et al., 2006). It follows that the oil could still dissolve CH_4 and CO_2. Thus, the chalk water, which undergoes a high $pCO_{2(g)}$ level in the Cretaceous chalk at elevated temperature and pressure conditions (compared to the Siri traps), releases $CO_{2(g)}$ due to the changes in temperature and pressure conditions. This released $CO_{2(g)}$ could dissolve in the unsaturated oil. The capacity of oil dissolving carbon dioxide is difficult to quantify. Therefore, it is estimated in the model that the unsaturated oil can dissolve so much $CO_{2(g)}$

that the thereby developing total concentration of $CO_{2(aq)}$ in the pore water corresponds to the total concentration of $CO_{2(aq)}$ in equilibrium with a $pCO_{2(g)}$ level of 0.01 atm under the reservoir conditions. Thus, the equilibrium phases in the oil leg and at the OWC additionally includes gaseous carbon dioxide compared to the water leg.

Table 13: Chemical composition of aqueous solutions in different reservoir parts at starting conditions prior to oil degradation at the generic oil-water contact and to inflow of chalk water sourced from the Cretaceous chalk into the conceptual Siri trap A.

	Irreducible water in oil column	Pore water at OWC	Pore water in water leg	Chalk water
pH (unitless)	10.271	10.271	10.271	5.410
pe (unitless)	−5.190	−5.190	−5.190	6.024
density (kg L^{-1})	1.025	1.025	1.025	0.982
Temperature (°C)	78	78	78	123
Pressure (atm)	230	230	230	380
Al[a]	1.07e-5	1.07e-5	1.07e-5	
Ca	1.33e-1	1.33e-1	1.33e-1	1.04e-2
total $CO_{2(aq)}$[b]				1.40e-1
Cl	1.049e0	1.049e0	1.049e0	5.15e-1
Fe	3.49e-10	3.49e-10	3.49e-10	
K	8.82e-3	8.82e-3	8.82e-3	
Mg	8.28e-11	8.28e-11	8.28e-11	
Na	7.97e-1	7.97e-1	7.97e-1	5.15e-1
Si	1.15e-2	1.15e-2	1.15e-2	
Hexadecane[c]	7.58e-4	7.58e-4	7.58e-5	

[a] total concentration of aqueous species in mol kgw^{-1};
[b] total concentration of inorganic carbon species dissolved in aqueous solutions in mol kgw^{-1};
[d] total concentration of aqueous *n*-hexadecane species in mol kgw^{-1}.

These hydrogeochemical and geochemical data are included in the hydrogeochemical input file of scenario 3DHRT. Due to lacking several field data, several parameters must have been pre-assigned by assumed values for the setup of the starting conditions, for instance, flux of the chalk water, pCO_2 prevailing in the Cretaceous chalk, and $pCO_{2(g)}$ resulting in dissolution of carbon dioxide in oil. Consequently, additional modeling scenarios considering alternative values of such unknown parameters are calculated to test how these parameters affect the modeling results, especially the temporal and spatial distribution of newly formed calcite.

5.4.3 Modeling results

(1) Scenario 3DHRT

Scenario 3DHRT calculates the inflow of the calcium-bearing aqueous solution sourced from the Cretaceous chalk for steady-state conditions during a modeled period of 2.0 Ma. Its pre-assigned hydraulic data (section 5.4.2) establish a gradient of hydraulic head of one per mil between the regions of the inflow of the chalk water and its discharge (Fig. 64). In analogy to the 1D diffusion-driven transport model, several hydrogeochemical processes additionally including strong calcite formation proceed in the 3DHRT modeling.

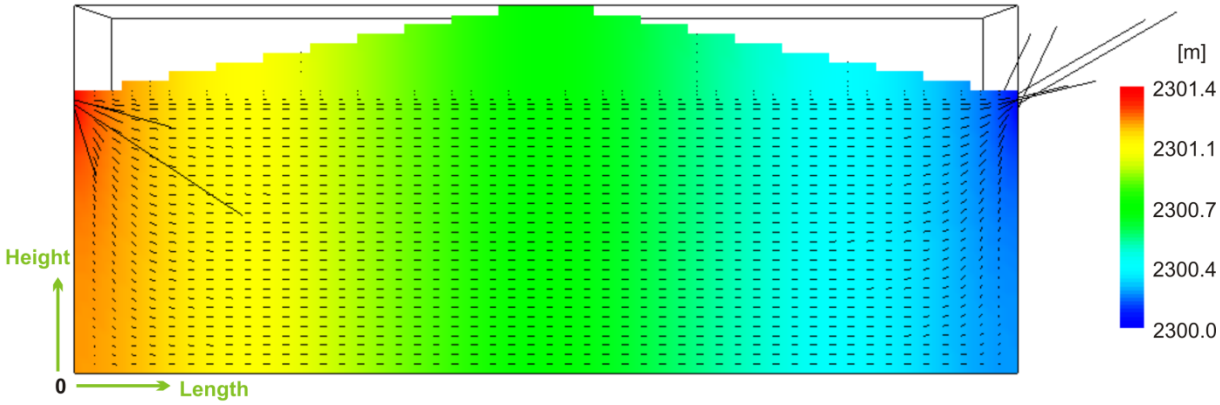

Fig. 64: Modeled distribution of hydraulic head and velocity vectors within scenario 3DHRT.

The spatial distribution of the modeled pH after a modeled period of 1.3 Ma can be roughly divided into two parts: a high pH level of 7.8 prevailing in the oil column, and a pH level of 5.6 characterizing the most reservoir parts of the water column and of the conceptual OWC (Fig. 65). Such spatial distribution of the modeled pH, which strongly vary from 5.6 to 7.8, leads to a heterogeneous spatial distribution of mineral conversion temporally developing within the reservoir sandstone analogue. Several unrealistic pH (e.g., down to 1.4 and 1.6 after 150,000 and 300,000 years, respectively, Appendix A11; the dark blue patches in Fig. 65) are calculated for the region close to the inflow of the chalk water. In close vicinity, the calculated pH reach a much higher level. This considerable pH variation is spatially very restricted, and consequently, is probably caused by numerical problems.

Glauconite dissolution proceeds differently in reservoir parts. Close to the location of the chalk water inflow, the pre-assigned reactive glauconite is completely consumed (Fig. 65). The chalk water flowing into the Siri trap A is undersaturated with regard to glauconite, which causes glauconite dissolution. In other parts of the reservoir, glauconite is less dissolved due to oil degradation and to the dispersive transport of the chalk water undersaturated with glauconite (Fig. 65). At starting conditions,

each conceptual reactor filled with one liter of pore water contains 0.38 mole anorthite (per 5.3 kg solids) and represents the entire reservoir sandstone. After 1.3 Ma, the reactive anorthite completely dissolves near the inflow of the chalk water and at the OWC (Fig. 65). Due to high pH and high salinity of pore water, albite firstly forms, but later partly dissolves due to oil degradation and an albite undersaturation of the chalk water (Fig. 65). In comparison to plagioclase, K-feldspar is fully consumed and partly transformed to muscovite (Appendix A11).

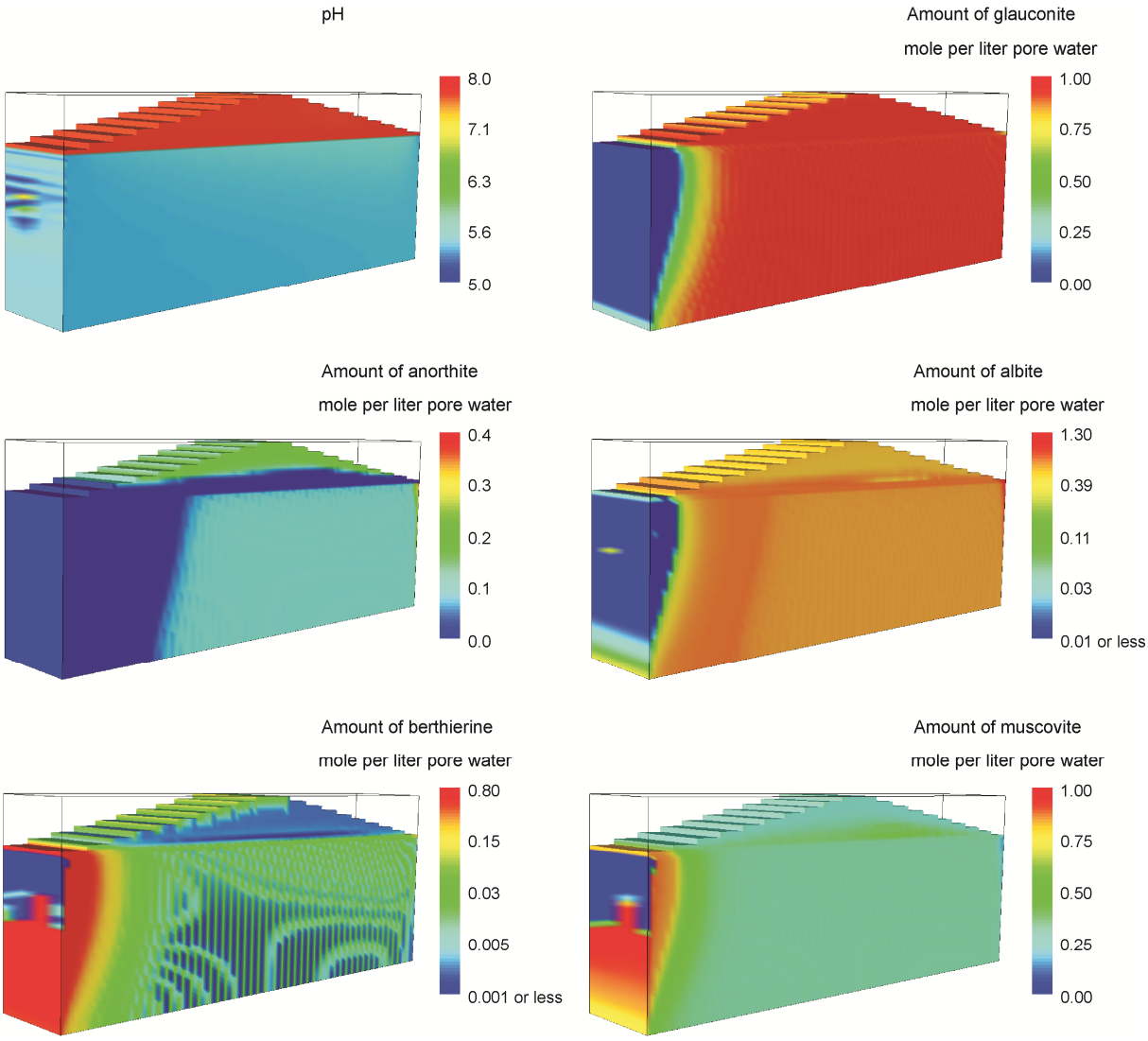

Fig. 65: Modeled distribution of pH and silicate amounts in the conceptual Siri trap A within scenario 3DHRT after a modeled time of 1.3 million years (Ma).

A consequence of glauconite dissolution is berthierine formation. It forms most strongly in the regions, where glauconite completely dissolves and at the conceptual OWC (Fig. 65). The calculated results of the batch modeling demonstrate that berthierine is exclusively transformed in expense of glauconite under reducing conditions (section 5.2.3). Consequently, the distribution of newly formed

berthierine (Fig. 66) indicates (1) that the oil degradation products CH_4 and H_2 diffuse from the oil column and OWC towards the water column, and/or (2) that the dissolved *n*-hexadecane species are transported towards the water column where they are degraded (Fig. 66). The modeled pH of the pore water in the water column are kept on a relative low level of ca. 5.6 due to inflow of the chalk water with a low pH level. However, newly formed berthierine occurs randomly in the reservoir sandstone except for the region of the chalk water inflow (Fig. 65). This distribution of secondary berthierine demonstrates that berthierine is stable under reducing conditions despite a relative low pH level (e.g., of 5.6). Close to the region of the chalk water inflow, a strong berthierine undersaturation of the chalk water leads to its dissolution at the final modeling step (Appendix A11 and Fig. 65).

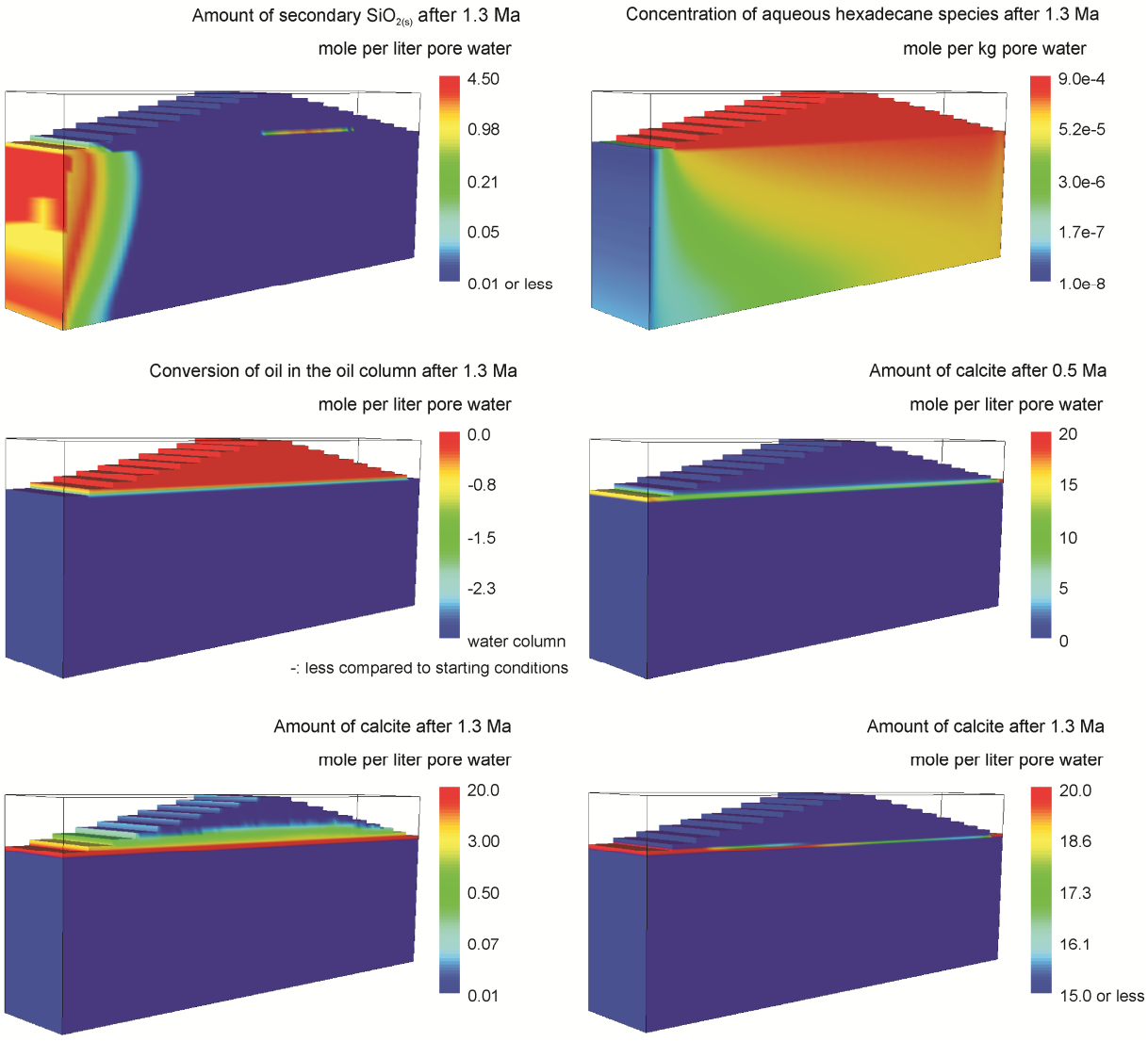

Fig. 66: Modeled distribution of the concentration of aqueous *n*-hexadecane species, of oil conversion in the oil column and of newly formed calcite in the conceptual Siri trap A within scenario 3DHRT after different modeling steps. Ma: million years.

Muscovite formation is accompanied by berthierine precipitation (Fig. 65). Similar to berthierine, muscovite almost forms in all reservoir parts except for the region directly next to the inflow of the chalk water. Muscovite is most strongly precipitated close to the chalk water inflow where also complete dissolution of glauconite occurs (Fig. 65). Dissolution of glauconite and feldspar leads to release of silica species into the pore water. The aqueous silica species, which are not bound to berthierine and muscovite, are partly removed from the pore water by formation of secondary $SiO_{2(s)}$ (Fig. 66). With ongoing simulation steps, the newly formed $SiO_{2(s)}$ partly dissolves (Appendix A11 and Fig. 66), because the chalk water is undersaturated with regard to any silicates. Secondary $SiO_{2(s)}$ is intensively precipitated close to the inflow of the chalk water, whereas glauconite completely dissolves (Fig. 66).

Diffusive mass transport processes and flow of the chalk water along the conceptual OWC results in a concentration gradient of aqueous *n*-hexadecane species after 1.3 Ma (Fig. 66). The high oil saturation in the oil leg keeps the concentration of aqueous *n*-hexadecane species in the leg on the same level for the starting conditions, although oil degradation constantly proceeds during the modeled period of 1.3 Ma. In comparison to starting conditions, a combination of several processes reduces the oil content (Fig. 66). These are (1) oil degradation, (2) diffusion transport of aqueous *n*-hexadecane species from the oil column towards to the OWC and to the water column, and (3) discharge of *n*-hexadecane species in the aqueous solution migrating from the modeled reservoir trap.

The chalk water equilibrates with calcite under a higher $pCO_{2(g)}$ level in the Cretaceous chalk prior to its inflow into the conceptual Siri trap. Such hydrogeochemical processes lead to higher calcium concentrations and a lower pH compared to the original pore water of the reservoir sandstone. The low pH level of ca. 5.4 in the chalk water results in a dominance of aqueous $CO_{2(g)}$ over other carbonate species (e.g., $HCO_3^-{}_{(aq)}$) in the distribution of carbonate species. The low pH of the chalk water induces dissolution of glauconite and feldspar, and consequently increases. Moreover, the low $pCO_{2(g)}$ level at the OWC and in the oil column, which results from the high solubility of CO_2 dissolved in the oil phase, could lead to dissolution of CO_2 in the conceptual oil phase, in other words, to CO_2 outgassing from the pore water. This process can furthermore increase the pH of the chalk water at the OWC. Consequently, the thereby triggered increase in pH of the chalk water causes an oversaturation of the pore water regarding to calcite and results in calcite formation. Figure 66 shows the temporal and spatial distribution of newly formed calcite. With increasing modeled time, newly formed calcite is constantly enriched at the OWC (Fig. 66). Calcite mainly forms at the conceptual OWC and to a lower degree within the oil leg (Fig. 66). On the contrary, the mineral assemblage of the reservoir sandstone in the water column contains no calcite (Fig. 66). After 1.3 Ma, a thin and continuous horizon is established at the conceptual OWC and stretches over the entire flow distance. In this horizon, the calculated amount of calcite cement slightly varies. On average, the calculated amount of calcite at the OWC accounts for ca. 17 moles per 5.3 kg solids (corresponding to 3.85 wt.-

% TIC), which suits the TIC measured in the bulk samples at the OWCs (3.8 wt.-%; see section 4.3.4). In comparison to the central reservoir part, more calcite forms, where the chalk water enters and leaves the conceptual Siri trap (Fig. 66). In these regions, the hydraulic data and the defined hydraulic boundary conditions dramatically change within limited distances. This could result in strong numerical problems. Except for calcite, no other carbonates (e.g., siderite or dolomite) form in the 3DHRT model, although iron- and magnesium-rich glauconite is strongly altered and even completely dissolves in several reservoir parts.

The modeling results of scenario 3DHRT can reproduce the main hydrogeochemical features as the batch and the 1D diffusion-driven transport models. All the three modeling types are checked for plausibility by a good match between the modeled results and the results of petrographic investigations (e.g., alteration of glauconite and feldspar, precipitation of berthierine, muscovite and secondary $SiO_{2(s)}$). In contrast to the batch and 1D diffusion-driven transport models, the results calculated by scenario 3DHRT are additionally capable of quantitatively reproducing the strong calcite cementation at the OWC. This good agreement between the observed and modeled data confirms the working hypothesis that inflow of calcium-bearing aqueous solutions sourced from the Cretaceous chalk resulted in the strong calcite cementation observed at the OWC.

(2) Scenario 3DHRT_flux

Scenario 3DHRT includes several parameters of which the values are assumed or pre-assigned, as such field data are practically unavailable. Although the modeling results of scenario 3DHRT well coincide with the observations in the reservoir sandstone of the well Siri A, alternative scenarios are calculated to test how such parameters affect the modeling results, especially the temporal and spatial development of newly formed calcite. One of these parameters to be tested is the flux of the chalk water. Within scenario 3DHRT_flux, only the flux of the calcium-bearing aqueous solution, which is sourced from the Cretaceous chalk, is changed to 2.0 m $year^{-1}$ compared to scenario 3DHRT with a flux of 1.0 m $year^{-1}$.

In comparison to scenario 3DHRT, the same hydrogeochemical processes proceed within scenario 3DHRT_flux: dissolution of glauconite and feldspar, formation of berthierine, muscovite, secondary $SiO_{2(s)}$ and calcite (Fig. 67 and Appendix A12). Moreover, the temporal and spatial development of most parameters displays a similar trend within the both scenarios (Fig. 67 and Appendix A12). The pH calculated in scenario 3DHRT_flux account for 7.8 and 5.5 in the oil and water column, respectively (Fig. 67). Close to the inflow of the chalk water, the calculated pH markedly vary from 5.0 to 8.0 in a small region. This could result from the numerical problems.

K-feldspar fully dissolves and is partly transformed to muscovite (Appendix A12). Alteration of glauconite and albite occurs most intensively near the inflow of the chalk water (Fig. 67 and Appendix

A12). Berthierine forms almost in the entire reservoir sandstone and most strongly, where glauconite is completely consumed (Fig. 67).

With ongoing modeled time, more calcite is enriched at the conceptual OWC (Fig. 67). In comparison to scenario 3DHRT, an increase in the flux of the chalk water can supply more calcium species within the same modeled period in scenario 3DHRT_flux, which are bound to calcite cement. Thus, the modeled intensity of calcite cementation at the OWC reaches the observed level already after 0.95 Ma (Fig. 67), whereas calcite formation with the same amount (17 moles per one liter of pore water) needs 1.3 Ma within scenario 3DHRT (Fig. 66). This indicates that an increase in the flux of the chalk water into the reservoir sandstone can markedly shorten the modeled period, within which the intensity of calcite formation achieves the same level. Moreover, an increase in the chalk water flux leads to development of a thinner horizon cemented by calcite at the OWC compared to lower flux conditions reproduced by the 3DHRT model (Figs. 66 and 67).

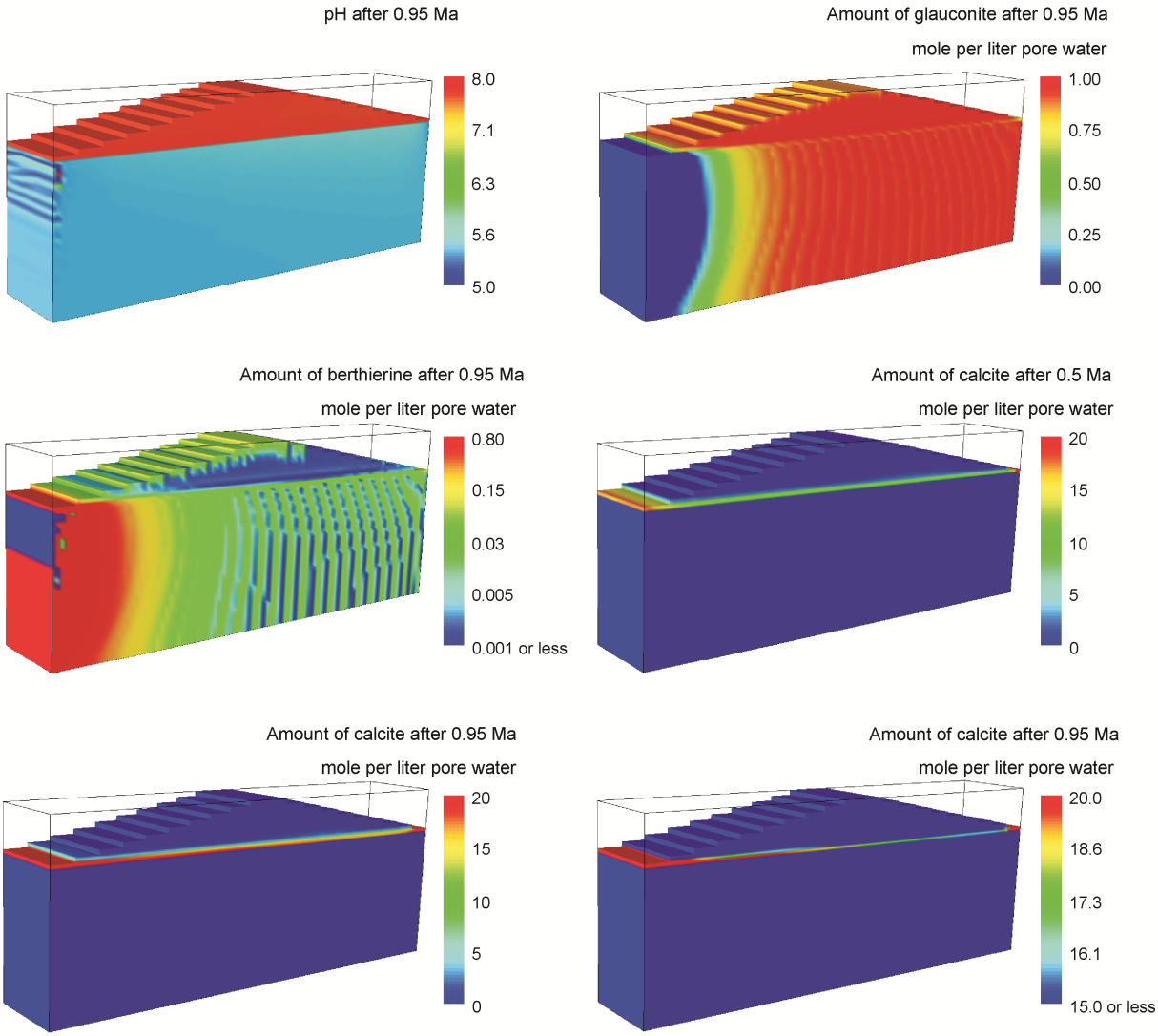

Fig. 67: Modeled distribution of pH, glauconite, berthierine and calcite within scenario 3DHRT_flux for different modeling steps. Ma: million years.

(3) Scenario 3DHRT_chalkCO2

Scenario 3DHRT_chalkCO2 aims to test how the chemical composition of the chalk water affects the modeled temporal and spatial alteration of the mineral assemblage. Thus, this scenario considers a calcium-bearing aqueous solution that equilibrates with a $pCO_{2(g)}$ level of 40 atm in the Cretaceous chalk (20 atm within scenario 3DHRT). Other parameters remain unchanged compared to scenario 3DHRT.

A higher $pCO_{2(g)}$ level of 40 atm in the Cretaceous chalk decreases the pH of aqueous solutions, and correspondingly, increases the total calcium concentration, provided that other parameters (temperature and pressure conditions as well as the salinity of solutions) remain unchanged. This high $pCO_{2(g)}$ level controls the kind of the conceptual chalk water, which is characterized by the following chemical composition at 123 °C and a total pressure of 380 atm: pH = 5.2, the total concentrations of aqueous inorganic carbon, calcium, chloride and sodium (in mol kgw^{-1}): 0.254, 0.013, 0.515, and 0.515, respectively. A slight decrease in pH of the chalk water results in minor changes in the pH of the pore water in the reservoir sandstone (Fig. 68). The temporal and spatial development of the distribution of glauconite, berthierine, secondary $SiO_{2(s)}$, muscovite and feldspar, which is calculated by scenario 3DHRT_chalkCO2, displays a similar trend in comparison to scenario 3DHRT. Thus, such modeling results are not presented here (for detail, see Appendix A13).

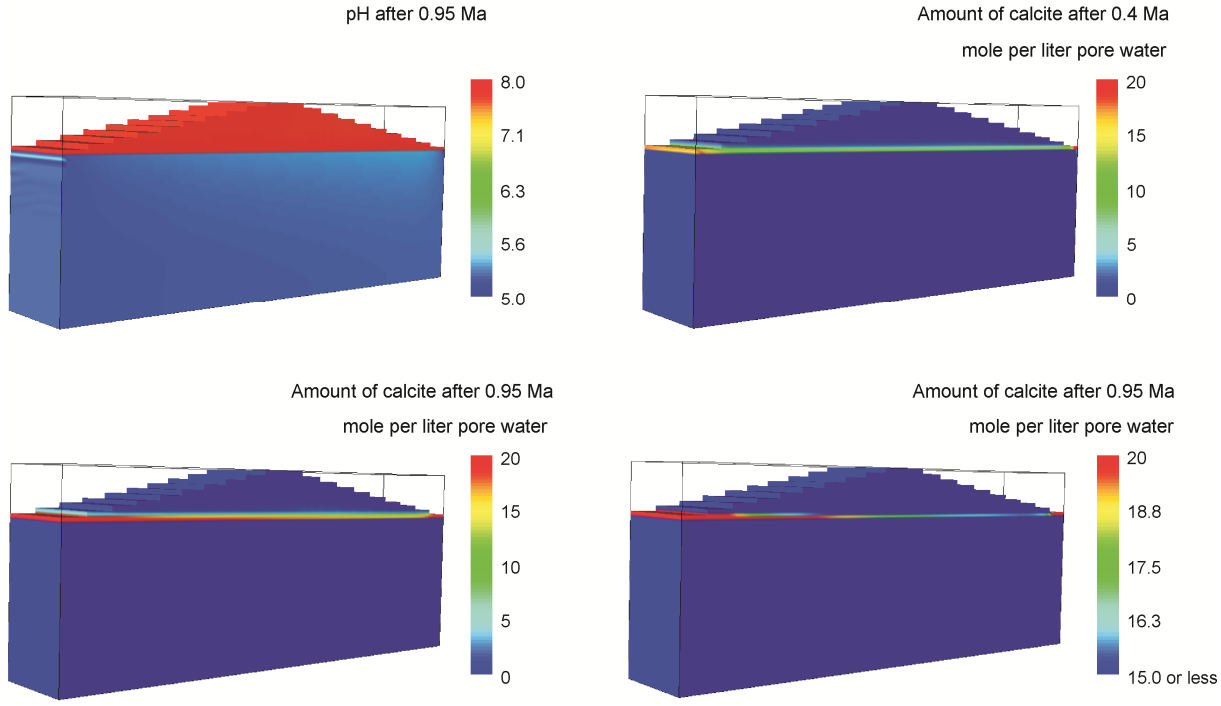

Fig. 68: Modeled distribution of pH and newly formed calcite within scenario 3DHRT_chalkCO2 for different modeling steps. Ma: million years.

A higher total calcium concentration in the chalk water provides a higher amount of calcium species into the reservoir for a same modeled period, when other parameters remain unchanged. After 0.4 Ma, a sandstone horizon cemented by calcite is established along the OWC and throughout the reservoir body (Fig. 68). The modeled degree of calcite cementation at the OWC reaches the observed level of ca. 17 moles per liter pore water (correspondingly 3.8 wt.-% TIC of the bulk sandstone) after 0.95 Ma.

(4) Scenario 3DHRT_pCO2

Dissolution of CO_2 in oil can lower oil viscosity. Under temperature and pressure conditions of 10 °C and 10 atm, the solubility of CO_2 in ester oils accounts for 0.5 in mole fraction (Fig. 5 in Bobbo et al., 2006). High solubility of CO_2 in oil can lead to CO_2-outgassing from aqueous solutions, but the effect of this process is difficult to quantify. Thus, the effect of $pCO_{2(g)}$ on dissolution of carbon dioxide in oil is assumed and pre-assigned in the model. To test its effect on the temporal and spatial evolution of the calcite cement distribution, scenario 3DHRT_pCO2 reduces the $pCO_{2(g)}$ which leads to carbon dioxide dissolution in oil by one order of magnitude compared to scenario 3DHRT. Scenario 3DHRT_pCO2 considers a $pCO_{2(g)}$ level in the oil column and at the OWC, which accounts for 0.001 atm and which results in dissolution of carbon dioxide in oil. Other parameters remain unchanged.

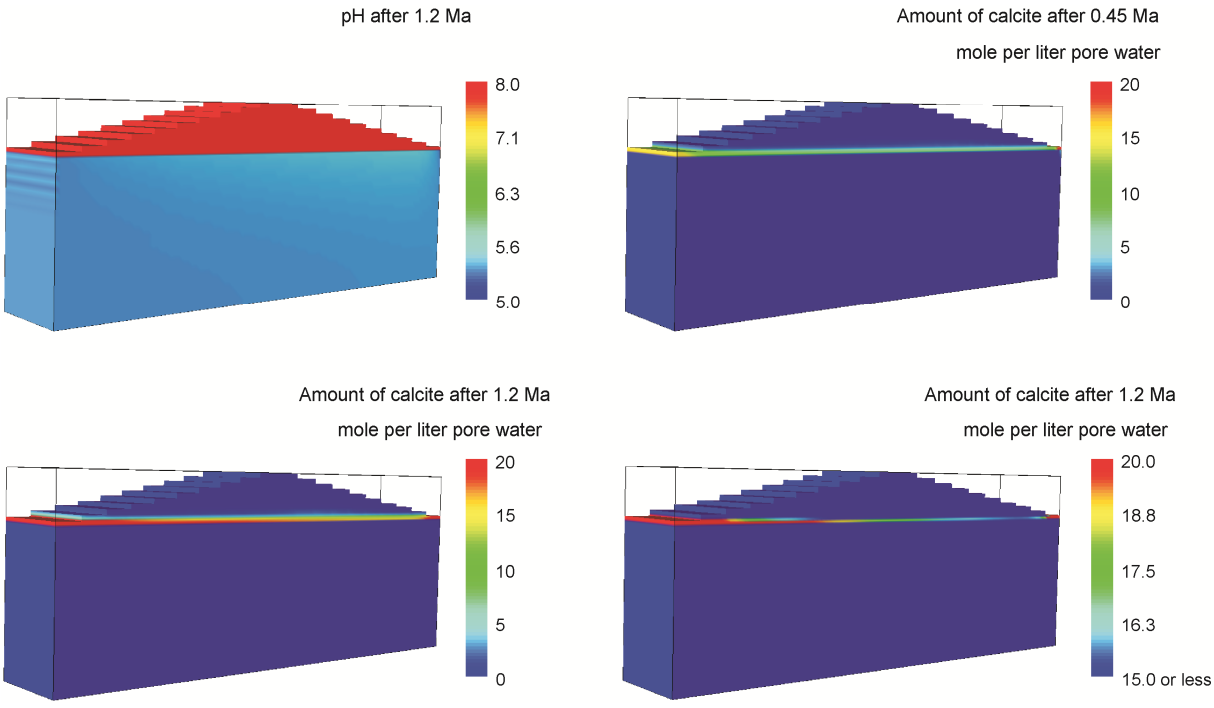

Fig. 69: Modeled distribution of pH and newly formed calcite within scenario 3DHRT_pCO2 for different modeling steps. Ma: million years.

Only the modeled pH and distribution of secondary calcite in scenario 3DHRT_pCO2 are presented here, because the modeled results of other parameters within this scenario display a similar trend compared to scenario 3DHRT (for detail, see Appendix A14). The decrease of the $pCO_{2(g)}$ level in the oil column and at the OWC slightly increases the modeled pH in the water leg as well as in the oil column (Fig. 69). Such a pH increase of the aqueous solutions enhances the activity of aqueous carbonate species. Consequently, a continuous cement horizon, which coincides with a calcite amount of 8 moles per 5.3 kg solids (in other words per one liter of pore water), develops along the OWC after 0.45 Ma. After 1.2 Ma, the modeled calcite cementation achieves the observed level (3.8 wt.-% of the bulk sandstone; corresponding to 16.7 moles calcite per liter pore water).

5.4.4 Limitations of modeling

The calculated results of the 3DHRT model and its alternative scenarios offer a reproduction of the observed diagenetic features and a quantitative retracing of the massive calcite cementation at the OWCs by using the computer code PHAST. PHAST is incapable of calculating the pressure dependence of equilibrium constants. On the contrary, the computer code PHREEQCI, which is incapable of simulating 3D transport processes, can complete this demanding task. To minimize the pressure effects, the equilibrium constants of all minerals dissolved or potentially newly formed were separately calculated by PHREEQCI and defined in the input file of the 3DHRT model. Wesolowski et al. (2004) stated that the majority of isocoulombic homogenous actions are commonly insensitive to pressure changes at a constant temperature, provided that the temperature is lower than 250 °C. Thus, the pressure effects on equilibrium constants of dissociation or association of species, which are involved in the hydrogeochemical reaction chain of the Siri oilfield's reservoir sandstone, are ignored in this study.

In reality, minerals are precipitated from pore water until they fully occupy the pore space. The computer code PHAST simulates water-saturated flow systems. Thus, calculations performed by PHAST allow mineral precipitation until the pore water involved within the system is no longer oversaturated with any minerals. Consequently, PHAST allows more minerals to precipitate than they can fully fill pore space. Thus, minerals can be unrealistically enriched at the specified sites and the intensity of mineral precipitation at other sites can be underestimated. For more exactly forecasting mineral distribution, such effects should be corrected.

The results of laboratory experiments performed by Vaughan (1987) and Meier (2012) demonstrate that a slight increase in porosity can dramatically reduce permeability. Petrographic observations of the core samples taken from the OWCs in the well Siri A clearly show that calcite cement almost totally occupies the pore space of the reservoir sandstones (section 4.3.2). The investigations of the porosity-permeability properties performed by Schovsbo (2009; pers. com.)

reveal the changes in porosity and the correlation among calcite content, porosity and permeability in the well Siri A. The measured porosity decreases from 33% in the oil and water leg, where calcite cement was not observed, to 12% in average at the OWCs which display a measured calcite content up to 40 wt.-% (Schovsbo, 2009; pers. com.). Correspondingly, the measured permeability displays a significant reduction from 250 mD (in average) in the oil and water leg to several mD (Schovsbo, 2009; pers. com.). Thus, the reservoir sandstone at the OWCs, which is strongly cemented by calcite, can be considered to be impermeable. Consequently, such calcite formation strongly affects the flow conditions, and can even redirect the flow direction with increasing intensity. However, the modeling performed by PHAST excludes this effect. The porosity-permeability properties are pre-assigned in the hydraulic model part in the computer code PHAST prior to calculations. Thus, the application of this computer code is restricted to changes in porosity-permeability properties during calculations. Consequently, the effects of mineral precipitation or dissolution on the reservoir porosity-permeability properties cannot correctly be reproduced by the 3DHRT model developed in this study. Subsequently, the flow conditions and the temporal and spatial distribution of the mineral assemblage calculated by the 3DHRT model can slightly differ from the geological reality.

5.4.5 Conclusions of 3D reactive transport modeling

The results calculated by the batch and the 1D diffusion-driven transport models highlight that (1) the single calcium-bearing primary anorthite, which is available in the entire sandstone column, and (2) the carbonate clasts and the marls underlying the glauconitic reservoir sandstone are incapable of providing sufficient amounts of aqueous calcium species to have caused the massive calcite cementation observed at the OWCs. Therefore, a 3D hydrogeochemical reactive transport (3DHRT) model considers a conceptual OWC and an external calcium source for the conceptual Siri trap. Andresen et al. (2009) suggested that tectonic activities caused widespread and intense fluid expulsion in the Siri Fairway region during the mid-Miocene (ca. 15 Ma). The 3DHRT model developed in this study assumes that calcium-bearing aqueous solutions migrated from the underlying Cretaceous chalk along the Coffee Soil Fault into the sandstones of the Siri trap and along the OWC. It considers an average flux (e.g., in m $year^{-1}$) for inflow of such chalk water under steady-state conditions over the entire modeled period. The 3DHRT model excludes kinetic calculations of mineral formation and dissolution for a total modeled time of 2.0 Ma during which rock-water-gas interactions may achieve equilibrium in oil reservoirs (e.g., less than two years in the Miller oilfield; Fu et al., 2012, 2013b). However, this model includes the kinetic degradation of petroleum components dissolved in aqueous solutions (aqueous *n*-hexadecane species in the model).

Investigations on the reservoir sandstones in the wells Siri A and Sandra A were performed by using a combination of different analytical methods, for instance, XRD, XRF, petrographic

microscopy, SEM, and HRTEM. The investigation results clearly show that the reservoir sandstones of the wells Siri A and Sandra A are characterized by different diagenetic features (section 4). The batch model, the 1D diffusion-driven transport model and the 3D hydrogeochemical reactive transport (3DHRT) model can reproduce most of the observed diagenetic features (dissolution of glauconite and feldspar, as well as precipitation of berthierine, muscovite and secondary $SiO_{2(s)}$). Moreover, the 3DHRT model is capable of quantitatively reproducing the massive calcite cementation observed at the oil-water contact (OWC). The good match between the modeled and measured content of calcite at the OWC confirms the plausibility that calcium-bearing solutions from the Cretaceous chalk migrated into the reservoir sandstones and along its OWC, where massive calcite formation took place. In the well Siri A, a horizon, which is also strongly cemented by calcite and located at the depth of 2093 m (above the recent OWC), is named "palaeo OWC" in this study. This is because that this calcite cemented horizon displays identical properties as at the recent OWC (e.g., mineralogical composition and diagenetic features; for detail, see section 4.3). Thus, the good agreement between the measured data from the recent OWC in the well Siri A and the calculated calcite content at the conceptual OWC suggests that the palaeo OWC named in this study may have resulted from the inflow of chalk water induced by seismic pumping at an earlier geological time. To additionally confirm the conclusion drawn from the modeling that the massive calcite cement resulted from inflow of chalk water, analytical investigations (e.g., isotope analysis) on the core samples cemented by calcite should be furthermore performed for determining whether the calcium ions bound to the carbonate cement are sourced from the Cretaceous chalk.

The setup of the 3DHRT model includes pre-assigned values for several parameters if they are unavailable, for instance, the chemical composition of the chalk water flowing into the reservoir sandstone, and also the flux (e.g., m $year^{-1}$) of this chalk water. Thus, calculations of alternative modeling scenarios were performed to test how such parameters affect the calculated temporal and spatial distribution of the mineral assemblage, especially of secondary calcite. The modeling results of scenarios show that

(1) calcite is constantly enriched at OWC with increasing modeled time;

(2) a greater $pCO_{2(g)}$ difference between the chalk and the reservoir sandstone increases the rate of calcite formation at OWC;

(3) a higher velocity (in other words, a greater flux) of the chalk water flowing into the reservoir sandstone accelerates the calcite formation at OWC; and

(4) the rate of calcite formation at OWC determines the thickness of the horizon cemented by calcite; in other words, a higher rate of calcite formation leads to the thinning of the horizon cemented by calcite.

There are further implications from the modeling results calculated under the pre-assigned steady-state and hydraulic-hydrogeochemical conditions. The modeling results indicate that ca. 1.0 to 2.0 Ma are needed to develop a continuous calcite cement horizon extending over ca. 1 km in the flow direction. In the geological past, the seismic pumping induced flow of aqueous solutions and must have been of transient character. As a result, the real time period, which was needed to develop such a continuous calcite cement horizon (characterized by 3.8 wt.-% TIC in the bulk sandstone) in an oil trap, could have markedly been increased, as seismic pumping was periodical and variable in their intensity compared to the calculated time period.

Andresen et al. (2009) suggested that tectonic events were activated in the Siri Fairway region during the mid-Miocene (ca. 15 Ma). This triggered intense seismic pumping, and subsequently, caused widespread and intense fluid expulsion in the Siri Fairway (Andresen et al., 2009). In combination of that, the modeling results suggest that the Siri oil traps or other oil gas traps in the Siri Fairway, which are located close to faults connecting the Cretaceous chalk to the reservoir sandstones, potentially also have horizons strongly cemented by calcite. Such calcite cement horizons should be located at the former or recent oil-water or gas-water contacts. The development of such horizons cemented by calcite in an oil or a gas trap is affected (1) by the duration of seismic pumping activities, (2) their frequency, (3) their intensity, and (4) the distance between this trap and the faults efficiently connecting the Cretaceous chalk with the reservoir sandstone. These factors (1 to 4) could regulate the degree of calcite cementation and the thickness of calcite cement horizon. Moreover, factors 1 to 4 may affect whether the calcite cement horizon laterally continues in oil or gas traps or whether calcite cements are laterally discontinuously distributed in the sandstones. Three dimensional reactive transport modeling including different scenarios allows specifying the temporal and spatial development of the distribution of the mineral assemblage alteration, especially of newly formed calcite. Moreover, it helps to evaluate the effects of rock-water-gas interactions on the porosity-permeability properties in the reservoir aquifers. Such forecasts for production-interfering processes are important and basic for successful reservoir engineering.

Figures

Tables

References cited

Abdallah, W., J.S. Buckley, A. Carnegie, J. Edwards, B. Herold, E. Fordham, A. Graue, T. Habashy, N. Seleznev, C. Signer, H. Hussain, B. Montaron, M. Ziauddin, 2007, Fundamentals of Wettability: Oilfield Review, v. 19, p. 44–61.

Andresen, K.J., O.R. Clausen, and M. Huuse, 2009, A giant (5.3×10^7 m^3) middle Miocene (c. 15 Ma) sediment mound (M1) above the Siri Canyon, Norwegian–Danish Basin: Origin and significance: Marine and Petroleum Geology, v. 26, p. 1640–1655.

Amouric, M., and C. Parron, 1985, Structure and growth mechanism of glauconite as seen by high resolution transmission electron microscopy: Clays and Clay minerals, v. 33, p. 473–482.

Arning, E.T., Y. Fu, W. van Berk, and H.-M. Schulz, 2011, Organic carbon remineralisation and complex, early diagenetic solid–aqueous solution–gas interactions: Case study ODP Leg 204, Site 1246 (Hydrate Ridge): Marine Chemistry, v. 126, p. 120–131.

Arundhathi, R., B. Sreedhar, and G. Parthasarathy, 2010, Chamosite, a naturally occurring clay as a versatile catalyst for various organic transformations: Clay Minerals, v. 45, p. 281–299.

Ayan, T., 1965, Chemical staining methods used in the identification of carbonate minerals: Bulletin of the Mineral Research and Exploration, v. 65, p. 133–147.

Azaroual, M., Fouillac, and C., Matray, J.M., 1997. Solubility of silica polymorphs in electrolyte solutions, II. Activity of aqueous silica and solid silica polymorphs in deep solutions from the sedimentary Paris Basin: Chemical Geology, v. 140, p. 167–179.

Bailey, S.W., 1988, Odinite, a new dioctahedral-trioctahedral Fe^{3+} rich 1:1 clay mineral: Clay minerals, v. 1988, p. 237–247.

Baines, S.J., and R.H. Worden, 2004, The long-term fate of CO_2 in the subsurface: natural analogues for CO_2 storage, *in* S.J. Baines and R.H. Worden eds., Geological Storage of Carbon Dioxide: Geological Society of London Special Publication, v. 233, p. 59–85.

Barth, T., 1991, Organic acids and inorganic ions in waters from petroleum reservoirs, Norwegian continental shelf: A multivariate statistical analysis and comparison with American reservoir formation waters: Applied Geochemistry, v. 6, p. 1–15.

Bobbo, S., L. Fedele, and R. Stryjek, 2006, Oil structure influence on the solubility of carbon dioxide in POE lubricants: International Refrigeration and Air Conditioning Conference at Purdue, July 17–20, 2006.

Bozau, E., 2013, Prozessmodellierung hochsalinarer Wässer mit einem erweiterten PHREEQC-Datensatz: Grundwasser, v. 18, p. 93–98.

Bearman, G., 1989, Ocean Chemistry and Deep-Sea Sediments: Pergamon Press, Sydney.

Bedrikovetsky, P.G., E.J. Mackay, R.M.P. Silva, F.M.R. Patricio, and F.F. Rosário, 2009, Produced water re-injection with seawater treated by sulphate reduction plant: Injectivity decline, analytical model: Journal of Petroleum Science and Engineering, v. 68, p. 19–28.

Berge, L.I., J.Å. Stensen, B. Crapez, and E.A. Quale, 2002, SWAG injectivity behavior based on Siri Field data: SPE75126, presented at SPE/DOE Improved Oil Recovery Symposium, Oklahoma, USA, 13–17 April 2002.

Bethke, C.M., 2008, Geochemical and Biogeochemical Reaction Modeling, second ed.: Cambridge University Press, New York, p. 435–442.

Bhattacharyya, D.P., 1983, Origin of berthierine in ironstones: Clays and Clay Minerals, v. 31, p. 173–192.

Brindley, G.W., 1982, Chemical composition of berthierines−a review: Clay and Clay Minerals, v. 30, p. 153−155.

Busenberg, E., and L.N. Plummer, 1986, The solubility of $BaCO_{3(cr)}$ (witherite) in CO_2–H_2O solutions between 0 and 90 °C, evaluation of the association constants of $BaHCO_3^+{}_{(aq)}$ and $BaCO_3^0{}_{(aq)}$ between 5 and 80 °C, and a preliminary evaluation of the thermodynamic properties of $Ba^{2+}{}_{(aq)}$: Geochimica et Cosmochimica Acta, v. 50, p. 2225–2233.

Chen, T., A. Neville, and M. Yuan, 2006, Influence of Mg^{2+} on $CaCO_3$ formation–bulk precipitation and surface deposition: Chemical Engineering Science, v. 61, p. 5318–5327.

CMG, 1999, STARS Technical Manual. Computer Modeling Group, Calgary, Canada, 4th Edition.

Dapples, E.C., 1967, Diagenesis of sandstones, *in* G. Larsen and G.V. Chilingar eds., Diagenesis in sediments: Amsterdam, Oxford, New York, Elsevier, p. 91-126.

Dean, J.A., 1999. Lange's Handbook of Chemistry, 15th ed., McGraw-Hill, Inc., New York.

Dickson, J.A. D., 1965, A modified technique for carbonates in thin section: Nature, v. 205, p. 587.

Ehrenberg, S.N., and K.G. Jakobsen, 2001, Plagioclase dissolution related to biodegradation of oil in Brent Group sandstones (Middle Jurassic) of Gullfaks field, northern North Sea: Sedimentology, v. 48, p. 703–721.

French Creek Software, Inc., 2012. Extreme Chemistry – Rigorous Solutions: DownHole SAT™, http://www.frenchcreeksoftware.com/DownHoleSAT, (accessed December 10, 2012).

Friis, H., M.L.K. Poulsen, J.B. Svendsen, and L. Hamberg, 2007, Discrimination of density flow deposits using elemental geochemistry−Implications for subtle provenance differentiation in a narrow submarine canyon, Palaeogene, Danish North Sea: Marine and Petroleum Geology, v. 24, p. 221–235.

Fritz, S.J., and T.A. Toth, 1997, An Fe-berthierine from a Cretaceous laterite: Part II. Estimation of Eh, pH and pCO_2 conditions of formation: Clays and Clay Minerals, v. 45, p. 580–586.

Fu, Y., W. van Berk, and H.-M. Schulz, 2012, Hydrogeochemical modelling of fluid–rock interactions triggered by seawater injection into oil reservoirs: Case study Miller field (UK North Sea): Applied Geochemistry, v. 27, p.1266–1277.

Fu, Y., W. van Berk, and H.-M. Schulz, 2013, Modellierung hydrogeochemischer Prozesse bei der Injektion von Meerwasser in offshore-Öllagerstätten: Erdöl Erdgas Kohle, v. 129, Jahrgang, Januar 2013, Heft 1, URBAN-VERLAG Hamburg/Wien GmbH, p. 23–28.

Fu, Y., W. van Berk, and H.-M. Schulz, 2013b, Temporal and spatial development of scale formation: one-dimensional hydrogeochemical transport modeling: Journal of Petroleum Science and Engineering, v. 112, p. 273–283.

García, A.V., 2005, Measurement and modeling of scaling minerals. Ph.D. Thesis, Technical University of Denmark.

Gilkes, R.J., R.C. Young, and J.P. Quirk, 1972, The oxidation of octahedral iron in biotite: Clays and Clay Minerals, v. 20, p. 303–315.

Gordon, L., C.C. Remer, and B. Burtt, 1954, Distribution of strontium with barium sulfate precipitated from homogeneous Solution: Analytical Chemistry, v. 26, p. 842–846.

Gunter, W.D., E.H. Perkins, and I. Hutcheon, 2000, Aquifer disposal of acid gases: modelling of water–rock reactions for trapping of acid wastes: Applied Geochemistry, v. 15, p. 1085–1095.

Hamberg, L., G. Dam, C. Wilhelmson, and T. Ottesen, 2005, Paleocene deep-marine sandstone plays in the Siri Canyon, offshore Denmark-southern Norway, *in* A.G. Doré and B.A. Vining, eds., Petroleum Geology: North-West Europe and Global Perspectives-Proceedings of the sixth Petroleum Geology Conference: Petroleum Geology Conferences Ltd, The Geological Society, London, p. 1185–1198.

Haszeldine, S., J. Lu, M. Wilkinson, and G. MacLeod, 2006, Long-timescale interaction of CO_2 storage with reservoir and seal: Miller and Brae natural analogue sites, the North Sea: Proceedings of the 8th International Conference on Greenhouse Gas Control Technologies, Trondheim, Norway.

Head, I., M., D.M. Jones, and S.R. Larter, 2003, Biological activity in the deep subsurface and the origin of heavy oil: Nature, v. 426, p. 344–352.

Helgeson, H.C., A.M. Knox, C.E. Owens, and E.L. Shock, 1993, Petroleum, oil field waters, and authigenic minerals assemblages: are they in metastable equilibrium in hydrocarbon reservoirs?: Geochimica et Cosmochimica Acta, v. 57, p. 3295–3339.

Hornibrook, E.R.C., and F.J. Longstaffe, 1996, Berthierine from the Lower Cretaceous clearwater formation, Alberta, Canada: Clays and Clay minerals, v. 44, p. 1–21.

Houston, S.J., 2007, Formation Waters in Petroleum Reservoirs; their Controls and Applications (Ph.D. Thesis): The University of Leeds, p. 69–92, Appendix V.

Houston, S.J., , B.W.D. Yardley, P.C. Smalley, and I. Collins, 2007, Rapid fluid–rock interaction in oilfield reservoirs: Geology, v. 35, p. 1143–1146.

Humphreys, B., S.A. Smith, and G.E. Strong, 1989, Authigenic chlorite in Late Triassic sandstones from the Central Graben, North Sea: Clay minerals, v. 24, p. 427–444.

Iijima, A., and R. Matsumoto, 1982, Berthierine and chamosite in coal measures of Japan: Clays and Clay minerals, v. 30, p. 264–274.

Karlsen, D.A, and J.E. Skeie, 2006, Petroleum migration, faults and overpressure, part I: Calibrating basin modelling using petroleum in traps − A review: Journal of Petroleum Geology, v. 29, p. 227−256.

Kazerouni, A.M., H. Friis, J.P.V. Hansen, 2010, Diagenetic chlorite and its relation to reservoir properties in Tyr Member sandstone, Siri Canyon, Danish North Sea: *in* P. Tuisku and J. Nemliher eds., Res Terrae, Ser. A, No.31, Proceeding of the 5th Annual Meeting of Nordic Mineralogical Network, Tallinn, 14-18, June 2010.

Kinzelbach, W., and R. Rausch, 1995, Grundwassermodellierung: eine Einführung mit Übungen: Gebrüder Borntraeger, Berlin Stuttgart, p. 38.

Kodama, H., and A.E. Foscolos, 1981, Occurrence of berthierine in Canadian Arctic desert soils: Canadian Mineralogist, v. 19, p. 279–283.

Johnson, J.W., E.H. Oelkers, and H.C. Helgeson, 1992, Supcrt92: A software package for calculation the standard molal thermodynamic properties of minerals, gases, aqueous species, and reactions from 1 to 500 bar and 0 to 1000 °C: Computers and Geosciences, v. 18, p. 899–947.

Jones, D.M., I.M. Head, N.D. Gray, J.J. Adams, A.K. Rowan, C.M. Aitken, B. Bennett, H. Huang, A. Brow, B.F.J. Bowler, T. Oldenburg, M. Erdman, and S.R. Larter, 2008, Crude-oil biodegradation via methanogenesis in subsurface petroleum reservoirs: Nature, v. 451, p. 176–180.

Larter, S., A. Wilhelms, I. Head, M. Koopmans, A. Aplin, R. Di Primio, C. Zwach, M. Erdmann, N. Telnaes, 2003, The controls on the composition of biodegraded oils in the deep subsurface—part 1: biodegradation rates in petroleum reservoirs: Organic Geochemistry, v. 34, p. 601–613.

Larter, S., H. Huang, J. Adams, B. Bennett, O. Jokanola, T. Oldenburg, M.Jones, I. Head. C. Riediger, and M. Fowler, 2006, The controls on the composition of biodegraded oils in the deep subsurface: Part II–Geological controls on subsurface biodegradation fluxes and constraints on reservoir-fluid property prediction: AAPG Bulletin, v. 90, p. 921–938.

Lee, D.R., charaterisation and the diagenetic transformation of non- and micro-crystalline silica minerals: www.geos.ed.ac.uk/homes/s0789516/microsilica.pdf.

Lu, J., M. Wilkinson, R.S. Haszeldine, and A.E. Fallick, 2009, Long-term performance of a mudrock seal in natural CO_2 storage: Geology, v. 37, p. 35–38.

Lu, J., M. Wilkinson, R.S. Haszeldine, and A.J. Boyce, 2011, Carbonate cements in Miller field of the UK North Sea: a natural analog for mineral trapping in CO_2 geological storage: Environmental Earth Sciences, v. 62, p. 507–517.

Mackay, E., T. Jones, and B. Ginty, 2012, Oilfield scale management in the Siri asset: Paradigm shift due to the use of mixed PWRI/seawater injection: SPE 154534, presented at the EAGE Annual Conference & Exhibition incorporating SPE Europec held in Copenhagen, Denmark, 4–7 June 2012.

Mackenzie, K.J.D., C.M. Cardile, and I.W.M. Brown, 1988, Thermal and mössbauer studies of iron-containing hydrous silicates, VII. Glauconite: Thermochemica Acta, v. 136, p. 247–261.

Marchand, A.M.E., P.C. Smalley, R.S. Haszeldine, and A.E. Fallick, 2002, Note on the importance of hydrocarbon fill for reservoir quality prediction in sandstones: American Association of Petroleum Geologists Bulletin, v. 86, p. 1561–1571.

McRae, S.G., 1972, Glauconite: Earth-Science Reviews, v. 8, p. 397–440.

Meier, A., 2012, Experimentelle Untersuchungen zu Reaktionen von Erdölverbindungen (n-Alkanen) mit Hämatit-Kutanen in klastischen Erdölspeichergesteinen (Ph.D. Thesis): Friedrich Schiller University Jena, p. 12–14, 69–75, and 100–106.

Meier, A., C. Ostertag-Henning, F. Holtz, P. Scholz and R. Gaupp, 2012, Experimental investigations to reactions of n-alkanes with hematite in clastic reservoir rocks: DGMK/ÖGEW-Frühjahrstagung 2012, Fachbereich Aufsuchung und Gewinnung, Celle, 19/20 April, 2012.

Merdhah, A.B.B., and A.A.M. Yassin, 2009, Scale formation due to water injection in Malaysian sandstone cores: American Journal of Applied Sciences, v. 6, p. 1534–1542.

Millero, F.J., P.J. Milne, and V.L. Thurmod, 1984, The solubility of calcite, strontianite and witherite in NaCl solutions at 25 °C: Geochimica et Cosmochimica Acta, v.48, p. 1141–1143.

Moghadasi, J., M. Jamialahmadi, and H. Müller-Steinhagen, 2003, Scale formation in oil reservoir and production equipment during water injection (Kinetics of $CaSO_4$ and $CaCO_3$ crystal growth and effect on formation damage): SPE 82233, presented at the SPE European Formation Damage Conference in the Hague, Netherlands, May 13–14 2003.

Murakami, T., S. Utsunomiya, T., Yokoyama, and T. Kasama, 2003, Biotite dissolution processes and mechanisms in the laboratory and in nature: Early stage weathering environment and vermiculitization: American Mineralogist, v. 88, p. 377–386.

Nice, P.I., H. Takabe, and M. Ueda, 2000, The development and implementation of a new alloyed steel for oil and gas production wells: NACE International, presented at CORROSION 2000 held in Orlando, 26-31 March, 2000.

Ohm, S.E., D.A. Karlsen, A. Roberts, E. Johannessen, and O. Høiland, 2006, The Paleocene sandy Siri fairway: an efficient “pipeline” draining the Prolific Central Graben?: Journal of Petroleum Geology, v. 29, p. 53–82.

Palmer, S.E., 1993, Effect of biodegradation and water washing on crude oil composition, *in* M.H. Engel and S.A. Macko eds., Organic geochemistry: Principles and applications: New York, Plenum Press, p. 511–534.

Parkhurst, D.L., and C.A.J. Appelo, 1999, User's guide to PHREEQC (Version 2) – A computer program for speciation, batch-reaction, one-dimensional transport, and inverse geochemical calculations: U.S. Geological Survey. Water-Resources Research, Inv. Rep. 99–425, U.S. Geological Survey, Denver, Colorado.

Parkhurst, D.L., K.L. Kipp, and S.R. Charlton, 2010, PHAST Version 2−A program for simulating groundwater flow, solute transport and multicomponent geochemical reactions: U.S Geological Survey, Techniques and Methods 6−A35.

Parkhurst, D.L., and C.A.J. Appelo, 2013, Description of input and examples for PHREEQC version 3−A computer program for speciation, batch-reaction, one-dimensional transport, and inverse geochemical calculations: U.S. Geological Survey Techniques and Methods, book 6, chap. A43, 497 p., available only at http://pubs.usgs.gov/tm/06/a4 3/.

Pe-Piper, G., and S. Weir-Murphy, 2008, Early diagenesis of inner-shelf phosphorite and iron-silicate minerals, Lower Cretaceous of the Orpheus graben, southeastern Canada: Implications for the origin of chlorite rims: AAPG Bulletin, v. 92, p. 1153–1168.

Pettijohn, F.J., P.E. Potter, and R. Siever, 1987, Sand and Sandstone, 2nd ed., Springer-Verlag, New York Inc., p. 187.

Pichler, H., and C. Schmitt-Riegraf, 1993, Gesteinsbildende Minerale im Dünnschliff: 2., völlig neu bearbeitete Auflage mit Fotos von Manfred Pfleghaar: 436 Einzelabbildungen, 16 Farbbilder, 22 Tabellen, 1 Farbtafel: Ferdinand Enke Verlag Stuttgart.

Puchelt, H., 1978, Abundance in rock-forming minerals (I) and barium minerals (II), *in* K.H. Wedepohl eds., Handbook of Geochemistry II-4: Springer-Verlag, Berlin, Heidelberg, New York, p. 56-D.

Qu, F., Q. Chen, C. Lian, J. Zhang and F. Cai, 2008, Distribution and accumulation of oil and gas in southern Huanghua Depression. Petroleum Exploration and Development, v. 35, p. 294–300.

Raju, K.U., and H.A. Nasr-El-Din, 2004, Calcium sulphate scale: Field tests and model predictions: NACE 04397, NACE International.

Rivard, C., M. Pelletier, N. Michau, A. Razafitianamaharavo, I. Bihannic, M. Abdelmoula, J. Ghanbaja, and F. Villiéras, 2013, Berthierine-like mineral formation and stability during the interaction of kaolinite with metallic iron at 90 °C under anoxic and oxic conditions: American Mineralogist, v. 98, p. 163–180.

Rivas-Sanchez, M.L., L.M. Alva-Valdivia, J. Arenas-Alatorre, J. Urrutia-Fucugauchi, M. Ruiz-Sandoval, and M.A. Ramos-Molina, 2006, Berthierine and chamosite hydrothermal: genetic guides in the Pena Colorada magnetite-bearing ore deposit, Mexico: Earth Planets Space, v. 58, p. 1389–1400.

Rooksby, S.K., 1991, The Miller field, blocks 16/7b, 16/8b UK North Sea, *in* I.L. Abbotts eds., United Kingdom Oil and Gas Fields, 25 years: Commemorative Volume: Geological Society of London Memoir, v. 14, p. 159–164.

Ryan, P.C., and S. Hillier, 2002, Berthierine/chamosite, corrensite, and discrete chlorite form evolved verdine and evaporite-associated facies in the Jurassic Sundance Formation, Wyoming: American Mineralogist, v. 87, p. 1607–1615.

Ryan, P.C., and R.C. Reynolds Jr., 1996, The origin and diagenesis of grain-coating serpentine-chlorite in Tuscaloosa Formation sandstone, U.S: Gulf Coast: American Mineralogist, v. 81, p. 213–225.

Rice University Brine Chemistry Consortium, 2009, ScaleSoftPitzer™ (Version 13.0): Energy & Environmental Systems Institute, Rice University, Houston TX 77005. http://cohesion.rice.edu/engineering/brinechemistry/emplibrary/ACF3404.xls, (accessed October 08, 2012).

Sass, B.M., N. Gupta, J.A. Ickes, M.H. Engelhard, D.R. Baer, P. Bergman, and C. Byrer, 2002, Interaction of rock minerals with carbon dioxide and brine: a hydrothermal investigation: Journal of Energy & Environmental Research, v. 2, p. 23–31.

Schovsbo, N.H., 2009, Siri Canyon: Isotope Study: Presentation, Geological Survey of Denmark and Greenland, Denmark (unpublished).

Seewald, J.S., 2001, Aqueous geochemistry of low molecular weight hydrocarbons at elevated temperatures and pressures: constraints from mineral buffered laboratory experiments: Geochimica et Cosmochimica Acta, v. 65, p. 1641–1664.

Seewald, J.S., 2003, Organic-inorganic interactions in petroleum producing sedimentary basins: Nature, v. 426, p. 327–333.

Sibson, R.H., J.Mc.M. Moore and A.H. Rankin, 1975, Seismic pumping − a hydrothermal fluid transport mechanism: Journal of the Geological Society, v. 131, p. 653–659.

Slack, J.F., W. Jiang, D.R. Peacor, and P.M. Okita, 1992, Hydrothermal and metamorphic berthierine from the Kidd Creek volcanogenic massive sulfide deposit, Timmins, Ontario: Canadian Mineralogist, v. 30, p. 1127–1142.

Sorbie, K.S., and E.J: Mackay, 2000, Mixing of injected, connate and aquifer brines in waterflooding and its relevance to oil field scaling: Journal of Petroleum Science and Engineering: v. 27, p. 85–106.

Stueber, A.M., 1978, Abundance in rock-forming minerals; strontium minerals, *in* K.H. Wedepohl, eds., Handbook of Geochemistry II-4: Springer-Verlag, Berlin, Heidelberg, New York, p. 38-D.

Stokkendal, J., H. Friis, J. B. Svendsen, M.L.K. Poulsen, and L. Hamberg, 2009, Predictive permeability variations in a Hermod sand reservoir, Stine Segments, Siri Field, Danish North Sea: Marine and Petroleum geology, v. 26, p. 397–415.

Thomas, M.M., J.A. Clouse, and J.M. Longo, 1993, Adsorption of organic compounds on carbonate minerals: 3. Influence on dissolution rates: Chemical geology, v. 109, p. 227–237.

Thompson, G.R., and J. Hower, 1975, The mineralogy of glauconite: Clays and Clay minerals, v. 23, p. 289–300.

Tissot, B.P., and D.H. Welte, 1987, Petroleum formation and occurrence: A new approach to oil and gas exploration: Springer-Verlag, Berlin Heidelberg New York, p. 188–190.

Todd, A.C., and M.D. Yuan, 1992, Barium and strontium sulfate solid solution scale formation at elevated temperatures: SPE Production Engineering, v. 7, p. 85–92.

Turekian, K., 1968, Oceans: Prentice-Hall, Englewood, Cliffs, NJ.

van Berk, W., H.-M. Schulz, and Y. Fu, 2009, Hydrogeochemical modelling of CO_2 equilibria and mass transfer induced by organic–inorganic interactions in siliciclastic petroleum reservoirs: Geofluids, v. 9, p. 253–262.

van Berk, W., H-.M. Schulz, and Y. Fu, 2013, Controls on CO_2 fate and behavior in the Gullfaks oilfield (Norway): how hydrogeochemical modeling can help decipher organic-inorganic interactions: AAPG Bulletin, v. 97, p. 2233–2255.

Vaughan, P.J., 1987, Analysis of permeability reduction flow of heated, aqueous fluid through Westerly Granite, *in* C.F. Tsang eds., Coupled processes associated with nuclear waste repositories: Academic Press, New York, p. 529–539.

Vieillard, P., 2000, A new method for the prediction of Gibbs free energies of formation of hydrated clay minerals based on the electronegativity scale: Clays and Clay Minercals, v. 48, p. 459–473.

Vieillard, P., 2007, THERMOCHIMIE - Estimation des enthalpies de formation des phyllosilicates anhydres (7 Å , 10 Å et 14 Å): Hydrasa- UMR, v. 6269. p. 20.

Vieillard, P. and R. Mathieu, 2009, A predictive model for the enthalpies of hydration of zeolites: American Mineralogist, v. 94, p. 565–577.

Vieillard, P., P. Blanc, C.I. Fialips, H. Gailhanou, and S. Gaboreau, 2011, Hydration thermodynamics of the SWy-1 montmorillonite saturated with alkali and alkaline-earth cations: A predictive model: Geochimica et Cosmochimica Acta, v. 75, p. 5664–5685.

Wagman, D.D., W.H. Evans, V.B. Parker, R.H. Schumm, I. Halow, S.M. Bailey, K.L. Churney, R.L. Nuttall, 1982, The NBS tables of chemical thermodynamic properties: selected values for inorganic and C1 and C2 organic substances in SI units: Journal of Physical and Chemical Reference Rata, v. 11, Supplement no. 2.

Wallander, H., and T. Wickman, 1999, Biotite and microcline as potassium sources in ectomycorrhizal and non-mycorrhizal Pinus sylvestris seedlings: Mycorrhiza, Springer-Verlag, v. 9, p. 25–32.

Weibel, R., H. Friis, A.M. Kazerouni, J.B. Svendsen, J. Stokkendal, and M.L.K. Poulsen, 2010, Development of early diagenetic silica and quartz morphologies – Examples from the Siri Canyon, Danish North Sea: Sedimentary Geology, v. 228, p 151–170.

Welton, J.E., 1984, SEM petrology atlas: The AAPG methods in exploration series, no. 4: AAPG, p.38–49 and 138–141.

Wesolowski, D.J., S.E. Ziemniak, L.M. Anovitz, M.L. Machesky, P. Bénézeth, and D.A. Palmer, 2004, Solubility and surface adsorption characteristics of metal oxides, *in* D.A. Palmer, R. Fernández-Prini and A.H. Harvey eds., Aqueous systems at elevated temperatures and pressures: Physical chemistry in water, steam and hydrothermal solutions: Elsevier, p. 493–595.

Wiewióra, A., A. Wilamowski, B. Łącka, M. Kużniarski and D. Grabsaka, 1998, Chamosite from oolitic ironstones: The necessity of a combined XRD–EDX approach: The Canadian Mineralogist, v. 36, p. 1547–1557.

Worden, R.H., and S. Morad, 2003, Clay minerals in sandstones: controls on formation, distribution and evolution, *in* R.H. Worden and S. Morad eds., Clay mineral cements in sandstones: International Association of Sedimentologists Special Publications, v. 34, p. 3–41.

Wylde, J.J., G.D.M. Williams, F. Careil, P. Webb, and A. Morris, 2006, Deep downhole chemical injection on BP-operated Miller: experience and learning: SPE 92832, presented at the 2005 SPE International Symp. Oilfield Chemistry Houston, Texas, USA, 2–4 February 2005, SPE Production & Operations, v, 21, p. 188–193.

Xu, H., and D.R. Veblen, 1996, Interstratification and other reaction microstructures in the chlorite-berthierine series: Contributions to Mineralogy and Petrology, Springer-Verlag, v. 124, p. 291–301.

Xu, T., J.A. Apps, and K. Pruess, 2004, Numerical simulation of CO_2 disposal by mineral trapping in deep aquifers: Applied Geochemistry, v. 19, p. 917–936.

Yan, F., D. Jia, H. Lu, and G. Xu, 1999, Seismic pumping mechanism of hydrocarbon migration in Dongying Depression, Shandong, China: Oil and Gas Geology, v. 20, p. 295–298.

Yuan, M.D., and A.C. Todd, 1991, Prediction of sulphate scaling tendency in oilfield operations: SPE 18484, SPE Production Engineering, v. 6, p. 63–72.

Yuan, M.D., A.C. Todd, and K.S. Sorbie, 1994. Sulphate scale precipitation arising from seawater injection: a prediction study: Marine and Petroleum Geology, v. 11, p. 24–30.

List of abbreviations

1DHT:	One-dimensional hydrogeochemical transport
1DRM:	One-dimensional reactive mixing
1DNRM:	One-dimensional non-reactive mixing
3DHRT:	Three-dimensional hydrogeochemical reactive transport
$c_{tot}i_{(aq)}$:	Total concentration of the aqueous species i
EDX	Energy dispersive X-ray
HRTEM:	High-resolution transmission electron microscopy
kf:	coefficient of permeability
kgw:	Kilo gram water
L:	Liter
Ma:	Million years
mD:	Millidarcy
mV:	Millivolt
NRM:	Non-reactive mixing
ODP:	Oil degradation product
OWC:	Oil-water contact
φ:	Porosity
ppm:	parts per million
pCO_2:	Partial pressure of carbon dioxide
RM:	Reactive mixing
SEM:	Scanning electron microscopy
TIC:	Total organic carbon
TS:	Petrographic investigation in thin section
XRD:	X-ray powder diffraction
XRF:	X-ray fluorescence

Appendix

A1. PHREEQC input file for the separate PHREEQC exercise of section 3.2.4 (excerpt).

```
TITLE separate PHREEQC exercise

SOLUTION 1  # Parkhurst and Appele, 1999; modified according to Fu et al. (2012), and reference there ein.
pH              8.22
pe              8.451
density         1.023
units           ppm
temp            4
Ca              412.3
Mg              1291.8
Na              10768.0
K               399.1
Fe              0.002
Mn              0.0002
Si              4.28
Cl              19353.0
Alkalinity      141.682 as HCO3
S(6)            2712.0
Ba              0.02
Sr              8.1
Li              0.17
Al              0.001

END

SOLUTION 2    #formation water sample no. 5, Lu et al., 2010; additional concentration of Li, Al Zn and Si
#taken from Houston (2017) at equilibrium with secondary phases
pH              7.5
density         1.055  #assumed
units           ppm
temp            120
Ba              643
Ca              307
Mg              82
Na              25898
K               1399
Fe              1
Mn              0.1
Si              70
Cl              41767
Alkalinity      2221  as HCO3
S(6)            4
Sr              39
Li              28
Al              1
Zn              0.4

EQUILIBRIUM_PHASES 2
Barite          0.0   0.0
Celestite       0.0   0.0
Anhydrite       0.0   0.0

SAVE SOLUTION 2
END

USE SOLUTION 1
```

```
USE SOLUTION 2

MIX 11 #10% sea in the produced water
1       0.1
2       0.9

REACTION_TEMPERATURE 11
120

EQUILIBRIUM_PHASES 11
Barite          0.0 0.0
Celestite       0.0 0.0
Anhydrite       0.0 0.0

END
```

(omission of the modeling steps 2 to 74)

```
MIX 19
1       0.9
2       10.1

REACTION_TEMPERATURE 19
120

EQUILIBRIUM_PHASES 21
Barite          0.0 0.0
Celestite       0.0 0.0
Anhydrite       0.0 0.0

END
```

A2. Modeling results calculated by scenario 1DRM-MQ.

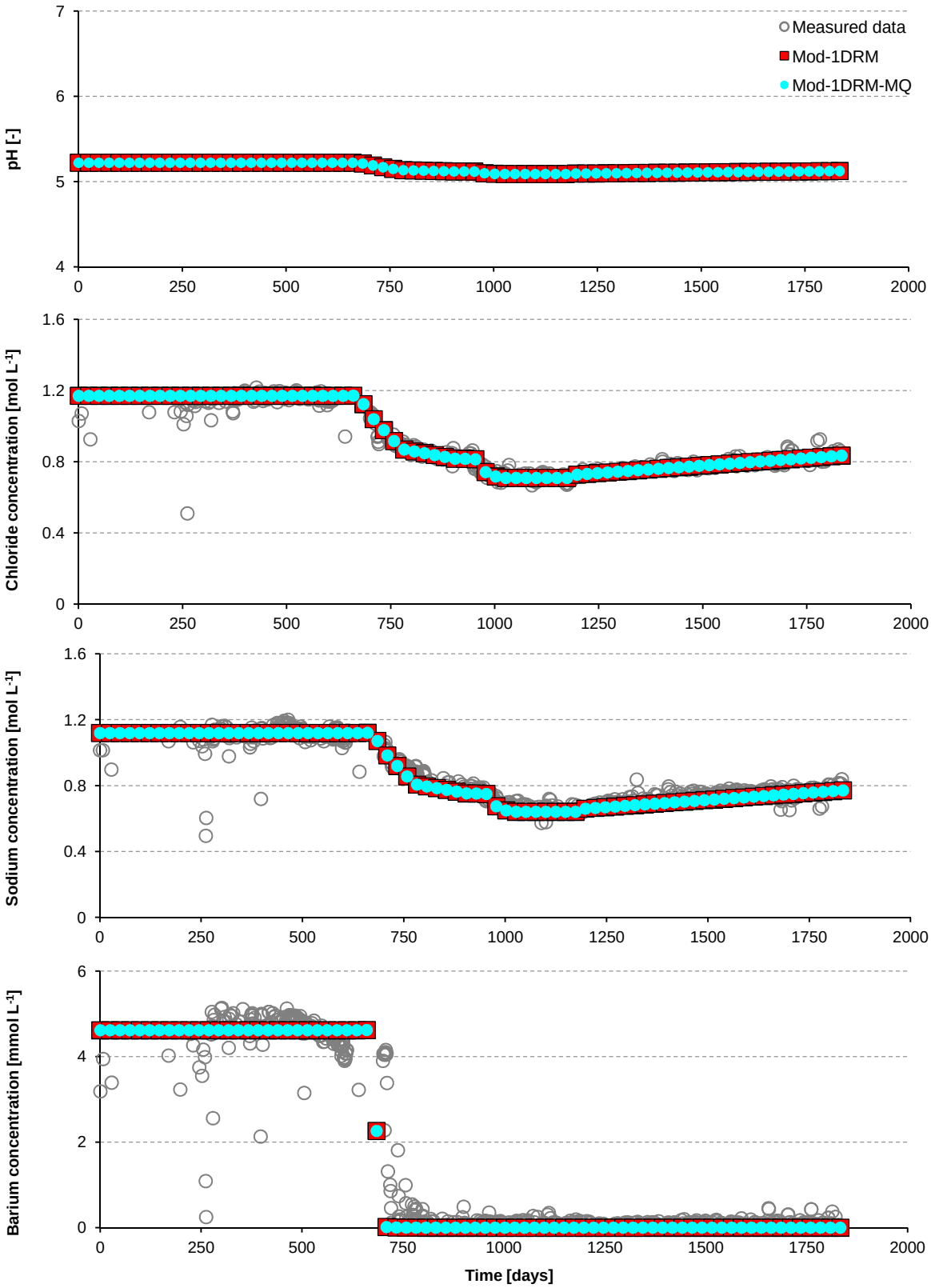

Fig. A1: Measured and modeled pH as well as concentrations of chloride, sodium and barium in the produced water calculated by scenarios 1DRM and 1DRM-MQ. Measured data: taken from Houston, 2007.

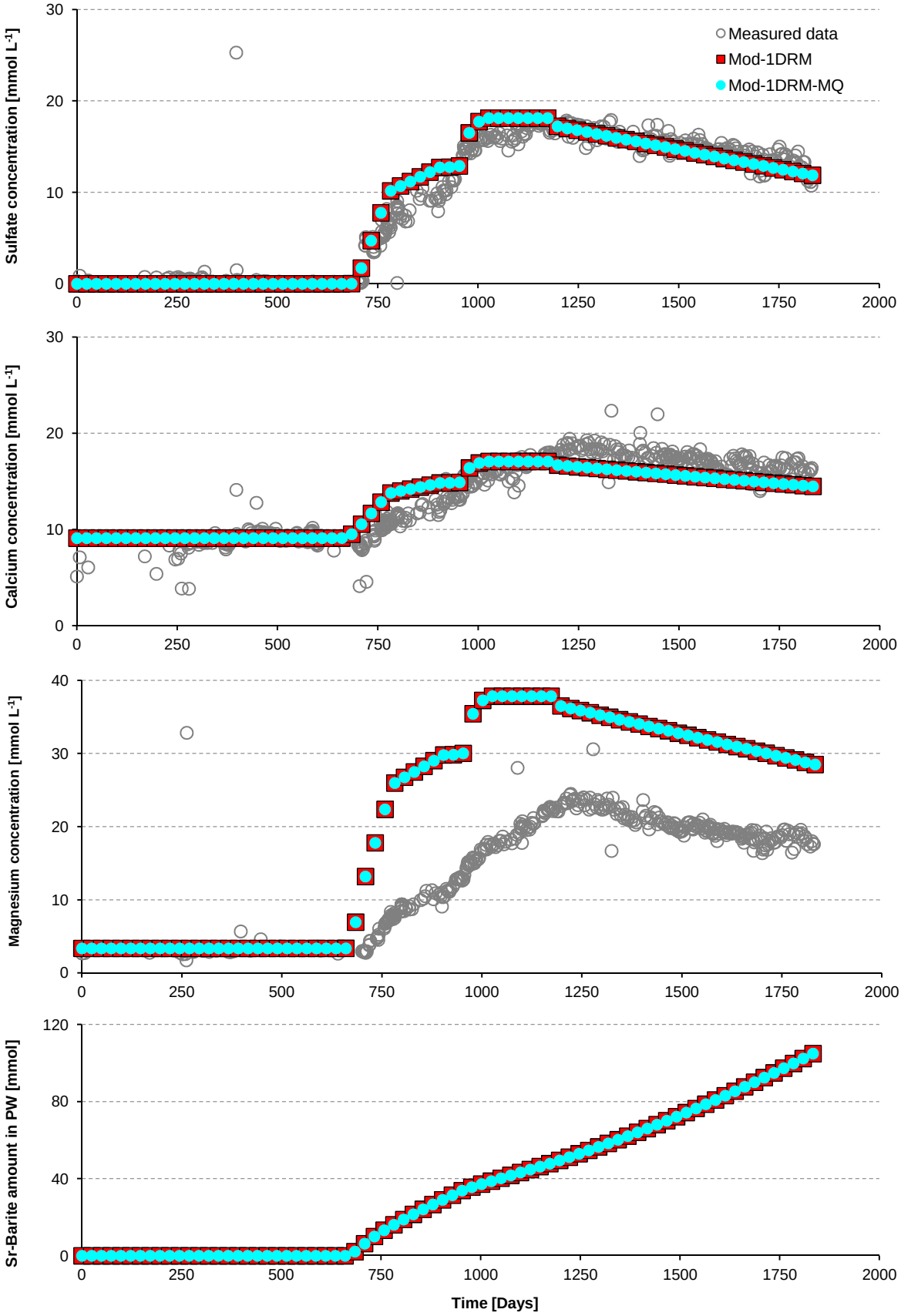

Fig. A2: Measured and modeled pH as well as concentrations of chloride, sodium and barium in the produced water calculated by scenarios 1DRM and 1DRM-MQ. Measured data: taken from Houston, 2007; PW: the production well.

A3. Modeling results calculated by scenario 1DRM-An.

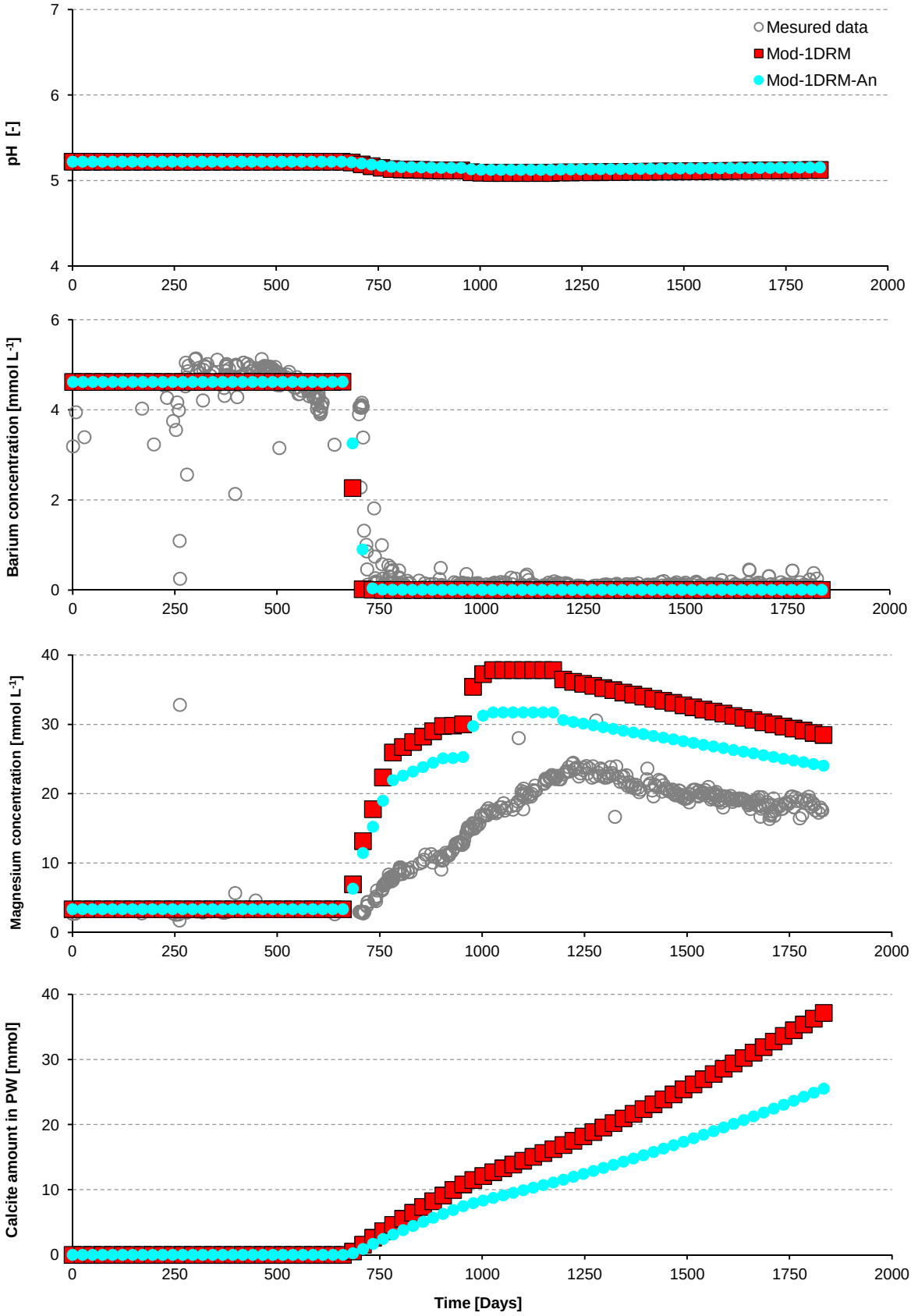

Fig. A3: Measured and modeled pH, concentrations of barium and magnesium, as well as the amount of calcite newly formed in the production well (PW) per 75 liters of produced water from scenarios 1DRM and 1DRM-An. Measured data: taken from Houston, 2007.

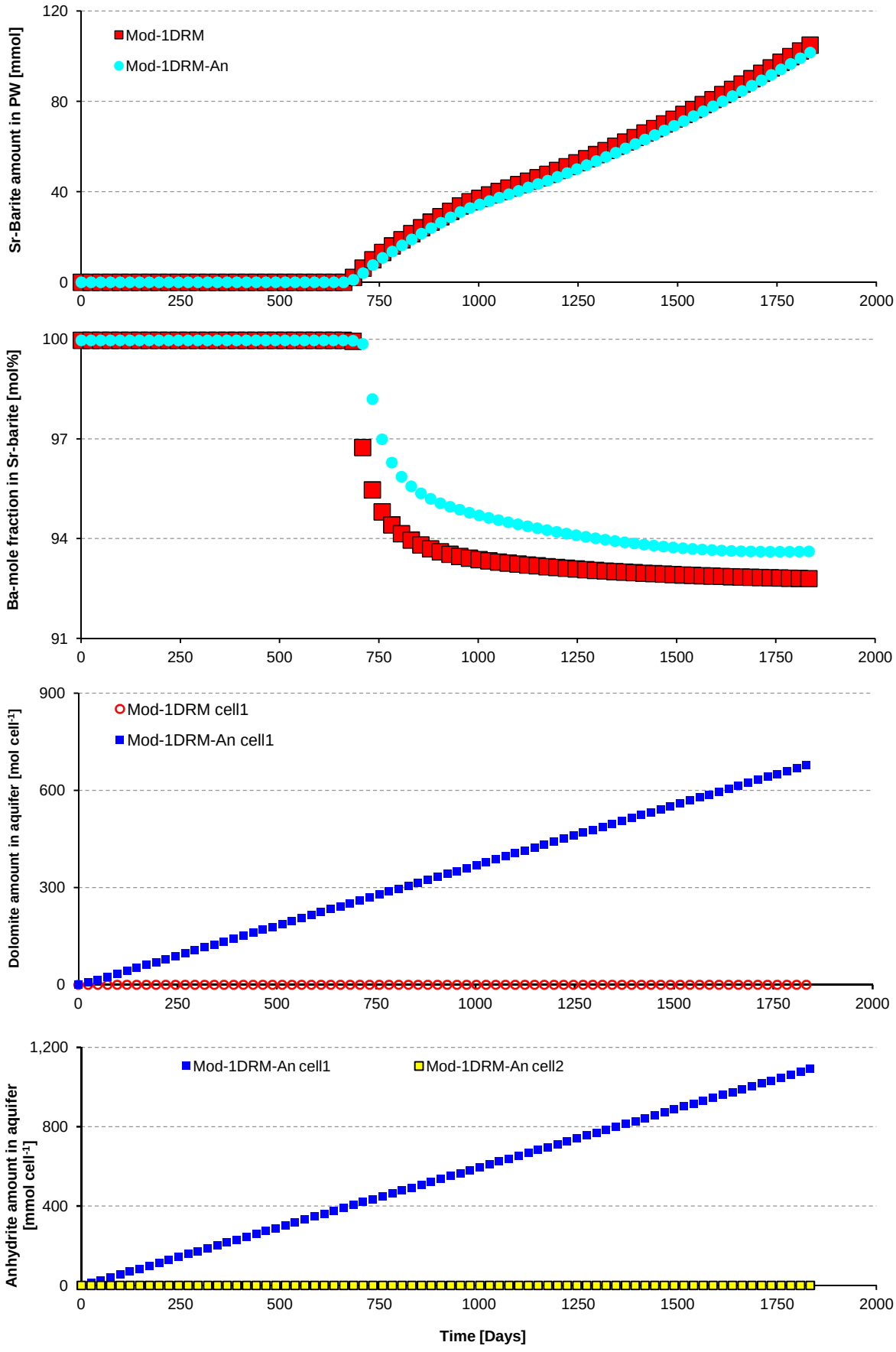

Fig. A4: Modeled amount of Sr-barite in the production well (PW), its barium mole fraction, amount of dolomite and anhydrite in aquifer per 75 liters produced water from scenarios 1DRM and 1DRM-An.

A4. Modeling results calculated by scenario 1DRM-Ex.

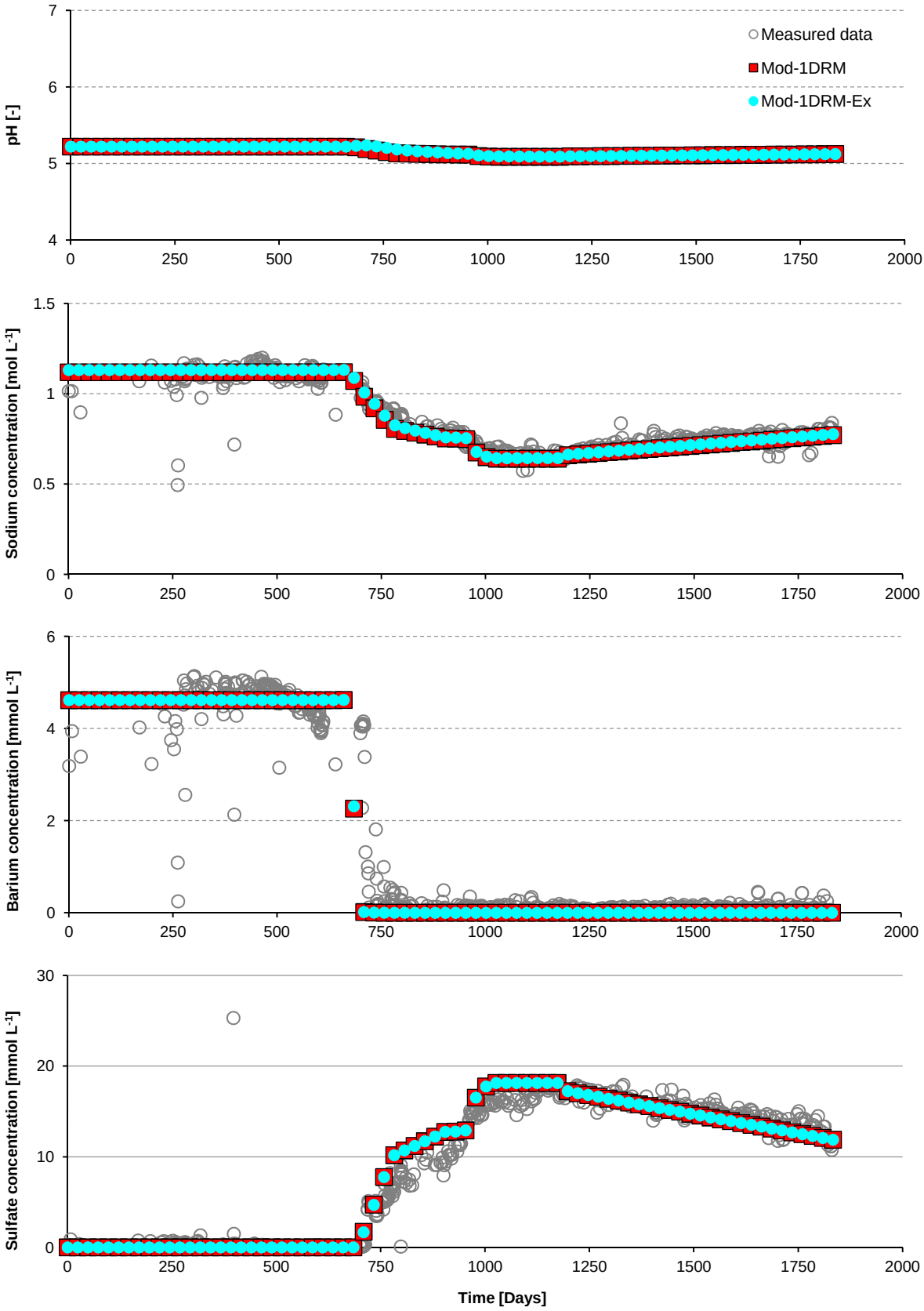

Fig. A5: Measured and modeled pH and concentrations of sodium, barium and sulfate in the produced water from scenarios 1DRM and 1DRM-Ex. Measured data: taken from Houston, 2007.

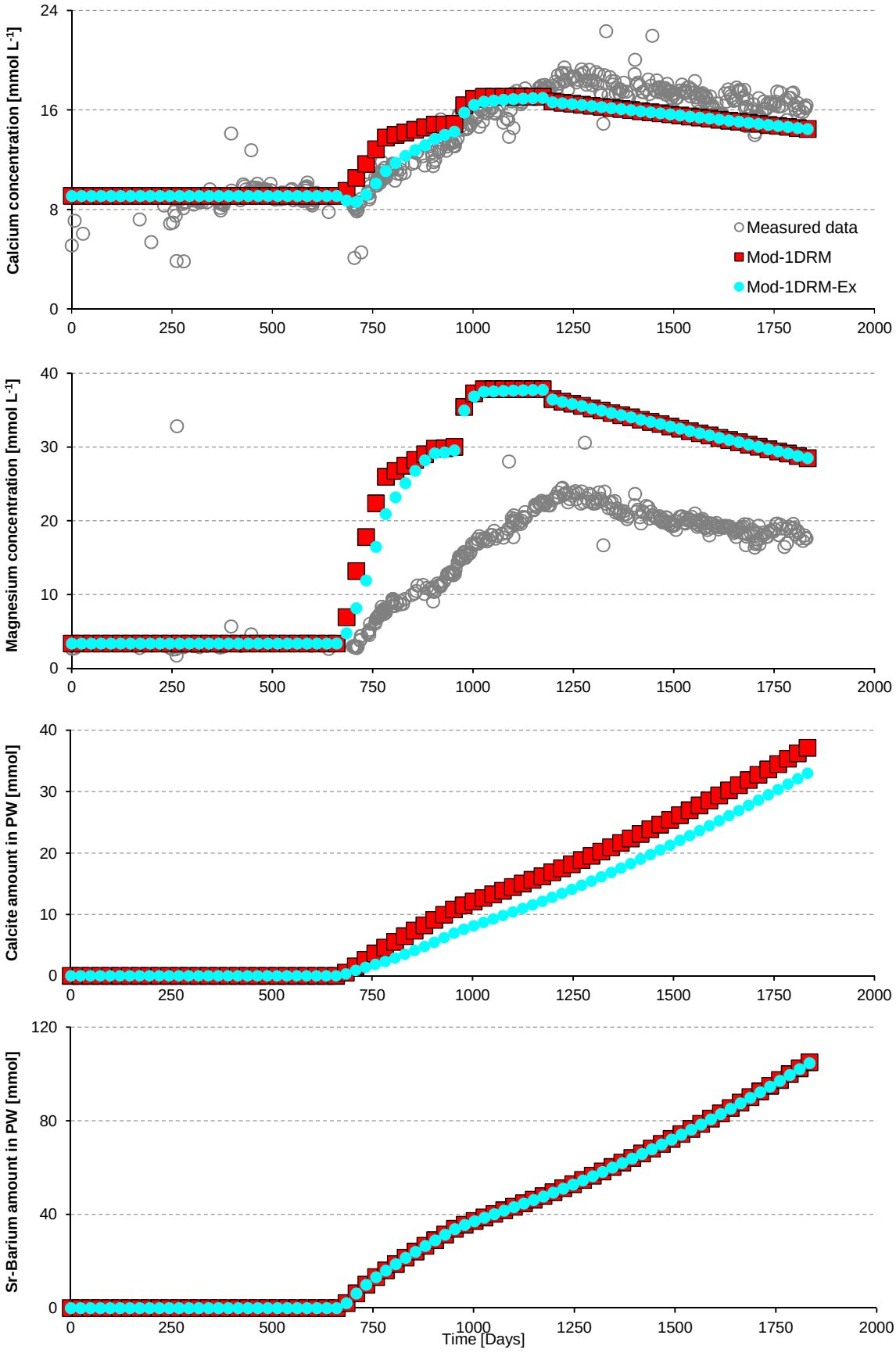

Fig. A6: Measured and modeled concentrations of calcium and magnesium as well as the amount of calcite and Sr-barite in the production well (PW) per 75 liters produced water from scenarios 1DRM and 1DRM-Ex. Measured data: taken from Houston, 2007.

A5. Modeling results calculated by scenarios 1DRM-Dis1 and 1DRM-Dis100.

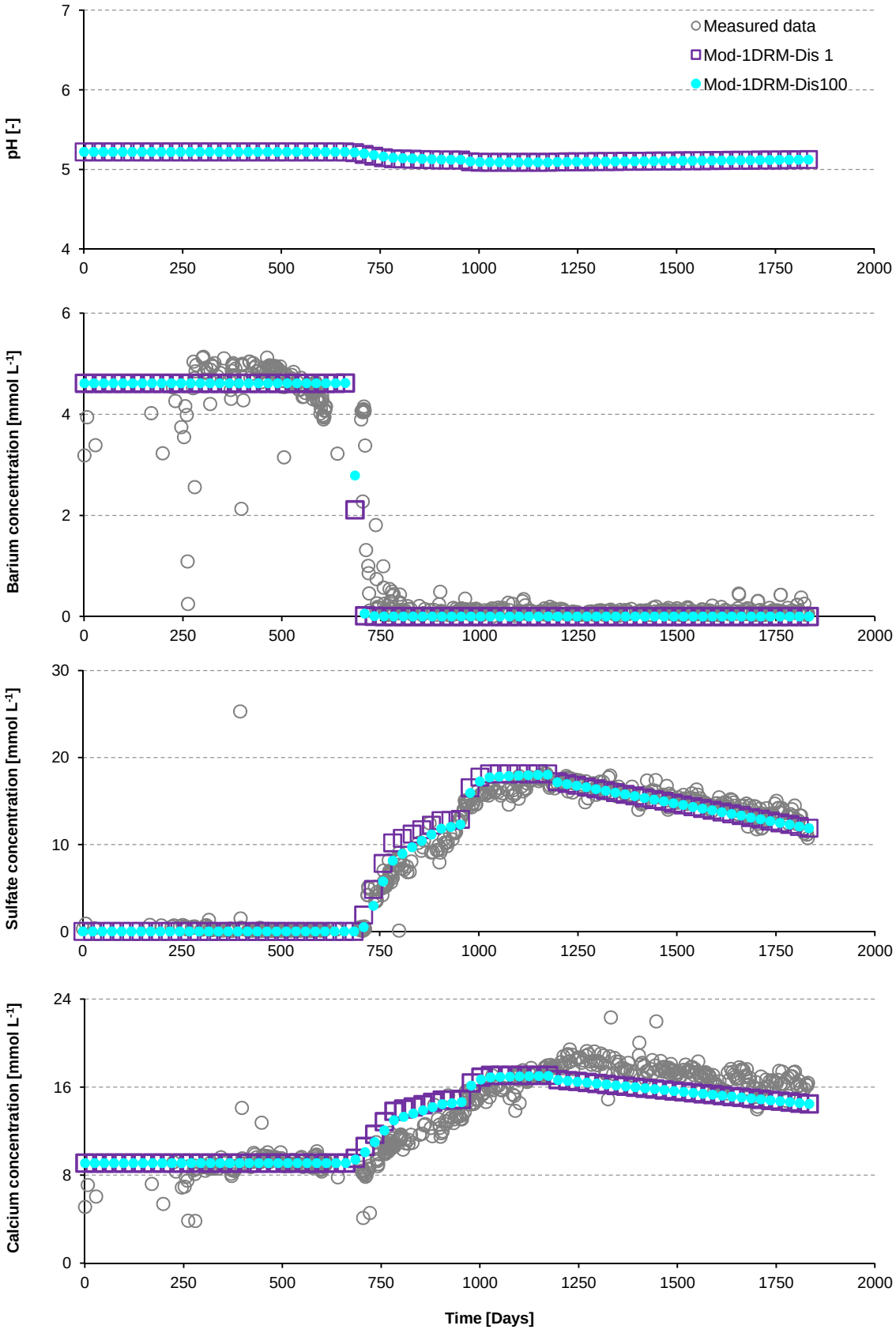

Fig. A7: Measured and modeled pH as well as concentrations of barium, sulfate, and calcium in the produced water from scenarios 1DRM-Dis1 and 1DRM-Dis100. Measured data: taken from Houston, 2007.

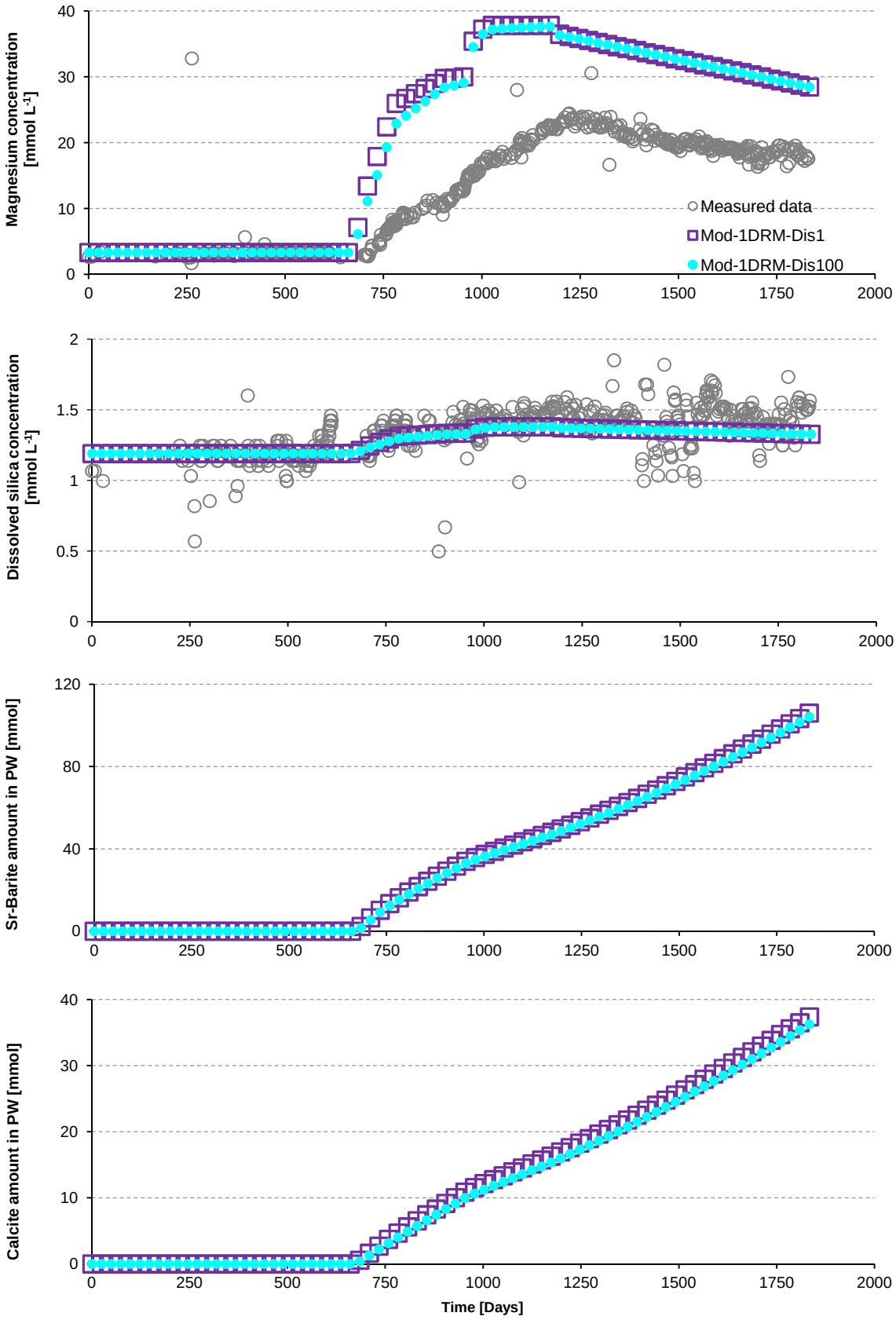

Fig. A8: Measured and modeled concentrations of magnesium and dissolved silica in the produced water and amount of Sr-barite and calcite newly formed in the production well (PW) per 75 liter produced water from scenarios 1DRM-Dis1 and 1DRM-Dis100. Measured data: taken from Houston, 2007.

A6. Modeling results calculated by scenario 1DRM-Pi.

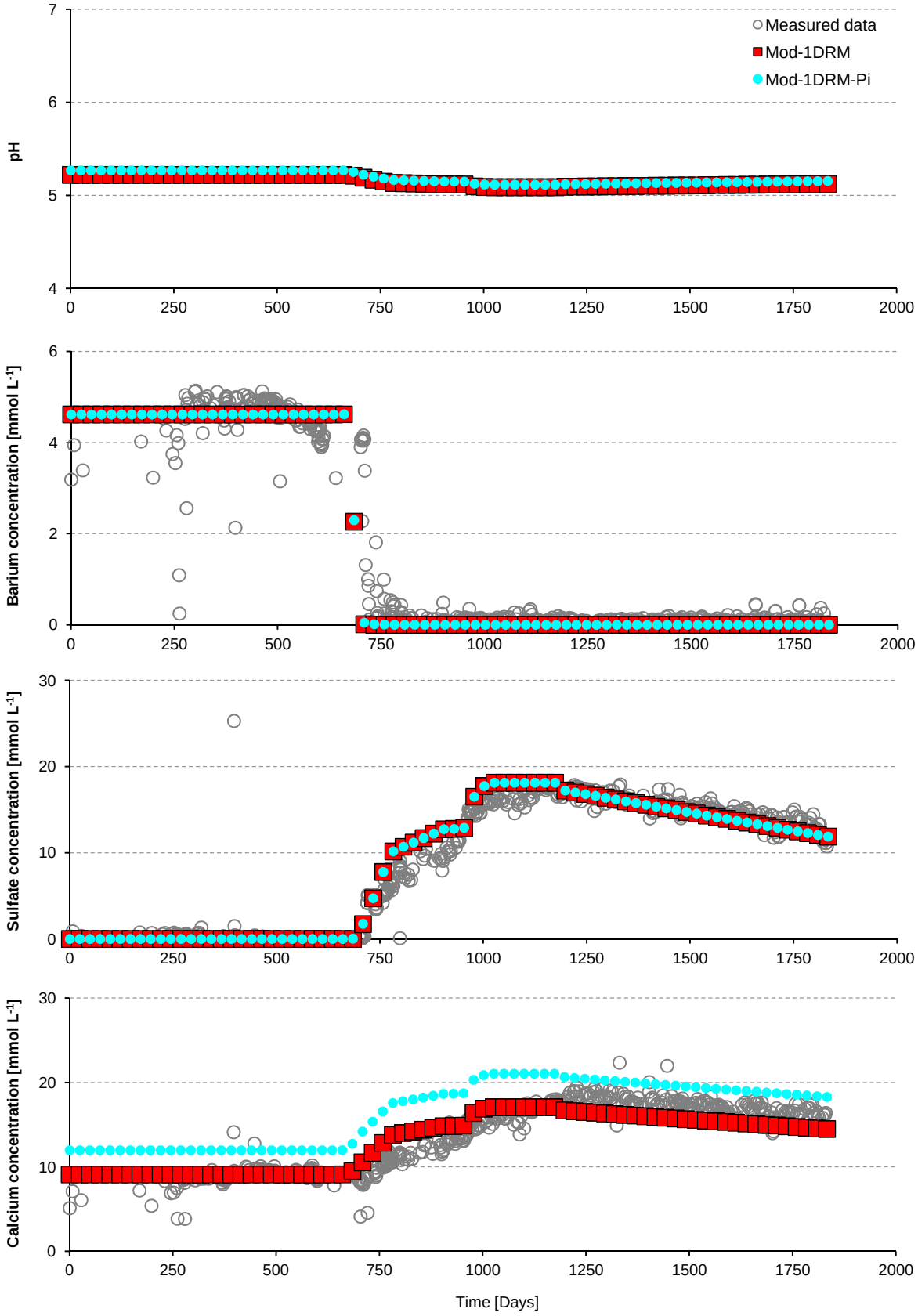

Fig. A9: Measured and modeled pH as well as concentrations of barium, sulfate and calcium in the produced water from scenarios 1DRM and 1DRM-Pi. Measured data: taken from Houston, 2007.

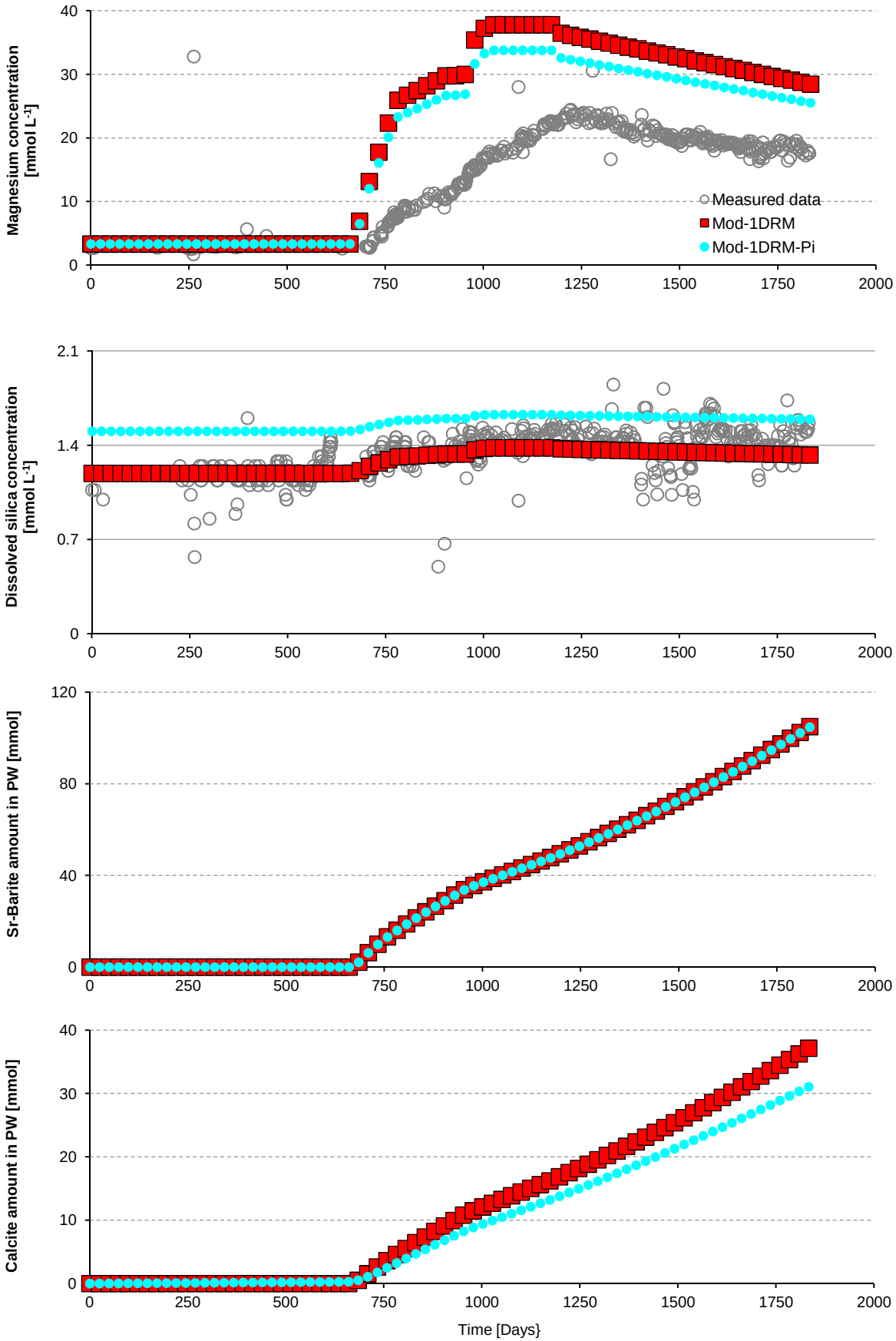

Fig. A10: Measured and modeled concentrations of magnesium and dissolved silica as well as the modeled amount of Sr-barite and calcite in the production well (PW) per 75 liter produced water from scenarios 1DRM and 1DRM-Pi. Measured data: taken from Houston, 2007.

A7. Measured X-ray diffraction pattern of the bulk samples taken from the well Sandra A.

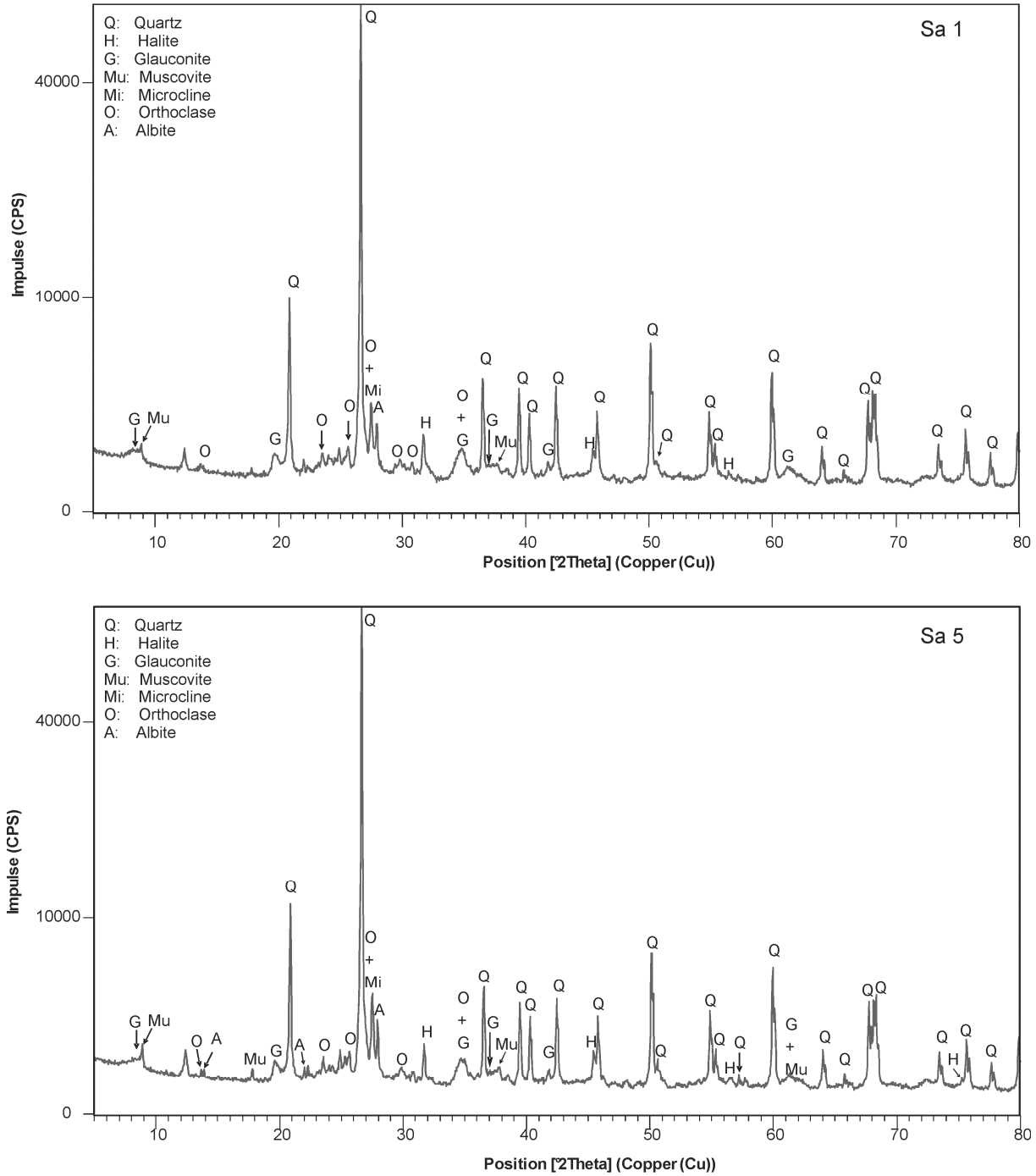

Fig. A11: Measured X-ray diffraction pattern of the bulk samples Sa 1 and Sa 5.

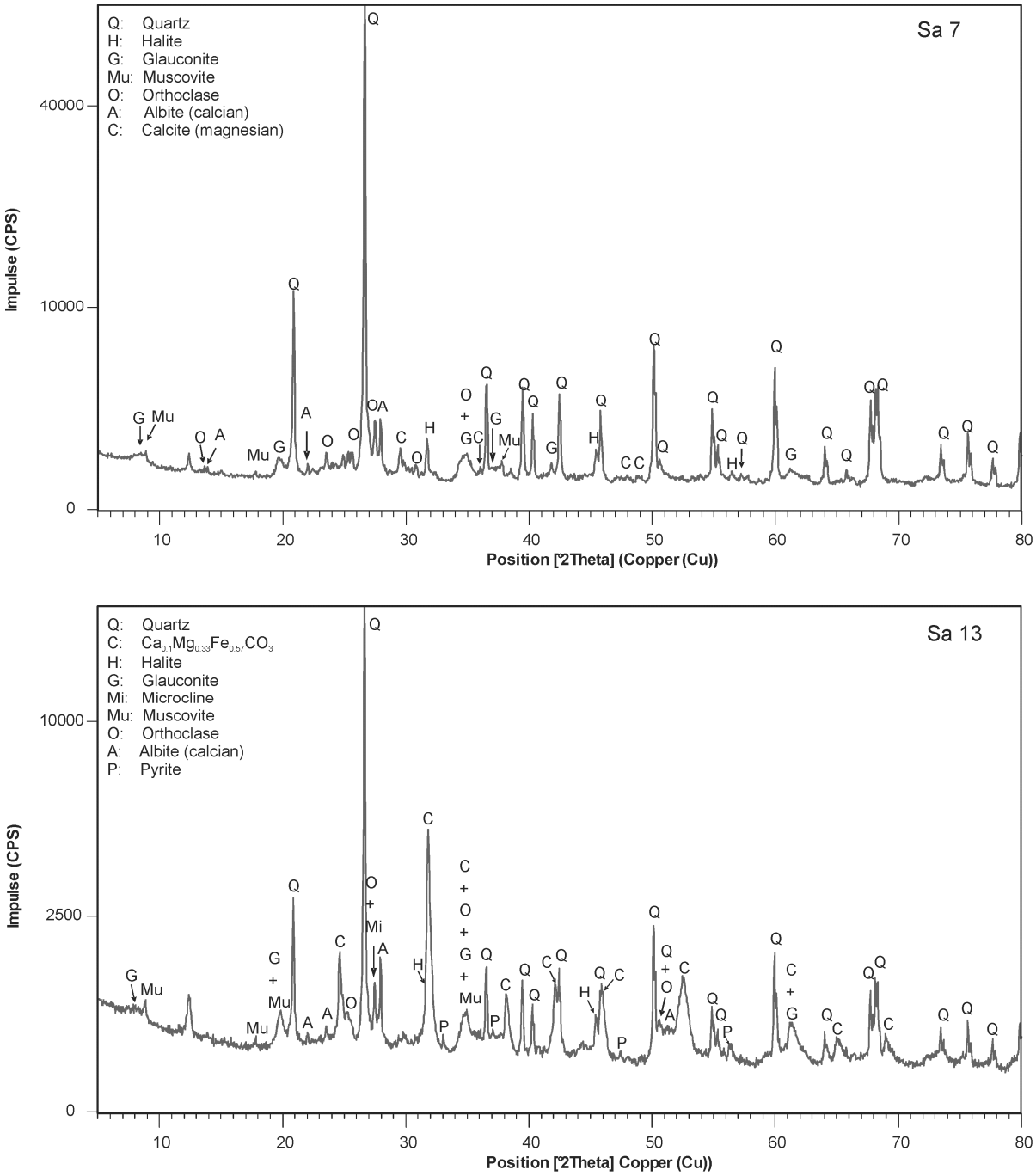

Fig. A12: Measured X-ray diffraction pattern of the bulk samples Sa 7 and Sa 13.

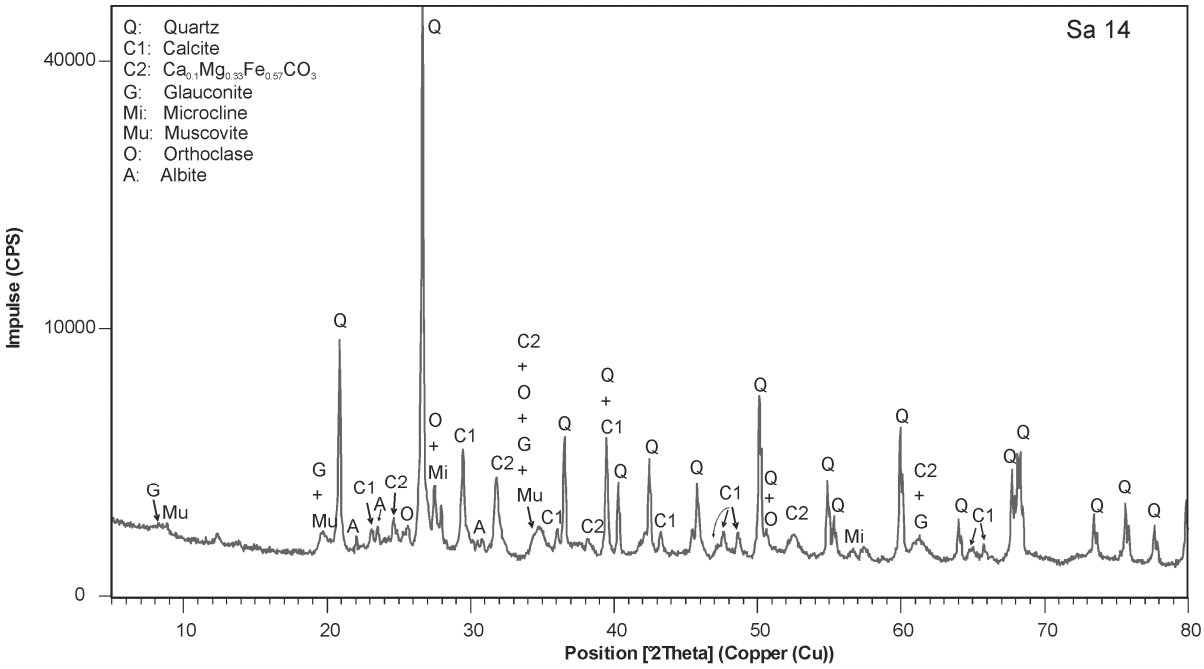

Fig. A13: Measured X-ray diffraction pattern of the bulk sample Sa 14.

A8. Geochemical composition of the bulk rock samples taken from the well Siri A and Sandra A by using XRF.

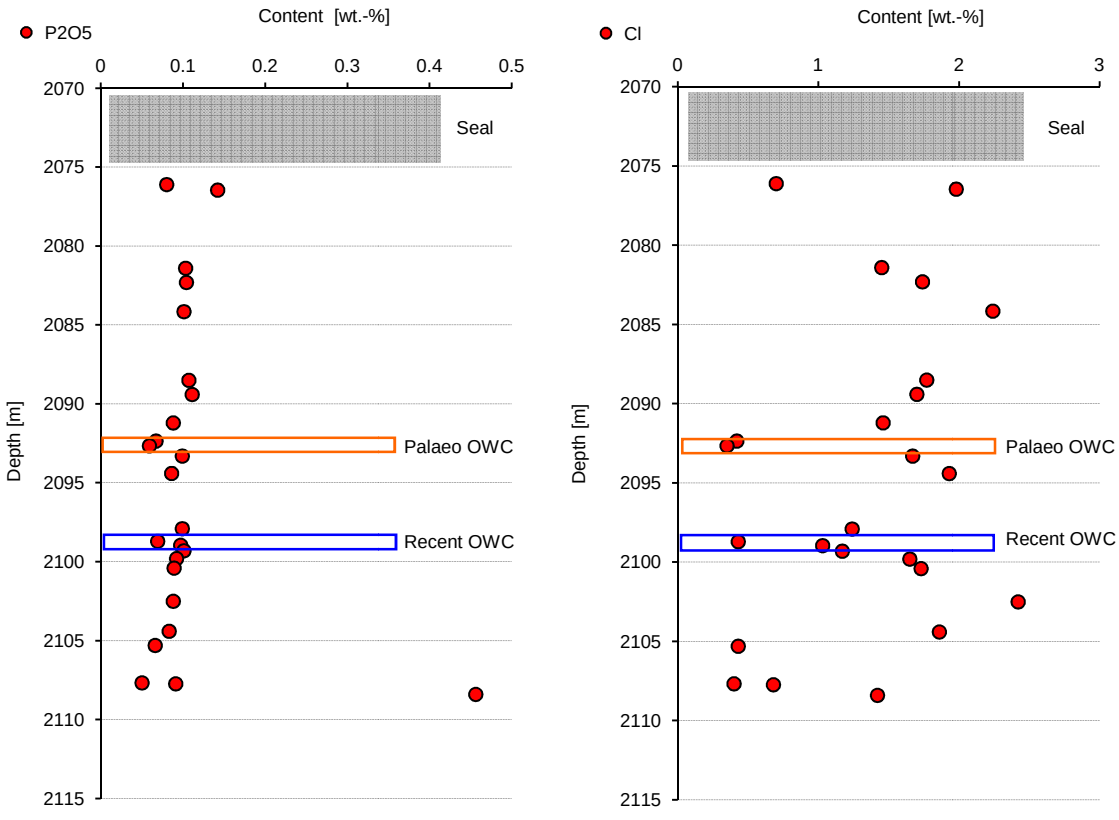

Fig. A14: Measured content of phosphorus and chloride in the bulk samples of the well Siri A.

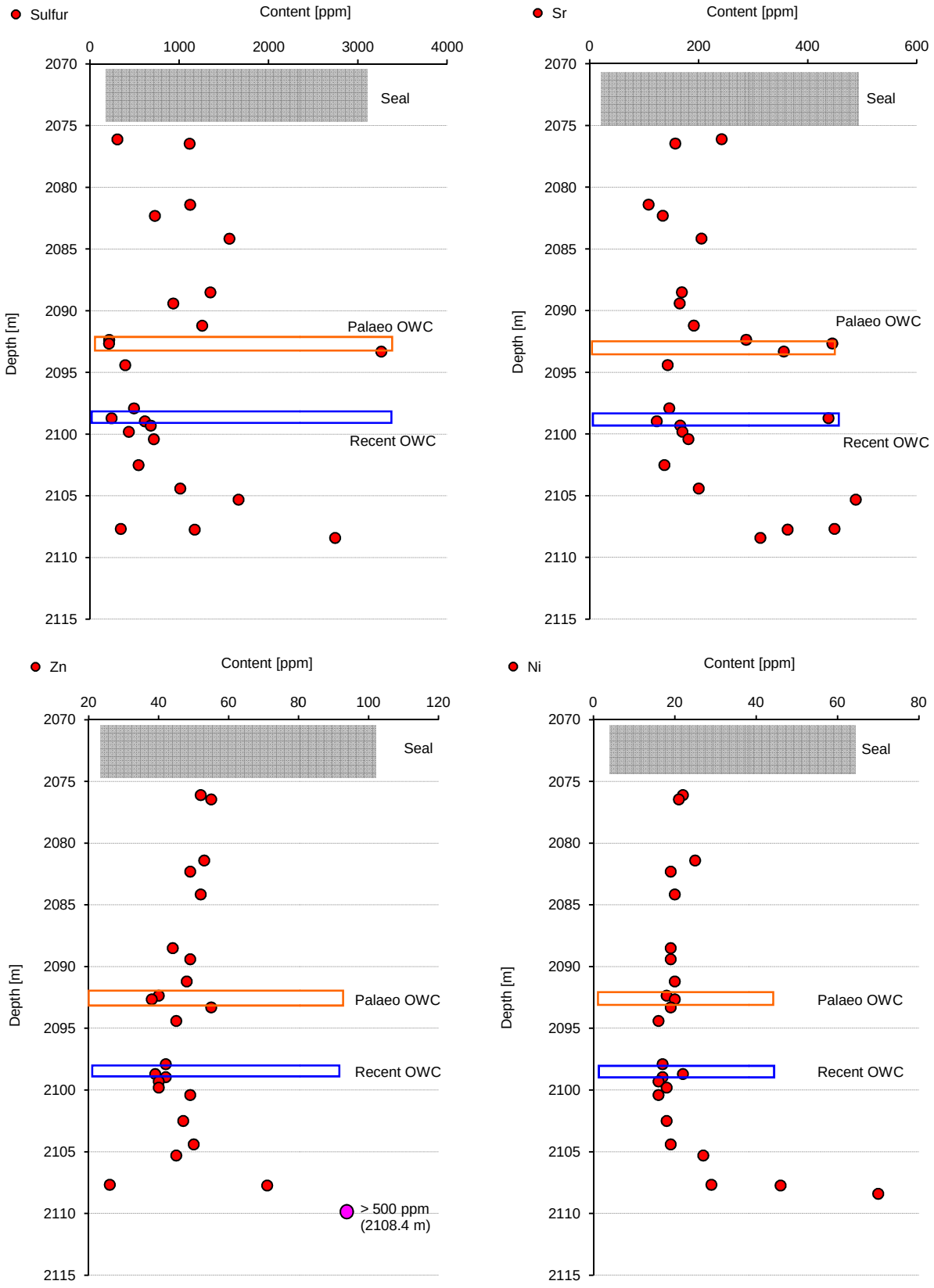

Fig. A15: Measured content of sulfur, strontium, zinc and phosphorus and nickel in the bulk samples of the well Siri A.

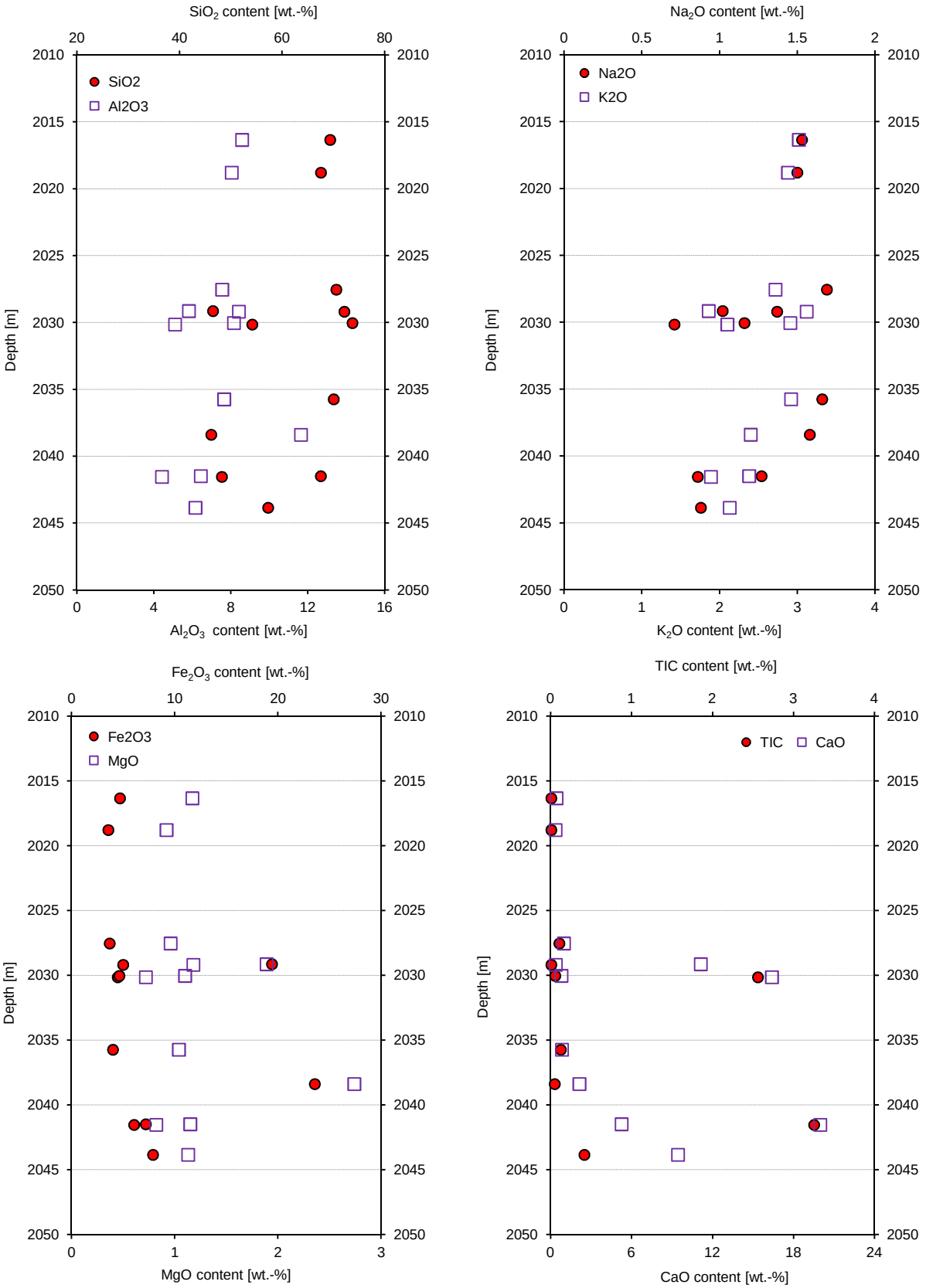

Fig. A16: Measured content of silica, aluminum, sodium, potassium, iron, magnesium, TIC, and calcium in the bulk samples of the well Sandra A.

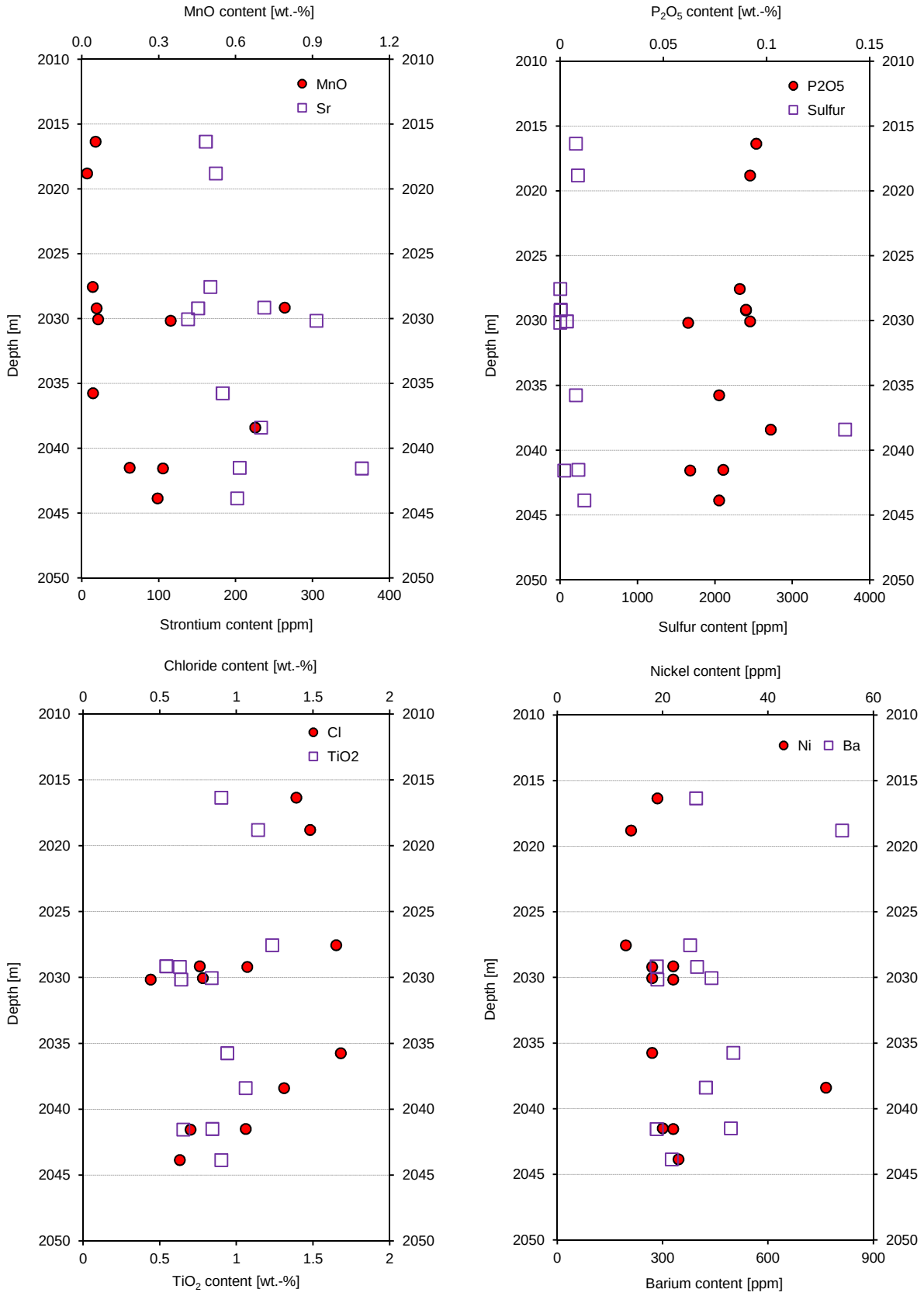

Fig. A17: Measured content of manganese, strontium, phosphorous, sulfur, chloride, titanium, nickel and barium in the bulk samples of the well Sandra A.

A9. PHREEQCI input file for modeling scenario Gl1_ODP.

```
PHASES
Glauconite
        K0.489Na0.045Mg0.281Al1.387Fe1.183Si3.327O10(OH)2 + 10H2O = 0.489K+ + 0.045Na+ +
0.281Mg+2 + 1.387Al(OH)4- + 1.069Fe+3 + 0.114Fe+2 + 3.327H4SiO4 + 3.144OH-
        -log_k          -71.43
        -delta_h        42.492 kcal
        -Vm 154.79 cm3/mol

Berthierine
        Fe1.738Mg0.417Al0.95Si1.71O5(OH)4 + 7.16H+ = 1.738Fe+2 + 0.417Mg+2 + 0.95Al+3 +
1.71H4SiO4 + 2.16H2O
        -log_k          16.059
        -delta_h -60.27 kcal
        -Vm 109.63 cm3/mol

Chlorite7A              #from wateq4f.dat
        Mg5Al2Si3O10(OH)8 + 16H+ = 5Mg+2 + 2Al+3 +3H4SiO4 + 6H2O
        -log_k          71.752
        -delta_h -155.261 kcal

Magnesite               #from wateq4f.dat
        MgCO3 = Mg+2 + CO3-2
        -log_k          -8.029
        -delta_h -6.169 kcal


Solution 1
pH              6.314
temp            78      # Nice et al., 2000
units           mol/l
density         1.012
Cl              1.0
Na              1.0

Equilibrium_Phases 1
Quartz                  0.0 52.92
Glauconite              0.0 0.951
Berthierine             0.0 0.0
Kaolinite               0.0 0.0
Chalcedony              0.0 0.0
Chlorite7A              0.0 0.0
Fe(OH)3(a)              0.0 0.0

Reaction_Pressure 1
230

Save Solution 2
END

Use Solution 2
Equilibrium_Phases 2
Quartz                  0.0 52.92  dissolve_only
Glauconite              0.0 0.951
Albite                  0.0 0.0
K-Feldspar              0.0 0.0   dissolve_only
K-mica                  0.0 0.0
Berthierine             0.0 0.0
Calcite                 0.0 0.0
Dolomite                0.0 0.0
```

Magnesite 0.0 0.0
Siderite 0.0 0.0
Kaolinite 0.0 0.0
Chalcedony 0.0 0.0
Chlorite7A 0.0 0.0
Fe(OH)3(a) 0.0 0.0

Gas_Phase 2
-fixed_pressure
-pressure 230
CO2(g) 0.0
CH4(g) 0.0
H2(g) 0.0

Reaction 2
CH4 1.0
CO2 2.0
H2 5.0
0.1 moles in 10 steps

END

A10. Equilibrium constants (log_K) of minerals which calculated by the computer code PHREEQCI under the reservoir conditions (78 °C and 230 atm) for the 3DHRT model.

K-Feldspar_78_230
KAlSi3O8 + 8H2O = K+ + Al(OH)4- + 3H4SiO4
log_K -17.21

Albite_78_230
NaAlSi3O8 + 8H2O = Na+ + Al(OH)4- + 3H4SiO4
log_K -15.15

Anorthite_78_230
CaAl2Si2O8 + 8H2O = Ca+2 + 2Al(OH)4- + 2H4SiO4
log_K -18.22

Berthierine_78_230
Fe1.738Mg0.417Al0.95Si1.71O5(OH)4 + 7.16H+ = 1.738Fe+2 + 0.417Mg+2 + 0.95Al+3 + 1.71H4SiO4 + 2.16H2O
log_K 9.61

Calcite_78_230
CaCO3 = Ca+2 + CO3-2
log_K -8.77

CH4(g)_78_230
CH4 = CH4
log_K -3.17

CO2(g)_78_230
CO2 = CO2
log_K -1.96

Dolomite_78_230
CaMg(CO3)2 = Ca+2 + Mg+2 + 2CO3-2
log_K -17.76

Glauconite_78_230
K0.489Na0.045Mg0.281Al1.387Fe1.183Si3.327O10(OH)2 + 10H2O = 0.489K+ + 0.045Na+ + 0.281Mg+2 + 1.387Al(OH)4- + 1.069Fe+3 + 0.114Fe+2 + 3.327H4SiO4 + 3.144OH-
log_K -66.10

Kaolinite_78_230
Al2Si2O5(OH)4 + 6H+ = 2Al+3 + 2H4SiO4 + H2O
log_K 3.43

K-mica_78_230
KAl3Si3O10(OH)2+10H+=K+ +3Al+3 +3H4SiO4
log_K 6.03

Quartz_78_230
SiO2 + 2H2O = H4SiO4
log_k -3.28

Siderite_78_230
FeCO3 = Fe+2 + CO3-2
log_K -11.00

A11. Modeling results of scenario 3DHRT.

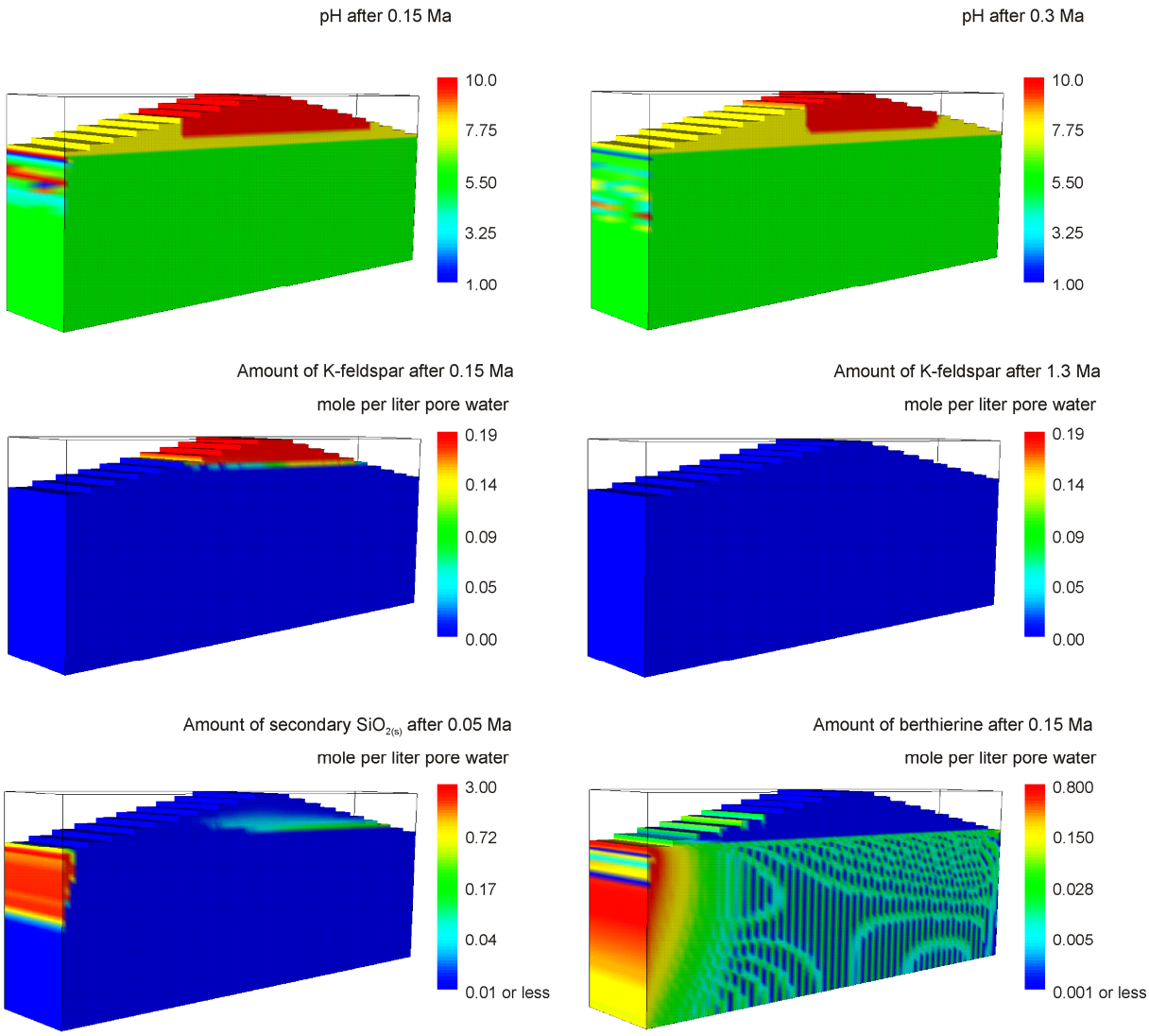

Fig. A18: Additional modeling results calculated by scenario 3DHRT for different modeling steps.

A12. Modeling results of scenario 3DHRT_flux.

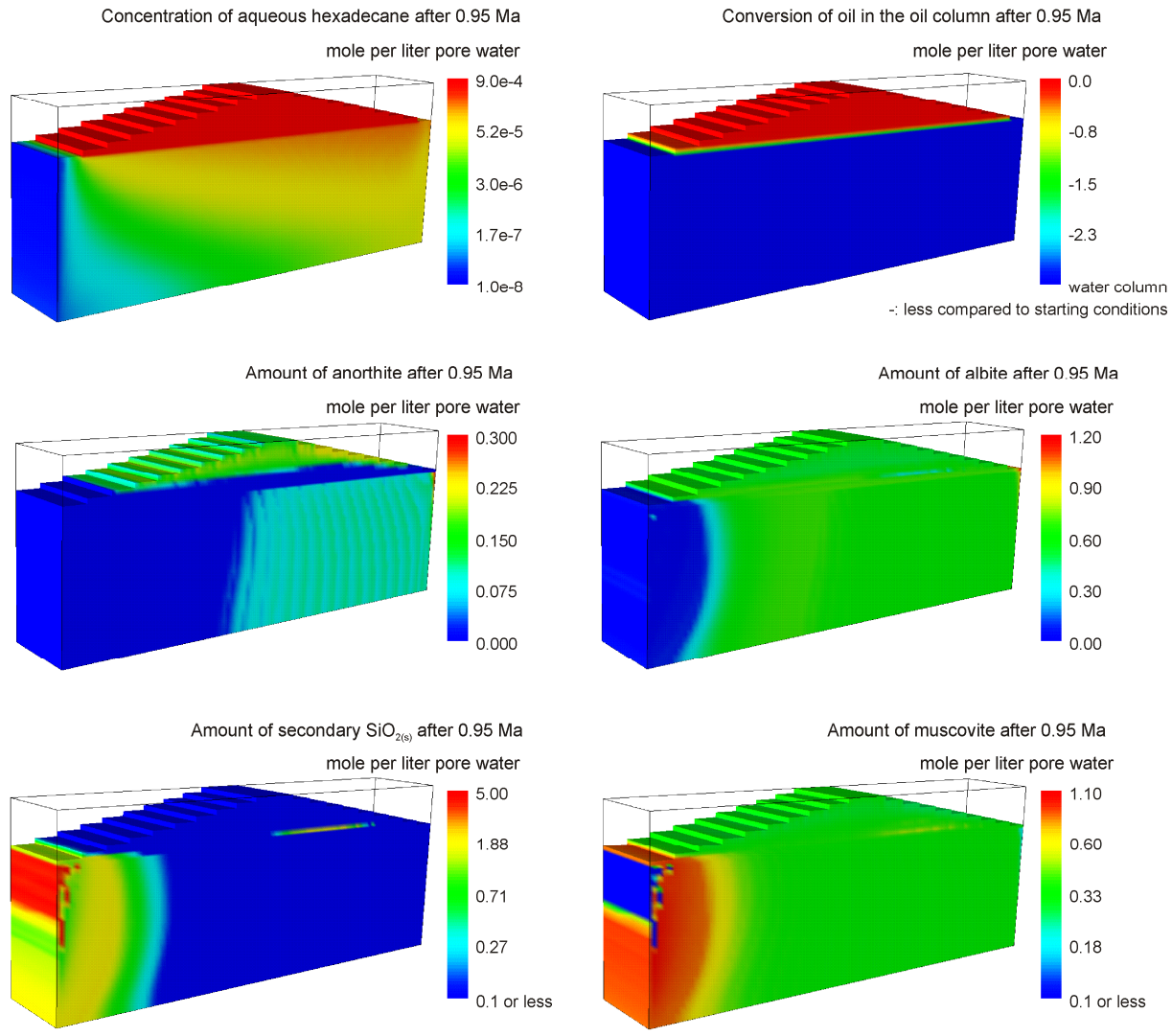

Fig. A19: Additional modeling results calculated by scenario 3DHRT_flux.

A13. Modeling results of scenario 3DHRT_chalkCO2.

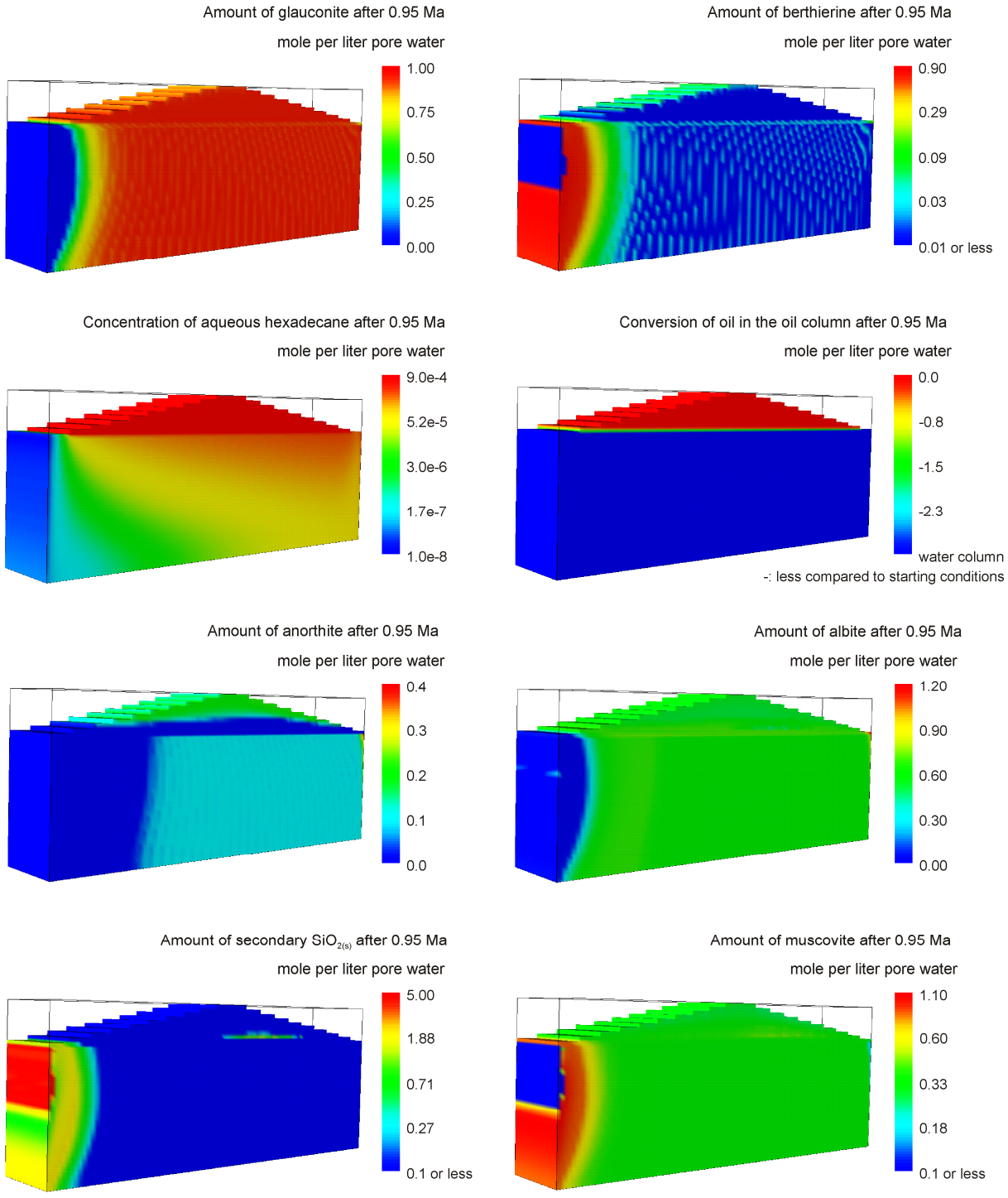

Fig. A20: Additional modeling results calculated by scenario 3DHRT_chalkCO2.

A14. Modeling results of scenario 3DHRT_pCO2.

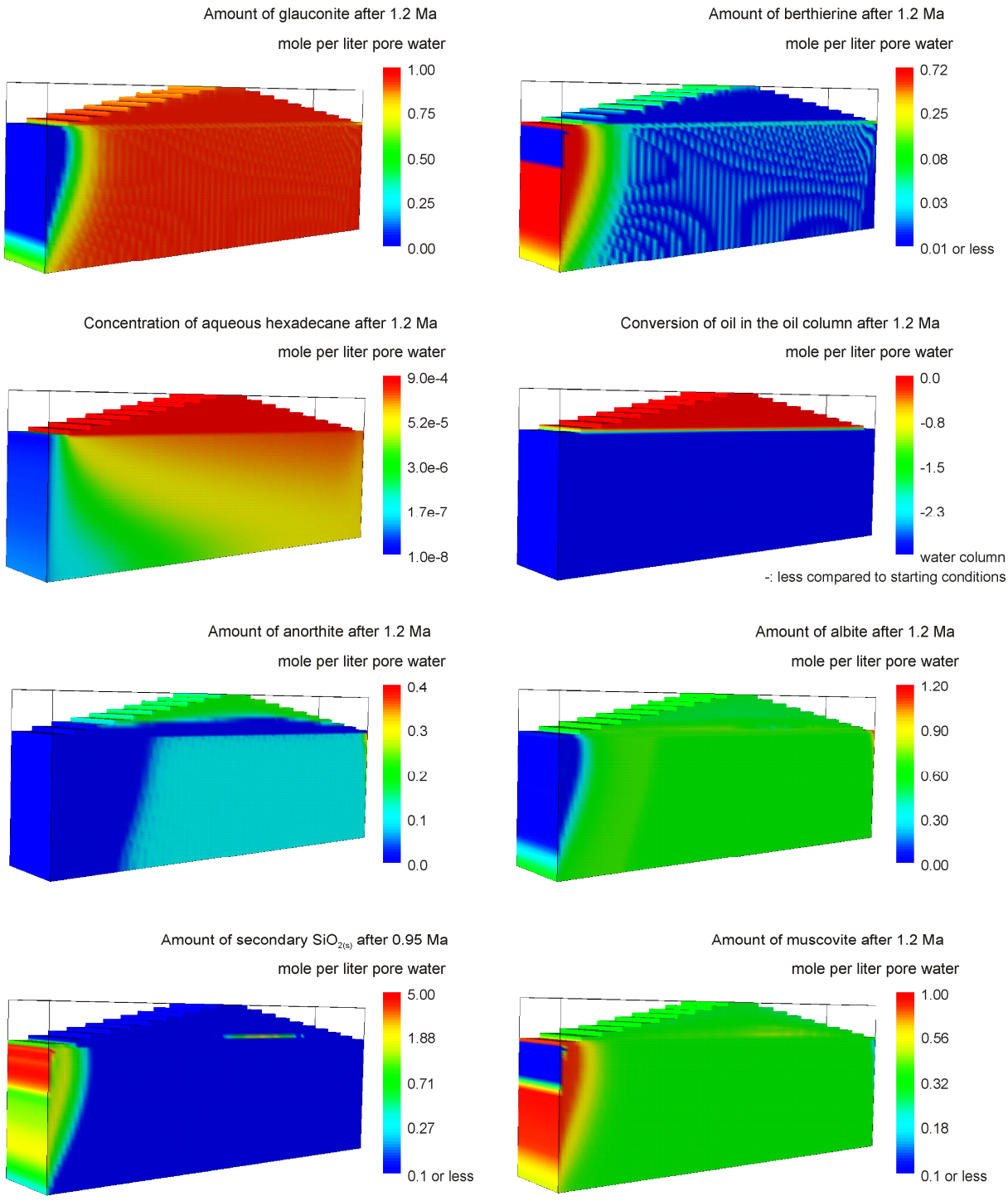

Fig. A21: Additional modeling results calculated by scenario 3DHRT_pCO2.